

Aerodynamic Impact of Swirling Combustor Inflow on Endwall Heat Transfer and the Robustness of the Film Cooling Design in an Axial Turbine

Vom Fachbereich Maschinenbau
an der Technischen Universität Darmstadt
zur
Erlangung des Grades eines Doktor-Ingenieurs (Dr.-Ing.)
genehmigte

D I S S E R T A T I O N

vorgelegt von

Holger Werschnik, M.Sc.


aus Mainz

Berichterstatter:	Prof. Dr.-Ing. Heinz-Peter Schiffer
1. Mitberichterstatter:	Prof. Thomas Povey, BA, MA, DPhil
Tag der Einreichung:	27. April 2017
Tag der mündlichen Prüfung:	19. Juli 2017

Darmstadt 2017

Bibliografische Information der Deutschen Nationalbibliothek:

Die Deutsche Nationalbibliothek verzeichnet diese Publikation in der Deutschen Nationalbibliografie; detaillierte bibliografische Daten sind im Internet über <http://dnb.d-nb.de> abrufbar.

 Creative Commons Lizenz (CC BY 4.0 International), 2017.
Freies Vervielfältigen und Weiterverbreiten – Namensnennung

Editor's preface

The series *Research Reports by the Institute of Gas Turbines and Aerospace Propulsion* accounts for the advances in research and development in the field of turbomachinery at Technische Universität Darmstadt. Because of the strong orientation on applications in this research field, the academic problems reflect industrial development trends.

The changing political, economic and ecological framework influences the current development focus and keeps carrying the turbomachine to the border of technological feasibility. As a result, it is not unusual for findings to be directly transferred to the industrial application.

Within this environment, the industry and application oriented research works of this series originate. They describe current findings of experimental investigations and numerical simulations which were obtained at the Institute of Gas Turbines and Aerospace Propulsion at Technische Universität Darmstadt.

Heinz-Peter Schiffer

Darmstadt, 2017

Author's preface

This dissertation originated during my time as a research assistant at the Institute of Gas Turbines and Aerospace Propulsion at Technische Universität Darmstadt. First of all, I would like to express my gratitude to my advisor Prof. Dr.-Ing. Heinz-Peter Schiffer, head of the Institute, for giving me the opportunity to work on the Large Scale Turbine Rig. I enjoyed to work on this challenging project and I am especially thankful about the great responsibility that I have been assigned and the involved possibility to develop personally and scientifically. I appreciate his tremendous support and confidence during the course of my time at the institute.

Prof. Thomas Povey, DPhil from the Osney Thermo-Fluids Laboratory at the University of Oxford I thank for his interest in this thesis and the co-review of it.

I acknowledge the financial support within the framework of "AG Turbo" by the Federal Republic of Germany, Ministry for Economic Affairs and Energy, according to a decision of the German Bundestag (FKZ: 03ET2013K) as well as by Rolls-Royce Deutschland GmbH and Ansaldo Energia.

Furthermore, I want to thank the LSTR-Turbine-Group, namely Claudius Linker, Sebastian Schrewe, Alexander Krichbaum, Manuel Wilhelm, Tom Ostrowski, Sebastian Leichtfuss, Johannes Eitenmüller and Leonhard Gresser. They all have their share in setting up this unique test rig and its capabilities. I enjoyed the great working atmosphere in the office, the lab or our "networking events" such as the turbine group hiking and barbecue events.

I would like to thank the LSTR partners at Rolls Royce Deutschland, Roland Wilhelm, Knut Lehmann, Christoph Lyko and Thomas Janson and at Alstom/Ansaldo Marc Henze and Jörg Krückels. Their contribution of technical expertise were a great asset for my research and I appreciate the support to publish my results on several turbomachinery conferences and in journal papers.

All the colleagues at the institute I thank for the great working atmosphere during my time at the GLR. I especially appreciate the support of Marius Schneider and Manuel Wilhelm for proofreading my dissertation

Not to the last, I want to thank all my students, namely Carlos Sánchez-Utgés, Marcel Adam, Fari Bakhtiari, Daniel Arenz, David Neubauer, Johannes Stroh, Christoph Steinhausen, Nam Wahrenberg, Viktor Arne, Janina Herrmann, Sebastian Wiemer, Niklas Apell, Yannick Fischer, Peter Allard and Daniel Markus. They all have taken care of a part of the project tasks in their Bachelor-/Master-Thesis or

as a student assistant in the laboratory and in this way helped to finish it successfully.

Besonderer Dank gilt an dieser Stelle zudem meinen langjährigen Freunden Sascha Hell und Christian von Pyschow, mit denen ich die Doktorandenzeit gemeinsam und unter anderem bei zahlreichen Mensa-Mittagessen durchlebt habe.

Für die stete Unterstützung und Motivation während meines gesamten Studiums und der Promotion danke ich meinen Eltern Iris und Herbert sowie meinem Bruder Nils.

Ich danke meiner Tochter Lea, die mir geholfen hat, die "komplexen" Problemstellungen im richtigen Verhältnis zu betrachten und mich dabei immer mit guter Laune und ablenkenden Alternativbeschäftigungen versorgt hat. Es especial, quiero agradecer un monton a mi esposa Galina por el tremendo soporte y el buen animo que me dio durante todos los años de mi doctorado.

Holger Werschnik

Darmstadt, 2017

Abstract

The development of new gas turbines and aero engines is dedicated to reduce pollutant emissions in addition to the continuous strive to improve component efficiency and the consumption of fossil fuels. To foster this trend, new combustion concepts have come into play such as lean combustion. Whereas the emission of carbon dioxide can be reduced by lower fuel consumption, the formation of thermal nitrogen oxide can only be hindered by a leaner fuel-to-air mixture: Lower peak temperatures and avoiding a stoichiometric concentration in the combustion chamber slow the thermal reaction process responsible for the formation of nitrogen oxides.

Swirl and a recirculation zone are used to stabilize the combustion process and a redistribution of mass flow towards the endwalls occurs. Additionally, a changed temperature profile with reduced peak temperature, but increased temperature near both endwalls due to the reduced injection of dilution air in the combustor approaches the subsequent turbine stage. Associated, positive and negative incidence, high turbulence intensities and increased thermal load to the endwalls challenge the turbine design.

To improve the understanding of the complex aerodynamic and aerothermal interaction, the aerodynamic impact of combustor swirl on the first vane row of a turbine, the nozzle guide vane (NGV), is investigated. The experiments are conducted at the Large Scale Turbine Rig (LSTR) in Darmstadt, which consists of a 1.5-stage axial turbine that is subject to an engine-representative swirl. A combustor simulator is used to vary the inflow to the turbine. Further goals of the investigation are to evaluate the robustness of its endwall film cooling design and to investigate endwall heat transfer and film cooling effectiveness experimentally by using infrared thermography and the auxiliary wall method.

As a reference, axial and low-turbulent inflow to the turbine is investigated. A variation of the coolant mass flow rate highlights the influence on Nusselt numbers and film cooling effectiveness as well as the aerodynamic flow field. An increase of Nusselt numbers by up to 80 % is observed with a concurrent increase of the film cooling effectiveness by up to 25 %. In a combined analysis a significant heat flux reduction due to film cooling by 30 % is achieved. A coolant mass flow rate (MFR) of one yields the greatest benefit. For higher MFR the further improvement of the film cooling effectiveness is counteracted by the even greater increase in heat transfer.

With applied swirl, the flow field changes significantly. Averaged whirl angles of 15° to 20° and a mass flow redistribution to the endwalls are detected. The NGV exit flow exhibits a dominating influence of swirl on pressure losses instead of the coolant flows as it had been observed for the baseline. For similar settings of the stage parameters, an increase in Nusselt numbers by up to 40 % is observed. The film cooling effectiveness is reduced because of the mass flow redistribution. For MFR greater than 1.5, the increase in Nusselt numbers is less decisive and remains at a similar level to the reference case. To achieve the same level of film cooling, the

double amount of coolant air is necessary. These general trends are resolved for two clocking positions between swirler and vanes, whereby local differences are observed. The combined analysis of the thermal parameters shows a local increase of endwall heat flux and a local influence on the coolant injection. The coolant injection is still beneficial in reducing the heat flux for low injection rates, but the local extent varies much more. For higher injection rates above 1.5, only sections of the endwall face an improvement and there is a growing area, where increased heat flux and in consequence higher thermal load is applied in comparison to the reference.

Kurzzusammenfassung

Neben der Zielsetzung hoher Komponentenwirkungsgrade und niedrigem Brennstoffverbrauchs wird bei der Entwicklung neuer stationärer Gasturbinen und Flugtriebwerke angestrebt, die Schadstoffemissionen weiter zu verringern. Um diesen Entwicklungstrend weiterführen zu können, ist der Einsatz neuer Verbrennungskonzepte wie der Magerverbrennung notwendig. Während eine Reduktion der Kohlenstoffdioxidemissionen durch eine Verbrauchsminderung erreicht werden kann, ist für eine Senkung der Stickoxidemissionen ein mageres Brennstoff-Luft-Gemisch unerlässlich: Die thermische Bildung von Stickoxiden wird durch geringere Maximaltemperaturen sowie die Vermeidung stöchiometrischer Konzentrationen in der Brennkammer vermindert. Dieser Verbrennungsprozess wird durch eine starke Drallströmung und die einhergehende Ausbildung einer Rezirkulationszone stabilisiert, und eine Umverteilung des Massenstroms zu den Endwänden tritt auf. Weiterhin entsteht ein flacheres Eintrittstemperaturprofil in der Zuströmung der nachfolgenden Turbine durch den reduzierten Einsatz von Zumischluft im Brennkammeraustrittssektor. Bei der Auslegung der Turbine müssen aus diesem Grund hohe Turbulenzgrade, Inzidenz sowie eine erhöhte thermische Belastung der Endwände beachtet werden.

Um das Verständnis für die komplexen aerodynamischen Vorgänge und aerothermischen Interaktionen zu verbessern, wird die Auswirkung erhöhten Brennkammerdralls auf die erste Leitschaufelreihe am Large Scale Turbine Rig (LSTR) in Darmstadt an einer 1,5-stufigen Axialturbine untersucht. Die verdrallte Zuströmung ist dabei repräsentativ für eine reale Maschine. Ein Brennkammermodul ermöglicht Variationen in der Zuströmung der Turbine, um auf diese Weise die Robustheit der Endwandkühlung zu untersuchen. Der Wärmeübergang sowie die Filmkühleffektivität auf der Endwand werden experimentell mit Hilfe von Infrarotthermographie und der Hilfswandmethode untersucht.

Dabei wird eine axiale Zuströmung mit niedrigem Turbulenzgrad als Referenz untersucht. Eine Variation des Massenstroms, der zur Endwandkühlung eingeblasen wird, verdeutlicht den Einfluss auf Nusseltzahlen, Filmkühleffektivitäten sowie das aerodynamische Strömungsfeld. Die Nusseltzahlen erhöhen sich mit steigendem Kühlluftmassenstrom im Mittel um 80 %, während die Filmkühleffektivität nur um 25 % zunimmt. Mit einer kombinierten Auswertung der beiden Parameter kann die Minderung des Wärmestroms bestimmt werden. Dabei zeigt sich bei einer Einblaserate von 1 % des Hauptmassenstroms das Optimum für die vorliegende Geometrie. Bei höheren Einblaseraten wird die eintretende Verbesserung der Kühlung durch die stärkere Erhöhung des Wärmeübergangskoeffizienten größtenteils aufgezehrt.

Bei aufgeprägtem Brennkammerdrall ändert sich das Strömungsfeld in der Statorreihe deutlich: Mittlere Drallwinkel von 15° bis 20° und eine Umverteilung des Massenstroms zu den Endwänden werden festgestellt. Die Abströmung der NGV-Stufe wird vornehmlich durch die Auswirkung des Dralls auf die Druckverluste charakterisiert. Der große Einfluss der Kühlluft einblasung, der für die Referenzkonfiguration

festgestellt wurde, tritt nicht mehr auf. Bei gleicher Einstellung der Stufengrößen im Vergleich zum Referenzfall liegen die Nusseltzahlen um bis zu 40 % höher, wogegen die Filmkühleffektivität um bis zu 40 % niedriger ist. Bei Einblaseraten über 1,5 % ist die Steigerung der Nusseltzahlen im Vergleich zur Referenzkonfiguration gering und ein ähnliches Niveau wird erreicht. Um die gleichen Werte für die Filmkühleffektivität wie im Fall der axialen Zuströmung zu erreichen, wird jedoch in etwa die doppelte Kühlluftmenge benötigt. Diese allgemeinen Feststellungen werden für beide untersuchten Relativpositionen zwischen Drallerzeuger und Schaufelvorderkante beobachtet, wobei sich lokale Unterschiede einstellen. Bei der kombinierten Analyse beider Parameter ergeben sich lokal zudem Gebiete, in denen eine Erhöhung des Wärmestroms stattfindet. Eine Reduktion des Wärmestroms wird für kleine Einblasemengen weiterhin erreicht, jedoch variiert das lokale Niveau deutlich stärker. Bei großen Einblaseraten treten hingegen größere Wärmeströme auf als im Referenzfall und die Endwand wird somit stärker thermisch belastet.

Contents

1	Introduction	1
1.1	Motivation	1
1.2	Research context and connection to other research projects	4
1.3	Outline	5
2	Theoretical background and literature review	7
2.1	Combustion and emissions	7
2.2	Combustor-turbine interaction	8
2.3	Endwall film cooling	14
2.4	Endwall heat transfer	22
2.5	Resulting heat flux reduction due to film cooling	27
2.6	Definition of research objectives for the thesis	28
3	Experimental setup	31
3.1	The Large Scale Turbine Rig	31
3.2	Combustor module	33
3.3	Operating point	37
3.4	Vane passage nomenclature	41
4	Experimental methods	43
4.1	Infrared thermography - auxiliary wall method	43
4.2	Gas concentration measurements	50
4.3	Pneumatic measurements	54
5	Investigation of the reference configuration	59
5.1	Aerodynamic flow field	59
5.2	Endwall film cooling	69
5.3	Endwall heat transfer	77
5.4	Resulting Heat Flux Reduction	80
5.5	Summary of the findings for the reference case	82
6	Investigation of swirling combustor inflow	85
6.1	Aerodynamic flow field	85
6.2	NGV aerodynamic loading	92
6.3	Endwall film cooling	102
6.4	Endwall heat transfer	111
6.5	Heat Flux Reduction due to film cooling	115
6.6	Summary of the findings for the swirling inflow case	117
7	Summary and Outlook	121
7.1	Suggestions for further research	123

Bibliography	127
Nomenclature	141
List of Figures	147
List of Tables	151
A Appendix: Overview	153
B Full measurement results for swirling inflow	155
C Comparison to the measurement uncertainty in comparable studies	163
D Commissioning measurement results	165
D.1 Operating point	165
D.2 Results	165
E Increased turbulence intensity inflow	169
E.1 Aerodynamic flow field	169
E.2 Endwall heat transfer and film cooling	169
E.3 Summary of the findings for the increased turbulence intensity case . .	172
F Endwall streamline detection	173
G Curriculum Vitae	175

1 Introduction

This chapter illustrates the intention and the background of the thesis and gives an overview on the research field. Furthermore, the research focus and the importance of the combustor-turbine interface for engine design are explained. Finally, the research objective and the outline of the thesis are presented.

1.1 Motivation

Gas turbines are the most common machines for aircraft propulsion and are also widely deployed in power generation. They are heat engines and convert chemical energy into mechanical work. In the case of a propulsion device, they generate kinetic energy as well. Among their advantages is the production of a very large amount of power with respect to their dimension and weight (Lechner and Seume [86]). Since the first machines, built by von Ohain and Whittle, the main components have not changed (c.f. Fig. 1.1):

- The air is compressed in the **compressor** to a high pressure level to achieve high efficiency. Large gas turbines usually feature axial flow compressors with multiple stages. A part of the compressed air is extracted and used for cooling purposes of the subsequent hot sections.
- In the **combustion chamber** fuel is injected and combusted, increasing the gas temperature to a very high level of up to 1900 K.
- The hot gas is expanded within several **turbine** stages and mechanical power is generated. This is partly used to drive the compressor, mounted on the same shaft. In the case of a stationary gas turbine, the remaining shaft power is converted into electric power and in the case of an aircraft propulsion gas turbine the air is exhausted with significant kinetic energy to produce thrust.

The design of the components requires specialized knowledge, expertise, design tools and models. Usually, the aerodynamic and mechanical design process is split and executed by dedicated groups among gas turbine manufacturers. The design implies a profound knowledge of the boundary conditions at each station for a good design. With the uncertainty involved in the complex flow field and the strive to limit safety margins to only the necessary, an integrated design process is aspired. This is where combustor-turbine interaction (CTI) research comes into play. The interface between the two main components (c.f. Fig. 1.1) is crucial in engine design, because it constitutes the hottest area in the gas path and is therefore subject to very high thermal load. Knowing the boundary conditions of the turbine inflow with more detail is an asset in improving the performance of the turbine. Due to the complex flow field uncertainties remain. The robustness of a design to deviations from the design conditions is a very important aspect. In addition, the trend to use stationary

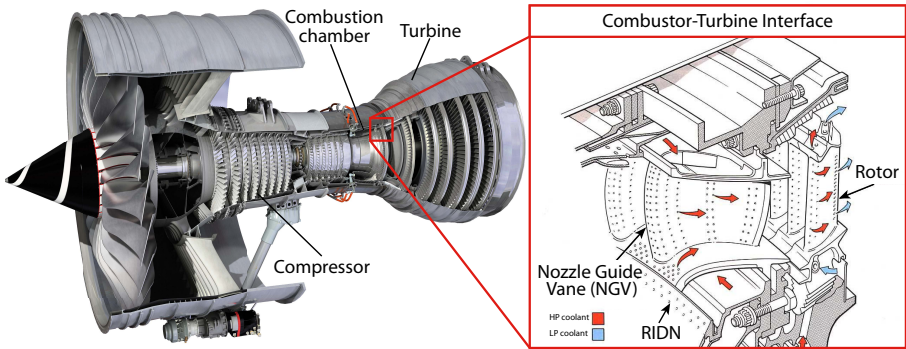


Figure 1.1: Modern gas turbine engine. Illustration of the main components and zoomed view on the combustor-turbine interface, showing the location of the RIDN coolant injection (adapted from Rolls-Royce [106][107])

gas turbines in a more flexible way to compensate load variations in national power grids require a more frequent operation at off-design conditions. In this context, an optimized design requires exact awareness of the incoming flow profile and any deviation can lead to inferior performance or even a lack of functionality. A robust design on the other hand can encounter deviations and ensure that the system retains its specifications also under altered conditions. Furthermore, combustor-turbine interaction is inherent in the design process. Not only does the combustor outflow influence the downstream turbine design. The presence of the turbine determines in the same manner the design of the combustor, as upstream effects of the turbine on the combustor flow occur. In addition, achievable swirl levels that could assist in improving the combustion process need to be limited to narrow the complexity of the flow field in the turbine to a predictable level (Turrell et al. [128]).

The fuel consumption of the gas turbine is a major cost contributor in air travel. Consequently, in the early years of the development, reducing the fuel consumption had been the focus of the development. Environmental awareness has led to legislative requirements regarding emissions and are complimented by the application of noise-ban rules. Therefore, a goal triangle in the design of gas turbines exist, with the aim to reduce noise and emissions in addition to the fuel consumption.

With component efficiencies of both combustor and turbine exceeding 90 %, a major optimization area of the gas turbine is its secondary air system (Schuler [118]), responsible for the coolant air supply. In the gas turbine cycle, the use of compressor air for cooling purposes is a significant contribution to the overall losses. Up to 30 % of the compressor air is used for cooling purposes in the combustor and turbine (Bräunling [22]). Thereby up to 10 % is injected to cool the first turbine stage. Cooling air constitutes a penalty to the engine efficiency because it does not fully contribute to the thermodynamic cycle. On the other hand, cooling air is required to control the material temperature of the turbine components. Furthermore, this is necessary in all operating point of the engine to ensure sufficient component life-

time. The gas temperature entering the high pressure turbine (HPT) is well above the melting temperature of the material of the vanes and blades. Thermal barrier coatings applied to the surfaces increase the bearable temperatures, but the thermal load needs to be taken care of by external and internal cooling methods for the engine parts. Efficient cooling techniques and a proper understanding of heat transfer parameters are necessary for the engine design as a consequence.

The recent development of lean burn combustors challenges turbine design. This development is driven by legislative requirements as well. For example, the Advisory Council for Aviation Research and Innovation in Europe (ACARE) to the European Commission has set a goal of a 90 % reduction of NO_x emissions compared to the year 2000 in its *Flightpath 2050* vision [2]. Furthermore, the ICAO Committee on Aviation Environmental Protection (CAEP) emits emission standards that apply to the type designs of future aircraft. Because air travel has experienced annual growth rates of 5% over the last decades and is forecast to increase with similar numbers in the future, the development of new technologies is necessary to limit the environmental impact. IATA envisions an environmentally sustainable growth and has suggested means to even achieve a reduction of the emissions. Data by Airbus [3] shows that within the recent 15 years, the fuel consumption and the CO_2 -emission has been reduced by 34 % per passenger and trip. However, significantly more advancements are to be made to achieve the IATA vision.

The application of lean combustion is such a technological breakthrough. However, less dilution air is used in the combustor and thereby a changed inlet temperature profile with increased temperature near the endwalls is imposed to the turbine. A crucial field is the thermal design of the turbine endwall. New design philosophies have to be developed to cope with the altered boundary conditions imposed by new combustor outlet flow profiles. This sets the scene for the present investigation.

The hub side endwall cooling of the first stator vane is of special interest to this thesis. The coolant air is injected at the CTI interface (c.f. zoomed view in Fig. 1.1) and denoted as RIDN-cooling (Rear Inner Discharge Nozzle). Whereas this coolant in early engine developments had mainly been used to set the desired radial temperature profile at turbine inlet by injecting colder air, it is used as for platform cooling nowadays. Its ejection characteristics and associated cooling capability largely depend on the adaptation to the incoming flow. In the context of this thesis, inlet boundary conditions representative for a lean combustor are investigated. This inflow includes residual swirl, imposed incidence at the first vane leading edge, an altered radial mass flow distribution and increased turbulence intensity. The robustness of the cooling design to these conditions needs to be evaluated. A proper distribution of the cooling air is crucial for a safe engine operation and sufficient lifetime of all components. For axial inflow there is large expertise of the factors of influence and various publications exist among the literature on cooling optimization under laboratory conditions. The complex flow field at the exit of a lean combustor however requires further investigation. An experimental investigation that models this inflow with a great level of detail is used to examine the robustness of a cooling design to inflow variations as specified above.

1.2 Research context and connection to other research projects

This investigation is part of a comprehensive approach to investigate the interaction between combustor and turbine within the research framework of "AG Turbo" during the course of several years (Werschnik et al. [136]). The content of this thesis is thereby primarily based on the project AG Turbo 2020 3.2.5 (grant number "FKZ 03ET2013K"), dedicated to the aerodynamic impact on endwall heat transfer and film cooling effectiveness on the hub of the NGV. In addition, some results have been acquired within the projects AG Turbo 3.2.1 A & C (grant numbers "FKZ 0327719F" and "FKZ 0327718R"). The focus in these projects is the aerodynamic effect of the swirling inflow on the turbine flow field. The measurement period and rig setup has been shared for the three projects. They are jointly funded by the German ministry of energy and transport, according to a decision of the German Bundestag, and by the industry partners Rolls-Royce Deutschland, Ansaldo Energia.

Subsequently, the projects COOREflex 3.1.1 (grant number "FKZ 03ET7021K") and 3.1.2 (grant number "FKZ 03ET7071O") continue the investigation with the focus on rotor hub and tip aerodynamics, film cooling and heat transfer.

Preceding work with respect to combustor-turbine interaction at the institute GLR include the dissertations of Giller [46], who investigated the aerodynamics of a stator row in a linear cascade with special regard to the influence on the film cooling ejection at the leading edge. Schmid [112] numerically investigated three test cases with increasing complexity: Giller's linear cascade, the LSTR setup and the Engine-3E (Klinger et al. [74]). The numerical approach is continued by Schneider and Schiffer [115] with a parametrized model of combustor exit flow conditions, that is used to study various turbine design optimizations and their robustness.

All research projects are conducted within the context of the University Technology Centre (UTC) of Rolls-Royce at Technische Universität Darmstadt with the focus on the aerothermal interaction of combustor and turbine.

1.3 Outline

The thesis begins with three basic chapters to familiarize the reader with the topic and the experimental setup:

Chapter 2: Theoretical background and literature review

An overview of the preceding work and the theoretical background is given. Relevant findings in the field of combustor-turbine interaction and a literature review on film cooling and heat transfer is presented. As a conclusion of the chapter, research objectives for this thesis are defined.

Chapter 3: Experimental setup

In this chapter, the Large Scale Turbine Rig (LSTR) and the experimental setup used for the present investigation is introduced.

Chapter 4: Experimental methods

The developed and applied measurement methods are illustrated.

The main part with the presentation and discussion of the experimental results is split into two chapters and followed by a summary:

Chapter 5: Investigation of the reference configuration

This chapter presents the findings for the axial inflow reference case.

Chapter 6: Investigation of swirling combustor inflow

The results for swirling inflow and its associated impact on the aerodynamic flow field, endwall heat transfer and film cooling effectiveness is investigated. The findings are presented in comparison to the reference case. The robustness of the endwall film cooling design to swirling inflow is evaluated based on the results.

Chapter 7: Summary and Outlook

A brief summary of the main results is given, followed by suggestions for future research.

2 Theoretical background and literature review

This chapter contains review on relevant literature regarding the content of this thesis. Two main aspects are addressed:

- Recent research findings from **combustor-turbine interaction** studies, both numerically and experimentally, are presented. The contribution of working groups to the understanding of the inherent changes to the incoming flow field towards the turbine and the derivation of design rules for the turbine are emphasized.
- A discussion of findings from past **endwall heat transfer and film cooling** studies. In this way, the theoretical background associated for the present investigation is illustrated.

2.1 Combustion and emissions

In the combustion chamber, fuel is injected into the flow and energy is added to the flow. The highly complex combustion process has to fulfill requirements on flame stability, safe operation and a desired exit temperature profile to maintain the turbine within the operating conditions. Furthermore, the chemical reaction and its conditions decide about the composition of the exhaust gas. Carbon dioxide (CO_2) is generated during the combustion and the amount increases proportional with the fuel consumption. In contrast, the formation of other pollutants such as carbon monoxide (CO), unburnt hydrocarbons (UHC), soot and nitrogen oxides (NO_x) largely depend on the peak temperature, the equivalence ratio Φ and the residence time in the combustor (Hennecke and Wörrlein [58]). Similar to CO_2 they can be reduced by a lower fuel consumption, the specific chemical reactions can be further controlled to set the total emissions to a minimum. Whereas CO and UHC are fostered by lower combustion temperatures, the thermal formation of NO_x increases rapidly with the combustion temperature and reaches its peak in the stoichiometric regions, i.e. $\Phi=1$.

Conventional RQL combustion

State-of-the-art combustion chambers operate with the principle of "Rich Burn - Quick Quench - Lean Burn" (the so called RQL-combustor). They use a primary zone with an equivalence ratio greater than one to ensure a stable combustion. The injection of dilution air brings the flow rapidly to a lean mixture. Nevertheless, the mixture passes the stoichiometric region and pollutants are formed. Therefore, this concept limits the reduction of NO_x emissions.

Lean combustion

A solution is offered by the lean-premixed-prevaporized (LPP) combustion principle. The formation of NO_x can be significantly reduced by avoiding the stoichiometric region completely, by staging below equivalence ratios Φ of about 0.6 within the entire combustion chamber. To ensure a continuous and safe combustion process, i.e. proper mixing and flame stabilization, swirl stabilization is used (Huang and Yang [61]). This causes high turbulence intensity and strong shear regions due to velocity differences and in this way enhances the mixing of fuel and air. A recirculation zone develops as consequence of a vortex breakdown and the associated adverse pressure gradient. The flame is stabilized in the shear region at the boundary of the recirculation zone. The swirler vortex core proceeds towards the turbine in a precessing motion, leading to an unsteady and non-uniform pressure distribution at turbine inlet (Jacobi et al. [64]). About 80% of air enters the combustor already at the swirler nozzle (compared to 20% in a RQL-combustor (Schiffer [110])) and no dilution ports are used. Usually, effusion cooling is applied to the combustor liners. This difference has two major consequences for the turbine inflow: A flatter temperature profile with increased thermal load on the endwalls and increased residual swirl enters the turbine (Bunker [23]). On contrary, in a conventional combustor, they are both attenuated by the dilution ports. As a result, lean combustion poses new challenges to the turbine design. This and other changes that have connected the design of combustor and turbine very closely have led to the research field of combustor-turbine interaction.

2.2 Combustor-turbine interaction

The term combustor-turbine interaction refers on one hand the strong interaction between these two main components of a gas turbine that exists due to the complex flow field. On the other hand, it also refers the design process, because the components are usually designed in individual, highly specialized teams. Whereas the overall efficiency of the machine can be increased by optimizing individual component efficiencies, a more accurate design process requires an exact knowledge of boundary conditions at the interfaces. Within an engine development program, these boundary conditions are frequently exchanged, changed and altered, based on the detailed design-engineering work.

With lean combustion, combustor-turbine interaction becomes very important, since the boundary conditions at the interface are far away from laboratory conditions as they are assumed and modeled in many test setups and studies. Over the recent years, the complex flow field has been numerically modeled and experimentally investigated in detail by several research groups. In the following, an overview on findings with special emphasis on the turbine is given.

Stagnation line shift

The vane stagnation line is altered by the combustor inflow: For inversely oriented swirl to the vane turning direction and high swirl level, negative incidence occurs near the hub and positive incidence near the casing (Giller [46]). The leading edge film cooling flows of the airfoil are therefore influenced which may lead to the situation that they are washed to the opposing side of the vane as they were designed for.

Furthermore, due to the pressure difference between SS and PS, the stagnation line shift impresses a span wise pressure gradient at the leading edge. This causes a change in static pressure ratio across the film cooling holes, leading to outflow variations. Yin et al. [143] and Griffini et al. [51] illustrate this influence on the shower-head cooling of a vane. They determine strong local inhomogeneities of film cooling effectiveness and heat transfer, leading to an increase of the net heat flux in the shower-head region.

Interaction between vane and the inlet pressure distortion

Due to the recirculation zone in the combustor, a 2-dim. total pressure deficit approaches the vane row. The radial pressure gradient in combination with the incoming swirl thereby causes the formation of additional vortices in the vane passage as it approaches the vane leading edge (Illustrated according to Jacobi et al. [64]):

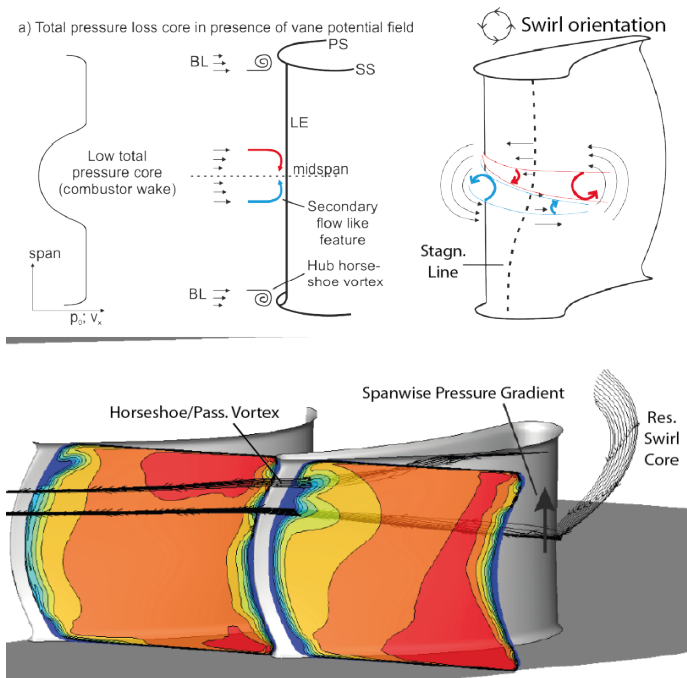


Figure 2.1: Formation of the swirl-/leading edge interaction vortex. The low-pressure zone triggers the formation of a vortex pair at mid span, that persists through the vane passage and merges with the passage vortex (Adapted from Jacobi [64])

Approaching the leading edge, the flow is decelerated and a static pressure gradient in span wise direction results. This evokes a secondary flow feature (shown by red and blue arrows in Fig. 2.1) that travels to both sides of the airfoil. It becomes attenuated

and mitigated depending on the swirl orientation and a resulting vortex pair develops. In addition, a second span wise static pressure gradient is impressed by the stagnation line shift at the leading edge, as explained before. Jacobi identifies that the vortex pair travels according to this pressure gradient; i.e. towards the casing if the swirl is inversely oriented in relation to the vane turning direction and to the hub endwall if they have a concordant orientation. Turrell et al. [128] have observed this behavior in a similar manner for a different swirler geometry. Depending on the extent of the phenomenon, the vortex merges with the passage vortex, but is in any case an additional loss term in the stator exit flow field. In addition, Jacobi determines a decrease in airfoil heat transfer along its trajectory.

Hot-Streaks

Because the use of a lean fuel-to-air mixture alleviates the required number of dilution ports or even cut them completely, the recirculation zone and the inherent flame stabilization mechanisms create a strong non-uniform temperature profile with discrete hot-streaks at turbine inlet, as Andreini et al. illustrate [4]. The pattern factor cannot be controlled as well as with conventional combustors. The clocking of the hot-streak relative to the turbine vanes is of great importance. When it is directed towards the vane passage, it passes relatively unchanged towards the rotor row, resulting in a non-uniform temperature profile at the rotor inlet as well. This can be attenuated by directing the hot-streak towards the vane leading edge. This has the drawback, that the associated peak temperatures cannot be shielded properly from reaching the vane surface, as Koupper et al. [80] illustrate. They investigated a comparison of a passage aligned swirler to a leading edge aligned swirler. Whereas for the leading edge alignment, the hot streak is split into neighboring passages and a relatively homogenous temperature distribution is detected at the vane exit, for the passage alignment, the hot streak travels relatively unchanged through the vane row and discrete temperature peaks are encountered by the rotor blades.

Beard et al. [17] determine a detrimental effect on performance due to an engine-realistic inlet temperature distortion. Whereas the NGV's aerodynamic behavior was rather unaffected, off-design conditions are observed in the rotor. The observed mass flow redistribution towards the hub and casing endwalls where the local work contribution is lower resulted in reduced efficiency.

Griffini et al. [51] numerically examine the clocking of the hot streak with respect to the leading edge for a film-cooled vane. A passage oriented hot spot and swirl orientation is compared to a leading edge oriented position. The leading edge position was determined more problematic and showed increased airfoil wall temperatures. Moreover, the shift of the stagnation line influences the coolant mass flow ejection in the showerhead region.

The location of the hot-streak depends on the design of the combustor and the operating regime. Lean combustors with a pilot/main flame staging exhibit a hot streak position downstream of the swirler center in pilot mode and in the interaction zone in between in main flame mode. This is due to higher shear levels between adjacent swirlers, which stabilize the flame and therefore the highest temperature is located here.

To study the propagation of hot streaks, the gas concentration method is used as

well. Cha et al. [29] investigate the combustor outflow profile by introducing CO_2 as a tracer through the fuel supply tubes in a gas turbine combustor. Butler [28] investigated an inlet temperature distortion by the same method, introducing a hot streak of CO_2 upstream of a vane cascade. They determined that the spatial extent of the hot streak does not increase significantly across the vane row.

Hall et al. [55] illustrate design issues to develop a non-reacting combustor simulator, which is capable of producing a range of swirl and temperature distortion profiles. They have highlighted the importance of the occurring total pressure and turbulence distribution. They also have modeled an inlet temperature distortion to achieve an engine-realistic design.

Migration of the swirl core

A migration of the swirl core in lateral direction (Fig. 2.2) along its trajectory towards the turbine has been observed. Insinna et al. [62] identify a gyroscopic effect to be responsible: In their geometry, the mean radius of the combustor increases towards the vanes due to the inclined hub endwall. Because it is forced upward, the swirler vortex tube deflects sideways in response to the change in direction. In the experiment of Hall et al. [55] for a similar geometry, a lateral movement is observed as well. Furthermore, a combination of both an annular geometry and an inclined swirler is studied numerically and experimentally by Bacci et al [10] [11] and Koupper et al. [80] with a similar finding.

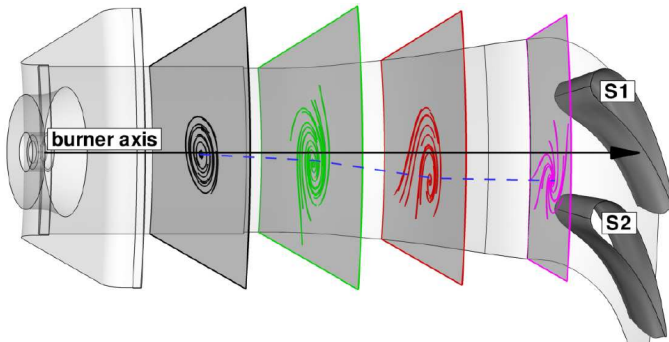


Figure 2.2: Lateral deflection of the swirl core observed by Insinna et al. [62] for counter-clockwise rotating swirl with respect to the main flow turning direction

On the other hand, this migration is not observed in investigations with linear, non-inclined cascades, e.g. Giller [46] and Jacobi et al. [64]. Vagnoli and Verstraete [130] add that the migration is favored by an annular combustor geometry as well: Because the volume above the swirler axis is greater than the volume below due to the curvature of the annulus, more fluid is attracted from the outer section into the low-pressure swirler core. This results in a momentum imbalance and a migration of the core in the flow direction of the fluid near the casing endwall occurs.

The momentum imbalance is thereby already imposed at the combustor inlet by the swirler itself, as Fig. 2.3 illustrates. The LSTR swirler with three concentric rings is shown with the associated orientation. The turning angle of the outer ring is very small and hence the overall imposed swirl of this configuration is counter-clockwise oriented with respect to the main flow turning direction. Radial and whirl components have to be evaluated in polar coordinates to calculate the resultant. At any arbitrary position along the circumferential line at midspan, each area element above the line introduces a positive whirl component and each area element below a negative whirl component. Peak whirl components result along the mirror line of the swirler. In sum, the positive whirl component is greater than the negative component, because the area above the midspan line is greater. Consequently, a shift of the swirler center in positive whirl direction results, which is to the left in the figure.

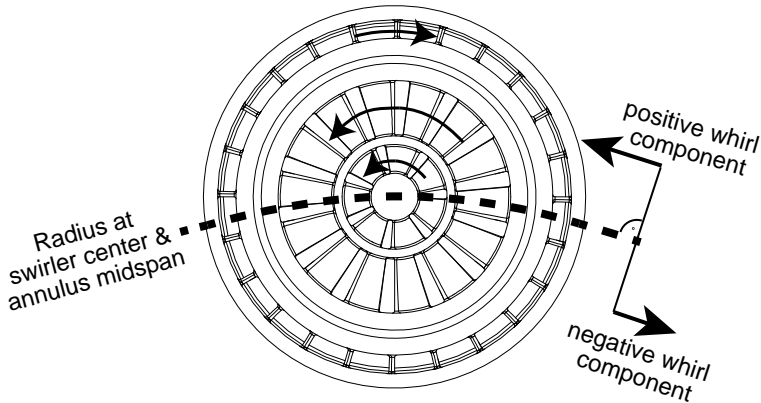


Figure 2.3: Momentum imbalance imposed by the swirler (Schematic shows the swirler of the present investigation). For an annular rig geometry, the mean radius divides the swirler into a larger upper section and a smaller lower section with associated whirl components and a resulting global shift of the flow field downstream of the swirler exit in the whirl direction of the upper section

The migration of the swirl core is relevant to the engine design, because its relative position to the vane's leading edge including the hot streak alters the wall temperatures at the turbine. Schneider and Schiffer [115] have shown that a small variation of 1° in the position of the swirler core can drive the hot-streak downward to reach the endwall and evoke peak temperatures that need to be considered for the cooling design.

Turbulence intensity

The swirler causes an unsteady distribution of turbulence intensity and length scales. The influence of moderate inlet turbulence quantities has been widely investigated in

cascade rigs (Giel et al. [45], Arts and Lambert de Rouvroit [9], Cresci et al. [34]). Due to the highly complex and unsteady flow field, only few studies exist, that take into account high turbulence intensities as they are observed in the combustor outflow, such as van Fossen and Bunker [131], Koupper et al. [79] and Bacci et al. [10]. At turbine inlet, turbulence intensities up to 35% are encountered (Cha et al. [30] [29]). The turbulence level depends mostly on the geometry, the swirl level and secondary flows. The combustion process itself has only inferior contribution to the turbulence level, but the temperature and velocity increase due to the combustion reduces the swirl level and the turbulence level. To achieve engine-representative swirling inflow in a cold flow setup, great care has to be taken. Therefore, the use of real engine hardware requires an adaptation of the simulator design (Bacci et al. [10]). The range of turbulence length scales at the combustor exit is increased when effusion cooling is applied to the combustor liner. Small length scales are generated (Koupper et al. [79]) near the cooled wall. Accurate modeling of turbulent quantities is key in the numerical investigation of the interaction between combustor and turbine, as Schmid [112] illustrates.

Different combinations of swirl orientation have been studied to evaluate their mixing capability and effects on the flow field. Merkle et al. [96] show typical pressure, velocity and turbulence quantities and their distribution for a co-swirl combustion chamber, i.e. with all swirlers oriented into the same direction of rotation and counter-swirl with alternating orientation. Schmid [112] presents a similar study for a linear cascade.

Numerical approaches to combustor-turbine interaction

Existing numerical approaches to combustor-turbine-interaction studies that take care of the discussed effects are presented in the following. Schmid et al. [113] numerically examine a HPT stage with aerodynamic boundary conditions of an aero-engine lean combustor and find increasing heat transfer levels and decreasing stage efficiency compared to a low-turbulent, axial inflow. The influence of turbulence intensity is modeled separately and is determined to be responsible for nearly half of the total efficiency penalty observed with swirl. Additional losses occur depending on the swirler orientation and clocking position. The latter aspects are also of importance for the thermal load in the turbine. Qureshi et al. [104] determine a great impact of swirl orientation and clocking position on endwall heat transfer as well: Both a significant increase or a slight decrease in Nusselt numbers is observed, the local divergence and convergence of wall streamlines and an accumulation or dissipation of boundary layer fluid to be responsible. This working group in addition investigates an integrated combustor vane concept (Rosic et al. [108]), showing benefits in terms of cooling air requirements without an adverse effect on aerodynamic performance, compared to a standard design.

Numerical studies further include coupled simulation approaches with separate domains for combustor and turbine. They include two solvers that run unsteady and simultaneously but are coupled in each iteration. Such studies are conducted by Insinna et al. [62] and Vagnoli [130] [129].

The influence of combustor inflow on leading edge cooling is investigated by Yin et al. [143]. Experimental and numerical studies of combustor outflow turbulence

intensity and length scales of an engine representative combustor simulator have been conducted by Koupper et al. [80] The simulator is dedicated for combustor turbine interaction studies in a high speed turbine rig. Cha et al. [29] highlight the importance of the turbulence distribution at turbine inlet for a correct numerical estimation of turbine aerodynamics and performance. They investigate in addition the migration of the burner core using a passive CO₂ tracer to investigate the flow field numerically and to identify the NGV upstream effect.

Klapdor [73] investigates the combustor-turbine interaction with the Rolls-Royce in-house combustor code *PRECISE*, into which compressibility is included. With the integrated simulation, the extension of the NGV upstream effect in the combustor is specified to be one axial chord length and the influence on the combustor flow field is analyzed in detail.

2.3 Endwall film cooling

Within the present investigation, a film cooling design for a NGV endwall is to be analyzed. Relevant factors of influence on film cooling effectiveness and the measures to quantify it are presented in the following section.

Requirement of endwall cooling

The efficiency of gas turbine is optimized by increasing the compressor pressure ratio to higher values. Following the equation of state, with a higher pressure, the combustor inlet temperature increases. To obtain the same work output the turbine inlet temperature needs to be increased as well. Over the recent years, temperatures are raised up to 1900 K. This is beyond operational temperatures of the materials used in the turbine. Therefore, cooling is required. The use of coolant air is intended at a minimum, since it constitutes a penalty and does not fully contribute to the cycle. Furthermore, component life increases significantly with a reduction in material temperature. Hence, efficient cooling techniques and a profound understanding of the flow mechanisms are required to cope with the design changes imposed by lean pre-mixed combustion concept. A crucial component area to be looked after with special care when applying a lean burn combustor is used, is the endwall.

Cooling methods and definition of the film cooling effectiveness

The cooling techniques used in gas turbines to maintain the material temperature within the limitations of their mechanical strength can be categorized as follows (Bräunling [22], Baldauf [12]):

- **Passive cooling techniques;** So called **thermal barrier coatings (TBC)** are applied to the surface. They are capable to withstand extreme temperatures and have a low thermal conductivity to minimize the heat conduction into the base material.
- **Internal Cooling** techniques maximize the heat removed from the material and in this way reduce the material temperature. Techniques applied belong to the **convective cooling** methods in internal vane or blade cooling passages

to increase the internal heat transfer rates. A special case is **impingement cooling**, such as it is applied in the leading edge region or below the combustor or turbine casing liner, where very high heat fluxes occur.

- **External cooling** includes **film cooling**. This techniques reduces the driving temperature by introducing a film of colder air through slots or holes on the surface, resulting in a mixing temperature above the wall, denoted as the film temperature T_f . Film cooling is the method in focus for this study.
- The **combination of internal and external cooling** is represented by **effusion cooling**, whereby a large number of small holes is applied to the surface, a combustor liner for example. Whereas the primary effect is due to the the cooling film, the surface temperature is in addition reduced by the extensive heat conduction in the perforated surface as well.

To quantify the utilization of the available temperature difference between coolant and main flow for a film cooled wall, the film cooling effectiveness η is defined according to equation 2.1. The coefficient is usually presented as the adiabatic film cooling effectiveness and the film temperature is replaced by the adiabatic wall temperature. This temperature is achieved at the wall with zero heat flux into the wall.

$$\eta = \frac{T_\infty - T_f}{T_\infty - T_c} = \frac{T_\infty - T_{aw}}{T_\infty - T_c} \quad (2.1)$$

In high speed flow, the compressibility of air needs to be taken into account to include the influence of the diffusion. According to Schiffer [109], this requires that in the definition of the film cooling effectiveness in the above equation, the recovery temperatures of both the main flow and the coolant flow need to be used.

Factors influencing film cooling

The film cooling performance has been improved since its first application and new manufacturing techniques have allowed to optimize geometries using shaped cooling hole geometries (Bunker [24]). Numerous studies have identified factors of influence, whereby the study of Baldauf [12] presents both an extensive review and a wide experimental parameter study. Friedrichs [41] gives an overview with special regard on endwall film cooling of axial turbines. Below several parameters of influence are discussed briefly without making a claim to be complete and further reading to the topics is provided:

- **Blowing ratio** M and the **momentum ratio** I of the coolant injection¹: Thole et al. [125] show that the penetration depth of film cooling jets into the main flow is dependent on I . According to Baldauf et al. [14], the decisive parameter in the near hole region is I , whereas the film cooling effectiveness correlates with M in the downstream region.
- The **density ratio DR** of coolant and main flow: In the real engine, the temperature difference between the two air flows results in a DR of about two.

¹The definition of these parameters is given in section 3.3

For studies at ambient conditions this makes it impossible to match both M and I at the same time, when the DR cannot be matched (Thole et al. [125]). The use of a foreign gas with a greater density than air as a coolant is a method to overcome this difference and to replicate both M and I simultaneously in the experiment.

- **Thickness and shape of the boundary layer** of the flow approaching the holes: The coolant jets protrude through a thin boundary layer with respect to the cooling hole diameter. A thicker boundary layer thereby allows the coolant jets to remain within the boundary layer and to energize it (Dückerhoff [37]). However, the shear forces responsible for the turning of the jet are greater. Therefore, a general statement to the influence of the boundary layer thickness is difficult and other parameters of influence have to be considered at the same time.
- **Turbulence intensity** and length scales in the main flow and boundary layer: Increased turbulence intensity favor lateral and radial mixing, resulting in increased lateral film cooling effectiveness but quicker dilution with downstream distance according to Baldauf et al. [14]. For film cooling ejection with jet interaction, i.e. for narrow hole spacing, the influence of the freestream turbulence decreases accordingly. Similar findings were observed by Burd et al. [25]
- Favorable or adverse **pressure gradients** i.e. accelerated or decelerated boundary layers: They are imposed by shape of the airfoil surfaces (Dückerhoff [37]).
- **Cooling hole interior flow** and the flow direction of the incoming flow in the supply plenum.
- The **potential field** of downstream components: Thomas [126] illustrates the upstream effect of the leading edge (LE). It is responsible for local blowing rate variations of endwall cooling holes upstream of the LE in the case of endwall cooling. The reduced main flow velocity causes the coolant flow to detach from the surface, resulting in inefficient cooling.

Furthermore, geometrical parameters of the film cooling configuration are relevant:

- The **L/D ratio**, i.e. ratio of diameter D to length L of the cooling hole. Small L/D-ratio holes favor "jetting" of the coolant farther into the main flow due to a more inhomogeneous velocity profile at the hole exit, whereas high L/D-ratio favors the jet attachment to the wall. According to Burd et al. [25] with high free stream turbulence these differences diminishes.
- **Lateral and radial inclination** of the cooling hole to the main flow direction: A lateral inclination influences the vortex system of the coolant jet in a way, that one of the main vortices is attenuated and the other becomes mitigated. The new vortex system is less prone to lift off of the surface, according to Wolff [141]. Baldauf et al. [14] state, that steep radial injection angle promote the interaction between neighboring coolant jets.

- Various **shapes** of the cooling hole have been widely studied in the literature. A common method to reduce the momentum ratio for a coolant hole is fan-shaping. The coolant hole outlet area is increased in lateral and/or axial direction. This is beneficial to the cooling effect on the wall, as shown by Bogard and Thole [21] and Dittmar et al [35][36].
- **Lateral spacing** to adjacent cooling holes, as identified by Cresci [34], has a great influence on the performance of a film cooling row. A closer spacing favors the attachment. A lateral spacing of at least $3D$ is used in practice to maintain the structural integrity, according to Kodzwa and Eaton [78].
- **Surface curvature**: Schwarz et al. [119] showed, that a convex shaped surface can be beneficial for the downstream film cooling effectiveness, whereby the effect depends on the blowing ratio M . A pressure gradient is introduced in the radial direction of the curvature.
- **Hole pattern** and both lateral and axial spacing to subsequent or preceding cooling rows: The importance of coolant injection on the NGV inlet flow field was highlighted by Cresci et al. [34]. In the experiment, a double row of cylindrical holes was investigated, highlighting the influence of hole spacing on the local coolant-to-main flow momentum ratio. A closer spacing helps to prevent film-lift-off, since the effective bulk flow velocity for the second row is increased due to the injection from the first row and the effective blowing rate is reduced. Burdet and Abhari [26] show that a row of cooling holes is significantly influenced by the flow field of its preceding row. A staggered configuration was determined to have superior performance because their counter-rotating vortex pairs (CRVPs) combine to a downward influence that keeps the coolant jets more attached. On contrary, the in-line configuration of cooling holes rows increases the tendency of the trailing cooling hole jet to lift off the surface. The CRVP between different rows interact in a different manner, depending on distance and pattern, which can be beneficial or detrimental, in addition to the effect of the preceding row on the effective bulk velocity (Kodzwa and Eaton [78]). To evaluate the cooling performance, Kirollos and Povey [70] addressed the superimposition of subsequent cooling films with an energy-based method. Similarly, Kneer et al. [76] addressed the superimposition effect as well.
- Surface **roughness** of the wall and the hole interior is addressed by Schroeder and Thole [117] and (Lorenz [93]).

Even though all of the above-mentioned parameters have been investigated in detail isolated from other effects, in the real turbomachine, they appear simultaneously and interact with each other. Kodzwa and Eaton [78] present existing approaches to encounter this aspect.

Coolant injection vortex system and near hole flow field

A box with a length of 3 hole diameters both in lateral and in axial direction around each cooling hole is referred to as the near-hole flow field in film cooling problems. There exists a characteristic flow field that can be idealized as a jet-in-crossflow with

an inclination angle. Although the flow field in general has been widely studied among the literature and an agreement about its flow features exists, their origin is disputed. Dückershoff [37] has illustrated the vortices that typically develop due to a coolant injection (Figure 2.4). Studies of Andreopoulos and Rodi [6] and Burdet et al. [27] support these findings. According to Burdet et al. [27], additional vortices may develop due to vorticity entering the coolant hole from its plenum.

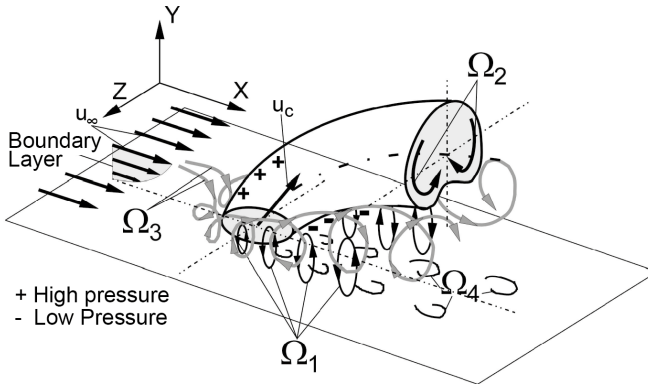


Figure 2.4: Vortex system due to a coolant jet injection (Dückershoff [37])

The common understanding of the vortex system is summarized by Dückershoff [37] to consist of four individual vortices, designated Ω_1 through Ω_4 in Figure 2.4. In the stagnation region upstream of the jet, similar to an obstruction by a cylinder in crossflow, the static pressure increases. Downstream, a wake zone with low static pressure is found. The gradient and the inertial forces of the free stream causes the coolant jet to bend. Dückershoff [37] argues, that a Von-Karman vortex shedding occurs (Ω_4 in Fig. 2.4), similar to the wake of a cylinder in crossflow. Burdet et al. [27] on contrary states, that the flow has a rather potential character and the main mechanism is entrainment of main flow into the low-pressure wake zone. Similarly, due to the obstruction by the jet, a horseshoe-vortex system forms (Ω_3 in Fig. 2.4). The dominant flow feature is the counter-rotating vortex pair (CRVP, Ω_2 in Fig. 2.4) or kidney-vortices, which form due to the pressure gradient upstream and downstream of the jet, according to Dückershoff [37] and Fric and Roshko [40]. Burdet et al. [27] and Moussa et al. [98] however account a vorticity ring, which develops inside the cooling hole, responsible for the CRVP. They agree that this vortex structure assists in the entrainment of main flow into the jet's wake. Leylek and Zerkle [89] have investigated the flow inside a cooling hole and validated, that a CRVP exists in the cooling hole already. Lemmon et al. [88] continued the investigation, comparing a simulation without boundary layers inside the cooling hole to the datum configuration. Accordingly, decisive for formation of the CRVP in the near-hole flow field is the free shear layer between jet and mainstream. The main flow is accelerated around the coolant jet, leading to pressure gradients and a compensating secondary flow (Ω_1 in Fig. 2.4).

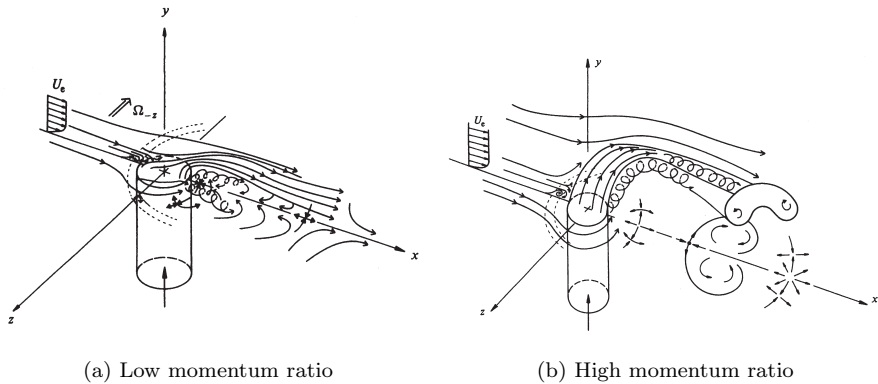


Figure 2.5: Jet-in-crossflow model by Andreopoulos and Rodi [6] for normal injection and varied momentum ratio

Mixing between the flow occurs around the coolant jet. The momentum ratio of coolant and main flow is decisive on whether the jet lifts off or remains within the boundary layer flow. This aspect is also observed by Andreopoulos and Rodi [6] (Figure 2.5) for a jet-in-crossflow with normal injection. They observe an increased radius of the curvature of the jet trajectory with increased blowing rate. Kodzwa and Eaton [78] argue that for low momentum ratio, the flow exiting the cooling hole is obstructed and hindered by the freestream in the upstream half of the hole. This effect diminishes with increasing momentum ratio. However, also at very low momentum ratios, a downstream wake region forms with very low flow velocity, that allows the main flow to penetrate underneath the jet core. This is experimentally illustrated by Bernsdorf et al. [19]. They identify, that this main flow air is extracted from the boundary layer, which therefore becomes locally thinned. This in turn increases heat transfer. Baldauf et al. [15] demonstrate that this increase is concordant with the increase in blowing ratio.

Classical view on secondary flows in the vane passage

Because of its great importance for endwall cooling, the flow field in a vane passage is discussed in detail. The classical view with a typical boundary layer, i.e. an uncooled endwall is illustrated first. Subsequently, the radial equilibrium equation is illustrated and the influence of coolant injection on the passage flow field is discussed. The secondary flows influence the endwall heat transfer in a vane passage as well and the aspects are discussed with this respect in the next section.

Goldstein and Spores [48] have illustrated the common understanding of the vane flow field:

Accordingly, two pressure gradients are responsible for the formation of the secondary flows: The horseshoe vortex (Fig. 2.6, item 1. & 2.) is induced by the radial stagnation pressure gradient in the incoming boundary layer. It is converted into a

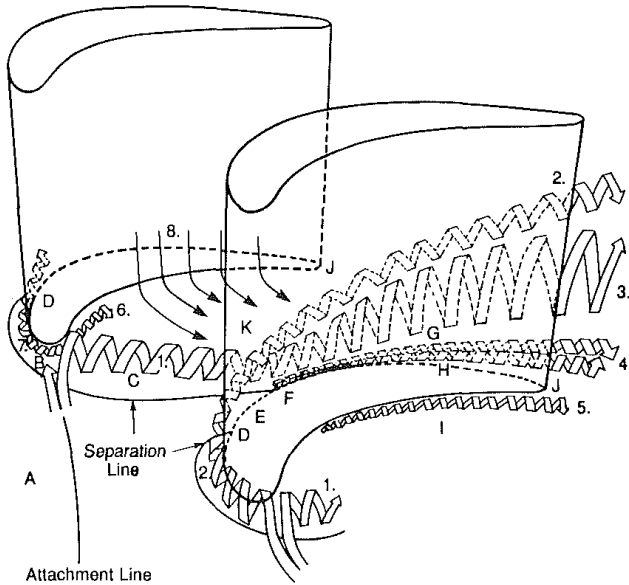


Figure 2.6: Secondary flows in a vane passage (Goldstein and Spores [48])

static pressure gradient when approaching the leading edge of the vane due to the flow deceleration. This forces the flow to turn towards the endwall, and thus breaking up into two vortex structures. One leg enters the passage along the suction side (SS) of the vane (Fig. 2.6, item 2.) and the other along the pressure side (PS) of the vane (Fig. 2.6, item 1.) with opposing rotational direction. The turning of the vanes induces the second important pressure gradient from the PS to the SS of the vane. The passage vortex develops (Fig. 2.6, item 3.), where the pressure side leg of the horseshoe vortex encounters the vane surface at its shoulder, after crossing the vane passage. The SS leg of the horseshoe vortex remains close to the endwall up to a certain point, where it lifts off as well and starts to roll around the passage vortex with opposing rotational direction. Further low-momentum vortices, denoted corner vortices, develop at the airfoil corners (Fig. 2.6, item 4., 5. & 6.). They are a result of additional boundary layers in radial direction, which develop due to the horseshoe vortex' trajectory at the leading edge. This induces a boundary layer in radial direction and as a consequence, vortices form in the corners.

Horseshoe and passage vortex cause the formation of a three-dimensional separation line for the inlet boundary layer. Downstream of the separation line, a highly skewed new boundary layer develops and is fed by a downwash from the vanes pressure side (Fig. 2.6, item 8.). Friedrichs [41] states that as a consequence, the area downstream of the separation line is crucial in endwall film cooling because the cooling air in the boundary layer as well separates from the endwall. With the downwash from the PS, airfoil coolant air may be transported towards the endwall and contribute to the

cooling there. Nevertheless, typical gas turbine endwalls usually need to be cooled with additional passage cooling holes in this region. The benefit of such an injection at the spot has to be compared to the increased mixing losses because of the higher velocities. Benton et al. [18] state that a coolant injection upstream of the vane row is beneficial from this point of view.

Radial equilibrium in the passage flow and influence of coolant injection

As it has been discussed, the passage flow field causes coolant air that is injected with low momentum is observed to detach from the endwall at the separation line. In consequence, uncooled areas appear downstream. Responsible is a passage cross flow from the PS to the SS. This in turn results due to the radial equilibrium with respect to the turning in the vane passage, as Thomas and Povey [127] illustrates (Fig. 2.7).

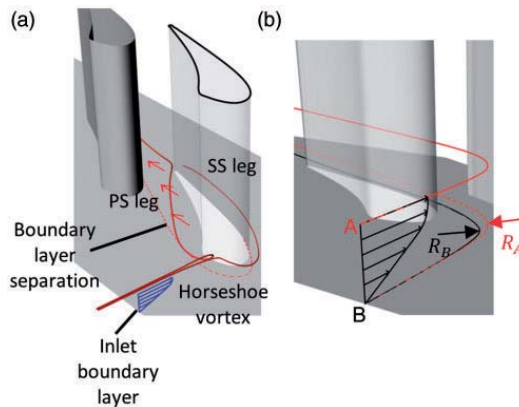


Figure 2.7: Mechanism responsible for the passage cross flow according to Thomas and Povey [127]

The mechanism is driven by the pressure gradient from PS to SS. Because the static pressure through a fully developed boundary layer is constant, low-velocity fluid (V_A) particles near the endwall are subject to this gradient. The radial equilibrium according to equation 2.2 requires a smaller radius R_A in contrast to a higher-velocity (V_B) fluid particle outside of the boundary layer.

$$\frac{\delta P}{\delta n} = \rho_A \frac{V_A^2}{R_A} = \rho_B \frac{V_B^2}{R_B} \quad (2.2)$$

In analogy, a greater velocity flow near the wall than in the main flow, e.g. caused by coolant injection through film cooling holes upstream of the NGV-leading edge, reverses the crossflow direction. This is discussed in the work of Thomas [126] (Figure 2.8). The study examines a film cooling configuration with a double row of cylindrical holes on the endwall and varying coolant injection rates. Accordingly, the classical view on the dominant influence of secondary flows holds only true without

coolant injection or for low coolant-to-mainflow momentum ratios. For increasing momentum ratios, the boundary layer holds a surplus of momentum and overcomes the adverse pressure gradient imposed by the vane pressure field. The mechanism due to the radial equilibrium is reversed and as a consequence the passage cross flow is inverted compared to the common direction. In this way, no boundary layer separation and uncooled region is observed for higher injection rates of 3% and 6% because the near-wall flow migrates from SS to PS of the vane. This explains the observed cold-streak on the endwall at the TE as well; the coolant is driven towards the PS on the endwall. The formation of secondary flows can be hindered or mitigated in this way by the coolant injection. A similar observation determine Colban et al [32][33] and Knost and Thole [77] for a slot ejection upstream of a vane row.

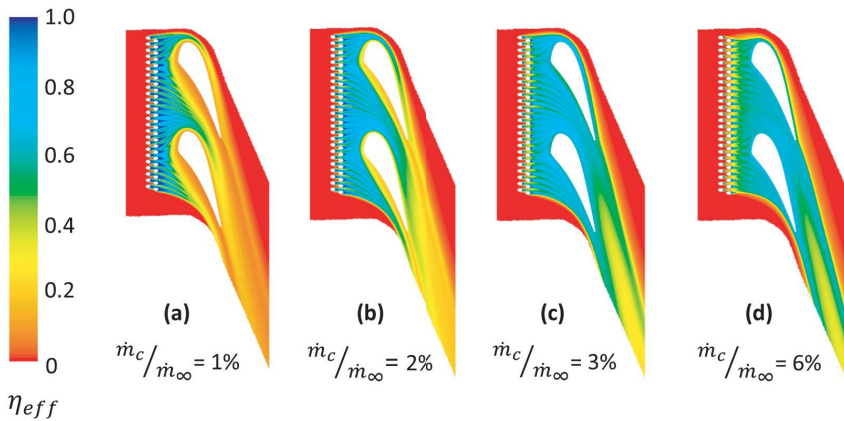


Figure 2.8: Endwall film cooling contours for varied coolant injection rates (Thomas [126])

2.4 Endwall heat transfer

The material temperature in the turbine depends on the heat load, i.e. heat flux, imposed by the near wall flow field. It depends on driving temperature difference, which in turn results from the incoming temperature profile, the film cooling performance and the the local heat transfer situation.

It is predominantly influenced by the shape and size of the boundary layer. Flow components normal to the wall, as they are imposed by vortices and secondary flows, drive main flow fluid towards the wall. This reduces the boundary layer thickness and increases heat transfer.

Theoretical considerations and definition

The wall-normal heat flux into the flow at any point along a surface is derived with the local temperature gradient at the wall:

$$\dot{q} = \lambda \frac{\delta T}{\delta y} \Big|_{y=0} \quad (2.3)$$

Thereby, λ is the thermal conductivity of the fluid near the wall ($y \approx 0$). Due to its small scale, it is hardly possible to resolve the gradient $\frac{\delta T}{\delta y}$ experimentally (Han and Goldstein [56]). As a simplification, the thermal transport is treated as a boundary layer problem. The local heat transfer coefficient h is defined as the local heat flux normalized by the temperature difference between the wall T_w and a certain reference temperature T_{ref} .

$$h = \frac{\dot{q}}{T_w - T_{\text{ref}}} \quad (2.4)$$

A number of studies use the stagnation temperature of the incoming flow, T_∞ as a reference. However, Moffat [97] states that it is beneficial to use the local adiabatic wall temperature instead. It is defined as the temperature that the wall would attain, if it was thermally isolated and no heat flux into the surface would occur. The heat transfer coefficient that uses this temperature as a reference is called the adiabatic heat transfer coefficient h_{ad} . In this form, it is linearly dependent on the temperature difference between the wall and this adiabatic temperature and only a function of the fluid properties and the flow characteristics. Experimental approaches to approximate this temperature by measurement as good as possible apply a very low conductive material to limit the heat flux into the surface to a minimum and the resulting wall temperature is measured. A more consequent approach is suggested by Goldstein [47] and Gritsch et al. [52]. T_{aW} and h_{ad} are determined by a superposition approach. This requires to measure at least two combinations of wall temperature and heat flux; both values are then calculated with a linear regression.

Overview on heat transfer measurement techniques in turbomachinery

A brief overview of measurement approaches to determine local heat transfer coefficients in turbomachinery is given below. Han and Goldstein [56] used a butt-welded small-scale thermocouple on a transferable mount to study thermal boundary layer profiles near a turbine stator endwall. The technique is limited by conduction errors in thin boundary layers and positioning accuracy of the probe in high flow velocities.

Blair [20] conducted research on local film cooling effectiveness and heat transfer values in a linear cascade. The study applied two separate experiments, where the first one used a low conductive material to determine adiabatic wall temperatures. For the second experiment multiple surface heaters were applied, maintaining the temperature level elevated, but constant for the whole endwall. To achieve this, varied heat flux from each heater was required and measured to quantify the local heat transfer value. Goldstein and Spores [48] used an indirect measurement method: The heat and mass transfer analogy with the naphthalene sublimation technique provides a way to acquire representative Stanton numbers. They discovered peak

heat transfer regions in the NGV endwall region and showed a correlation to the secondary vortex system in the passage. Moreover, they discovered evidence which helped in understanding the formation of the pressure side and suction side corner vortices. Airfoil and endwall heat transfer was also measured by Graziani et al. [49] in a linear cascade: Surface thermocouples were placed on strip heaters to achieve high spatial resolution in regions with strong gradients. The study also showed the effect of the inlet boundary layer thickness: For a thin boundary layer, the three-dimensional separation line moves further down into the passage. The streamlines downstream of the separation line were nearly perpendicular to the endwall pressure field, whereas the heat transfer contours exhibited an angle to it. A low heat transfer region was discovered near the pressure side. All methods are a challenge for experimental work, since both the heat flux and the driving temperature gradient have to be measured. This comes in addition to the limited accessibility in many test rigs.

Giel et al. [44] [43] studied heat transfer on turbine blades and endwalls, using a constant wall temperature approach. They applied thermochromic liquid crystals on well-conductive material, which was covered by a low-conductive material. The advantage of their approach was that conduction into the structure could be neglected since they measured the local heat flux across the covering material. A similar experimental technique is used by Laveau [82], who uses a thin layer of Kapton. This method is suitable for complex 3-dim. shapes and a contoured endwall. Xue et al. [142] use a transient technique to gather recovery temperatures, film cooling effectiveness and Nusselt numbers in a transonic turbine cascade. They apply a linear regression and two experiments with different coolant temperatures, but otherwise constant experimental parameters.

Another approach in a steady setup was used by Nicklas [100]. Series of Infrared measurements of a film-cooled endwall with multiple constant heat flux settings were evaluated using the superposition approach and a linear regression. In this way they determined adiabatic wall temperatures and heat transfer coefficients. An overview of other direct heat transfer measurement techniques was presented by Kaiser [66].

Endwall heat transfer peak regions

The importance of the vane flow field for endwall film cooling has been discussed already. The heat transfer in a vane passage as well depends largely on this flow field. Common areas of peak heat transfer have been determined within previous studies, summarized by Friedrichs [41]. A typical distribution for Nusselt numbers on a NGV endwall is shown in Figure 2.9, obtained at the LISA rig at ETH Zürich that has a comparable setup to the one used for the present work.

The following areas are typically prone to high heat transfer:

- The **stagnation region** upstream of the vane leading edge \textcircled{A} . It is detected in many investigations, both in cascade and annular rigs (Laveau [82], Panchal et al. [102], Graziani et al. [49], Goldstein and Spores [48]). In this area, increased heat transfer occurs due to the high wall normal flow transport caused by the formation of the horseshoe vortex. Main flow is swept down onto the endwall. The application of fillets limits the extent of the horseshoe vortex and reduces the peak (Shih and Lin [122]).

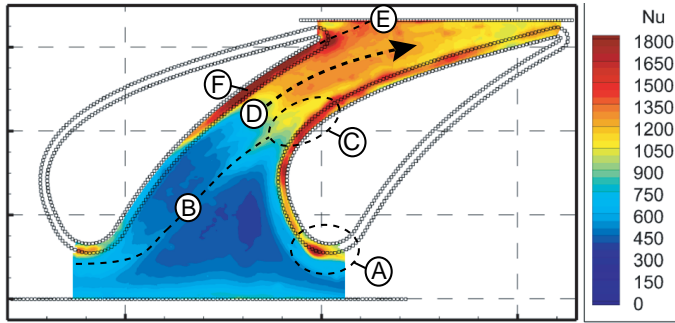


Figure 2.9: Endwall Nusselt numbers in an axial turbine without coolant injection showing typical peak heat transfer areas (adapted from Laveau [82])

- Following the **trajectory** of the PS leg of the **horseshoe vortex** (B) results in a heat transfer peak along its trace across the passage visible in the results of Laveau [82] in Figure 2.9.
- At the **suction side shoulder** (C), both legs of the horseshoe vortex merge to form the passage vortex (Friedrichs [41]), which then lifts off the wall. A peak in this area is also identified by Blair [20], Goldstein and Spores [48] and Graziani et al. [49]. In addition to the vortices, high velocities are regarded responsible for the heat transfer peak. The location often coincides with the onset of the corner vortex according to Panchal et al. [102]. The corner vortex causes increased wall-normal flow transport and therefore as well a peak HTC value along the **suction side corner**.
- The velocity increase in the **passage throat** (D) and downstream of it is responsible for peak Nusselt numbers. This is observed by Blair [20], Graziani et al. [49] and Laveau [82].
- The **trailing edge wake** (E) of the vane is subject to downwash from the vane wake and high velocities. This hot spot is observed by e.g. Goldstein and Spores [48] and Graziani et al. [49]
- A corner vortex forms in the **pressure side corner** (F) and together with the thin boundary layer in this region causes high heat transfer levels.

Influence of film cooling on heat transfer

Endwall coolant injection through a row of holes increases Nusselt numbers locally and then diminishes with the downstream distance on the endwall (Baldauf [12]). The mechanism has been investigated in detail in the literature and it is closely connected with the near-hole flow field, illustrated before. The wake region downstream of the coolant injection allows the main flow to penetrate underneath the jet core (Bernsdorf et al. [19]). This main flow air is drawn from the boundary layer, which therefore

gets locally thinned. The thinner boundary layer means that heat transfer rates are increased in the region downstream of the hole. This is shown by Baldauf et al. [15] [12] [13], who also demonstrate that this increase is concordant with the increase in blowing ratio. In addition, the local increase of the turbulence intensity, driven by the mixing and shear processes, results in increased heat transfer. The increase persists further into the flow direction, which is concordant with the blowing rate as well. Baldauf [12] presents three typical heat transfer regimes for a coolant injection, typically found with increasing blowing rate (Figure 2.10). It is notable, that the phenomena displayed for a single hole have been observed in an experiment with a row of holes. For blowing rates greater than $M=1.7$, the jet completely detaches from the surface (denoted "penetrating coolant jet") and the effect of a single hole becomes amplified by adjacent jets. Low heat transfer rates are found immediately downstream of the holes and enhanced heat transfer is observed sideways of the jet due to displacement effects of the ejected coolant. The vortex structure of the CRVP is responsible for this enhancement. It creates a secondary flow towards the surface between adjacent jets and a secondary flow away from the surface along the centerline of the hole and hence a zone of low heat transfer. The resulting striped pattern of low and high heat transfer can be observed to several multiple diameters downstream of the cooling hole, before the influence is dissipated and the heat transfer level reaches that of an uncooled reference.

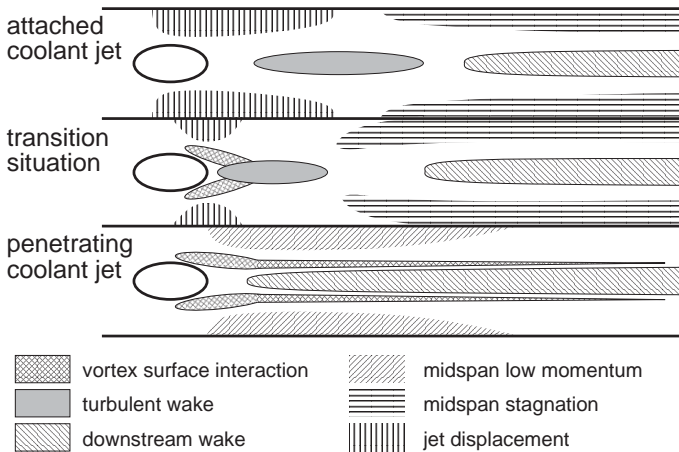


Figure 2.10: Characteristic heat transfer pattern and the origin of the observed contours downstream of a coolant injection in different flow regimes (Baldauf [12])

2.5 Resulting heat flux reduction due to film cooling

To assess the performance and benefits of a film cooling design to the engine, both thermal parameters have to be combined. To calculate the material temperature, the local heat flux needs to be analyzed. This heat flux however is specific to the achieved absolute wall temperature level, which is a priori unknown. In addition, this level depends on the local thermal conduction within the material and the convective heat transfer on the opposing side of the wall, enclosing the internal cooling system. To study this overall thermal performance experimentally, matching Biot numbers as well as a realistic internal cooling configuration are required (Chavez et al. [31]). Sen et al. [120] have proposed the concept of the "net heat flux reduction" (NHFR) to evaluate the design according to equation 2.5. This measure has been widely applied in turbomachinery (e.g. Popović et al. [103], Griffini et al. [50]).

$$\text{NHFR} = 1 - \frac{\dot{q}_W}{\dot{q}_0} \quad (2.5)$$

The parameter \dot{q}_W denotes the local heat flux for the film cooled design and \dot{q}_0 for the uncooled endwall.

This can be rewritten to

$$\text{NHFR} = 1 - \frac{h_f}{h_0} (1 - \eta\theta) \quad (2.6)$$

using the local values of the heat transfer augmentation due to film cooling h_f/h_0 , the local film cooling effectiveness η and dimensionless temperature ratio θ .

$$\theta = \frac{T_\infty - T_c}{T_\infty - T_W} \quad (2.7)$$

As a consequence, the coefficient NHFR is specific to a temperature level, which is not known a priori for a new design. A method to evaluate a design with absence of the actual wall temperature level and θ has been suggested by Baldauf [12] (Fig. 2.11). In the definition of a heat flux reduction Θ accounts for the total thermal transmittance to the internal cooling system. The heat transfer coefficient h_w from the wall to the back surface internal coolant is approximated with h_0 , the heat transfer coefficient on the main flow side. This assumes a 1-dim. conduction through the wall (Baldauf [12]) and that the heat flux is dependent on the external flow field. For the film cooled case, h_w is approximated with h_f , the heat transfer coefficient with film cooling on the cooled external surface. In this way, the equation² can be rewritten to:

$$\Theta = 1 - \frac{h_{f,\text{ges}}(T_{aW} - T_C)}{h_{0,\text{ges}}(T_\infty - T_C)} = 1 - \frac{h_f(h_w + h_0)}{h_0(h_w + h_f)} (1 - \eta) \quad (2.8)$$

²Baldauf uses T_G for the main gas temperature. To remain consistent with the nomenclature used in this thesis, it is changed to T_∞ in all equations of this section

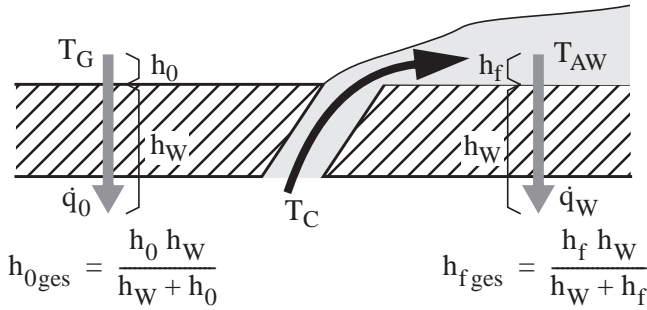


Figure 2.11: Heat flux analysis through the film cooled endwall according to Baldauf [12]

Furthermore it is assumed that invariant internal cooling is given i.e. that the heat flux is also transported ideally to the internal cooling system. This implies that $h_w = h_0$ and the equation is simplified to

$$\Theta = 1 - \frac{2h_f/h_0}{1 + h_f/h_0} (1 - \eta) \quad (2.9)$$

As a consequence, only the quotient of h_f/h_0 and no further assumption of a temperature level is required to assess the total heat flux reduction due to one or several cooling configurations. This assumption of ideal internal cooling is representative for a gas turbine. In their design it is intended to achieve a close matching between the internal cooling design and the imposed external heat load wherever possible.

Approaches that take this goal into account are discussed by Kirolos and Povey [69] [71] [72]. They investigate the requirements for such an optimized internal cooling system. For a given internal cooling air temperature they show that a reverse-flowing coolant to the exterior heat load allows for a significant reduction of the wall temperature.

2.6 Definition of research objectives for the thesis

With the discussion of relevant literature, open questions and research objectives are derived that are addressed with this thesis. The presented experimental research work is dedicated to achieve a comprehensive understanding of the interaction of combustor and turbine regarding film cooling effectiveness and heat transfer to foster a robust design. To achieve this, a suitable test specimen is needed. The first vane endwall has been identified as a crucial area concerning the development of lean burn combustors and is the focus area of this investigation. In summary, this yields two research objectives:

- To design a test rig setup that models the complex flow field with great detail. This includes a representative interface flow field of a lean combustor and a

fully cooled vane row, including endwall cooling, airfoil cooling and trailing edge ejection.

- To develop a measurement method that allows the simultaneous acquisition of heat transfer and film cooling effectiveness data on the turbine hub endwall with high spatial resolution.

With this setup and the defined measurement method, a cooling design is investigated for a reference case of axial inflow to understand the aerodynamic & thermal behavior. A coolant mass flow variation is applied to gain insight into factors of influence and the benefits and drawbacks of low to high-momentum injection. This is summarized by three aims:

- Understanding the interaction between the hub side coolant injection and the flow field in the turbine for a baseline case of axial, low-turbulent inflow.
- An investigation of the impact of varying Rear Inner Discharge Nozzle (RIDN) coolant mass flow rates.
- The use of a measure to evaluate the combined effect of both parameter sets. Baldauf [12] presented a suitable method for a representative assessment of the thermal benefit. This method is applied to the results.

To assess the impact of lean combustion on the turbine, an engine-representative interface flow field is applied to understand the imposed aerodynamic changes. Swirling inflow in a cold flow setup is used. Two additional aspects are addressed in this way:

- To determine and analyze the changes imposed by swirling inflow on the NGV flow field and its impact on heat transfer and film cooling.
- An evaluation of the robustness of the film cooling design to swirling inflow and to derive recommendations for an improved design.

In addition, the results obtained allow their dissemination and enlargement within following measurement campaigns and research projects in the same working group. The results acquired with steady measurement techniques presented in this thesis form the basis for the wider goal to achieve a comprehensive understanding of the aerothermal impact of swirling inflow on the turbine stage.

3 Experimental setup

This chapter describes the experimental setup used to acquire the results presented in this thesis. Specific emphasis, aside from the facility description, lies on the illustration of the combustor module for the CTI investigation and the endwall coolant geometry. An overview on the measurement campaign and the operating point is given to conclude the chapter.

3.1 The Large Scale Turbine Rig

The LSTR consists of a scaled-up 1.5-stage low Mach number turbine in a closed-loop configuration based on the aerodynamic design of a high-pressure turbine, scaled to low Mach-number conditions. It has been set up for the investigations of Linker [90] and Schrewe [116] to study the impact of purge flow injection. The main flow is provided by a radial compressor which delivers a mass flow of about 9.5 kg/s. The secondary airflow is provided by an accessory radial compressor which supplies a mass flow of up to 0.9 kg/s at a pressure ratio of 1.7. Both mass flows are varied depending on the coolant injection setting, resulting in a constant rotor inlet mass flow rate. The rig's general setup is shown in Fig. 3.1.

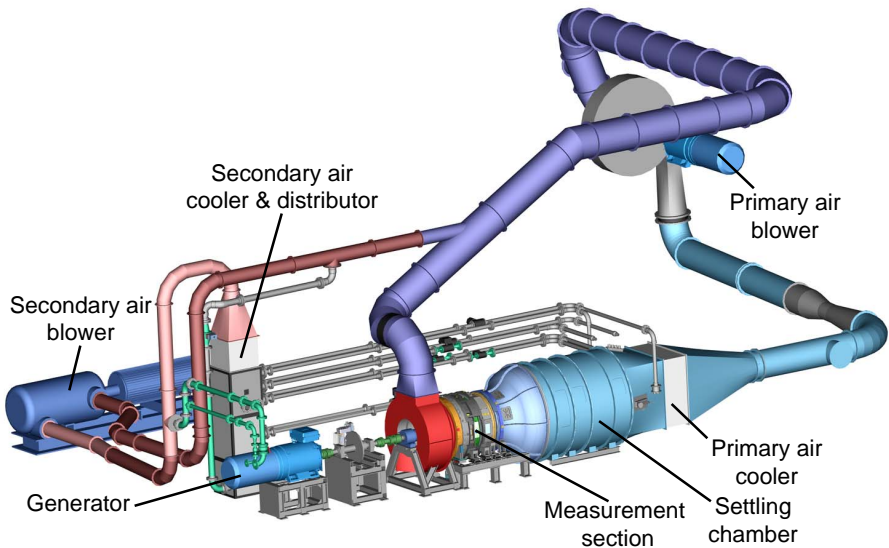


Figure 3.1: General setup of the Large Scale Turbine Rig

The mass flows and the rotor speed are adjusted according to the ambient conditions to maintain the Reynolds number of the system constant. A small influence of changing ambient conditions on the Mach number cannot be avoided at the same time, but is considered negligible, since the Mach number is low enough for the flow to be treated as incompressible throughout the turbine stage. The temperature of secondary and main flow can be adjusted independently using two water driven heat exchangers. This allows for a temperature difference between secondary and main flow of up to 20 K.

The test rig features a NGV1 row with 24 vanes, which also feature airfoil film cooling and a trailing edge slot ejection. The rotor row consists of 36 squealer-tip blades. An NGV2 row with 34 vanes directs the flow towards the outlet casing. Krichbaum et al. [81] present a description of the test rig and all capabilities.

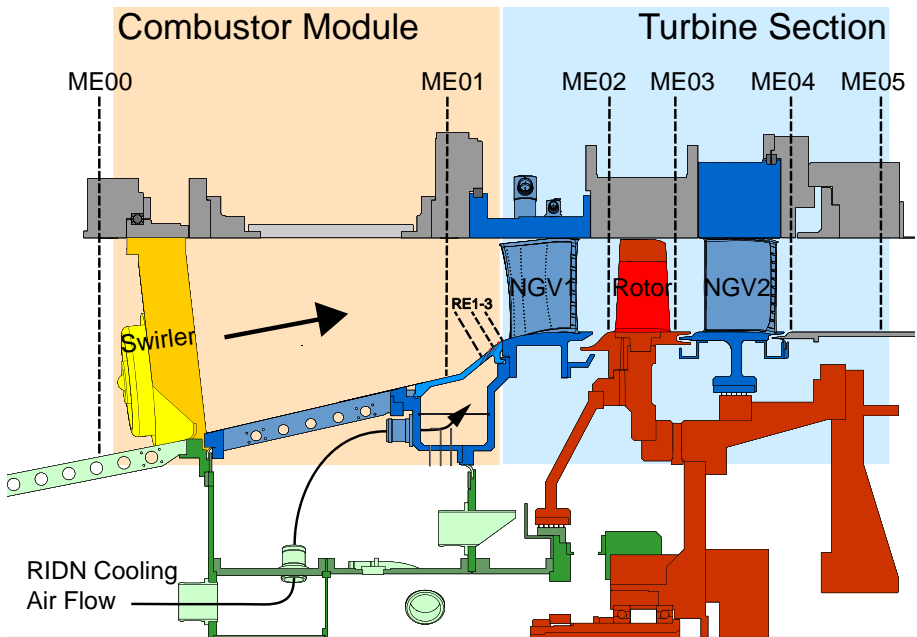


Figure 3.2: Cross section of the test rig, showing the measurement planes (ME) and RIDN boundary layer planes (RE) as well as a schematic of the RIDN cooling flow path. In this illustration the swirler module is rotated by 15° and is hence is displayed below midspan in the figure. The black arrow indicates the swirler center axis within the annulus.

The cross section of the test rig is shown in Fig. 3.2. Measurement planes (ME) are located upstream and downstream of all vane and blade rows. In ME01, the turbine inlet flow field is determined 0.9 axial chord lengths (C_{ax}) upstream of the NGV's

LE. The NGV outlet flow field is evaluated in ME02, $0.2 C_{ax}$ downstream of the TE, which equals to about one true chord length in the exit flow direction.

Scaling of the vane geometry from engine conditions

The vane geometry used for this investigation has been scaled from a high-speed turbine rig by the industry partner Rolls-Royce [94]. To achieve a representative geometry, the distribution of the pressure coefficient $c_{p,vane}$ of the high-speed vane has been maintained similar in the low-speed design. The flaw of this process is that using this design rule, a very small leading edge radius results and the airfoil shape is not similar to the one of the high-speed vane. Because this could cause other design features, such as the airfoil film cooling and flow features such as the secondary flows to differ from the engine, a compromise is used. The pressure coefficient is altered slightly in the leading edge region, such that a larger leading edge radius is achieved.

$$c_{p,vane} = \frac{p_{t,ME01} - p}{p_{t,ME01} - p_{s,ME02}} \quad (3.1)$$

3.2 Combustor module

A combustor module was used to vary the inflow to the turbine stage. The flow in the combustor module is non-reacting and hence isothermal with near ambient temperature. Two configurations were studied: A baseline case of an axial, low-turbulent inflow without any installations (denoted as AX configuration) and a swirling inflow configuration, representative for a lean combustor, with two clocking positions relative to the NGV (denoted SWL/SWP). The goal of the combustor module is to achieve an engine-representative whirl-angle and pressure profile at turbine inlet.

Annulus geometry near the RIDN injection

The hub endwall in the combustor module is inclined to the turbine axis, shaping a tapered annulus geometry. This provides an acceleration and a representative inflow to the turbine stage in the swirling inflow case. In a real engine, the heat release in the combustor decreases the density by about 60 % and accelerates the flow. This leads to an attenuation of the initial swirl level in the combustor, since the tangential components remain constant (Schmid [112]).

The wall inclination ϕ is 13° to the turbine axis downstream of the swirler and, beginning from a relative axial position of $-0.75 C_{ax}$ upstream of the LE, increases to $\phi=39^\circ$. The geometry and angle definitions are specified in Fig. 3.3 and table 3.1, with the values of wall inclination angle ψ and measurement plane inclination angle ψ for the three RIDN injection measurement planes RE1-3 and ME01 with respect to the turbine axis. The angles are also specified for the two injection rows at the intersection of their centerline axis with the hub wall.

The coolant injection holes are placed with a shallow relative angle of 21° to the surface (row 1) and 25° (row 2). Since the curvature of the hub wall begins at the onset of row 2, the relative angle changes from 21° at the windward side to 32° at the lee side of row 2. The position of the measurement planes is specified in axial direction with respect to the LE, non-dimensionalized with C_{ax} . In addition, the

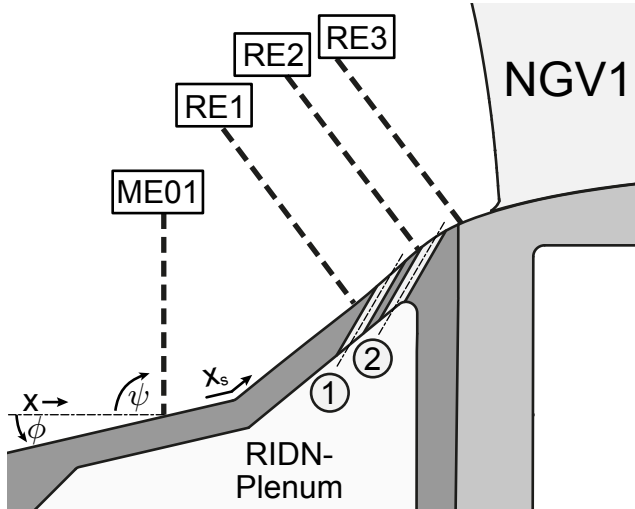


Figure 3.3: Main annulus geometry and measurement planes in the vicinity of the RIDN injection, dimensions specified in table 3.1

distance parallel to the endwall along its curvature x_s is listed with respect to the hole center axis, non-dimensionalized with the hole diameter D .

Swirling Inflow

A swirler insert manufactured from stereo lithography is mounted to a support structure to generate the swirling inflow (c.f. Fig. 3.6). It was designed by Lohmann [91] using numerical simulations.

LSTR Swirler Design A characteristic inflow at the turbine inlet with averaged whirl angles of $\pm 17^\circ$, representative for a state of the art lean combustor, has been achieved with the LSTR swirler. It is modeled on the basis of the *Engine-3-E*-swirler [74] and consists of three concentric rings with curved blades (Fig. 3.4). Two inner rings with high airflow turning angles create a strong swirl in counter clockwise direction with respect to the turbine axis. This high swirl forms a recirculation zone close to the swirler, which is typical for a lean combustor: In the real engine, this is used to enhance the mixing of fuel and air and to maintain flame stability. The flow is then accelerated due to the combustion. In the test rig, this acceleration is achieved by a tapered main annulus. The acceleration attenuates the whirl angles to engine-realistic values. The outer blade ring with a low turning angle, counter-rotating to the two inner rings, is used to adjust the swirl to the desired level at turbine inlet .

12 swirlers are placed within the measurement section. Together with the 24 NGVs and 36 rotors this yields a CFD friendly domain. Furthermore, the measurements can be conducted in representative sectors of 30° , assuming periodicity.

Table 3.1: Measurement planes and geometry near the RIDN injection

Measurement plane	ϕ [°]	ψ [°]	axial pos. [x/C_{ax}]	Surface pos. [x_s/D]
ME01	13	90	0.9 ←	30 ←
RE1	39	48	0.4 ←	3.5 ←
RIDN 1	39	150	0.33 ←	-
RE2	39	45	0.29 ←	→ 2.7
RIDN 2	34	150	0.24 ←	→ 4.5
RE3	23	42	0.19 ←	⇒ 2.5

← : upstream NGV LE, measured at hub endwall junction

← : upstream RIDN row 1, measured from the hole centerline

→ : downstream RIDN row 1, measured from the hole centerline

⇒ : downstream RIDN row 2, measured from the hole centerline

Clocking position Two clocking positions of swirler center relative to the NGV leading edge were studied: Leading Edge clocking (denoted as SWL), where the geometric center of the swirler hardware was aligned with the leading edge at 50 % span height and passage clocking (SWP), where it was aligned to the center of a vane passage, i.e. traversed by half a vane pitch equal to 7.5° ³. Twelve swirler modules were used and the swirler to vane count is 1:2. As a consequence, every other adjacent vane passage faces a different inflow condition, denoted as passages A and B (see Figures 3.5⁴). Hence, the two clocking positions result in four passage data sets for a complete analysis. For the measurement campaign, both a clean annulus configuration with axial, low-turbulent inflow (denoted as AX in the following) and a swirling inflow configuration, as described before, were examined.

Swirl number To describe swirl flows, the non-dimensional swirl number S is defined as the ratio of the axial flux of tangential momentum to the axial flux of axial momentum, multiplied with the swirler radius R as characteristic length (Gupta et al. [53], equation 3.2),

$$S = \frac{\dot{D}}{l_{char}\dot{I}} = \frac{\int_0^\infty [\rho u_{ax} u_{tan} + \overline{\rho u'_{ax} u'_{tan}}] r^2 dr}{R \int_0^\infty [\rho u_{ax}^2 + \overline{\rho u'^2_{ax}} + (p - p_\infty)] r dr}. \quad (3.2)$$

with the fluctuation part of the turbulent flow $\overline{u'_{ax} u'_{tan}}$ and $\overline{u'^2_{ax}}$ and the axial thrust due to the pressure difference with respect to the ambient pressure, $(p - p_\infty)$. The definition of the swirl is representative to characterize confined flow such as swirling

³The lateral migration of the core along its trajectory towards the vane leading edge is not accounted for by this definition.

⁴The nomenclature of vanes and passages is detailed on Fig. 3.9

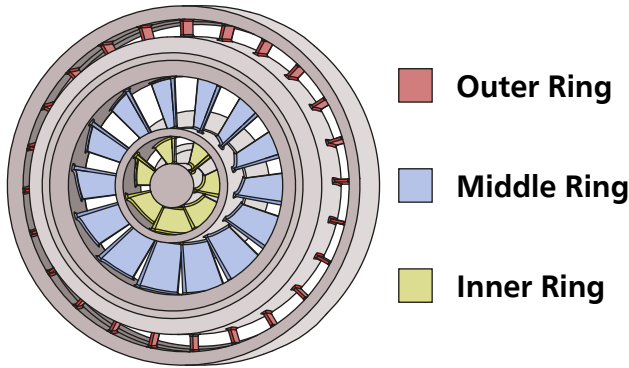


Figure 3.4: Triple flow LSTR Swirler design with three concentric blade rings, stream-wise view. Characteristic flow parameters are listed in table 3.2

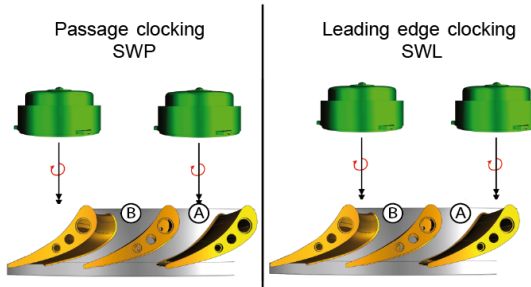


Figure 3.5: Illustration of clocking positions and vane passages A & B (Adapted from Steinhausen [124])

pipe flow. Its use to describe a complex flow field such as in the present setup for the combustor section is limited due to the additional interaction between several larger vortical structures (Giller [46]). To allow for a comparison to other studies, the initial swirl number at the swirler exit plane is presented, derived with a geometrical estimation according to Gupta et al. [53] for flat vane swirlers:

$$S_{\text{geom}} = \frac{2}{3} \left[\frac{1 - (R_i/R_o)^3}{1 - (R_i/R_o)^2} \right] \tan \phi \quad (3.3)$$

where ϕ is the swirler vane angle, R_i the inner and R_o the outer radius of each of the ring.

To design the LSTR swirler, Lohmann [91] conducted a parameter study, varying the swirler vane angle settings, axial combustor module length and swirler inclination with respect to the turbine axis. With the final design, the intent to match an engine-

representative whirl angle profile with averaged peak angles of $\pm 15^\circ$ in the turbine inlet plane ME01 has been achieved, based on the numerical results. With these values, using a simplified definition and assuming solid body rotation plug flow at the nozzle (Gupta et al. [53], equation 3.4) the swirl number denoted S_{CFD} is calculated:

$$S_{CFD} = \frac{\frac{G}{2}}{1 - \frac{G}{2}} \quad (3.4)$$

with G as the ratio of the maximum velocities in the exit plane:

$$G = \frac{u_{tan,max}}{u_{ax,max}} \quad (3.5)$$

For high turning angles, the actual flow turning is less than the geometrical turning of the vanes yielding a higher S_{geom} for high turning angles. For the present configuration, both S_{geom} and S_{CFD} are listed in table 3.2. It includes the mass flow distribution between the three rings that has been derived by the unsteady numerical simulation of Lohmann [91] as well.

Table 3.2: Characteristic flow parameters of the LSTR swirler

Swirler ring	blade angle [$^\circ$]	S_{CFD}	S_{geom}	mass flow fraction [%]
inner	50	0.57	0.91	7
middle	40	0.51	0.66	52
outer	-5	-0.07	-0.08	41

The calculated swirl numbers for the middle and outer ring, that comprise most of the mass flow agree considerably well with both approaches. A low swirl number in the outer section, between -0.07 and -0.08, and a counter oriented high swirl number between 0.51 to 0.66 in the center is determined. The latter the value represents the critical swirl number for the formation of a recirculation zone according to Mellor [95]. Due to this recirculation zone, the LSTR swirler is able to generate a representative pressure and velocity profile at turbine inlet. For the inner ring, the calculated swirl number deviates between geometrical calculation and the value found in the CFD. This is explained with the high vane turning angle. According to Gupta et al. [53], the actual turning is smaller than the turning given by the geometrical shape of the vanes.

The outer ring superimposes vorticity in the opposing direction to the two inner rings. In this way, the overall swirl becomes mitigated to the desired level until turbine inlet and representative whirl angles are achieved.

3.3 Operating point

Experiments have been conducted for one main operating point, with a variation of the mass flow rate to the RIDN coolant injection module. The operating point of the test rig is set in such a way, that the mass flow rate in the rotor row is at a constant

level. Based on the vane exit velocity and its real chord length, the Reynolds number of the system is maintained at 8.7×10^5 :

$$Re = \frac{\rho u C_{real,NGV}}{\nu} \quad (3.6)$$

One focus of the investigation is the influence of the vane coolant flows on the main flow field. In the following, all vane row coolant flows are described and their settings for the investigation are explained.

NGV row coolant flows

The LSTR vane row features RIDN endwall cooling, airfoil cooling, trailing edge ejection and wheel space purge flow. All of them are kept constant throughout the campaign, except for the RIDN coolant.

RIDN endwall coolant flow

The turbine stage features a hub side coolant injection through the Rear Inner Discharge Nozzle flow (RIDN), consisting of a double row of cylindrical holes. A test section view of the film-cooled NGV row and the upstream RIDN cooling holes is shown in figure 3.6. The RIDN coolant mass flux rate was varied, while the main flow was adjusted in the way that the inlet mass flow to the turbine stage is at a constant value. This value is referred to as \dot{m}_{inlet} and comprises the main flow \dot{m}_∞ and the RIDN flow \dot{m}_c .

$$MFR = \frac{\dot{m}_c}{\dot{m}_{inlet}} = \frac{\dot{m}_c}{\dot{m}_c + \dot{m}_\infty}, \quad M = \frac{\rho_c u_c}{\rho_\infty u_\infty}, \quad I = \frac{\rho_c u_c^2}{\rho_\infty u_\infty^2} \quad (3.7)$$

Experimental data has been acquired for eight different mass flow ratios MFR of the RIDN coolant, with the film cooling parameters shown in table 3.3.

MFR [%]	M [-]	I [-]
0	-	-
0.8	1	1
1	1.2	1.4
1.5	1.7	3.1
2.25	2.6	6.9
3	3.5	12.5
4	4.7	23
5	5.9	36

Table 3.3: Coolant injection parameters for the main measurement campaign, determined with stage mass flow values

The values for M and I are calculated according to equations 3.7. This takes the global mass flow values into the stage into account. For MFR 0, no coolant mass flow was supplied whereby the holes were left uncovered. The RIDN cooling design has been scaled from engine conditions, matching the blowing ratio M for the

representative value of MFR 1.5 ($M=1.7$). The number and diameter of the cooling holes has been specified numerically by Schmid [112]. Because the density ratio is equal to one, the momentum ratio scales to greater numbers in comparison to the engine conditions.

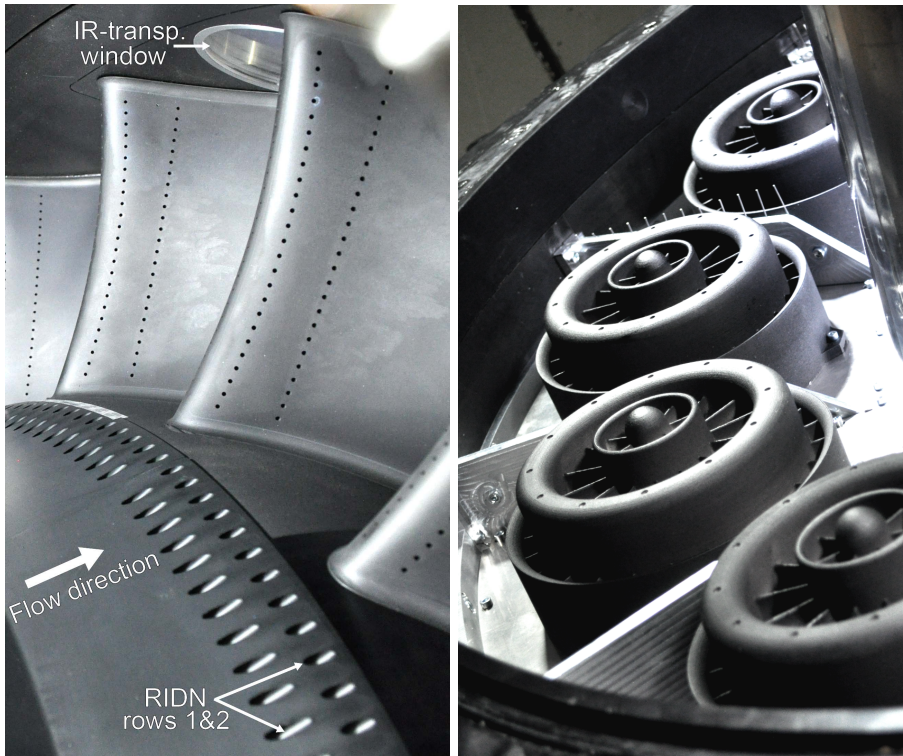


Figure 3.6: Test section views. NGV row and RIDN coolant injection rows (left), combustor module with installed swirlers from upstream (right)

For the investigation, a parameter variation including both lower and higher MFR is studied. Even though the momentum ratio becomes unrealistically high, compared to a real engine, MFR up to 5 are studied to emphasize on the observed effects on the flow field and endwall cooling. For SWL/SWP inflow, the aerodynamic measurements have been conducted with the two main settings of MFR 0 and MFR 3. MFR 3 has been selected in favor of MFR 1.5 such that any influence on the flow field due to the coolant injection is better pronounced. The data for the thermal evaluation of the film cooling design has been acquired for the full range of MFR 0 to 5 in all inflow configurations.

The pressure ratio Π_{RIDN} across the RIDN holes, calculated according to equation 3.8 increases (Fig. 3.7) quadratically with the MFR.

$$\Pi_{\text{RIDN}} = \frac{p_{s,\text{RIDN}}}{p_{s,\text{RE1}}} \quad (3.8)$$

A pressure ratio close to one is sufficient to supply the low MFR up to 1. For MFR 5, the pressure ratio Π_{RIDN} attains a value of 1.1. Cooling air reduces turbine efficiency because the air cannot fully contribute to the thermodynamic cycle. The increase in required pressure ratio can be correlated to a reduced turbine efficiency and hence give a value as an orientation. A realistic pressure ratio for the RIDN injection in an engine is of the order of 1.05 up to 1.06. Consequently, all coolant injection rates studied in the present investigation are in a realistic range, whereby MFR 5 requires some excess pressure supply.

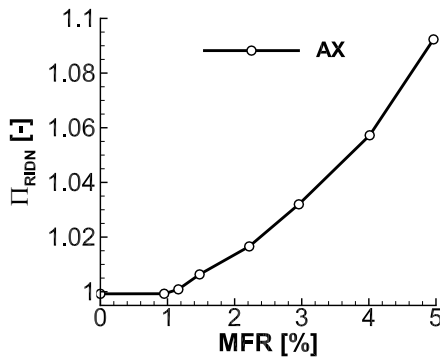


Figure 3.7: Pressure ratio across RIDN cooling holes with varied MFR

A double row of 19 (upstream row) and 20 (downstream row) holes per swirler passage was studied with a circumferential hole spacing of $3D$ and a L/D ratio of 6.5 . This corresponds to relative pitch spacing of $0.1 x/T$ per hole, normalized to one NGV pitch T . The staggering between the two rows is $0.05 x/T$, equal to $1.5D$. The RIDN holes of each 30° segment were supplied by a plenum, after passing two meshes for homogenization. A larger plenum connects 3 segments to a 90° sector with a common supply. The RIDN flow path is shown in figure 3.2 in the sectional rig view .

Airfoil cooling, trailing edge ejection and NGV-rotor wheelspace purge flow

Each vane features airfoil cooling films and a trailing edge slot. Both are supplied by two internal plenum chambers from the casing side. The schematic in Fig. 3.8 shows these plenum chambers and the location of pressure taps along the airfoil surface and inside the front and aft chambers at 20 % span height.

Whereas the front chamber supplies five coolant rows (2 rows with 25 holes and 1 row of 20 holes on the suction side, 2 rows with 25 holes on the pressure side,

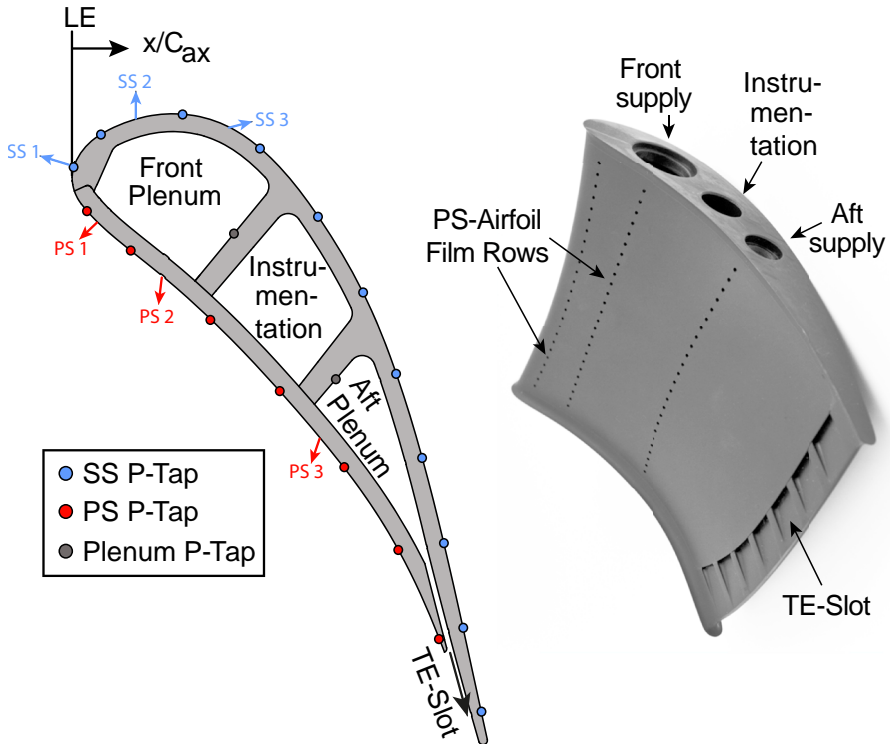


Figure 3.8: NGV coolant plenum and instrumentation chambers and pressure tap positions at 20 % span height. Arrows indicate position and direction of PS & SS film cooling rows (left), NGV photograph, showing the pressure side and the seven TE-Coolant Ejection Slots (right)

hole diameter $D=1.5$ mm), the aft chamber supplies one pressure side coolant row (25 holes and $D=1.5$ mm) and seven span wise slots (10 % span height each, 13 mm by 1.5 mm) in the trailing edge. A flow rate of 4.9 % of \dot{m}_{inlet} was ejected as NGV airfoil film cooling and 1.95 % of \dot{m}_{inlet} was ejected through the trailing edge slot. The cavity between NGV and rotor was supplied with 2 % of \dot{m}_{inlet} . Purge flow and the airfoil cooling flows are kept at constant flow rate for all experiments.

3.4 Vane passage nomenclature

Figure 3.9 illustrates the nomenclature of the vanes and defines the coordinates in the boundary layer measurement area. Whereas only one vane passage needs to be measured for the baseline inflow, the application of swirl requires data acquisition for two adjacent passages. This is achieved by traversing only the swirler casing ring, while the same NGV passage is recorded and the probe positions remain the same.

The first swirler measurement sector is denoted "Passage A", the other "Passage B". The relative pitch position, x/T is counted from the first row coolant hole that is geometrically positioned upstream of the leading edge, as shown in the illustration. Passage A is located at x/T from 0 to 1 and Passage B from 0 to -1. The vanes are denoted "Vane A" and "Vane B", whereby the central vane is "Vane B". The pitch position for the geometrical center of the swirler for both clocking positions SWL ($x/T = 1$) and SWP ($x/T = 0.5$) is indicated in the figure. For illustration purposes, this position is projected radially downward along the swirler mirror line⁵.

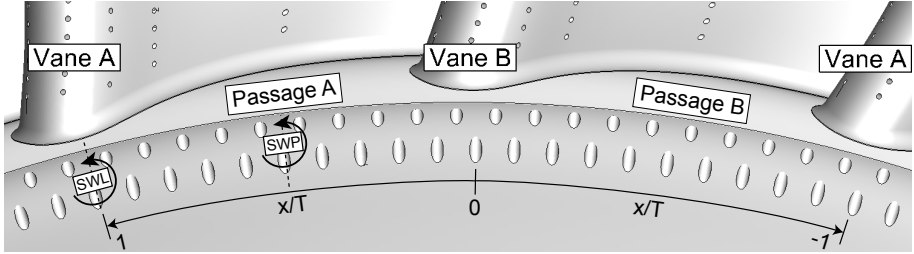


Figure 3.9: Vane passage nomenclature and pitch position of the swirler geometrical center for clocking positions SWL and SWP

⁵The swirler axis actually points at 50% span height as shown in Fig. 3.2

4 Experimental methods

In this chapter, the experimental methods that have been used for this study are described: Infrared thermography is used with the auxiliary wall method to study end-wall heat transfer and film cooling effectiveness with high spatial resolution. Foreign gas concentration measurements with CO_2 allow to study film cooling effectiveness and the propagation of coolant flows. Furthermore, the five-hole and boundary layer probe measurements are described.

The measurement results at the LSTR are obtained at different circumferential positions within the annulus. Infrared thermography, 4-Hole-Probe and boundary layer probe measurements are recorded at 270° , whereby the 0° reference position is at the top of the rig, and counting clockwise. The gas concentration sampling measurements are conducted in 90° because this is the second position in the NGV ring that allows an instrumentation carrier to be assembled. The 5HP measurements are conducted in 0° (ME01) and 330° (ME02). Finally, flow tracing results were acquired at the identical probe position at 330° in ME02.

Static pressure taps on the casing show that circumferential homogeneity is given in all regions of interest. A homogeneity within $\pm 5\%$ of the dynamic head in the respective measurement plane is achieved.

4.1 Infrared thermography - auxiliary wall method

To determine heat transfer and film cooling effectiveness values on the endwall, the auxiliary wall method was applied: A *FLIR x6540sc* infrared camera was used to detect surface temperatures on the stator endwall. Its *InSb* detector has a usable wavelength range of 2.5-5.1 μm and a resolution of 640x512 pixels. Data was recorded for 30 seconds with a frame rate of 10 Hz leading to 300 thermograms per camera position and temperature. In total, three camera positions were used to cover the whole end-wall area, resulting in a minimum spatial resolution of about 0.4 mm. Temperatures were recorded through a coated CaF_2 window with a transmissivity τ of an average of 0.98 in the range of 2.5-4 μm . The endwall aluminum body (Figure 4.1, item 1) was heated by *Kapton* heater foils (Fig. 4.1, item 3), establishing sixteen quasi-steady-state conditions with constant temperature in steps of 2 K between 323 K and 353 K. The body temperature is homogenized by the high thermal conductivity of the aluminum. Nine heater foils with a maximum power output of 1 kW and a 12 VDC power supply were applied and controlled by pulse width modulation. The temperature of the base body in this way is maintained to a lateral variation within ± 0.25 K for each temperature setting with respect to the full measurement area. The temperature in each measurement is accounted for in the data analysis.

The surface is covered by an auxiliary wall (Fig. 4.1, item 2) of *Ethylene-tetrafluorethylene (ETFE)* of an average thickness of 0.82 mm and a *Nextel Velvet Coating* paint of 0.12 mm with an emissivity of 0.97 according to Lohrengel and Todthen-

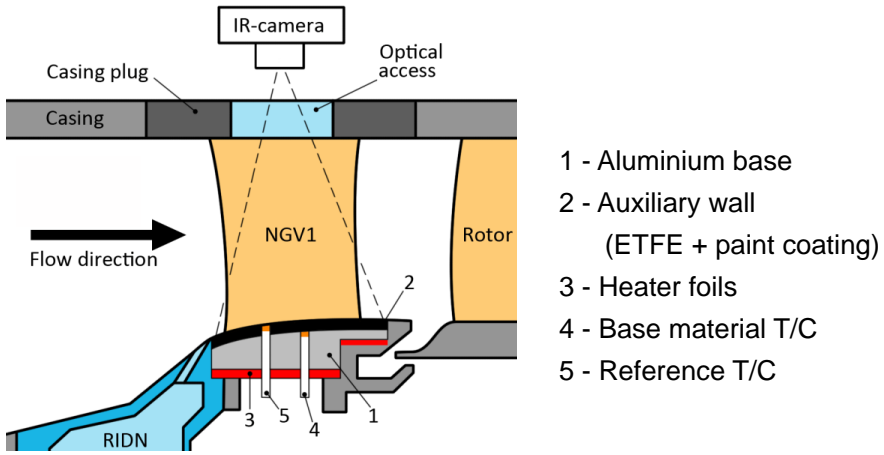


Figure 4.1: Schematic of the auxiliary wall method, applied to the NGV endwall (Werschlich et al. [134])

haupt [92]. It is used to determine the local heat flux. To calculate this value, the temperature difference across the auxiliary wall needs to be measured. The base material temperature was monitored by an array of 59 K-type thermocouples (Fig. 4.1, item 4). The variation is small due to the well conducting base material and the local value is estimated with a linear interpolation between the thermocouple measurement positions⁶. The temperature above the auxiliary wall varies locally, governed by the external flow situation. It is measured with the infrared camera. Because its detector reading is influenced by factors such as the viewing angle through the glass windows, the glass temperature, humidity in the air flow, among others (Ochs et al. [101]). Therefore, an in-situ calibration was performed for each measurement. 20 K-type thermocouples (Fig. 4.1, item 5) were placed underneath small cylindrical metal pins with a diameter of 1.5 mm. They were only coated by the paint layer and could be detected in the infrared image. In this way they served as geometrical reference for the transformation of the camera image as well.

Manufacturing and characterization of the auxiliary wall

The instrumentation carrier for the infrared thermography measurements was manufactured in several steps. The coated auxiliary wall was both geometrically and thermally characterized in detail by measurements to quantify the relevant properties for the calculation of the adiabatic heat transfer parameters. The calculation procedure is described subsequently.

⁶The typical variation for each heater setting in lateral direction in this way was maintained within ± 0.25 K

- The **manufacturing procedure** of the instrumentation carrier began with the machined aluminium body on a 5-axis-CNC-milling machine. *EN-AW-6082 (T651)* with a thermal conductivity of $170\text{--}220 \text{ W/mK}$ was used. The desired final endwall geometry was undersized by 1 mm and protruding cylinders with a diameter of 1.5 mm were machined at the reference temperature locations. The specimen contained designated planar reference areas for the geometric measurement (Fig. 4.2-A) with a laser profilometer. After an initial geometry scan, the reference areas were covered. In the next step, the base body was powder coated with ETFE in several layers to a final layer thickness of 1.5 mm, covering the reference cylinders (Fig. 4.2-B). Subsequently, the surface was CNC-machined with an undersize of 0.15 mm and then geometry-scanned for a second time (Fig. 4.2-C). Thereafter, the reference areas were removed by CNC-milling. The slightly reduced accuracy involved in this way was accepted to avoid damage of the paint layer by the milling process. This paint layer of *Nextel Velvet Coating* was applied with a thickness of about 0.1 mm. Afterward, the third geometric measurement was conducted. The base plate was finally instrumented with thermocouples and heater foils (Fig. 4.2-E) on the back side and assembled to the test rig, where it was leveled for a smooth fit into the NGV hub ring (Fig. 4.2-D) with a positioning accuracy of 0.05 mm.

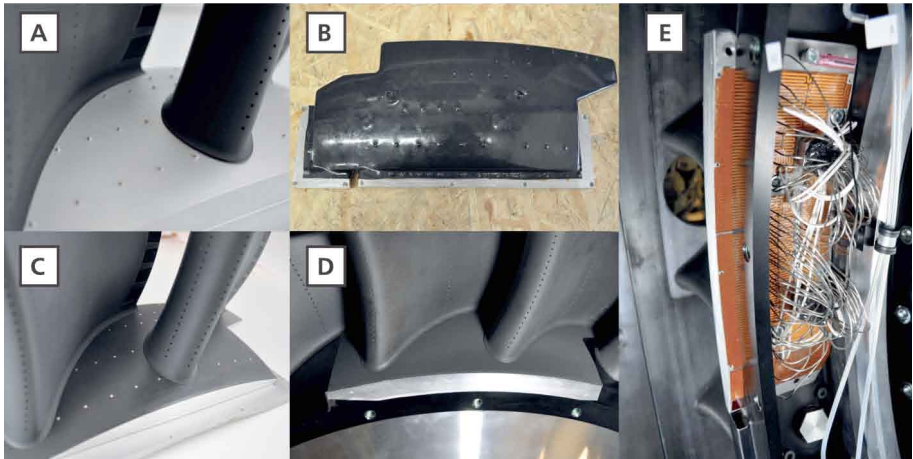


Figure 4.2: Manufacturing steps of the auxiliary wall and instrumentation carrier

- The three geometric measurements to determine the **layer thickness** of the auxiliary wall were conducted with a *Keyence LK-G152* laser profilometer, mounted to an *Aerotech AGS 10000* traverse system, formerly used for the investigations of Kloss [75]. Data was acquired with a resolution of 0.5 mm and a combined accuracy of 0.01 mm^7 . An average ETFE layer thickness s_{ETFE} of

⁷For a detailed uncertainty evaluation of this measurement method refer to the dissertation of Kloss [75]

0.82 mm and a paint layer thickness s_{paint} of 0.12 mm has been measured. The thickness distribution is depicted in Fig. 4.3.

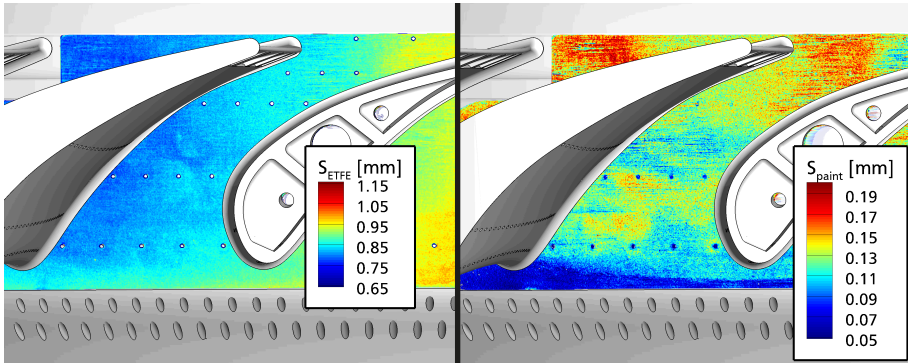


Figure 4.3: Layer thickness of ETFE- and paint-coating

The measured values vary locally, whereby larger fluctuations are measured for the paint layer. To avoid a systematic error in the local heat flux calculation, the exact local thickness in each pixel of IR image was accounted for in the data analysis procedure.

- The **thermal conductivity of the auxiliary wall** was determined experimentally to ensure that the thermal conductivity of the auxiliary wall does not vary with temperature within the range of interest for the measurements. It was measured in the laboratory of Netzsch [99] with a transient *LaserFlash 447*-procedure, which is the common industry standard for this characterization. No significant temperature influence was detected with a variation of less than 0.3%. The absolute value of $\lambda = 0.195 \text{ W/mK}$ however differs from the value of $\lambda = 0.24 \text{ W/mK}$ found in published data sheets. This difference results of filling materials in the coating material and of the manual manufacturing process. *Nextel Velvet Coating* has a spectral emissivity ϵ of 0.97 and a thermal conductivity of 0.199 W/mK . Both values were determined accurately by Lohrengel and Todtenhaupt [92] and the coating is used as a scientific standard for infrared measurement setups. Together with the measured local layer thickness, the thermal resistance at any arbitrary point in the area of interest can be calculated and is included in the data analysis.

NGV endwall measurement area

The measurement area, that is evaluated on the NGV endwall, reaches from a relative axial position of $-0.1 x/C_{ax}$ to $1.1 x/C_{ax}$ with respect to the NGV leading edge without fillets. Thereby only in the region between -0.05 and $1 x/C_{ax}$ the full passage pitch area is covered. This is a result of viewing angle limitations and a surface defect at the onset of the test plate that occurred during the assembly of the measurement carrier.

Calculation of the adiabatic heat transfer parameters

By applying a 3-dim.-2-dim. projective transformation, a correspondence between the camera image and the position in the experimental setup was established. Because the reference thermocouples were clearly identifiable in the thermograms they were used as geometric references. The local surface thickness and the thermocouple readings underneath the auxiliary wall were transformed and interpolated onto the grid of the camera image. A non-uniformity correction (NUC) was performed. The thermograms then have been averaged and calibrated at each constant heater setting. The object signals detected by the camera were calibrated in-situ using the reference thermocouples and a 3rd-order polynomial fit. Because the metal pins were also covered by the low-conductive paint layer, a temperature correction was necessary for the thermocouple reading⁸. Together with the readings of the thermocouples underneath the auxiliary wall and the local layer thickness, heat flux values \dot{q} were determined for each of the sixteen heater settings with equation 4.1.

$$\dot{q} = R_{th} (T_W - T_B) , \quad \text{with} \quad \frac{1}{R_{th}} = \frac{s_{ETFE}}{\lambda_{ETFE}} + \frac{s_{coat}}{\lambda_{coat}} \quad (4.1)$$

A similar method has been used by Laveau [83] [82] [85] [84] to study the effects of endwall contouring on heat transfer and adiabatic wall temperatures in a vane row of an axial turbine and by Giel [44] [43] to determine Nusselt numbers on airfoil and endwall surfaces of rotor blades in a cascade setup.

With the temperature difference between main flow and coolant, adiabatic heat transfer coefficients and film cooling effectiveness values were determined with the superposition approach, presented by Gritsch et. al. [52] and Goldstein [47]. A linear regression for each point in the measurement area is performed. The procedure is illustrated in Fig. 4.4 for two arbitrary points on the surface A and B. Using the 16 thermograms a linear relation for the heat transfer coefficient $h(\theta)$ is found (Eq. 4.4). The dimensionless temperature ratio θ is varied during the measurements by varying T_w with sixteen different heater settings. In this way, the adiabatic wall temperature is defined at the intersection of the regression fit with the abscissa. If the wall would attain this temperature, no heat flux from the surface would occur. The inverse of this temperature ratio gives the adiabatic film cooling effectiveness η_{aw} for each point. Finally, the adiabatic heat transfer coefficient h_{ad} is found at the intersection of the curve with the ordinate. The definition of θ shows that it is impossible to measure h_{ad} directly, but that it has to be determined with the regression. Its application in heat transfer measurements has the advantage (Moffat [97]) that it does not require a measurement of main flow temperature. There are setups, where e. g. temperature gradients or upstream heating elements make the measurement of a representative fluid temperature challenging.

$$h(\theta) = h_{ad} (1 - \eta_{aw}\theta) \quad (4.2)$$

⁸For this correction, the temperature gradient in the paint layer was calculated with the local heat transfer coefficient. This parameter is obtained with the data analysis procedure that is described in this paragraph. The involved linear regression is subsequently run again with the corrected wall temperatures.

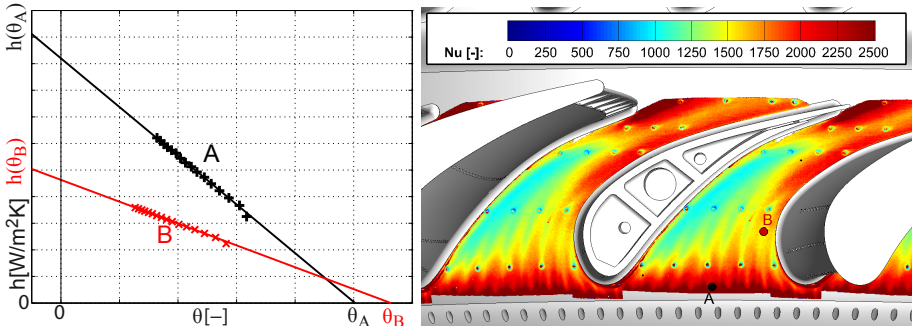


Figure 4.4: Linear regression procedure for data evaluation at to arbitrary points A and B in the measurement area

$$\theta = \frac{T_\infty - T_c}{T_\infty - T_w} \quad (4.3)$$

To apply the superposition principle, the injection parameters and the flow field need to be kept constant for all measurements that are taken into account in the regression. Therefore, the main flow temperature T_∞ and the coolant flow temperature T_c are monitored closely and maintained constant within $\pm 0.1K$. The temperature of the main flow is evaluated with a temperature rake that is positioned close to the measurement area. The coolant temperature is controlled with a thermocouple in the supply plenum.

In this way, the thermal parameters are calculated, whereby all data is interpolated onto the of the camera image beforehand. For the illustration, the resulting data is then transformed into the 3-dim. coordinate system of the vane passage, using the thermocouple markers as geometric reference. Data was averaged for areas, where information from more than one camera position was available. The heat transfer coefficient h_{ad} was further reduced to the dimensionless Nusselt number Nu (equations 4.4). The data analysis procedure was defined by Steinhausen [124].

$$Nu = \frac{h_{ad} C_{real,NGV}}{\lambda_{air,T_\infty}}, \quad \text{with } h_{ad} = \frac{\dot{q}}{T_w - T_\infty} \quad (4.4)$$

Experimental uncertainty

The procedure to calculate the experimental uncertainty for the infrared measurements follows the standard procedure described in the "Guide to the expression of uncertainty in measurement (GUM)" [65]. A Gaussian error propagation is calculated. The main parameters of influence are the uncertainty of the temperature measurements with thermocouples and the infrared camera, which were evaluated as type A uncertainties with a successive perturbation of the measurement data. Furthermore, the auxiliary wall layer thickness, composed of paint and ETFE, was estimated as type B uncertainty with $20 \mu m$ according to the manufacturer of the used laser-distance

profilometer. The thermal conductivity of the paint layer, λ_{coat} was estimated according to Lohrengel et al. [92] to 2 %. The thermal conductivity λ_{ETFE} was measured using a laser-response transition measurement with an uncertainty of 10 % in the laboratory of Netzsch[99]. This value is considerably high and contributes to about half of the absolute measurement uncertainty for both ΔNu and $\Delta \eta_{ad}$. Because only one instrumentation carrier and hence auxiliary wall was used for all experiments, only a negligible influence on the repeatability of the results is assumed. A more accurate determination of this parameter would require a complex setup, because the actual measurement needs to be performed on the measurement carrier itself.

The relative uncertainty at $Nu=1900$ and $\eta_{ad}=0.3$ in this way is calculated to be $\Delta \eta_{ad} = \pm 0.08$ and $\Delta Nu = 9.5$ %. The adiabatic wall temperature can be determined with an accuracy of ± 1.2 K. The relative uncertainty, $\Delta \eta_{ad,rel}$ is determined predominantly by the η_{ad} value. Peak values are found in regions of low film cooling effectiveness and high Nusselt numbers, i.e. between coolant streaks and in the trailing edge area of the endwall because the signal is very weak. A point wise comparison to CO_2 gas sampling data (Fig. 4.9) shows a good agreement. The latter technique has a smaller measurement uncertainty with respect to the film cooling effectiveness, as it is illustrated subsequently.

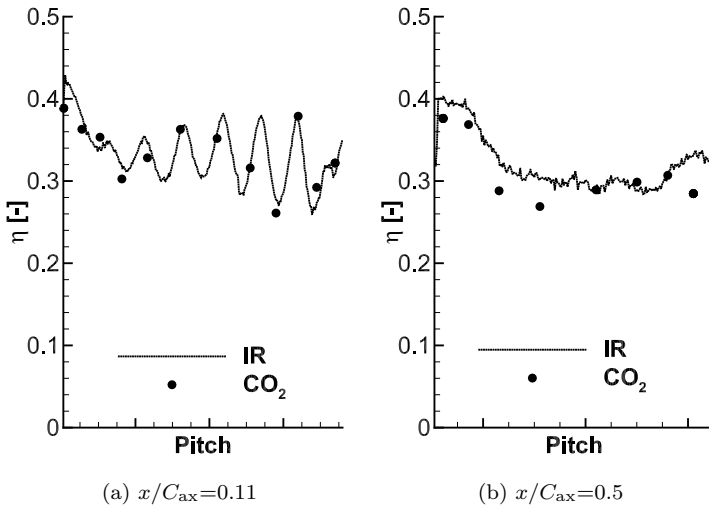


Figure 4.5: Comparison of IR and gas concentration data, AX MFR 3

Comparable studies of heat transfer and film cooling effectiveness show uncertainty values in the same order of magnitude [85] [142] [100] [33] (c.f. Appendix, section C).

4.2 Gas concentration measurements

To study the propagation of coolant flows in the turbine, gas concentration measurements were used. CO_2 was used as a foreign gas and added only to one of the coolant air flows at a time. Any of the eight individual coolant supplies at the LSTR could be seeded in this way. A secondary air exhaust was used to exchange a part of the air between the environment and the closed loop air flow system. In this way, a steady and elevated concentration of CO_2 was achieved in both primary and secondary air flow. Thereby, the secondary air was at a considerably higher concentration level than the main flow. Using three *Emerson XStream XEGP* four-channel gas analyzers, this concentration could be measured. A reference measurement in both the main flow path, c_∞ , and in the particular secondary flow path, c_{sec} , was conducted. c_{sec} was increased to a steady concentration of about 18.000 ppm and measured through a wall tapping in the coolant plenum. c_∞ was kept at a constant level of about 2.000 ppm by the partial open loop configuration of the test rig and measured through a pitot probe in ME01. Ten measurement channels are available, which could be connected to any pressure port in the stationary part of the test rig. This allowed for both surface tap sampling and traversing probe measurements in the main annulus. The technique was widely used in turbomachinery flows to study the propagation of coolant flows: Schrewe [116] and Lefrancois [87] have investigated the propagation of purge flow in a low-pressure turbine. The method had been successfully used also by Feiereisen [39]. Furthermore, Friedrichs [41] [42] used the technique and surface tap sampling results as a datum to calibrate the Ammonia-Diazo measurement technique.

The description of the experimental setup is divided into two sections, describing the application for effectiveness measurements via surface tap sampling and for flow tracing experiments. Associated measurement uncertainty and limitations are discussed.

Film cooling effectiveness measurements - surface tap sampling

CO_2 gas sampling with an array of small holes in the endwall was used to determine adiabatic film cooling effectiveness values by applying the heat and mass transfer analogy in a separate experiment. These measurements were used to assess the validity of the film cooling effectiveness values determined with the infrared measurements. A total of 120 measurement positions was used for gas sampling (Fig. 4.6-A), covering the hub side NGV endwall area between -0.055 and 1 x/C_{ax} , in eleven sets of holes with constant x/C_{ax} position. The holes had a diameter of 0.5 mm and were drilled perpendicular to the endwall surface. They were connected by plastic and metal tubes guided through the NGV to the gas analyzers (Fig. 4.6-B). The sampling flow rate was selected in a way, that no influence on the boundary layer occurs in accordance with the measurements of Schrewe [116]. The ten sampling channels were connected subsequently to all 120 measurements positions and adiabatic film cooling effectiveness values were calculated with equation 4.5 with the analogy of heat and mass transfer, assuming that the influence of thermal diffusion is negligible.

$$\eta_{aW} = \frac{c_\infty - c_w}{c_\infty - c_c} \quad (4.5)$$

In addition, 70 pressure taps, which are distributed in the NGV leading edge area (Fig. 4.6-C) and along the NGV airfoil at 20 % and 50 % span height were used for sampling as well. In this way, the cooling effect of the RIDN injection on airfoil surface cooling was studied with the same method.

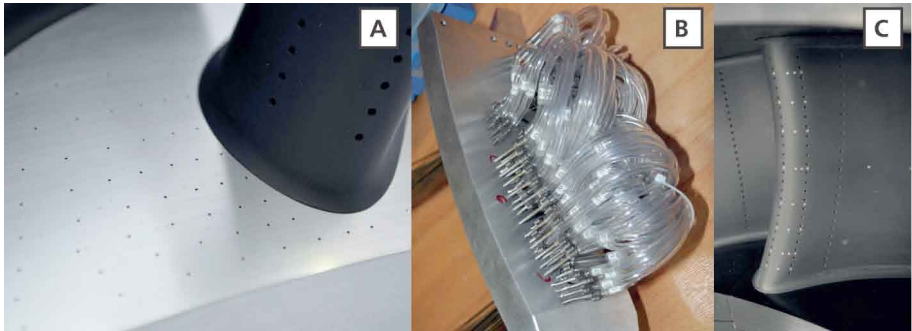


Figure 4.6: Surface tap sampling - measurement points on NGV hub endwall (A), guidance of measurement lines on the bottom side (B) and sampling taps on the NGV leading edge (C)

Coolant flow tracing in the NGV exit flow

To study the propagation of coolant flows in the turbine, CO_2 was added to one of the coolant flows (RIDN, TE, CAV) at a time and distributions of this particular coolant flow could be determined in ME02.

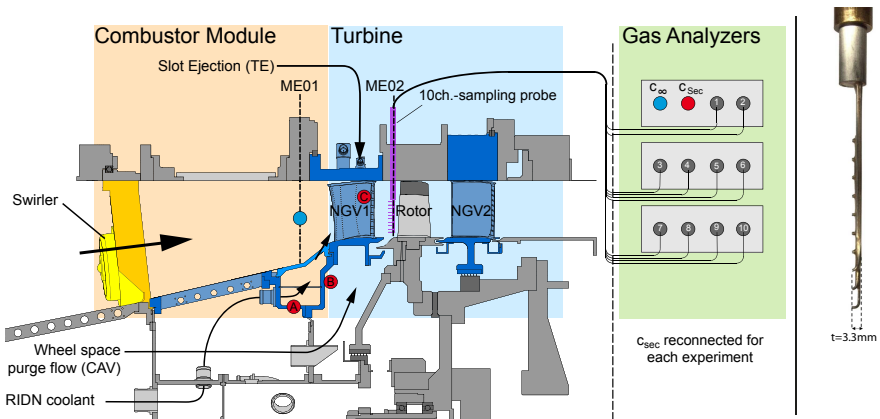


Figure 4.7: Flow tracing measurements, measurement locations and instrumentation. The reference position in the main flow (blue) and secondary flow (only one flow seeded and measured at each time, red) are illustrated. Adapted from Herrmann [59]. The 10-channel sampling probe is shown on the right

The sampling probe was designed by Herrmann [59] and had ten sampling tube channels. The probe was turned into the average main flow direction, deduced from the 5HP measurement. An isokinetic sampling rate was desired but could not be achieved by the extraction pump in the sampling system. Thus, the maximum possible flow rate was used for all channels. For the measurements, the operating point and the coolant injection rates were kept constant. By seeding only one coolant flow, distributions of the particular coolant flow paths can be determined. In this way, the coolant flows are allocated within the main annulus and flow features detected in the aerodynamic measurements can be attributed to them. Calculating the mixing effectiveness according to equation 4.6, the distribution of the coolant flow could be quantified as well:

$$\eta_{mix} = \frac{c_{\infty} - c_w}{c_{\infty} - c_c} \quad (4.6)$$

The concentration c_{∞} is measured at mid span in ME01 through a pitot probe and c_c is measured in the coolant flow of interest in each measurement: When the RIDN coolant is seeded, c_c is monitored in the lower coolant supply plenum (red marker, labeled "A" in Fig. 4.7). For TE-seeding, the aft chamber of the NGV coolant supply (marker "C", see also Fig. 3.8) is monitored and in the case of purge flow seeding a measurement position in the stationary wall of the NGV-rotor wheelspace (marker "B") is used.

Measurement uncertainty

The measurement accuracy of the gas concentration system used for the present investigation has been assessed by a Gaussian error propagation method. Dominant to the uncertainty is the accuracy of the gas analyzers, which was specified to 1 % of the measurement range by the manufacturer. Another factor that generally influences the signal reading is the ambient temperature in the test cell. This aspect could not be assessed quantitatively, but great care was taken to keep its influence unchanged during all measurement runs. In addition, the gas analyzers have been calibrated before each measurement day using a test gas to overcome a potential gain shift.

The relative measurement uncertainty follows a hyperbolic curve, dominated by the measured concentration level. Consequently, to reduce the uncertainty, the difference between the measured value and the reference concentration in the main flow is to be maximized. Fig. 4.8 shows the uncertainty curve for a main flow concentration c_{∞} of 2,000 ppm and a secondary air concentration c_c of 18,000 ppm, which are common values for this measurement campaign. In addition, the range typical of the measured data values for flow tracing and endwall effectiveness measurements is specified in the figure.

The surface tap sampling measurements are therefore in a range where a relative uncertainty of 4 % to 8 % is achieved. The concentration level that is measured with the flow tracing measurements is lower, leaving a measurement uncertainty that is worse. The comparison to a numerical simulation of the coolant flow propagation by Ivanov [63] shows a very good agreement nevertheless, not only qualitatively but with respect to the absolute value as well.

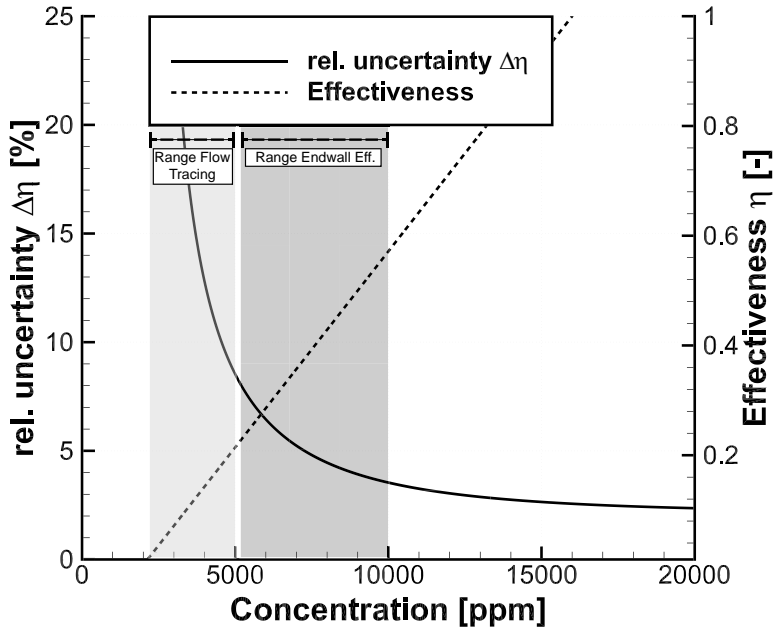


Figure 4.8: Measurement uncertainty - gas concentration measurements; the displayed curve shows the approximate measured concentration with the sampling probe and the sampling taps for reference values of $c_\infty = 2,000$ ppm and $c_c = 18,000$ ppm, typically set during the measurement. 0 - 20,000 ppm is the detector range of the gas analyzer

Surface tap sampling

In the case of the endwall effectiveness measurements, the uncertainty is lower in comparison to the infrared thermography measurements for similar values of η_{aw} (5% for $\eta_{aw} = 0.3$ compared to 25% with the IR-method). Therefore, this method is used to validate the linear regression approach for determining film cooling effectiveness values with the auxiliary wall method.

Fig. 4.6 illustrates that the sampling taps are connected via metal tubes and PVC-hoses on the underside of the instrumentation carrier. The metal tubes are then guided through the instrumentation cavity in the NGV to the exterior, where they are connected to the gas analyzer. Associated, a lot of sealing work was required and the assembly took place in a very small spaced environment in the NGV1-inner ring. Great care was taken and with leakage and through flow tests it was assured that damage was avoided. Only one measurement position was found blocked at the end. Outliers identified in endwall pressure measurements conducted with the same instrumentation carrier are not displayed in the experimental results.

The results gained with the sampling holes in the entrance area, where discrete coolant streaks are observed, are prone to measurement uncertainty. Compared to for example Schrewe's measurements [116] in a mixed-out seal air flow and Friedrich's [41] sampling positions along the center line of a cooling hole in a straight duct, the flow field in the present investigation is more complex. Especially for low MFR, the surplus in momentum in the cooling jets is low and their trajectory is very susceptible to deviations. The lowest possible suction rate was applied in the entrance area and an influence of the suction rate has been observed. The corresponding measurement locations have been identified as outliers and being systematic error components, they are left out in the comparison to the infrared measurements.

Flow tracing - probe geometry influence

The measured concentration level is considerably lower in the case of the flow tracing measurements, lying in a range of 2,000 - 5,000 ppm, due to the mixing of coolant and main flow up to the measurement plane ME02. Higher values would require the supply of an extensive amount of foreign gas which was not possible with the existing injection system. Despite of the increased uncertainty, the aim of visualizing the qualitative coolant flow propagation in the flow field is achieved with this technique.

The 10-channel probe can only be aligned for an averaged flow direction, unlike the 5HP, where a re-alignment is possible for each measurement position in the grid. Therefore, when high radial or whirl angles to the probe are present, the recorded data might be compromised. To assess the significance, the probe was installed in a free stream wind tunnel and total pressure measurements were conducted for all ten positions. Inflow angles of less than 10° to the probe, as they occur during the measurements⁹, were determined to be insignificant for a correct reading and hence it is assumed, that the sampled CO_2 -concentration is not compromised either.

4.3 Pneumatic measurements

Five-hole-probe measurements

Pneumatic measurements have been conducted to study the aerodynamic flow field with all inflow configurations. 5-Hole-Probes have been used in the main annulus; a 4-Hole-Probe and a boundary layer probe have been used near the RIDN injection. The measurements are further detailed below, followed by a discussion of the measurement uncertainty. Five hole probe (5HP) data has been acquired in ME01, ME02 and ME03 (see Fig. 3.2), i.e. upstream and downstream of both the NGV and rotor rows in the rig. The cobra-type probe had a head diameter of 1.6 mm and pyramid-shaped side surfaces (Fig. 4.9a). The probe was calibrated in the institute's free stream wind tunnel for the expected range of inflow angles and flow velocities. The probe was traversed along the radial direction at a fixed angular position on the rig. The relative movement of the probe with respect to the vanes and swirlers was realized by a simultaneous angular adjustment of the three casing rings that carry swirler modules and both vane rows in steps of 1° . The radial and angular traverses resulted in a measurement grid of 672 data points for the configuration AX, whereas 1302 data

⁹The inflow angle to the probe is specified based on 5HP measurements at the same position

points were acquired for the configurations SWP/SWL to cover two vane passages. The data has been recorded for 10s, after a settling time of 2s with a sampling rate of 10 Hz. A *Pressure Systems NetScanner 9116* with a measurement range of 5 psi has been used for data acquisition.

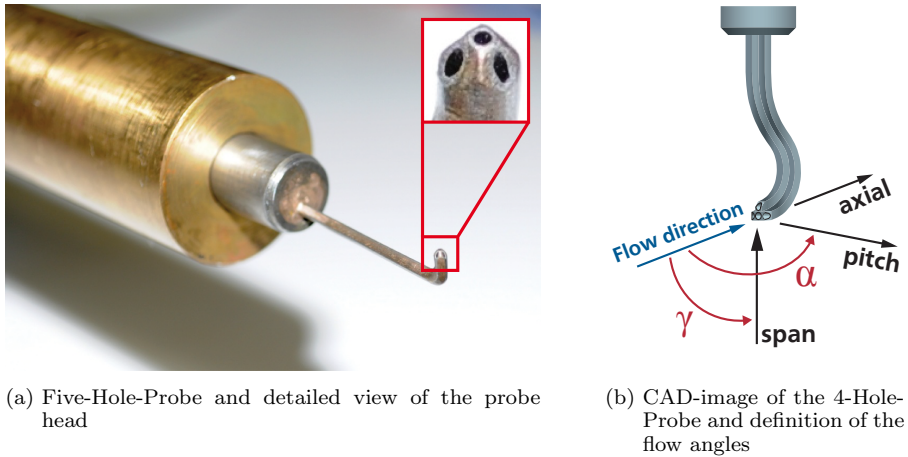


Figure 4.9: Pneumatic measurements

Boundary layer measurements

The boundary layer was examined using pitot probes for AX inflow near the RIDN coolant injection (Fig. 4.10).

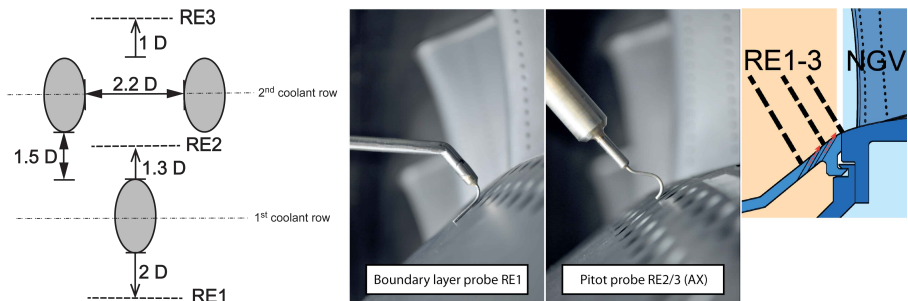


Figure 4.10: Boundary layer measurement planes RE1/2/3 and probes used for AX measurements (Adapted from Arne [8])

Three planes were used with the non-dimensional positions specified in Fig. 4.10 and 3.1: RE1 to study the incoming boundary layer upstream of the

first coolant row. The second plane, RE2, was in between the two rows and the third plane, RE3, downstream of the second row to study the impact of each row on the near-wall boundary layer individually. All planes were traversed perpendicular to the hub endwall. In plane RE1, a boundary layer probe was used to determine the total pressure in the incoming boundary layer.

The probe head was dimensioned with a long inflow tube to avoid from interfering potential effects of the support shaft. Because the axial distance between the two coolant rows limited the size of the probe, a different design was used for RE2/3 to measure the total pressure. It was verified with a traverse in RE1, that the results are comparable to the boundary layer probe. Solely close to the wall, differences were determined. Because the boundary layer probe had a smaller diameter it is thus considered more accurate. The boundary layer in RE1 was resolved with grid points in a radial spacing of 0.1 mm up to $y_D=0.5$ and 0.3 mm up to $y_D=3.75$. In RE2 and RE3, a grid was measured with a resolution of 0.3 mm in radial and 0.5 mm in circumferential direction, equaling a total number of 540 data values for RE2 and 783 for RE3 per cooling hole studied. The measurements have been conducted with a *Pressure Systems NetScanner 9116* with a measurement range of 5 psi for a recording time of 5 s at a sampling rate of 10 Hz.

The measured profile in the boundary layer is presented in form of the normalized total pressure, $P_{t,\text{ref}}$. It is calculated with equation 4.7:

$$P_{t,\text{ref}} = \frac{P_{t,\text{RE3}} - \overline{P_{s,\text{ME01}}}}{P_{t,\text{ME01}} - \overline{P_{s,\text{ME01}}}} \quad (4.7)$$

To visualize coolant jet contours, a pressure coefficient $C_{p,t,\text{ref}}$ is calculated according to equation 4.8. In this way, the excess total pressure within the RIDN jet is normalized by the dynamic pressure of the turbine inflow.

$$C_{p,t,\text{ref}} = \frac{P_{t,\text{RE},i} - \overline{P_{t,\text{ME01}}}}{P_{\text{dyn,RE},i}} \quad (4.8)$$

Whereas for axial inflow, a pitot probe was sufficient to identify the coolant jet contours at turbine inlet, greater flow angles are present for swirling inflow. A four-hole-probe (4HP) was manufactured, allowing the probe's center hole to be positioned closer to the wall due to the absence of a fifth hole. A CAD image of the probe and the definition of the flow angles is shown in Fig. 4.9b. The definition of the angles applies to all other probe measurements as well.

Measurement uncertainty and zoning algorithm

The manufacturer specifies an uncertainty of 0.05% of the range of the pressure scanner that is used for the pneumatic measurements. Each probe used for pneumatic measurements has been calibrated in a freestream wind tunnel for the expected range of Mach numbers and flow angles. A 7th order polynomial fit is calculated based on this data map. In this way, exemplary for the 4HP, a mean deviation of $\pm 1.5^\circ$ for flow angles is achieved in a range of $\pm 15^\circ$ for the radial angle and $\pm 30^\circ$ for the whirl angle and ± 0.003 for the Mach number, evaluated at the nodes of the polynomial. Thereby, the deviation is greater for smaller Mach numbers and decreases to $\pm 0.025^\circ$, if only the highest Mach number of 0.3 is evaluated.

A reasonable aerodynamic calibration is achieved in this way, at the standard of prior measurements by Linker [90] and Schrewe [116] on the rig. However, these values only serve as a matter of orientation. The complex flow field downstream of a swirler makes measurements challenging. Great care has been applied to remove systematic errors.

In the turbine inlet plane, the values approach the edge of the calibration map. Very low velocities are present in the swirl core and high flow angles appear. The 5HP is re-aligned such that the inflow remains within $\pm 4^\circ$ in each grid point. In this way, the necessary data range with respect to the whirl angle is small. The velocities that are included in the calibration are limited to the range of observed velocities in the measurement. In this way, the calibration is improved. The radial angles remain large and in consequence, there are data points for which the flow at the probe head is separated. A zoning algorithm is used to overcome this. The measurement is divided into four inflow zones and the data input of the hole in the separated flow area is not taken into account in the post-processing. This means that the calibration as well has to be evaluated with respect to the zones. The application of this method (Apell [7]) allows to use the full measurement grid with swirling inflow at the LSTR.

The same is applied for the 4HP measurement near the RIDN injection. In this region, in addition the small scale of flow structures has to be taken into account. Some of them have a similar dimension as the probe head, i.e. the probe cannot resolve them (Linker [90]). For example when the probe enters into a coolant jet, some of the probe's holes are still outside of the jet and a pressure gradient is detected. This gradient is interpreted as a flow angle by the data evaluation algorithm. These measurement values need to be removed in the post-processing. Irregular values are identified based on the calculated Mach number gradient to neighboring measurement points and with an iterative procedure, a limiting value is identified for this gradient, removing all problematic measurement points.

The 4HP for this reason has not been realigned to the flow direction during the measurements but with the turbine axis instead. The zoning algorithm is used as well. In this way, the usable range of the probe can be greatly increased. This allows to measure the whole flow field near the RIDN holes with applied swirl.

5 Investigation of the reference configuration

This chapter presents the first part of the experimental results. As a reference configuration, axial, low-turbulent inflow is investigated, whereby the combustor inlet section is left without installations. The analysis of the results emphasizes on two main aspects:

- The aerodynamic flow field is greatly influenced by the RIDN coolant injection. To illustrate this influence, the aerodynamic flow field is described in detail by 5HP measurements up- and downstream of the stator row. This is complemented by a detailed boundary layer investigation near the RIDN injection. By means of flow tracing, the propagation of the coolant is identified. The interaction with other coolant flows, namely the trailing edge ejection and the wheel-space purge flow injection and the associated formation of flow features is discussed.
- A variation of the mass flow ratio MFR to the RIDN injection is studied to characterize the coolant design. The two rows are observed to perform differently and the main contribution to the endwall film cooling comes from the downstream row. Both heat transfer and film cooling effectiveness are determined to increase with the MFR. Combining both values, the parameter Θ is calculated, defining the heat flux reduction due to film cooling. With this parameter it is shown that the increased film cooling effectiveness observed for MFR greater than 1.5 is counteracted by the concurrently increasing heat transfer, yielding a net benefit in only a few sections of the endwall.

To guide the reader through the discussion of the results, a flow model is developed that illustrates the observed findings in a schematic manner.

5.1 Aerodynamic flow field

The flow field in the turbine's NGV row is presented by the means of five-hole-probe (5HP) investigations in the inlet plane (ME01) and the NGV exit plane (ME02). In ME02, also flow tracing results are analyzed and loss contours are evaluated to identify their sources due to the three coolant flows in the investigation and to understand their propagation within the NGV row.

The flow field near the RIDN injection holes is analyzed in detail with four-hole-probe (4HP) and the boundary layer probe measurements.

Turbine inlet

Figure 5.1 shows the turbine inflow in ME01 with pitch wise averaged values for the Mach number and the radial angle γ . The average whirl angle remains at 0° (not

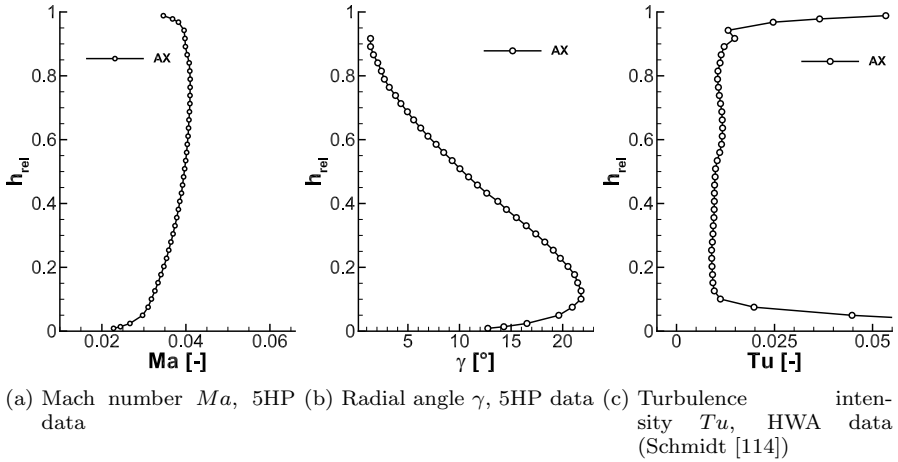


Figure 5.1: Turbine inflow in ME01, MFR 3, AX inflow

shown here). Both the Mach number and γ distribution show the influence of the main annulus' geometry. The hub endwall is inclined by 13.2° to the axial direction and thereby responsible for radial angles with only positive values. An upstream effect of the increased hub angle¹⁰ of 39° immediately downstream of ME01 is observed: Radial angles greater than the mentioned hub endwall inclination of 13.2° are measured in the lower annulus. The velocity profile has its highest values off the channel center at $0.7 h_{\text{rel}}$. A velocity gradient in the boundary layer of both endwalls is observed, beginning at approximately $0.075 h_{\text{rel}}$.

Turbulence intensity distribution The turbulence intensity in ME01 has been determined with hot-wire measurements by Schmidt [114]. The axial inflow has a turbulence intensity of about 1% in the passage center in ME01, based on the effective velocity at each measurement position. Towards the endwalls, beginning at a distance of about $0.1 h_{\text{rel}}$ the turbulence intensity increases to values of up to 10%, dominated by the reduced effective velocity (Equation 5.1).

$$Tu = \frac{\sqrt{\langle u'_{eff}{}^2 \rangle}}{\langle u_{eff} \rangle} \quad (5.1)$$

The probe has been calibrated a-priori in a free-stream wind tunnel and temperature corrections have been applied. Further discussion of the turbulence measurements including length scales is presented in Wilhelm et al. [140].

¹⁰The combustor geometry is shown in Fig. 3.3 and specified in table 3.1

Inflow boundary layer characterization

The flow field near the RIDN injection has been studied in detail. A boundary layer probe has been used in RE1 to determine the incoming boundary layer profile for MFR 3. Figure 5.2 shows the isentropic Mach number Ma_{is} . The wall distance y is normalized with the cooling hole diameter D to the relative wall distance y_D . The profile has been measured up to $y_D = 3.75$. Due to the tapered annulus, the cooling holes are placed in a favorable pressure gradient i.e. an accelerated boundary layer. A boundary layer thickness of $2.5 \delta/D$ is assessed when, according to Schlichting and Gersten [111], $u = 0.99u_\infty$ is used as a measure.

The displacement thickness δ_1 (equation 5.2) and the momentum thickness δ_2 (equation 5.3) were calculated assuming incompressible flow. The shape factor H_{12} is determined to be 1.1 with equation 5.4.

$$\delta_1 = \int_0^\delta \left(1 - \frac{u(y)}{u_\infty}\right) dx = 0.62 \text{ mm} = 0.18 D \quad (5.2)$$

$$\delta_2 = \int_0^\delta \frac{u(y)}{u_\infty} \left(1 - \frac{u(y)}{u_\infty}\right) dx = 0.56 \text{ mm} = 0.16 D \quad (5.3)$$

$$H_{12} = \frac{\delta_1}{\delta_2} = 1.1 \quad (5.4)$$

For this experiment, H_{12} is in the turbulent regime. It is smaller than the value of about 1.4, stated by Schlichting and Gersten [111] for a turbulent boundary layer on a flat plate. The present investigation examines an accelerated boundary layer with a favorable pressure gradient. Consequently, the shape factor, which is a good indicator of this gradient, has a smaller value.

2-dim. contours of whirl angle and Mach number have been determined in RE1 with the 4HP (Fig. 5.3).

Data has been recorded for one vane pitch but is displayed in two adjacent passages as well to illustrate the effect of the vane's leading edge and its potential field. The effective Mach number varies by $\pm 5\%$ for an average Ma of 0.038 within one vane pitch. The Ma-minimum is observed at $x/T = 0.8$. This position is geometrically upstream of the pressure side of the vane and represents the stagnation region. Peak Mach numbers are observed in the passage center, with the maximum at $x/T = 0.3$. The vane potential field influences the the whirl angle dis-

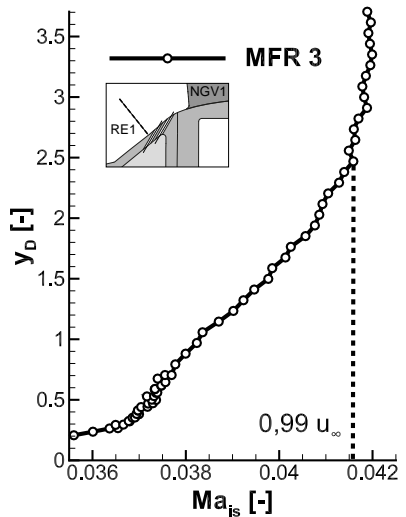


Figure 5.2: Boundary layer measurement in RE1, AX, MFR 3

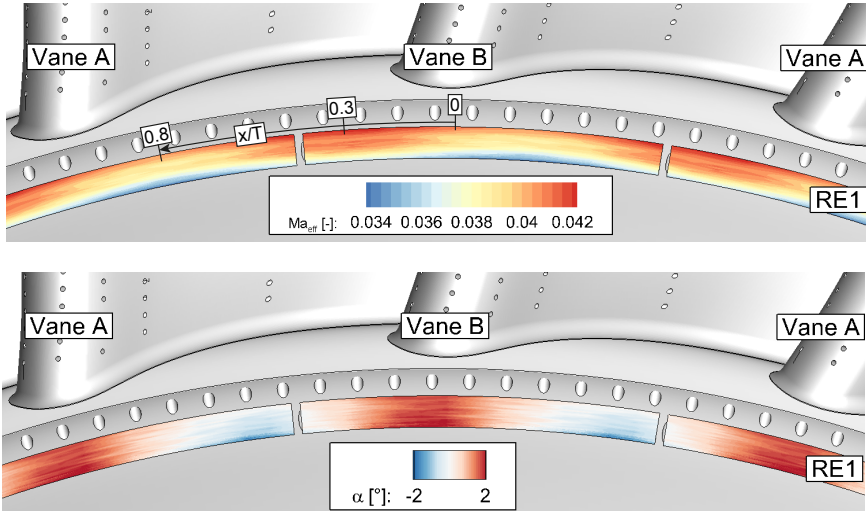


Figure 5.3: Mach number and whirl angle in RE1, 4HP data, MFR 3

tribution¹¹ as well. It varies within $\pm 2^\circ$ and shows that the flow is divided by the maximum and minimum Mach number locations into two adjacent passages, with $x/T = 0.8$ representing the stagnation line position in RE1.

RIDN influence on turbine inflow boundary layer The RIDN injection increases the total pressure in the boundary layer to a surplus. Fig. 5.4 shows the pressure coefficient $P_{t,\text{ref}}$ ¹² for a variation of the MFR and a relative wall distances y_D between 0.5 and 3 in RE3.

All MFR in this investigation have a blowing ratio¹³ of at least one and therefore increase the total pressure compared to the freestream near the wall. The flow is decelerated approaching the leading edge toward the stagnation point. Thereby, the existing radial total pressure gradient in the boundary layer converts into a static pressure gradient. For an uncooled endwall this effect is responsible for the formation of the horseshoe vortex. In this case, the streamlines on the vane show a radial downward tendency and fluid is washed from the pressure side down onto the endwall. With coolant injection upstream of the vane, the formation of the horseshoe vortex can be hindered, as Thomas [126] shows. For blowing rates greater than one, the wall streamlines on the vane tend radially upward instead. This happens also for the investigated setup, as it will be shown later. Downstream of the second RIDN row holes (Fig. 5.4b), the pressure surplus due to film cooling is even greater pressure, because a shorter distance has been covered between RE3 and the injection hole. The

¹¹Positive whirl angles point into counter-clockwise direction.

¹² $P_{t,\text{ref}}$ is evaluated according to equation 4.7

¹³Refer to table 3.3 for an overview

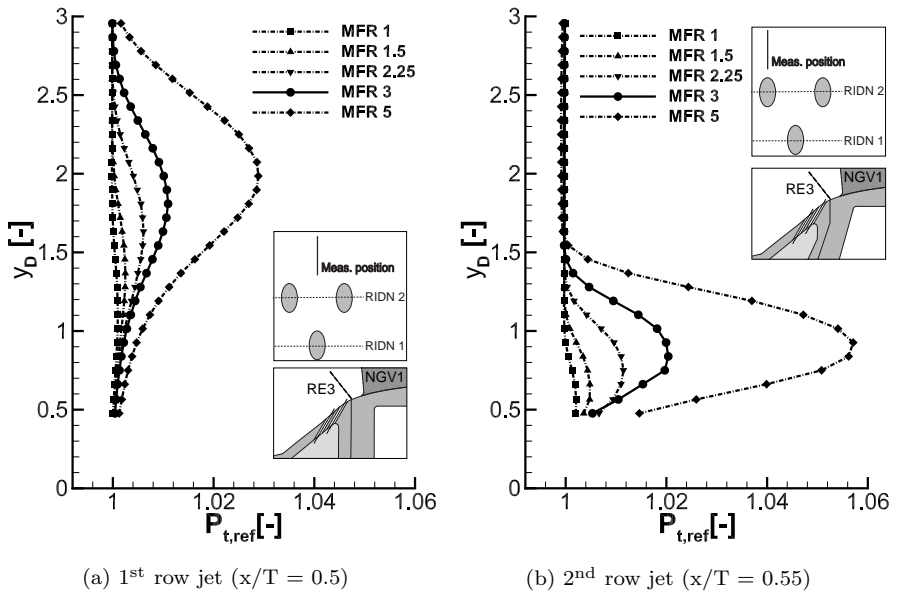


Figure 5.4: $P_{t,ref}$ in RE3 for both rows downstream of their hole centerline in the passage center for varied MFR

corresponding peak value is detected below 1D off the endwall, whereby its span wise position increases slightly with the MFR.

Estimation of the local blowing rate The local blowing rate is estimated for the reference configuration using the boundary layer probe measurements. For this, the Mach number in the jet core¹⁴ in RE2, $Ma_{RE2,jet}$ is normalized by the local Mach number in RE1 Ma_{RE1} . Thereby, constant density and temperature of both airflows is assumed.

$$M_{local} = \frac{Ma_{RE2,jet}}{Ma_{RE1}} \quad (5.5)$$

A variation within $\pm 3\%$ of the average M_{local} of 4.45 is calculated (Fig. 5.5). The Mach numbers of the inflow in RE1 and the jet core velocities in RE2 (not displayed here) indicate that the variation is not predominantly caused by an inhomogeneous velocity outflow distribution of the holes, but due to the potential effect of the NGV leading edge and the associated Mach number variation in RE1¹⁵. There is a minor variation in the total pressure of below 5% of the dynamic head measured across all fifteen holes in the passage.

¹⁴The jet core is defined by the nine highest measured p_T values per cooling hole

¹⁵This potential effect has as well been identified by Eitenmüller [38]

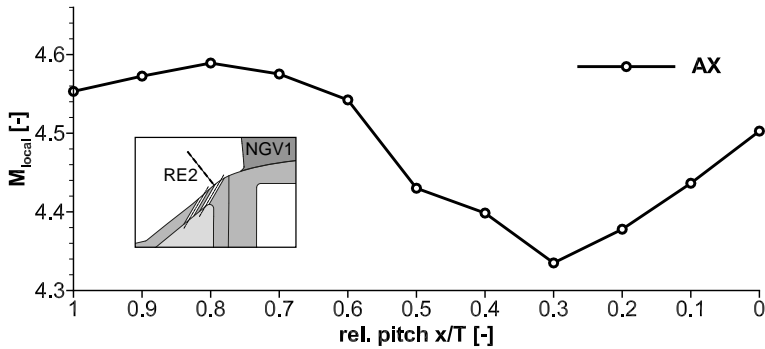


Figure 5.5: Local blowing rate variation for AX inflow, first RIDN row

The measured average value is 28% greater than the calculated film cooling parameter being $M=3.5$, considering both rows of RIDN holes. The stage mass flow is calculated according to equation 3.7, based on the inlet main mass flow \dot{m}_∞ , the entire RIDN coolant mass flow \dot{m}_c and the area ratio between them. This comparison highlights the importance of the local flow field measurement to assess the actual coolant flow parameters and to design the injection geometry accordingly. Assuming that the velocity profile approaching the RIDN injection remains similar with varied MFR¹⁶, the true blowing rates $M_{\text{corr,local}}$ can be assumed for the other injection ratios to increase as well by this factor (Table 5.1, estimated value printed in italics).

Table 5.1: Corrected local blowing ratios for axial inflow based on the measurement at MFR 3

MFR [%]	0	0.8	1	1.5	2.25	3	4	5
M [-]	-	1	1.2	1.7	2.6	3.1	4.7	5.9
$M_{\text{corr,local}}$ [-]	-	<i>1.3</i>	<i>1.5</i>	<i>2.2</i>	<i>3.3</i>	4.5	<i>6</i>	<i>7.5</i>

NGV exit flow field

The flow is accelerated in the vane passage to an average Mach number of 0.24 and at the row exit (ME02) a whirl angle of 75° is measured. The radial equilibrium in span wise direction is responsible for greater Mach numbers at the hub (Fig. 5.6). Below $0.05 h_{\text{rel}}$ the Mach numbers decrease again under the influence of the wheel space purge flow, which is injected upstream of the measurement plane. A split into trailing edge wake and passage flow dominates the contours. As an orientation, the

¹⁶The change in main flow velocity is smaller than $\pm 3\%$

wake is indicated in Fig. 5.6 by a dashed line connecting the local effective Mach number minima. The interaction between the trailing edge slot and the main flow results in low Mach numbers in the wake, if values for identical radial position are considered. Thereby, seven spots of low Ma_{eff} are identified¹⁷.

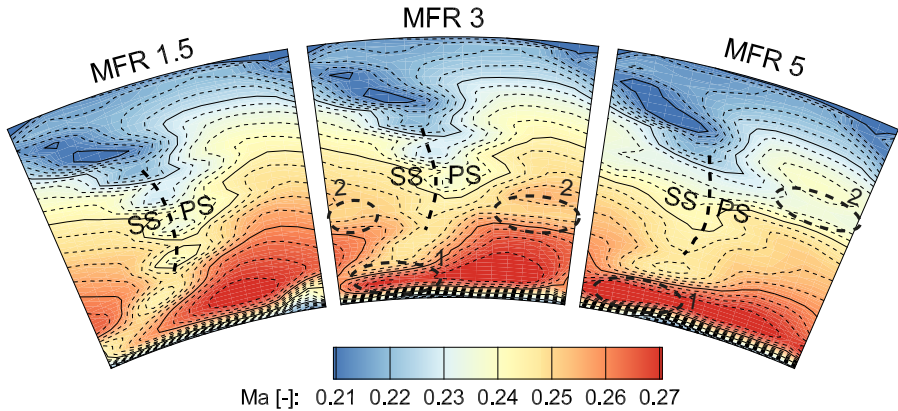


Figure 5.6: NGV exit Mach number, ME02, influence of the MFR (5HP data)

A variation of the RIDN-MFR strongly influences the flow field: Close to the hub, between $0.05 h_{\text{rel}}$ and $0.15 h_{\text{rel}}$ an increase is observed for MFR 3 and 5 (area indicated with "1"). The RIDN momentum helps to overcome the velocity deficit in the vane's wake. At a higher radial position in the annulus, at $0.35 h_{\text{rel}}$ for MFR 3 and at $0.6 h_{\text{rel}}$ for MFR 5, the Mach number is decreased (zone "2"). This deficit moves to greater span wise positions with increasing MFR.

The pressure coefficient $\zeta_{\text{ME0}i}$ is calculated with equation equation 5.6¹⁸. The subscript indicates, in which plane the data is analyzed.. Evaluated for ME02, it correlates the total pressure difference across the stator row with the dynamic head at vane exit. In the literature, this is denoted the pressure loss coefficient. The equation corrects for the change in ambient pressure during the measurement day, measured in the test cell ($p_{\text{amb,tc}}$). The total pressure at the inlet ($p_{t,\text{ME0}1}$) is corrected by this value as well and area-averaged¹⁹.

$$\zeta_{\text{ME0}i} = \frac{\overline{(p_{t,\text{ME0}1} - p_{\text{amb,tc}})} - (p_{t,\text{ME0}i} - p_{\text{amb,tc}})}{p_{t,\text{ME0}i} - p_{s,\text{ME0}i}} \quad \text{and } i = 1, 2 \quad (5.6)$$

There are seven spots of high ζ along the suction side/pressure side line in the wake (Fig. 5.7). Whereas the Mach number is decreased, the pressure loss coefficient increases in zone "2" for higher MFR. In Zone "1", in contrast, lower ζ values are

¹⁷This agrees with the number of seven trailing edge slots, see Fig. 3.8

¹⁸The same equation is used to evaluate the total pressure contour at turbine inlet in ME01 in chapter 6

¹⁹Because the RIDN injection is located downstream of ME01, its total pressure contribution is not included in this value. Therefore, numerical values are only compared for identical MFR settings with varied inflow condition in chapter 6

observed. Without RIDN injection (MFR 0, not shown), there is a ζ -maximum in this region. A loss band and low velocity is detected all along the hub endwall up to a span height of 5 %. This is correlates with the purge flow injection between NGV and rotor. In conclusion, the RIDN flow is responsible for a loss in the passage at higher span position, whereas its momentum helps to reduce the deficit in the wake near the hub²⁰.

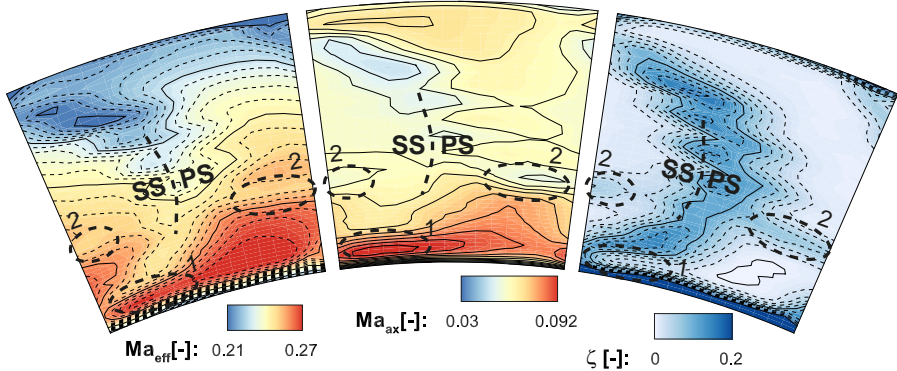


Figure 5.7: Comparison of effective and axial Mach number to the pressure loss coefficient ζ in ME02 for AX inflow, MFR 3 (5HP data)

Propagation of the coolant flows

To expand on the findings from the 5HP measurements, the coolant flow propagation is analyzed by CO_2 tracing and sampling. The results of the companion CFD simulation (Hilgert et al. [60], Werschlich et al. [138]) show the coolant streamlines to roll up at the leading edge (Fig. 5.8a). The CFD in addition indicates, that the 2nd-row air is initially washed up higher than the 1st-row air, before they mix out downstream.

In the experimental results for the leading edge pressure taps²¹ (Fig. 5.8b) this is observed as well. Increased film cooling effectiveness η_{aW} is detected at the leading edge and the span height with significantly elevated η_{aW} values increases with the MFR. Thereby, the measured cooling effect occurs only due to the RIDN injection, because the NGV film cooling air was not seeded with CO_2 and hence is not detected by the experiment.

Based on the results it is concluded that the trajectory of the coolant up to the leading edge initiates a secondary flow feature. Another velocity gradient in the boundary layer develops due to the span wise flow and forms a vortex, fed by the RIDN coolant. This results in the low-velocity zone "2" and a pressure loss. Due to the momentum of the coolant flow at MFR 5, the vortex reaches up to 57 % span height in ME02.

²⁰The supposed responsible mechanism is discussed in the following and illustrated by Fig. 5.11a

²¹A photograph of the vane with leading edge instrumentation is shown in Fig. 4.6-C

In the NGV exit plane ME02, the propagation of the RIDN-coolant (denoted RIDN in the figures), the NGV trailing edge slot ejection (TE) and the NGV-rotor purge flow (CAV) is investigated. Separate flow tracing experiments with only one flow seeded at time are conducted. The η_{mix} -contour for RIDN-seeding shows a coolant accumulation in zone "1" (Fig. 5.9) and further along the PS/SS-line in the NGV wake up to 33% span height. The RIDN flow is furthermore detected in zone "2", which agrees with the assumption of a RIDN-fed vortex and loss core. Notably, the TE-coolant is accumulated in this region as well. Therefore, it is not only fed by the initiating RIDN flow, but also by the TE-flow. The flow model in Fig. 5.11a illustrates this finding.

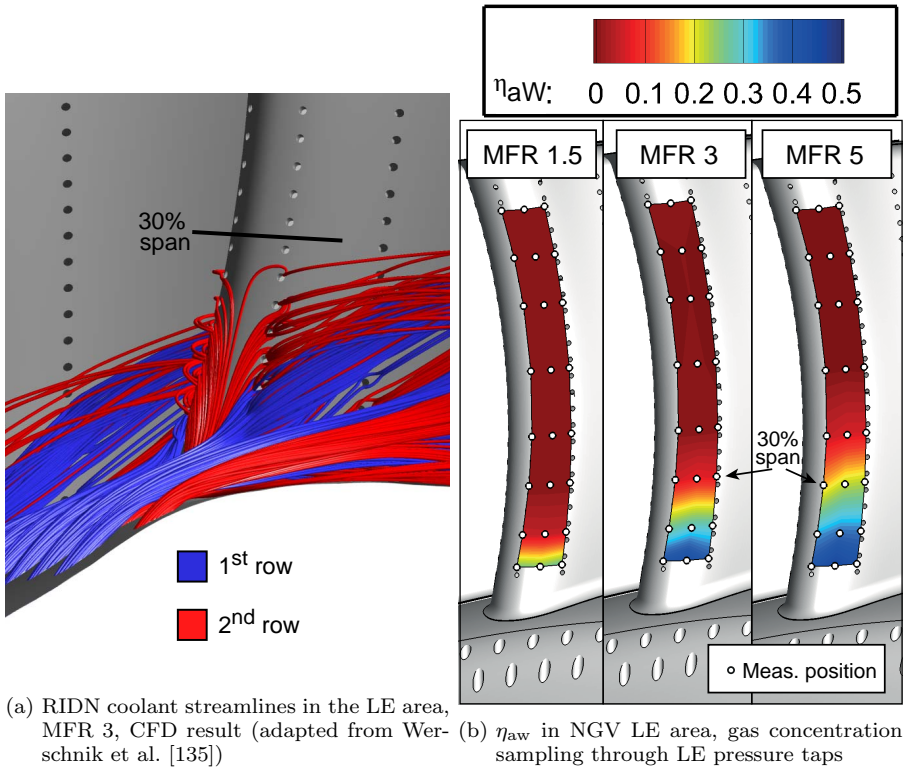


Figure 5.8: Flow field influence of the RIDN coolant injection

The TE-coolant is detected in the NGV wake at same position of the seven pressure loss cores²² as expected. CAV-seeding shows that up to ME02, the purge flow remains close to the hub. With increased MFR, the coolant flow propagation is in agreement with the 5HP-findings (Fig. 5.10, exemplary for TE-seeding):

²²Compare to Fig. 5.7 for the pressure loss coefficient

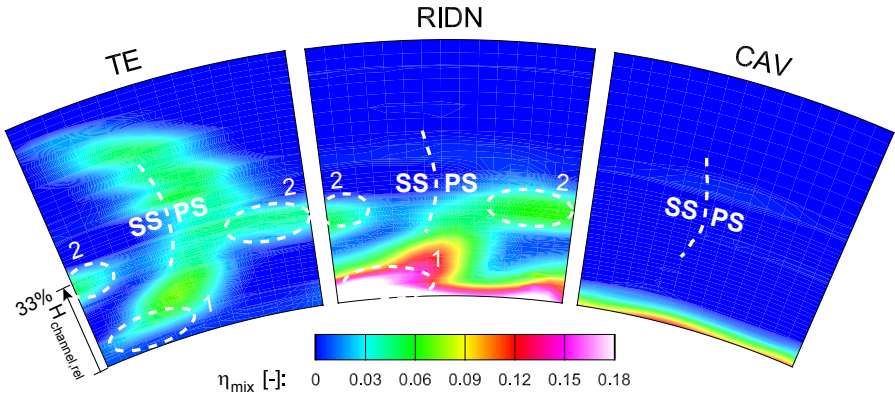


Figure 5.9: Flow tracing results for varied seeding, trailing edge ejection (TE), RIDN-coolant (RIDN) and purge flow (CAV); all for AX inflow, MFR 3 in ME02

At MFR 5, zone "2" is detected at 57% span height. This is observed with RIDN-seeding as well (not shown). Thereby, the TE-flow is transported further into the passage flow with increasing RIDN-MFR and zone "2" has a larger pitch wise extent. Similarly, the RIDN air is transported towards the passage mid-height region due to the span wise movement of zone "2". In zone "1" no TE-coolant is detected for MFR 3 and 5, whereas for MFR 0, TE-coolant is observed at the hub.

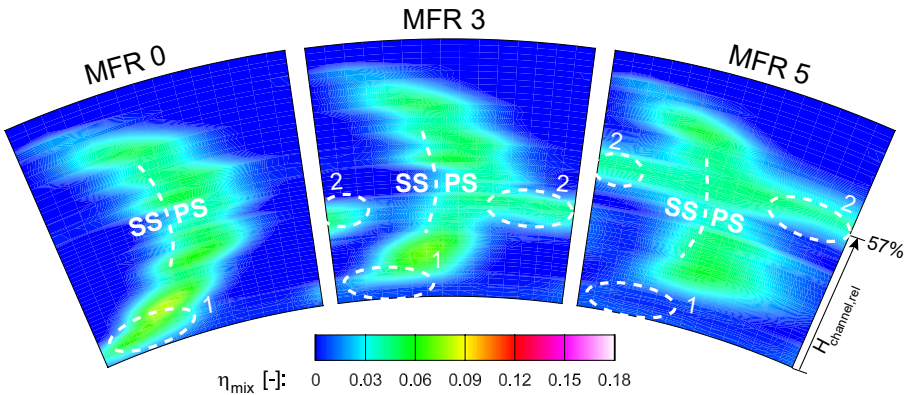


Figure 5.10: TE seeding with varied MFR; shows influence of the RIDN flow rate in ME02, AX inflow

The measured η_{mix} -level for TE-seeding is increasing towards the lower annulus heights. This is a consequence of the casing-side supply to the interior plenum in the vanes. The flow that enters as a jet through the supply tube at the top decelerates towards the hub. Thereby, the static pressure increases towards the hub (Kegalj

et al. [68]) and increased injection at lower span slots results. In addition, the static pressure in the main annulus decreases towards the hub as well. In conclusion, the mass flow fraction through the TE-slots increases towards the hub.

The pitch wise average in Fig. 5.11b points out that with increasing MFR, the level of RIDN air increases in the main annulus. This is a result of the trajectory illustrated in the flow model. The coolant peak in zone "2" results in averaged η_{mix} -values of 0.05 at h_{rel} of 0.33 for MFR 3. For MFR 5, a significant transport of RIDN air up to $0.7h_{\text{rel}}$ occurs with the intermediate peak at $0.57h_{\text{rel}}$.

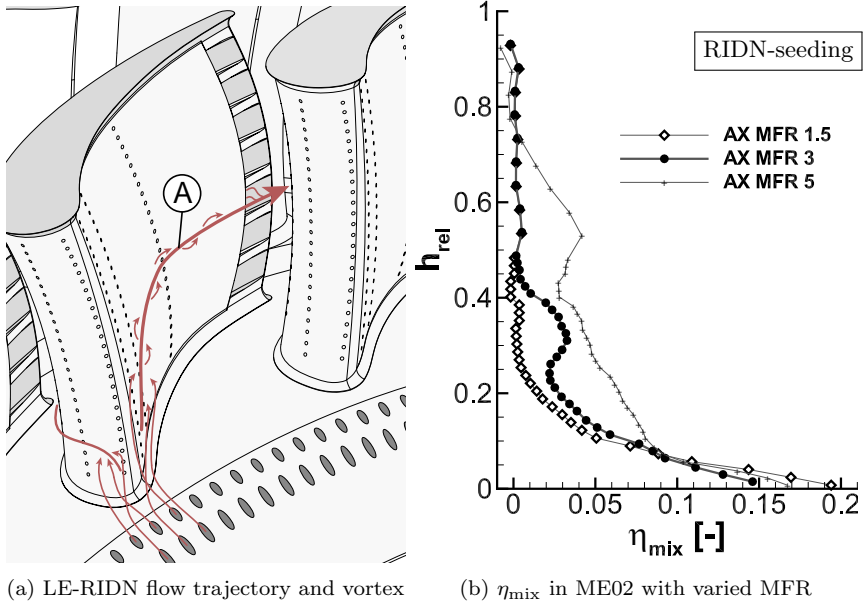


Figure 5.11: η_{mix} in ME02 with varied MFR for RIDN-seeding

5.2 Endwall film cooling

Fig. 5.13 shows the film cooling effectiveness contour on the hub side vane endwall for varied MFR, acquired by infrared thermography measurements. The nomenclature used to describe areas of interest is specified in the top left figure. An overview is given first before the observation is explained with additional experimental results in the following sections. In this way, the specific performance of this cooling design is characterized and the flow model (Fig. 5.12) is expanded. Three aspects are identified:

- The design is very efficient in cooling the pressure side corner area (Ⓑ).
- A stripe pattern is observed in the entrance area, which for low MFR results in uncooled areas (Ⓒ).

- By the high-momentum injection, a cooling coverage of the downstream TE-region is achieved.

At the lowest injection setting of MFR 0.8, the whole endwall receives coolant (Fig. 5.13). This is in contrast to literature findings, where usually an overturning of the coolant towards the SS is observed (e.g. Knost and Thole [77], Friedrichs [41]) for low MFR. However, whereas the blowing ratio, calculated with stage parameters is below 1, it has been shown that due to the annulus shape, the actual local values is greater than one. As a consequence, the coolant enters with excess momentum and is able to cover nearly the whole endwall surface. Whereas towards the trailing edge, a homogenous film cooling effectiveness in the range of 0.25 is determined, the entrance area shows a pronounced stripe pattern. Alternating low and high effectiveness values are measured, whereby high values are detected downstream of the second row of cooling holes. Downstream of the first row of holes, lower efficiency values are detected. This is specific to the present design and observed for other MFR as well. The coolant jets of the first row do not remain attached to the wall. This results in the formation of a stripe pattern, that is observed in the film cooling effectiveness distribution in the entrance region.

For MFR 0.8 it is furthermore notable, that the level of this stripe pattern differs between the center-passage holes (for a relative pitch position of x/T 0.3 to 0.8; the geometry is specified in Fig 3.9) and the holes upstream of the LE ($x/T > 0.8$ and $x/T < 0.3$): For the latter increased η is observed. For this setting, both blowing ratio M and momentum ratio I are equal to one and in combination with the horseshoe vortex system foster coolant downwash with the horseshoe vortex at the leading edge. This downwash keeps the coolant jets close to the wall and enhances the film cooling in the LE area. This effect disappears for MFR 1.5 and higher and it is concluded that the horseshoe vortex' influence diminishes for these MFR.

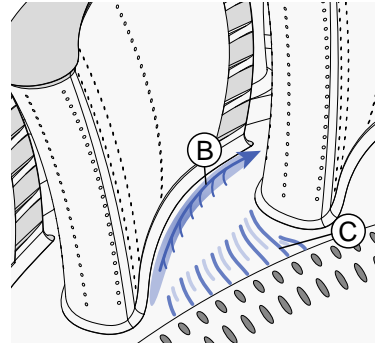


Figure 5.12: Flow model with end-wall film cooling results

The stripe pattern in the entrance area shows a great sensitivity to the blowing rate for low injection rates. For MFR 1, the effectiveness increases slightly for the whole passage due to the increase in cooling air. In contrast, for MFR 1.5 the cooling effectiveness decreases, which accounts for the LE-area as well. At about midpassage, an area of η_{aw} close to zero appears for MFR 0.8 to 1.5 (marked \otimes for MFR 1). This is in an overlap region of two camera positions and the measurement accuracy is compromised by the low absolute level and an artifact appears due to a slight reflection²³.

²³Because a low η_{aw} value causes a linear regression curve with a small slope, a combination with a reflection in the optical path makes the linear regression unstable and an artifact appears. Low accuracy as well is determined in the stripe pattern between coolant jets. In contrast to the artifact at midpassage, the comparison to the gas concentration measurements shows that the measured values are reasonable. This is discussed in the following section in detail.

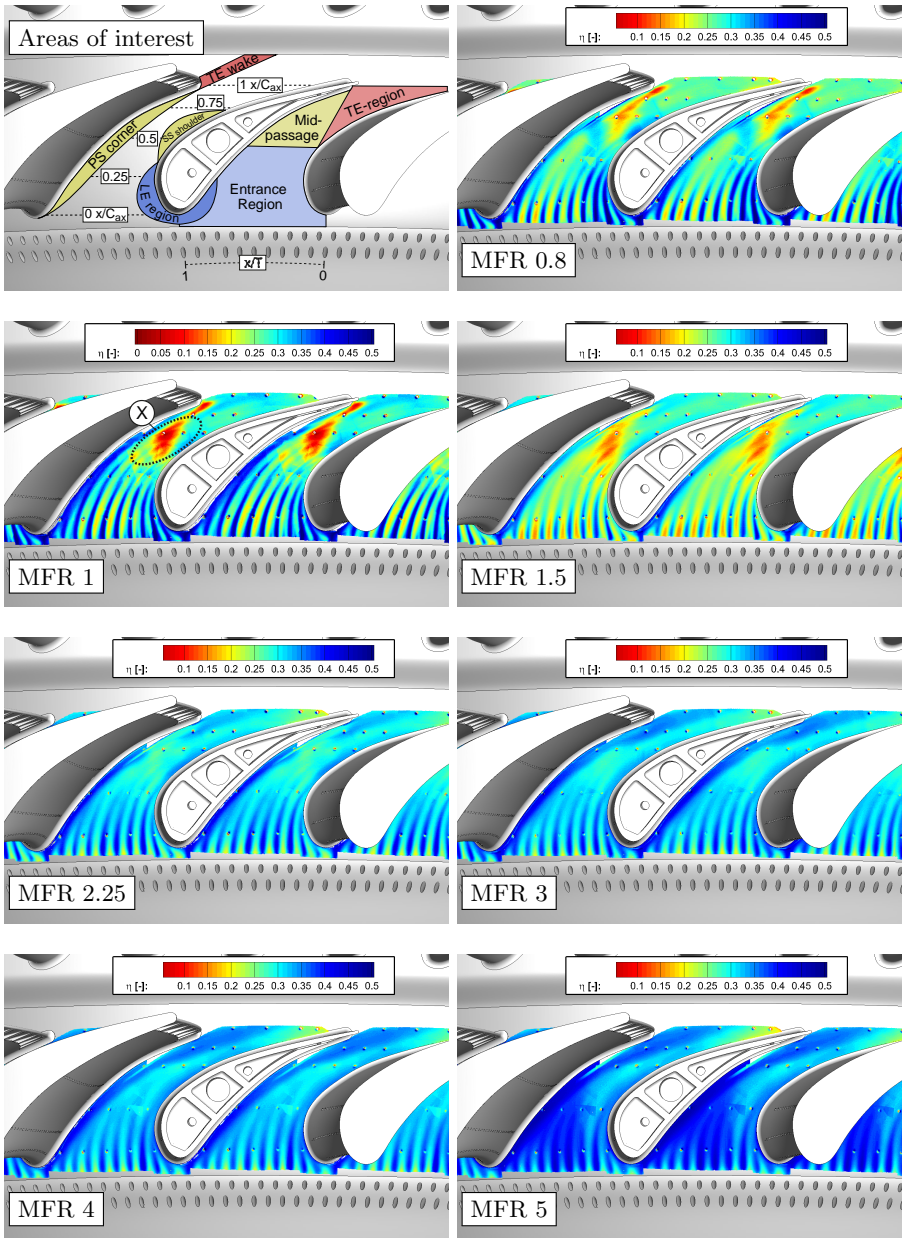


Figure 5.13: η_{aw} on NGV endwall, baseline case for varied MFR

Increasing the MFR further to 2.25 improves the film cooling effectiveness significantly to 0.3 on average. The stripe pattern in the passage entrance remains, but no levels lower than 0.25 occur. The pressure side corner area receives very good cooling with η -values of 0.4-0.45. The RIDN air accumulates here due to its high momentum, which allows it to overcome the vane pressure field. As illustrated in section 2.3, for higher velocity the radial equilibrium requires a trajectory with a larger radius and an overturning of the coolant jets results. Therefore, the near-wall flow direction is reversed and the coolant accumulates in the pressure side corner. This agrees with the flow field measurements: In zone "1" (cf. Figs. 5.6, 5.7), the velocity deficit in the vane's wake reduces with increasing MFR and with the flow tracing measurements, high η_{mix} value are detected (Fig. 5.9). This increase in zone "1" occurs in pressure side corner and spreads across the full passage pitch for MFR 5.

For MFR 3, 4 and 5, the distribution remains similar with increasing film cooling effectiveness throughout. The area of high η_{aw} -values in pressure side corner increases into the passage and spreads further downstream as well. As a result, the trailing edge area is divided into a region with higher values near the PS and lower values near the SS. Especially at MFR 5 this is obvious and near the trailing edge η equals to 0.2. Whereas the passage entrance is well cooled at the SS shoulder, downstream the film cooling effectiveness decreases and the coolant reaches the pressure side area with preference. As it has been discussed, for these high MFR an upwash of coolant air occurs near the leading edge. As a result, only a limited amount of coolant air is able to reach the suction side corner.

To ensure a cooling of the whole endwall, a MFR setting of 2.25 has to be selected, because otherwise uncooled stripes in the entrance region remain. Higher level of η_{aw} is achieved with a further increase of the MFR.

Coolant jet contours

With the pitot probe measurements in RE2 and RE3, the findings from the end-wall contours are supported. The results are analyzed with the pressure coefficient $C_{p,t,\text{ref}}$ ²⁴. In this way, the coolant jets are clearly identified: In RE2 (Fig. 5.14a) the jet has a circular shape with its core being 1D above the endwall, measured for MFR 3. In RE3 (Fig. 5.14b) the jets of both rows have a kidney shape, observed in the literature as well. The first row jet aligns centric in between the second row jets. It mixes out with the main flow and the maximum $C_{p,t}$ -value is halved compared to plane RE2. Whereas the center of the first row jet is at $y_D=1.9D$ in RE3, the second row jet centerline is at $y_D=0.9D$. Due to the closer distance to the endwall in this plane, the first RIDN row contributes less in cooling the endwall than the first row. This is specific to the studied injection geometry. The first row jets remain at a greater wall distance. This has been observed for the other MFR settings in the same manner (not shown here).

The jet contour in plane RE2 and the contours in RE3 have different shapes. Because the distance from injection to measurement plane is nearly identical at 2.5D, the difference results from the near-hole geometry: Whereas the first row air is injected with a shallow angle of 21° relative to the surface, the second row air is ejected with a steeper relative angle of 34° and therefore increased wall-normal momentum. Accord-

²⁴It is calculated according to eq. 4.8

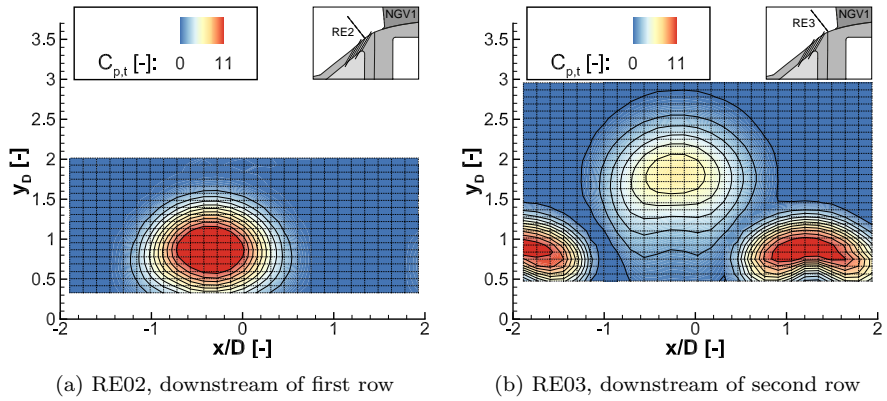


Figure 5.14: Total pressure coefficient $C_{p,t}$ of RIDN injection, $x/T=0.5$, MFR 3

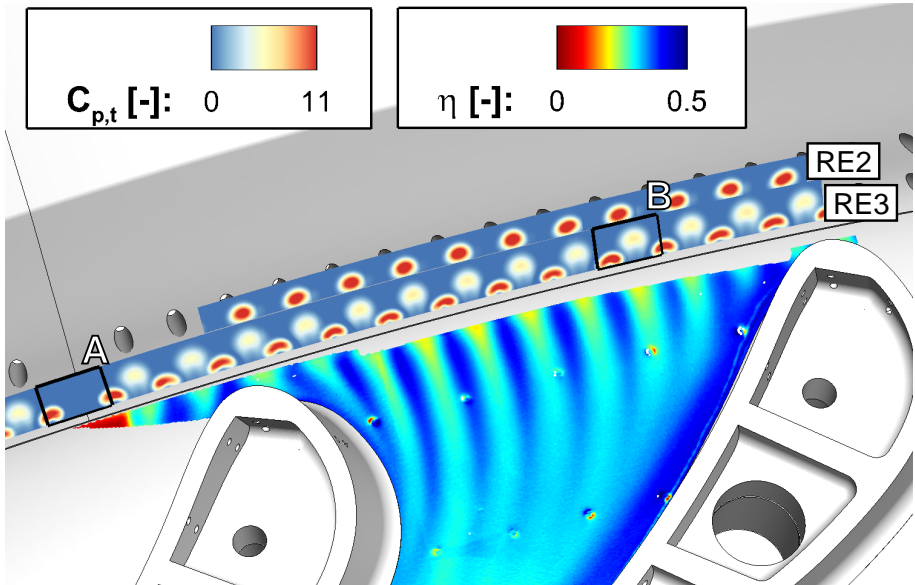


Figure 5.15: Boundary layer influence of RIDN injection for AX, MFR 3, view from downstream. Black framed boxes mark identical relative pitch positions.

ing to Baldauf [12] this steeper injection angle increases the interaction of neighboring jets, which in turn is beneficial for the film cooling effectiveness.

In addition, a displacement effect forces the main flow to squeeze in between the first row jets and thereby increases the effective main flow velocity. As a consequence, the effective blowing rate for the second row jets, that are placed at this exact location in the staggered configuration, is reduced. In addition, the momentum increase due to the first row jets themselves is beneficial and in consequence, the second row air attaches better to the endwall. It is detected closer to the hub surface than the first row. This means that a greater film cooling contribution on the endwall comes from the second row jets, until, due to mixing between main flow and coolant air, a cooling effect from the first row as well appears further downstream.

The observed coolant jet contours explain the stripe pattern and the different performance of the two rows in respect to endwall cooling (Figure 5.15). Downstream of the first row jets, lower η_{aw} values are detected. The second row stays close to the endwall and results in higher η_{aw} downstream. With increasing stream wise distance, mixing and the interaction between neighboring coolant jets results in a homogenous coolant film and a disappearance of the stripe pattern. This behavior remains for other MFR as well.

It is mentioned that the measurement data for RE2 and RE3 consists of 26 sets and a total number of 17,600 data points. It has been acquired within two weeks' time and the smooth fit between individual measurements underlines the high repeatability.

The discussed benefit of the first row on the performance of the second row is detailed with measurement results in the following.

First row influence on the second row

In fig. 5.15, the measured η_{aw} contour has not been duplicated to adjacent passages²⁵, to illustrate the importance of the first coolant row on the second row: Two boxes mark identical relative pitch positions of $x/T=0.7$ in the two adjacent passages. In box "A", one hole in the first RIDN row could not be manufactured, as it would have been at the location of a joint between two adjacent RIDN plates. Box "B" shows the regular configuration for comparison. Aside from the missing first row jet, the second row jets are smaller in circumferential extent and located at a higher span wise position, compared to the regular configuration in box "B". Only limited view on the endwall surface is available downstream, because the vane obstructs the optical path. Nevertheless, the η_{aw} -contour shows that downstream of the missing hole, the cooling effect of second row vanishes. This finding is in agreement with the numerical simulation of Hilgert et al. [60] for this geometry. One explanation is the reduction of the second row's effective blowing ratio by the increased velocity in the boundary layer. In addition, the displacement of mainstream fluid between neighboring first row jets increases the velocity in the boundary layer further. The result highlights the importance of the jet interaction for the development of a coolant film. Baldauf [12] determined that an increased η_{aw} is achieved with high momentum injection after

²⁵All other contour pictures of the endwall measurements are duplicated to adjacent passages, or in the case of swirling inflow, recorded subsequently with a swirler clocking by half a pitch. Therefore neither has the missing RIDN hole an impact on the results nor is it shown in other illustrations.

a streamwise distance of $18D$ from the injection, as long as the hole spacing is small in the order of 2-3.

Cresci et al. [34] observe this enhancement as well for a comparable cooling design to the present study. They determine a significant benefit for the hole spacing of $3D$, whereas a greater spacing decreases the cooling performance.

Comparison of infrared thermography and gas concentration measurements

Additional understanding of the endwall film cooling is gained by a comparison of the gas concentration (GC) sampling measurements with the infrared thermography (IR) results. Whereas the latter technique measures a temperature difference to study η -contours, the analogy between heat and mass transfer is applied to investigate the film cooling by gas concentration sampling.

At the LSTR, the temperature of all secondary air flows is adjusted by one secondary air cooler, whereby the control variable is the temperature of the RIDN air flow. It is maintained at a desired over-temperature to the main flow. All other secondary flows such as the airfoil film cooling are injected with the same over-temperature. As a consequence, any cooling effect of the pressure side coolant on the endwall appears therefore superimposed to the RIDN coolant effect with the infrared thermography measurement. The gas concentration data in contrast is a selective measure, and only the coolant flow of interest is seeded with CO_2 . Hence, the film cooling effectiveness due to only one specific coolant flow is determined with this method. In this way, the gas concentration data is used to exclude or specify the effect of the airfoil cooling among the measured endwall effectiveness.

Figure 5.16 shows the results for MFR 0.8 and MFR 1. The colored circles represent the gas concentration sampling results, whereas the contours display the infrared thermography results. The in general that is achieved between the two techniques

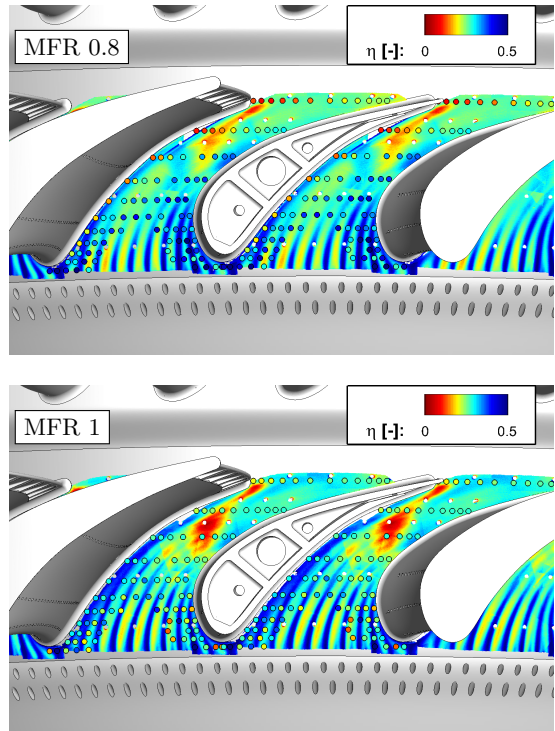


Figure 5.16: Comparison of GC (Data points) and IR (contours) measurements for MFR 0.8 and 1

is not observed for the low MFR injection settings. For higher MFR, the circles disappear within the contours. In the case of MFR 3 they are hard to be identified at all. On the other hand, the limitations of both techniques become obvious as well.

Especially in areas of discrete and attached coolant streaks, the point wise results do not allow for a conclusion on the trajectory of coolant jets in the entrance area. In contrast, downstream where the coolant jets become mixed out, the contours are represented well by the point wise information. The gas concentration method was determined to be susceptible to the extraction flow rate in the entrance area. Systematic errors occur and the corresponding sampling positions were removed from the shown data.

The pressure side corner area is of special interest in this comparison, because a cooling effect of the pressure side airfoil film cooling can be assessed. At MFR 0.8, a significant difference is observed for the measurement points directly at the pressure side corner. The infrared contours indicate $\eta_{aw}=0.2$ and the gas concentration measurements do not show any effect at all. Towards the trailing edge, the area with deviation spreads and reaches up to mid span at the last row of measurements. It is concluded that the low-momentum RIDN coolant overturns towards the suction side, leaving the pressure side corner without coolant. On the pressure side airfoil, a downwash occurs that carries airfoil film coolant onto the endwall and results in a cooling effect that is recorded by the infrared camera.

The flow tracing results indicate that no other coolant than RIDN cools the endwall from MFR 1.5 on. In consequence, whereas there is still a small difference between between IR and GC in the TE region for MFR 1, there are no differences anymore for MFR 1.5 and MFR 3 in Fig. 5.17.

The GC results furthermore allow to identify an artifact in the IR-contours for MFR 0.8 to MFR 1.5 where they indicate higher η_{aw} than the IR-measurement at the same location.

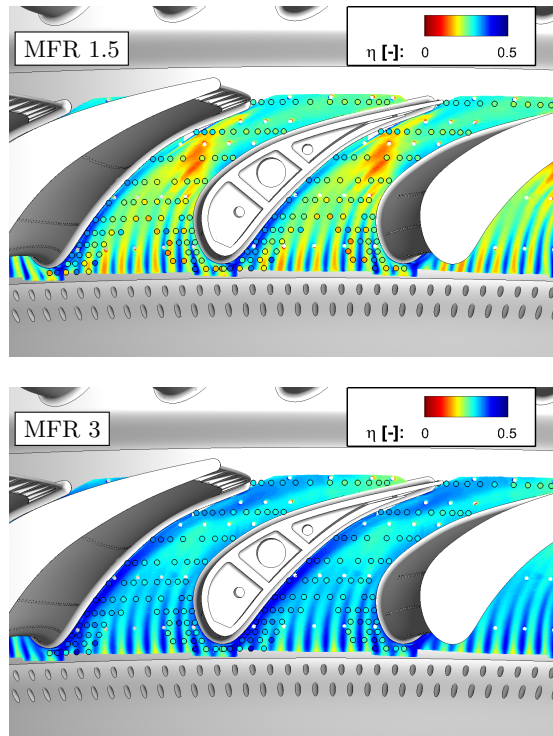


Figure 5.17: Comparison of GC (data points) and IR (contours) measurements for high momentum MFR 1.5 and 3

It occurs in the overlap region between two camera positions, where low η values are detected at the edge of the camera image. This brings higher uncertainty into the results. For MFR of 2.25 and greater, it is not detected anymore.

In conclusion, the cooling effect due to airfoil film cooling in the pressure side corner at low-momentum MFR has been assessed with the GC technique. For axial inflow, it occurs for blowing ratios up to one.

5.3 Endwall heat transfer

The endwall Nusselt number contours for the uncooled case (MFR 0, Fig. 5.18) show typical peak areas of heat transfer as discussed in section 2.4. In addition, the onset of the measurement area \textcircled{C} is observed with high values because of the RIDN cooling holes. They were left uncovered and flow disturbances occurred even though there was no mass flow ejected. The values decrease quickly with the growth of the boundary layer, before they rise again in the passage throat \textcircled{D} , beginning at the suction side shoulder. The flow acceleration in the passage thins out the boundary layer and increases the Nusselt numbers.

Peak values are observed in the TE wake \textcircled{E} , where in addition to the high velocity the wake itself increases the heat transfer. Additionally, very high Nu values are detected in the LE region \textcircled{A} under the influence of the horseshoe vortex, that transports main flow fluid in wall-normal direction and increases the heat transfer. Both along suction side and pressure side \textcircled{F} , heat transfer is increased due to the corner vortices. Only the trajectory of the horseshoe vortex cannot be clearly identified. This is a possible consequence of the fillets at the junction between vane and endwall that can significantly reduce the intensity of the horseshoe vortex (Shih and Lin [122]).

A small, protruding surface defect on the endwall results in a trace of increased heat transfer \textcircled{G} ²⁶. The characteristics is similar with slightly elevated Nusselt numbers for MFR 0.8 (Fig.5.20). The large region of low Nu in the entrance region remains, but increased values due to the coolant jets are observed.

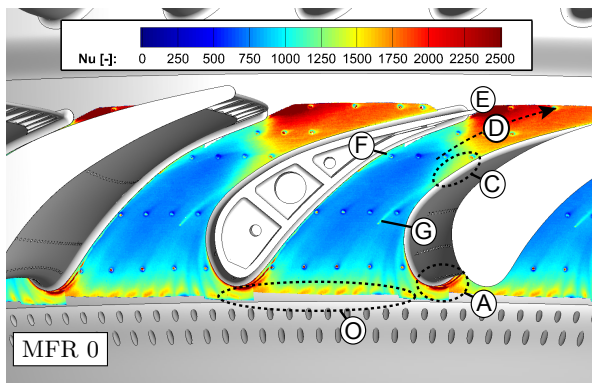


Figure 5.18: Nusselt contours for the uncooled endwall, showing the peak regions of heat transfer discussed in section 2.4

A small, protruding surface defect on the endwall results in a trace of increased heat transfer \textcircled{G} ²⁶. The characteristics is similar with slightly elevated Nusselt numbers for MFR 0.8 (Fig.5.20). The large region of low Nu in the entrance region remains, but increased values due to the coolant jets are observed.

²⁶This trace and similarly the one of the reference positions in the infrared image can be evaluated to identify endwall streamlines. This is illustrated in section F in the appendix.

At the onset of the measurement area, two local maxima are detected downstream of each second row hole (Fig. 5.19). These maxima result due to the vortex pattern induced by coolant jets; a pair of counter-rotating vortices, often referred to as the kidney vortices, is generated by the shear forces due to the interaction with the main flow. In the terminology of Baldauf [12] this is the heat transfer distribution of a row of "penetrating jets"²⁷.

The kidney vortices are responsible for wall-normal transfer of mainstream fluid into the jet wake, a thinned boundary layer and thereby increased heat transfer. After a certain distance the two local Nu maxima merge into a single one. The heat transfer enhancement due to the injection is mitigated and the distribution becomes similar to the uncooled case. Baldauf [12] has observed this enhancement up to a streamwise distance of 50 D.

The Nusselt number distribution remains similar for MFR 1. From MFR 1.5 on, all features are stronger pronounced and the heat transfer level significantly increased. A heat transfer gradient is observed along lines of constant x/C_{ax} within the passage from the suction side towards the pressure side. Well pronounced from MFR 3 on, high Nu are observed in the pressure side corner. The accumulation of coolant air and the associated acceleration in this region explains this. As explained in section 5.2, the near-wall velocity increases and the boundary layer becomes thinned out, resulting in higher Nusselt numbers.

Nusselt numbers are very high throughout the whole endwall at MFR 5. Bearing in mind, that for this MFR the cooling of the SS corner region near the trailing edge deteriorates, the resulting heat flux into the surface is of interest. Whereas the film cooling effectiveness increases along with the coolant MFR, there is a significant increase in heat transfer near the coolant injection as well. This might compensate the gain due to film cooling. Both aspects emphasize on the necessity of a combining measure for the two thermal parameters. A suitable measure has been suggested in section 2.5 with the heat flux reduction Θ due to film cooling according to Baldauf [12].

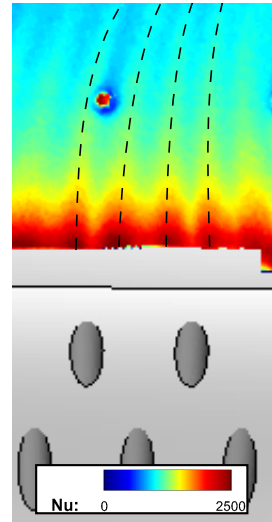


Figure 5.19: Local maxima (dashed lines) to the sides of each 2nd row hole

²⁷The regimes according to Baldauf's terminology and their schematic heat transfer contour are shown in Fig. 2.10

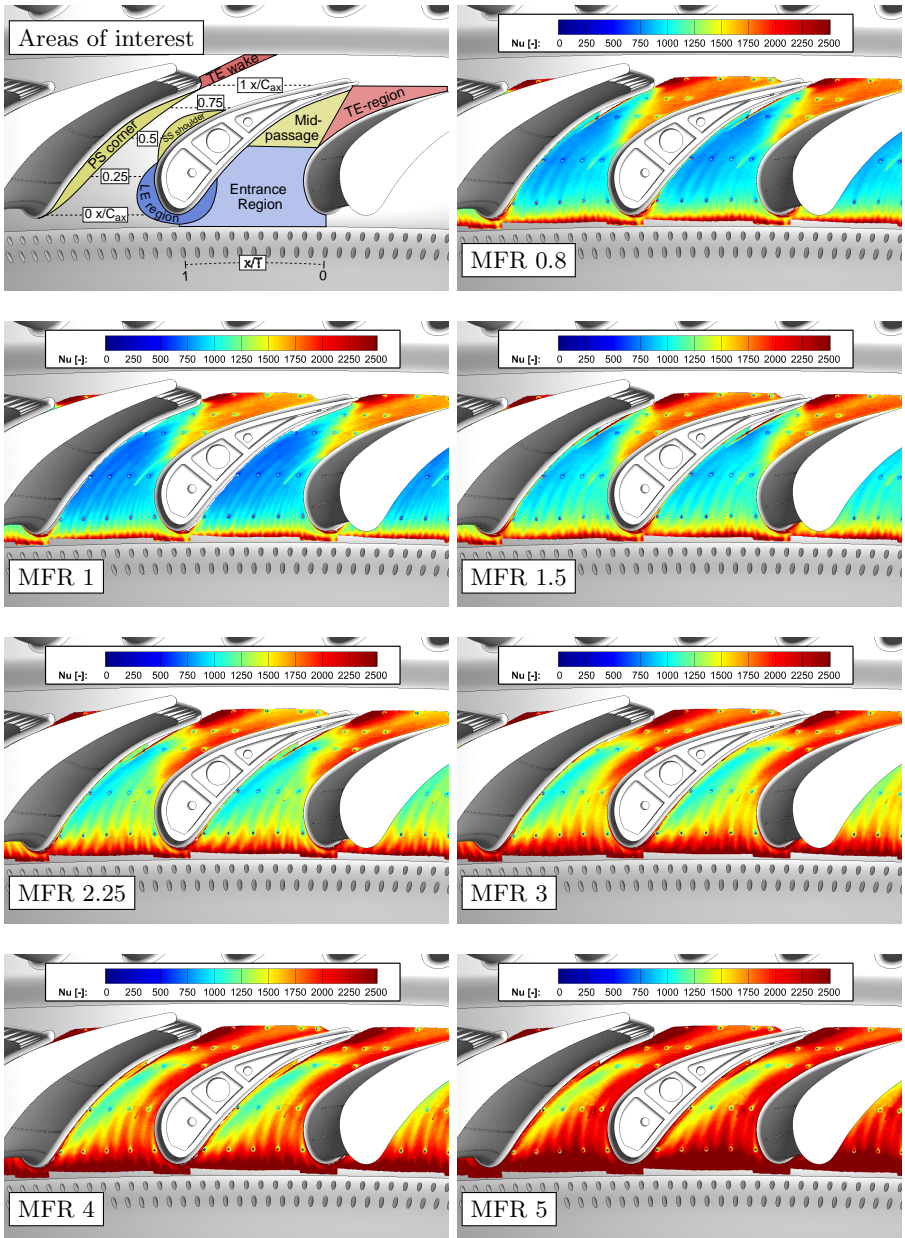


Figure 5.20: Endwall Nu-contours, baseline case for varied MFR

5.4 Resulting Heat Flux Reduction

To evaluate the benefit of the film cooling design and to identify the best MFR setting, the resulting heat flux reduction Θ combines the two thermal parameters, film cooling effectiveness and Nusselt number. If no other constraints apply, the optimum MFR can be selected based on this parameter. Per definition, positive values indicate a benefit and negative values a penalty. The colormap with positive values for colder sections in blue color and negative values indicating hot regions, colored in red, symbolizes this.

As it has been discussed in section 2.5, the definition of Θ has the assumption of ideal heat flux transmittance through the wall to an internal cooling system, that is adapted to the external heat transfer level.

Fig. 5.21 shows the resulting contours for varied MFR. In general, with axial inflow a benefit is observed for all settings²⁸. Hence, the heat load is reduced due to the film cooling by this configuration. However, it is observed that despite of the significant rise of η_{aw} with the MFR, the benefit is counteracted by the associated increase in endwall Nusselt numbers. As a consequence, the heat flux reduction is low in the entrance and mid-passage area for MFR greater than 1. Whereas the reduction is significant for a wide portion of the endwall for MFR 0.8 and 1, there is no heat flux reduction in the entrance area. The uncooled regions in between the coolant traces are responsible. Furthermore, the airfoil film cooling contributes to the heat flux reduction at MFR 0.8 along the pressure side corner and in the trailing edge region.

Throughout all settings, high values of Θ are observed in the pressure side corner region and in the trailing edge region. This area is a crucial area in the thermal vane design due to the high heat transfer in this area. In addition, according to Benton et al. [18], directing cooling air to this area is costly when air is ejected on the platform due to the higher flow velocity.

The best setting based on the parameter Θ is MFR 1. With respect to MFR 0.8, there is a smaller uncooled area in the entrance area and an improved cooling of the trailing edge region. This result underlines the importance of a combined analysis of the two parameters. A selection only based on the film cooling effectiveness level the higher MFR of 2.25 would have been chosen because the whole endwall is cooled.

²⁸ $\Theta = 0$ is marked by a red line and encircles all areas with increased heat flux compared to the uncooled endwall. With axial inflow, this does not apply, only due to the artifact in the midpassage area, a heat flux increase is calculated for MFR 0.8, 1 and 1.5.

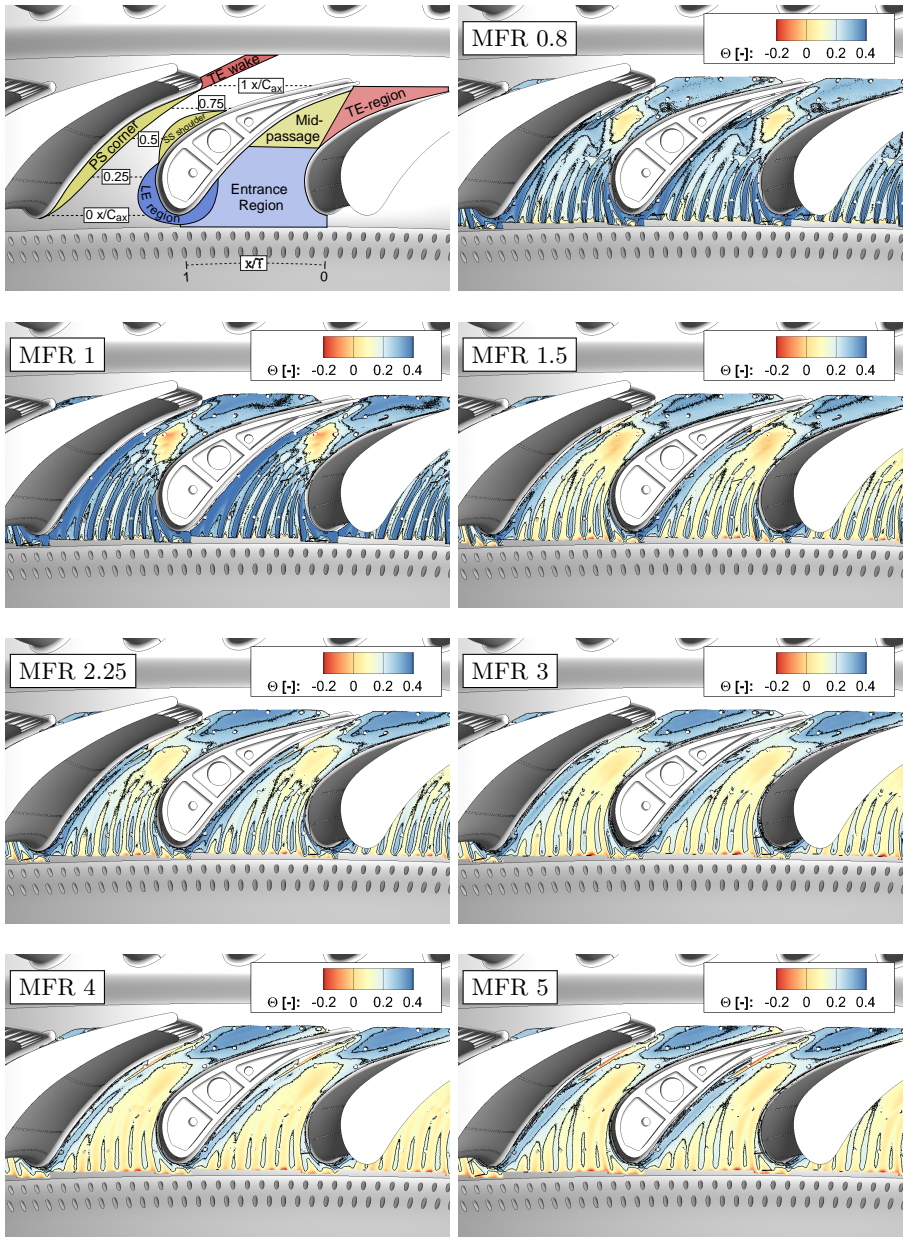
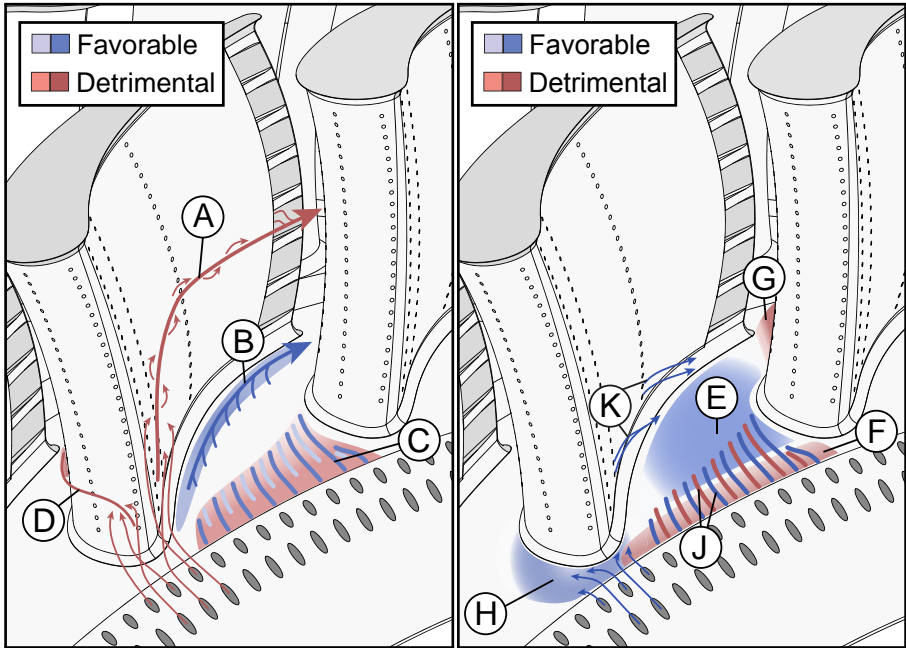


Figure 5.21: Heat flux reduction Θ due to film cooling, compared to the uncooled endwall

5.5 Summary of the findings for the reference case

The NGV flow model (Fig. 5.22) summarizes the findings for the reference case of axial inflow. Flow features observed both for low and high injection rates are shown. The illustrated trends may be stronger or weaker pronounced, depending on the applied coolant MFR setting. Detrimental (red) and favorable (blue) effects are illustrated, considered from an aerodynamic and thermal point of view.



- (a) High MFR: (A) Vortex triggered and fed by LE RIDN and TE-Slot; (B) RIDN coolant accumulation in PS corner, velocity increase and high Nu ; (C) High Nu -entrance region and η_{aw} -stripe pattern due to cooling injection; (D) SS trajectory of LE-coolant, causing high Nu in SS shoulder area
- (b) Low MFR: (E) Low Nu in central passage; (F) Confined increased Nu area due to coolant influence; (G) High Nu in throat and TE region due to velocity increase; (H) Well cooled LE region; (J) Stripe pattern with uncooled areas; (K) Downwash of airfoil coolant on endwall in pressure side corner

Figure 5.22: Schematic model of NGV flow features for the reference case. The coloring resembles whether the observed effect is detrimental or favorable with respect to the aerodynamic or thermal design

For high MFR, the near-wall flow is reversed relative to the usual flow direction in an uncooled passage. This explains the trajectory of the coolant air on the pressure

side, which initially lifts off at the leading edge and wraps around to the pressure side. (A in Fig. 5.22a). It also passes by the trailing edge slots and TE-coolant feeds the low-pressure, low-velocity zone, that is observed in the NGV exit flow. RIDN coolant furthermore accumulates in the pressure side corner, where peak effectiveness values are observed (B). The superior momentum of the coolant flow increases the near-wall velocity and the Nusselt numbers. By the RIDN coolant, the velocity deficit in the vane's wake is overcome in the lower annulus. Due to the radial equilibrium, this higher velocity flow follows a trajectory with a greater radius. As a consequence, the near-wall flow in the passage is directed towards the pressure side. As a compensating movement to the endwall flow, a low-pressure, low-velocity zone of vortex (A) is transported towards the SS into the passage.

Consequently, it is detected in the passage center of the NGV exit flow. The flow direction on both airfoil surfaces is also reversed to the common orientation in an uncooled passage. It is oriented downward on the SS and upward on the PS. Coolant air, that initially lifts off the endwall and winds around the LE to the suction side (D) is hence transported downward again. It reaches the hub endwall at the suction side shoulder and increases the Nusselt numbers there. The entrance region shows increased Nusselt numbers (C) and a stripe-pattern in the film cooling effectiveness contours due to the different behavior of the two rows of holes.

For low MFR, a flow field more similar to the common understanding in the literature for uncooled passages is detected. The leading edge area receives good cooling due to the downwash of coolant with the horseshoe vortex (H in Fig. 5.22b). High Nu levels are found in a confined region at the onset of the measurement area (F), in the throat area and downstream (G) due to the velocity increase. Low Nu are observed on the central passage endwall. The stripe pattern at the passage entrance (J) shows both very high values downstream of the second row holes and uncooled areas in between; because the first row coolant jets lift off the surface. The downwash on the pressure side carries airfoil coolant onto the endwall (K).

Evaluation of the cooling design

For the investigated film cooling design, increasing film cooling effectiveness has been observed with increased MFR. From a MFR of 2.25 on, the whole endwall is covered with values greater than 0.25. At the same time, a steep increase in heat transfer has been observed. This effect counteracts the benefit of the coolant injection. The performance of the film cooling injection can be generalized in the following: Low MFR up to one, where the injected coolant partly remains in the "attached jet" regime offer the best heat flux reduction capability following the approach of Baldauf [12]. The drawback is the existence of uncooled areas in between the second row jets in the entrance region.

The endwall can be divided into three sections with different film cooling performance: The entrance and mid-passage region, the pressure side corner region and the trailing edge region. For the latter, the net heat flux reduction remains significant in the order of 40% up to the highest investigated MFR of 5. At low MFR, the endwall cooling is partly cooled by airfoil cooling films that are washed down from into the pressure side corner for MFR smaller than 1.5. In the entrance area, with increasing

MFR, the concurrent increase of Nusselt numbers brings the film cooling design close to a net zero effect.

The contours of Θ have been determined greatly depending on the local film cooling effectiveness. In consequence, an improvement of the design should focus on the cooling of the entrance area. To reduce the stripe pattern in the entrance region, a shape optimization of the second row of holes can be conducted to increase the lateral spread of the jets. Bunker [23], Abdelmohimen [1] and Heidmann and Ekkad [57] discuss possible strategies. A shape optimization usually reduce the jet momentum as well. Shih and Na [123] mention that this reduces the downstream coverage and in consequence, it has to be carefully designed to maintain the trailing edge region's coverage high. The robustness of this cooling design and its capability to reduce the heat flux below the level for the uncooled endwall is evaluated with respect to the swirling inflow and the associated changes to the thermal parameters in the following section.

6 Investigation of swirling combustor inflow

The second part of the discussion of the results is dedicated to swirling combustor inflow. It follows the structure of the preceding chapter and compares the results to the reference inflow. Three main aspects are highlighted in the course of this chapter:

- A detailed discussion of the changes in the aerodynamic flow field, indicating the impact on the flow field and vortex system at turbine inlet. The propagation of the coolant flows and the flow field near the RIDN injection are investigated as well.
- Endwall heat transfer and film cooling effectiveness are analyzed and compared to the reference. The heat flux reduction Θ due to film cooling is calculated with respect to the axial inflow. In this way, the robustness of the cooling design to the imposed changes is evaluated.
- The clocking influence of the relative position between swirler and vane leading edge is analyzed with two settings: Leading-edge-aligned swirl (denoted SWL) and passage-center-aligned swirl (denoted SWP) as illustrated in Fig. 3.5. Given by the swirler-to-vane count of 1:2, adjacent vane passages face different inflow conditions.

In this chapter as well, schematic illustrations of the observed findings are guiding through the discussion of the results.

6.1 Aerodynamic flow field

The aerodynamic flow field with applied swirl is studied at turbine inlet in ME01 and the NGV exit in ME02 with the analysis of 5HP data. In addition, the propagation of coolant flows with the help of gas tracing is evaluated in ME02.

Turbine inlet

Pitch wise averaged values for the axial Mach number Ma_{ax} , whirl angle α and the turbulence intensity Tu are displayed in Fig. 6.1 for both SWL and SWP clocking. For comparison, the axial inflow (AX) is shown as a reference.

Schmid [112] and Hilgert et al. [60] have identified a recirculation zone in this setup of the combustor module. This is expected given by the strong initial swirl. It causes a low-pressure zone and low Mach numbers in the central annulus and higher Mach numbers near both endwalls. The axial Mach number increases towards both endwalls to 0.055. Especially at the hub, this is a significant change compared to axial inflow. Because the radial profile of Ma_{ax} resembles the mass flow distribution, it is assessed that the mass flow is redistributed towards both endwalls due to the swirl.

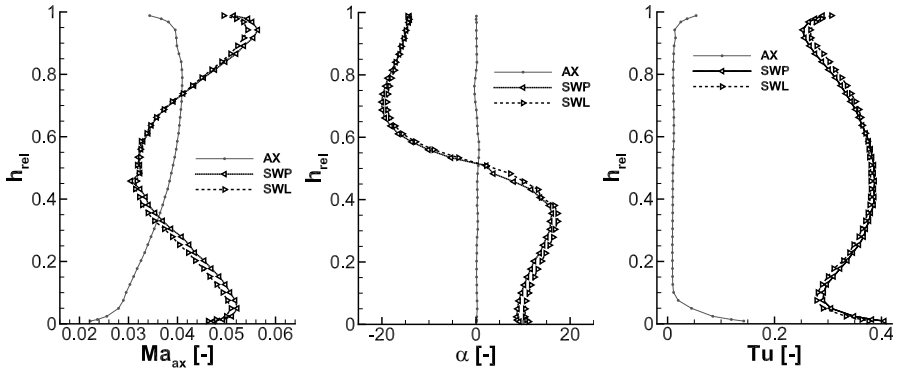


Figure 6.1: Pitchwise averaged data for swirling inflow in ME01. MFR 3, SWL and SWP clocking and comparison to AX baseline, 5HP data (Ma_{ax} and α), turbulence intensity acquired by hot wire anemometry (Schmidt [114])

Average whirl angles of up to 15° in the lower and up to -20° in the upper annulus are detected. Similar to the Mach number profile, no significant influence of the clocking position is observed. This agrees with the findings of Schmid [112] and Klapdor [73] in numerical simulations, that no upstream effect of the leading edge is present at this axial distance of about one axial chord length upstream of the NGV.

The turbulence intensity is not discussed in detail in this thesis, but the radial profile is shown to give a first impression of the imposed increase. In the pitch wise average a value of 30-35% is observed, with respect to the local effective velocity. A 2-dim. distribution with a peak value of 45% in ME01 is observed (Wilhelm et al. [140], Werschik et al. [139]). Similar to the other flow properties in this plane, no clocking effect is determined. Bacci et al. [11] have identified the swirler center as the global peak of the turbulence intensity distribution. Following this selection criterion, the LSTR swirler center shifts by 2° into the circumferential direction up to ME01, whereby it remains radially central in the annulus (Schmidt [114]). A similar behavior has been observed for other investigations with annular combustor geometry (Vagnoli and Verstraete [130], Insinna et al. [62]).

The inflow contour at ME01 is shown in Fig. 6.2 with low total pressure in light colors and high total pressure in blue. A global pressure minimum is observed for a 30° -sector. Similar to the investigation by Giller [46] for a linear cascade, a band of low total pressure is present in the annulus center and high total pressure towards the endwalls. In contrast to Giller's investigation, it is interrupted by regions of high total pressure that spread towards the center. Evaluating the flow field with the λ_2 -criterion²⁹ vortices can be identified. Giller [46] used the criterion for a similar inflow and a detailed discussion is given by Kegalj [67].

²⁹The criterion is used to identify a pressure minimum in a flow field. With the assumption that a vortex core coincides with a pressure minimum, it is identified in this way.

The vorticity ω ³⁰ of the velocity field shows that in the interaction region between the main swirl vortices (Fig. 6.2a - ④) of adjacent swirlers two additional vortices develop (Fig. 6.2a - ③ and ⑥). They are counter-oriented to the main swirl. Their peak value in the center is 2/3 of the main swirl peak value³¹.

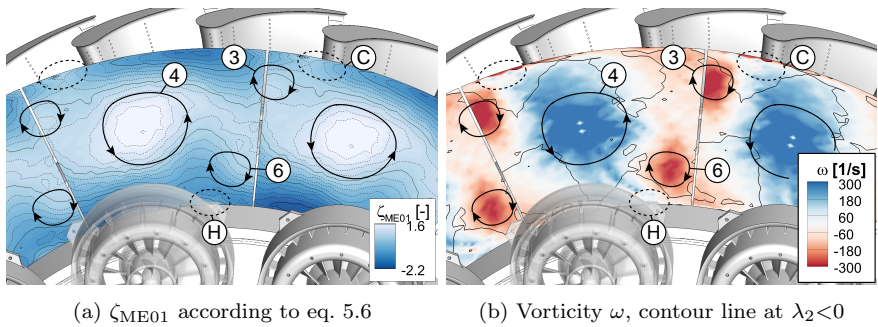


Figure 6.2: Inflow in ME01 for SWP clocking, 5HP data. Schematically indicated are vortices (③, ④ and ⑥) and regions of interest (Ⓒ and Ⓗ). For reasons of visualization, all vortices are only labeled once.

Near the hub and casing a high total pressure band characterizes the pressure contour. Region (Ⓗ) near the hub and region (Ⓒ) interrupt this band with low pressure. At this location, both vortices ④ and ⑥ point in radial direction at the hub. It is similar near the casing for vortices ④ and ③.

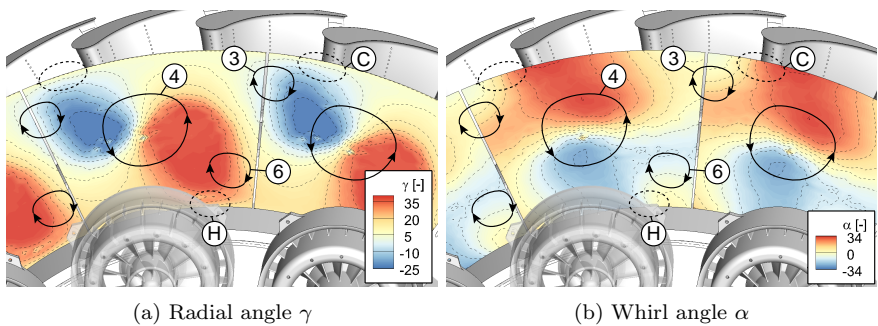


Figure 6.3: Flow angles for SWP clocking in ME01

In region (Ⓗ), whirl angles near zero are measured and a large radial angle near the hub (Fig.6.3). Similarly, this appears on the casing side in region (Ⓒ). In this way, the contours show a tilt of the symmetric axis in the rotational sense of the swirler. Koupper et al. [79] and Andreini et al. [5] have observed it as well in other investigation in annular rigs.

³⁰The in-plane vorticity ω in ME01 is calculated with $\omega = \frac{\partial v_y}{\partial z} - \frac{\partial v_z}{\partial y}$

³¹For visualization purpose the colormap has been adjusted so that all three vortices are visible. The maximum value for the main swirl is $520 \frac{1}{s}$

The vortex system in this way has an important impact on the flow field, because the whirl angle alternates between higher and lower values along the hub. This is in contrast to the investigation of Giller [46], who observed the flow field of neighboring swirlers to combine and form a band of positive whirl angle near the casing and negative whirl angle near the hub.

The propagation of the low-pressure zone near the hub within the remaining axial distance to the vane row and the development of the flow angles will be addressed in section 6.3 using detailed flow field measurements in the vicinity of the RIDN injection.

An upstream clocking influence due to the potential field of the vane's leading edge on the contours is not observed, shown exemplary with the Mach number contours in Fig. 6.4. Instead, the contours just move along with the swirler position³².

The Mach number near the hub in region ④ is very low. Furthermore, the figure shows the location of vortices for SWL clocking. They are identified with the same procedure as for SWP, using the λ_2 -criterion and the in-plane vorticity ω to specify the orientation. A difference between the two contours is that the vortex ③ appears with lower intensity than for SWP. Other than that no relevant differences between the two contours are observed. In both regions ④ and ⑤ low Mach numbers are detected.

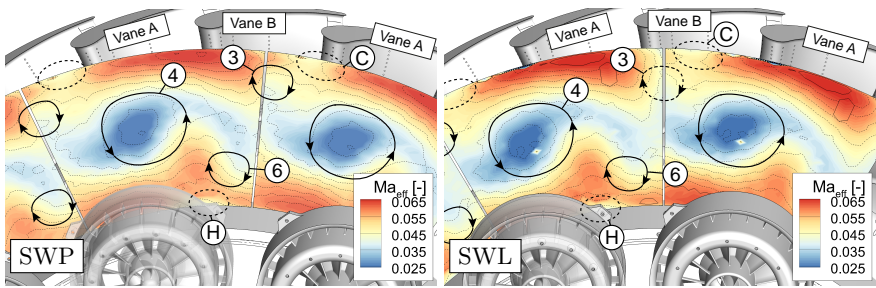


Figure 6.4: Effective Mach number for SWP and SWL clocking. Vanes A and B are labeled for the subsequent analysis of the vane loading.

The absence of a clocking effect is in agreement with the findings of Schmid [112] and Klapdor [73]. They only identify such an influence within a shorter axial distance to the vane leading edge. However, it is expected that clocking effects occur in the vane row, because the vortices enter at different pitch and span positions with respect to the vanes for the two clocking positions.

In the following sections, the results of the flow field measurements near the RIDN injection will be used to identify the trajectory and propagation of the vortices and flow field in the hub region. Furthermore, the NGV loading is investigated using pressure taps along the airfoil at 20 %, 50 % and 80 % span height. In this way, the clocking effect is analyzed. The analysis of the NGV exit flow field finally completes the picture of the vane aerodynamics.

³²In the following, it is discussed that there is a clocking effect within the vane row. It is detected in ME02 and

Flow field in the vicinity of the RIDN injection

Four aspects are investigated with the flow field measurements in the vicinity of the RIDN injection:

- The boundary layer is analyzed in the inflow to the RIDN holes.
- Near the hub, the whirl angle profile is investigated, showing the influence of vortex ⑥, identified with the 5HP measurements.
- A variation of the MFR shows the impact on the excess momentum in the turbine inflow
- The pitch wise variation of the local blowing ratio is quantified.

For all aspects, a comparison to the axial inflow illustrates the magnitude of the changes with applied swirl.

Boundary layer profile

Because of the mass flow redistribution towards the endwalls, the velocity near the hub endwall is significantly increased in comparison relative to the baseline case. This is detected with the inlet boundary layer measurement in plane RE01. Fig. 6.6 shows the comparison of AX and SWL inflow, averaged pitch wise in RE1 and at discrete pitch positions, specified in Fig. 6.5³³.

Based on the expected inflow angles with applied swirl, the 4HP has been used instead of the boundary layer probe for AX inflow. Due to the increased probe diameter, the measurements start at a greater wall distance³⁴. In addition to the already mentioned velocity increase from 0.04 for AX inflow to 0.055 for SWL inflow on average, another difference is that for a distance greater than $y_D=0.5$, the profile shows a decreasing characteristics.

Along the pitch, local variations in the boundary layer occur. Fig. 6.6b exemplary shows the results for three different pitch positions in comparison to the SWL average. At $x/T=0$ (data series marked with ①), span wise increasing and greater than average Mach numbers are observed. At $x/T=0.4$ the velocity in the boundary layer increases towards the endwall (series ②) and reaches the average value for greater span wise distances. At $x/T=0.8$ the velocity minimum is detected (series ③), whereby the

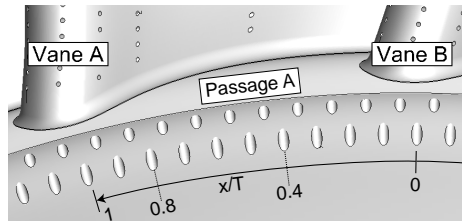
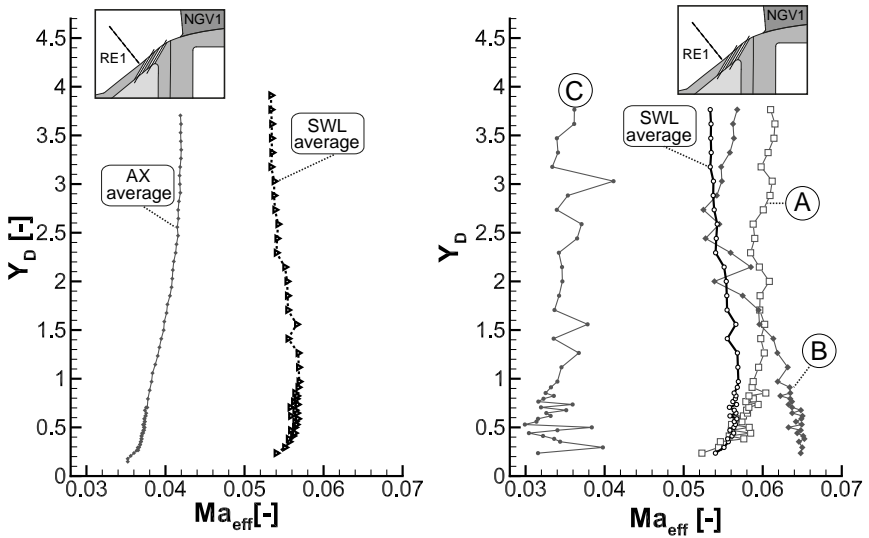


Figure 6.5: Position of the boundary layer evaluation in Fig. 6.6

³³The swirler has a pitch position of $x/T=1$

³⁴For axial inflow, no differences in the total pressure measurement have been observed using the two different probes. Because the boundary layer probe has a diameter of only 1 mm, it is favored over the 4HP for axial inflow. With swirl, the flow angles exceed the tolerable range of a single-hole probe and the 4HP is to be used



(a) Pitch wise average, comparison of AX and SWL inflow (b) Pitch wise variation for SWL inflow: (A): $x/T=0$; (B): $x/T=0.4$; (C): $x/T=0.8$; pitch wise average for comparison

Figure 6.6: Mach numbers in the boundary layer, 4HP results

data shows large variations close to the hub³⁵. The pitch position of the minimum, denoted as region (H)³⁶ is the same as in ME01.

Whirl angle variation near the hub

For axial inflow, the whirl angle has been observed to vary within $\pm 2^\circ$ due to the vane's potential field along the pitch (Fig. 6.7 - top). With applied swirl, the level of the variation increases³⁷ to $\pm 25^\circ$. Furthermore, the variation pattern is repeated every 30° for each swirler passage instead of 15° for one vane passage in the case of AX inflow. The appearance of vortex (G)²⁹ in this way is responsible for alternating incidence near the hub for vane A and B.

With a change of the clocking position to SWP, the whirl angle variation clocks concurrently. The alternating incidence for adjacent vanes remains. As a minor clocking effect, the extent of the positive whirl angle region is smaller than for SWL. Hence, a loading variation due to the measured whirl angles is expected. This is analyzed in the following section.

³⁵In the low velocity region, unsteady effects that cannot be resolved with the probe are expected to influence the measurement and cater for the fluctuations.

³⁶C.f. Fig. 6.4

³⁷The colormap for AX inflow in Fig. 6.7 has been adjusted for visualization purposes.

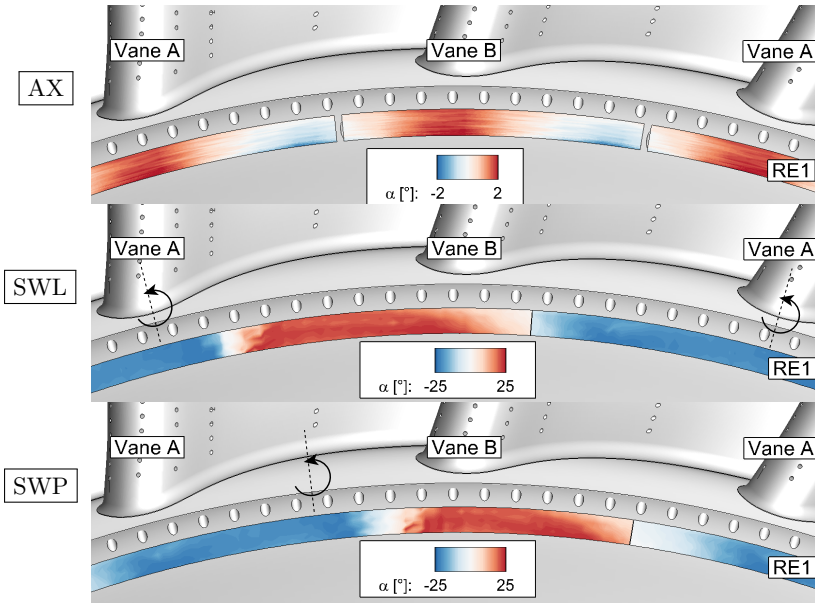


Figure 6.7: Whirl angle comparison for AX, SWP and SWL inflow, MFR 3 in RE1, 4HP measurement. The scale has been modified for AX inflow. The pitch position of the swirler is indicated in the SWL/SWP figures, projected in the illustration along its symmetry line.

Effect of a MFR variation

The total pressure near the hub increases with the MFR³⁸. Fig. 6.8 shows the results for SWL inflow evaluated in RE3 and at a pitch position of $x/T=0.5$. It is observed that the peak values in comparison to the axial inflow³⁹ at the same MFR are decreased downstream of the first row holes (Fig. 6.8a). For lower MFR, e.g. MFR 1.5, the radial profile nearly coincides with the uncooled case. Only very little excess total pressure is provided to the flow below $y_D = 1$. The reason is that because of the increased velocity near the endwall, the coolant injection does not hold a large surplus anymore. This is observed as well for the 2nd row of jets (Fig. 6.8b). To achieve the same excess total pressure, a higher MFR is necessary. In consequence, a smaller impact of the coolant injection on the flow field is expected in comparison to the observations for AX inflow.

Pitch wise variation of the local blowing ratio

The circumferential variation in local mass flow and Mach number results in a significant local blowing rate variation. Fig. 6.9 illustrates this for RIDN row 1 and MFR 3. The blowing ratio is evaluated with the measured inflow velocity in RE1 and the

³⁸As a measure, the pressure coefficient $P_{t,ref}$ according to equation 4.7 is used.

³⁹For comparison, also AX inflow is shown for MFR 3 and 5.

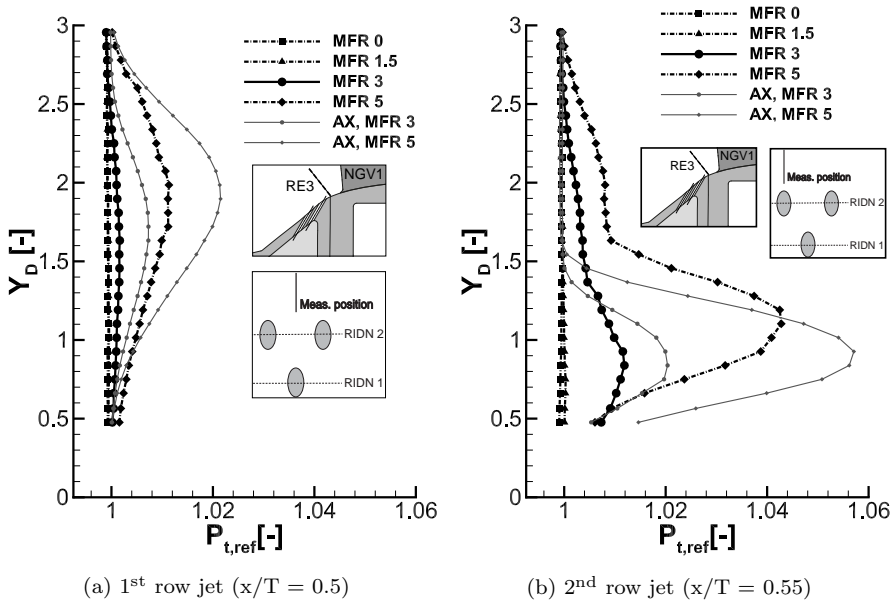


Figure 6.8: $P_{t,ref}$ in RE3 for both rows downstream of their hole centerline for SWL inflow and varied MFR

jet core velocity in RE2. To determine the location of the core, the nine measurement points with the highest values per cooling hole are evaluated.

As it has been discussed in section 5.1, the pitch wise variation for the baseline case is very low and triggered by the vane potential field. An average value of about 4.45 is determined. When swirl is applied, a variation of the blowing rate between values of 3 at $x/T < 0.5$ and up to 5.25 for $x/T > 0.5$ is observed. This analysis allows two conclusions: A strong local variation in the blowing rate will have an effect on the film cooling performance on the endwall. Likewise, a pitch wise variation is expected. Furthermore, the local blowing ratio is different from a blowing ratio calculated based on the coolant and main mass flow. This applies to both the average value and because of the local variation. This emphasizes that it is important to consider the local flow field for the film cooling design. The mass flow redistribution due to swirl means, keeping the coolant MFR constant with respect to the reference case, not enough coolant air is directed into the near endwall flow. In consequence, the film cooling effectiveness is expected to be lower.

6.2 NGV aerodynamic loading

Because of the whirl angle variation in ME01 and RE01, an effect on NGV aerodynamic loading is expected. Whereas negative incidence reduces the loading, positive incidence increases it. The NGV was designed for axial inflow and is hence exposed

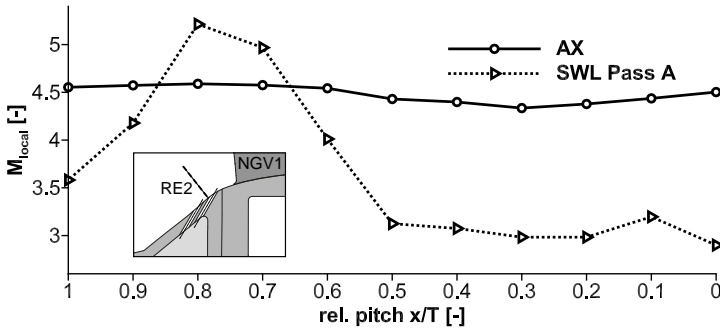


Figure 6.9: Variation of the local blowing ratio (M_{local} due to swirling inflow according to eq. 5.5. AX baseline compared to SWL, passage A, 4HP data

to misaligned inflow with swirl. In addition, the RIDN coolant injection is expected to influence the vane loading.

Fig. 6.10 shows the change in the isentropic Mach number⁴⁰ for SWL and SWP inflow at 20% span height⁴¹. For comparison, the results for the baseline case are shown as well.

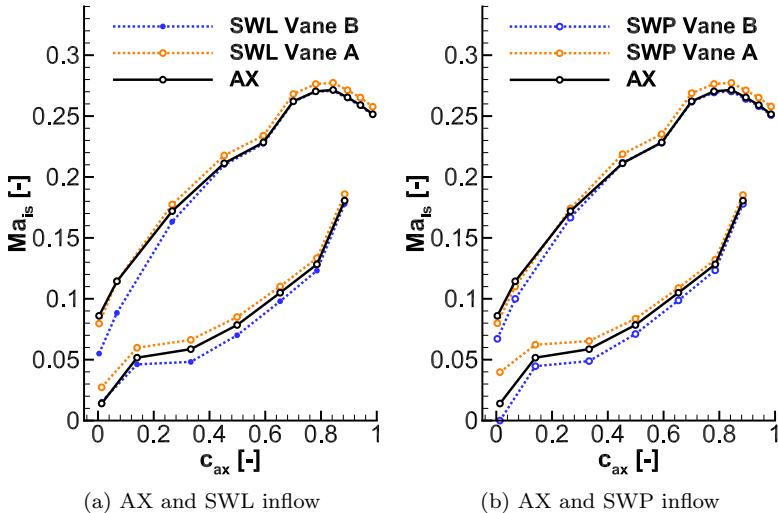


Figure 6.10: Isentropic Mach number at 20% span height, MFR 0

⁴⁰The isentropic Mach number was calculated with the static pressure obtained at the airfoil pressure taps, assuming constant total pressure within the NGV row at the level measured in ME01. The total pressure contribution of the airfoil film cooling is neglected. A comparison to a numerical simulation by Hilgert et al. [60], that considers the associated total pressure increase, shows no significant deviation to the measurement data.

⁴¹The nomenclature of the vanes and the swirler position is illustrated in Fig. 3.9

For SWL clocking and vane B especially the suction side velocity deviates from AX inflow near the leading edge and reduced loading occurs. This agrees with the measured positive whirl angle upstream of the suction side and the imposed incidence. Vane A remains relatively unchanged despite the negative incidence. An explanation could be the low velocity in the inflow to vane A due to region \textcircled{H} . Towards the trailing edge of the vane, the difference to the axial inflow becomes mitigated.

With SWP inflow at 20 % span height (Fig. 6.10b) Vane A is mostly affected. On the pressure side, higher Mach numbers are present until towards the trailing edge, where the difference to axial inflow becomes smaller again. The negative incidence at vane A in conjunction with the increased inflow velocity due to swirl decreases the loading. In contrast, vane B does not show significant loading changes.

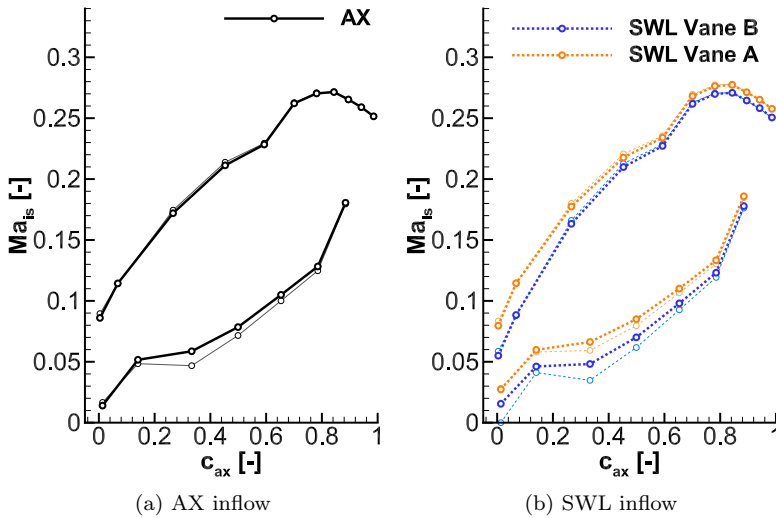


Figure 6.11: Influence of RIDN injection on NGV loading at 20% span height, uncooled (bold) and cooled (light colors)

When RIDN cooling is applied, the vane loading increases at 20% span height⁴² (Fig. 6.11) for all inflow configurations. The change occurs on the PS, whereas the SS remains unchanged. For AX inflow, between 0.2 and $0.6C_{ax}$, the Mach numbers decrease in relation to MFR0. Thereby between the second and third pressure tap, even a small flow deceleration is detected. The vortex due to the RIDN coolant, that forms at the leading edge and travels up the pressure side is responsible. The same change is observed with swirl. Because the momentum increase has been determined small in comparison to axial inflow, the vortex is expected to be weaker with applied swirl. Nevertheless, due to the increased loading, the velocity is smaller on the pressure side and vane aerodynamics more susceptible to perturbations. The change of the loading due to the RIDN injection is therefore even increased for vane B. In addition, for vane

⁴²MFR 0 is printed in bold and MFR 3 in light colors for AX and SWL inflow.

B, the stagnation point moves to the pressure side: The first pressure tap indicates zero velocity. The observations for SWP inflow are identical and not displayed here.

A loading influence only occurs at this span height. The RIDN air does not reach the other two positions. Therefore, only the results for the uncooled case are discussed in the following.

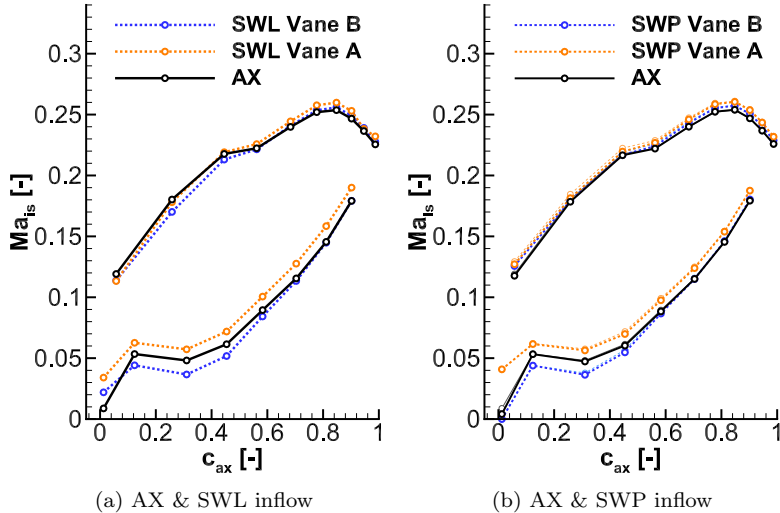


Figure 6.12: Isentropic Mach number at 50% span height, MFR 0

At 50 % span height, (Fig. 6.12) the swirl influences mainly the pressure side for both clocking positions. Vane A shows increased and Vane B decreased Mach numbers. The loading is slightly increased. Differences that indicating a shift of the stagnation point towards the suction side are observed at the leading edge, except for SWP Vane B.

At 80 % span height (Fig. 6.13), the loading is unchanged for SWP inflow. No values have been measured at the suction side for SWP inflow. For SWL clocking, both Vane A and B show a velocity reduction on the pressure side. For Vane B, the stagnation point moves to $0.12 C_{ax}$, which is beyond the first pressure side cooling film. Giller [46] has shown that the coolant film in such a case follows the main flow towards the pressure side. SWP inflow does not influence the vane loading at 80% span height.

With the point-wise pressure measurements along the airfoil, the incidence angle cannot be quantified. However, the qualitative changes are illustrated in a schematic for 20% span height (Fig. 6.14). For both clocking positions, Vane A is subject to negative incidence and Vane B to positive incidence. Schmid [112] investigated a similar incidence situation for a linear cascade and observed higher Nusselt numbers for the inflow region of passage B, whereby the wall-normal transport of fluid towards

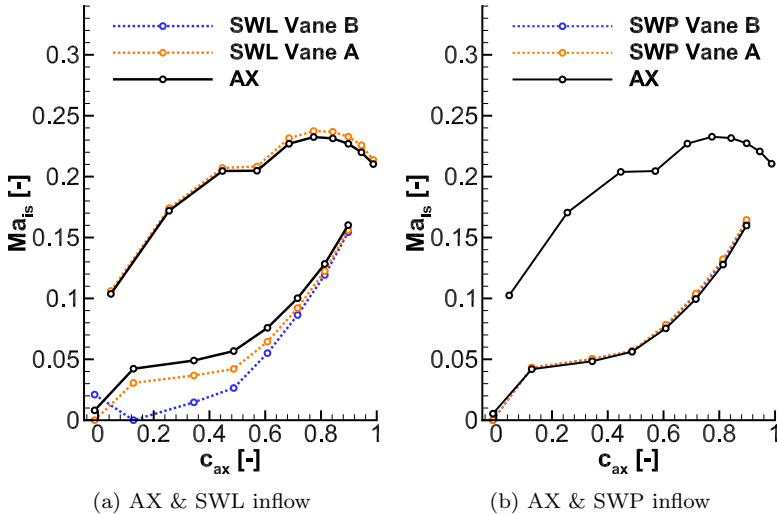


Figure 6.13: Isentropic Mach number at 80% span height, MFR 0

the endwall into passage B is responsible. Schmid investigated counter-rotating main swirl vortices for adjacent swirlers, whereby the number of swirlers and vanes is even. Every other vane passage thereby was exposed to either radial upward or downward flow. In this way, the heat transfer is increased at the hub and decreased at the casing or vice-versa for adjacent passages. This aspect is addressed again in section 6.4.

In summary, incoming swirl brings the NGV to an altered incidence situation. Whereas SWL inflow leads to positive incidence near the casing for both vanes, negative incidence occurs near the hub for vane A and slightly positive incidence for vane B. With applied RIDN cooling, the incidence increases further for vane B. In contrast, SWP inflow shows no change on the casing side compared to AX inflow whereas near the hub, positive incidence for vane B and negative incidence for vane A is observed. In both cases, the additional vortex ⑥ that has been determined with the 5HP is responsible. Whirl angles with opposing sign to the main swirl vortex appear in consequence.

Because of the incidence at vane A for SWL inflow, a span wise pressure gradient towards the casing appears. With this observation in turn, a radial migration of the main swirl vortex towards the casing is expected, given by its position in the flow field. This assumption is verified with the 5HP measurements in the following section: The pressure loss coefficient maximum is observed at a higher span wise position for SWL than for SWP.

Furthermore it is concluded that the NGV's aerodynamic design is robust enough to encounter the imposed incidence. Any differences observed at the leading edge are mitigated and similar exit Mach numbers are detected for swirling and axial inflow.

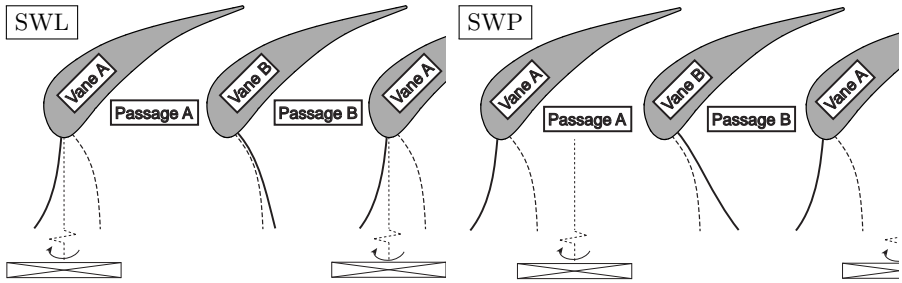


Figure 6.14: Incidence situation at 20% span height (schematic). The figure indicates the swirler clocking positions and schematically illustrates the shift of the stagnation point for AX (dashed) and swirling inflow (solid).

The numerical simulation by Hilgert et al. [60] agrees well with the findings in the experiment.

NGV exit flow field

Based on the results discussed so far, clocking effects are expected for the NGV exit flow as well. The flow field in ME02 changes significantly compared to the reference case, when swirl is applied, as the radial profiles in Fig. 6.15 illustrate. The axial Mach number profile visualizes that the mass flow redistribution towards the endwalls at turbine inlet persists through the vane row. Compared to axial inflow Ma_{ax} decreases by up to 20% in the central annulus. The swirl core⁴³ is observed at $0.58h_{rel}$ for SWL and at $0.48h_{rel}$ for SWP clocking in ME02. The span wise pressure gradient at vane A is responsible for this increased radial transport of the main swirl vortex. Near both endwalls, a small velocity increase is observed, whereby the increase is greater on the casing side.

The effective Mach number profile has a 5% higher level for SWP clocking. Because setting of the operating point imposes identical inlet mass flow into the turbine in all configurations, the axial Mach number does not show this an offset. Instead, the flow turning is different at the same span wise position and explains the difference in the effective Mach number.

Bearing in mind that the whirl angle has been observed with inverse sign between hub and casing side at turbine inlet, the exit flow profile yields the conclusion, that the vane is robust to the swirler-imposed inflow angles. Underturning by 1.5° near the hub and by 3° near the casing occurs. In the central annulus there is overturning by 3° in comparison to axial inflow. Responsible for this is the mass flow redistribution with applied swirl. The Ma_{ax} profile resembles this. The vane cannot handle the additional massflow near the endwalls and reduced turning results. In the annulus center, the situation is vice versa. In this way, the mass flow redistribution is transported through

⁴³The swirl core is specified here by the lowest velocity in the profile, excluding the near-endwall region

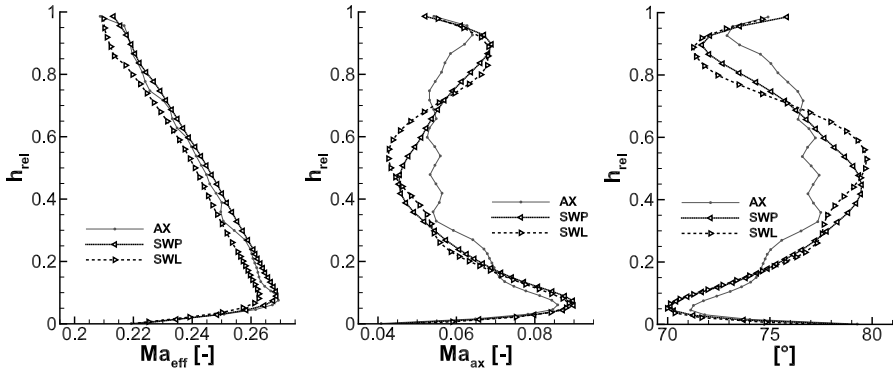


Figure 6.15: 5HP data in ME02, pitch wise averaged, MFR 3

the vane row exit and enters the rotor stage in the form of incidence angles and an altered Ma_{ax} profile.

In the contour of the effective Mach number in ME02 (Fig. 6.16), the NGV wake is less pronounced and low-Mach number zones due to the trailing edge slots, that had been observed for the reference case⁴⁴, are not detected with swirl.

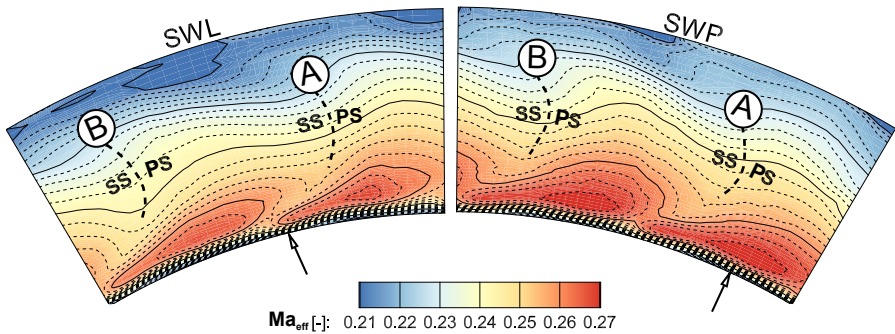


Figure 6.16: Mach number contours for SWL and SWP clocking, trailing edge of vane A and B indicated. 5HP results, MFR 3. The arrows indicate the streamwise projected swirler center

The pressure loss coefficient⁴⁵ increases for swirling inflow. The contours (Fig. 6.17) are smeared in comparison to AX inflow⁴⁶. The wake, indicated by the SS/PS line, is

⁴⁴For comparison, refer to Fig. 5.6 for the Ma_{eff} -contour of the reference case

⁴⁵The pressure loss coefficient is calculated according to eq. 5.6, i.e. the pressure contour at turbine inlet is area-averaged to one reference value.

⁴⁶The pressure loss contour for axial inflow is shown in Fig. 5.7

less pronounced. In contrast to the axial inflow the contribution of the vane coolant flows is not dominant anymore: Neither loss cores due to the TE-slot ejection nor due to the RIDN ejection can be identified.

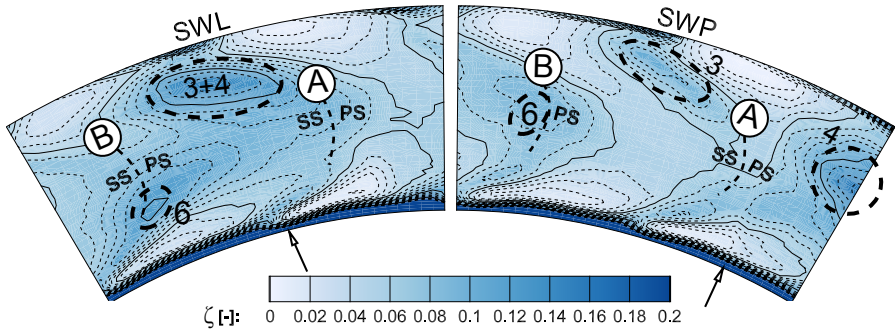


Figure 6.17: Pressure loss coefficient ζ contours for SWL and SWP clocking, 5HP results, MFR 3, ME02, arrows indicate streamwise projected swirler center

Instead, a global pressure loss maximum for SWL clocking is observed at about 85% span height (Fig. 6.17, label "3+4") downstream of the suction side of vane A. The pressure loss in this region results of both vortices ③ and ④, that had been identified in ME01⁴⁷. Vortex ⑥ causes increased pressure loss in the lower span of vane B, which agrees with its position upstream of the vane. With SWP inflow, the loss cores due to the vortices ③ and ④ are observed in adjacent passages. The contour due to vortex ③, which had been detected with lower vorticity than for SWL inflow, is observed at 85% span height downstream of the SS of vane A (Fig. 6.17, label "3"). The swirler core itself passes through passage A and is detected at 65% span height in ME02 (labeled as zone "4"). As mentioned before, the swirler core is transported further towards the casing for SWL inflow due to the spanwise pressure gradient at the leading edge of vane A. The loss contour due to vortex ⑥ is identified at midspan close to the suction side of vane B.

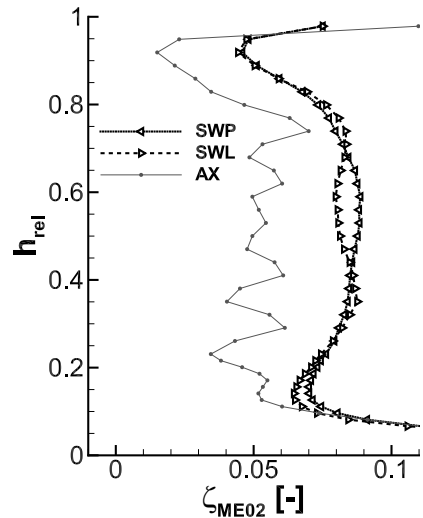


Figure 6.18: Pitch wise averaged pressure loss coefficients for swirling inflow and MFR 0; AX inflow shown for comparison

⁴⁷The λ_2 -criterion cannot be applied in this plane because the main flow direction is not in the measurement plane, but angled by about 75° to it.

In addition to these qualitative aspects, the pitch wise average in Fig. 6.18 illustrates the NGV pressure loss increase as well. The absolute value is 30 % greater with swirling inflow at MFR 0 (0.078) than for the reference case and the same coolant injection setting (0.06). Whereas for SWP clocking the maximum pressure loss, excluding the endwalls is observed at 60 % span height, there are two maxima, at 75 % and 35 % for SWL clocking. In comparison to the axial inflow, the profile is a lot smoother and without the additional peaks due to the trailing edge slots. Increasing the coolant MFR to 3, the same increase of 30 % in pressure loss is observed if AX and SWL/SWP inflow are compared. No additional increase due to the coolant interaction with main flow occurs. The more similar velocity of coolant and near-wall flow with applied swirl explains this (c.f. Fig. 6.8). As a consequence there is only a minor influence on the vane row losses. There is no additional radial movement of the pressure loss maximum in the main annulus if more RIDN coolant is applied. In conclusion, the incoming flow field decides on the vane flow field and row exit contours.

Propagation of the coolant flows

Using flow tracing, the propagation of the coolant flows is analyzed in the vane exit flow. Both for SWP (Fig. 6.20a) and SWL (Fig. 6.20b) clocking, the CAV-seeding shows significant presence of wheel space purge flow only within the lower 8 % span. The radial spread into the passage increases compared to the reference case⁴⁸. The level at identical span height is increased as well (illustrated by the pitch wise average in Fig. 6.19) and increased mixing of purge flow and main flow can be reasoned.

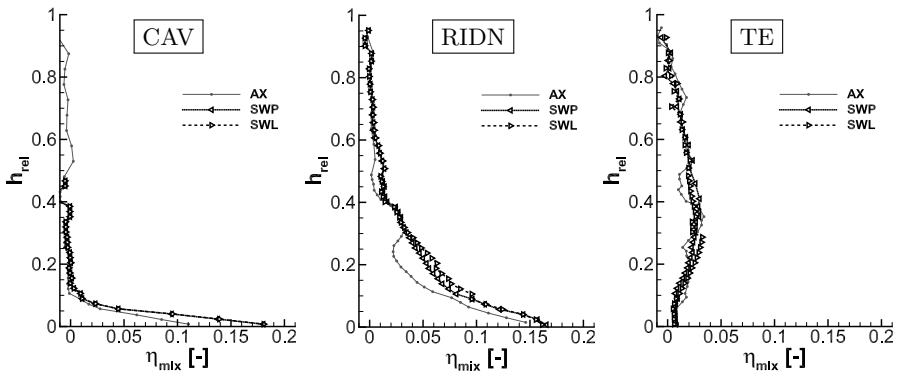


Figure 6.19: Pitchwise averaged η_{mix} for SWL/SWP and AX, ME02, MFR 3 and varied coolant flow seeding

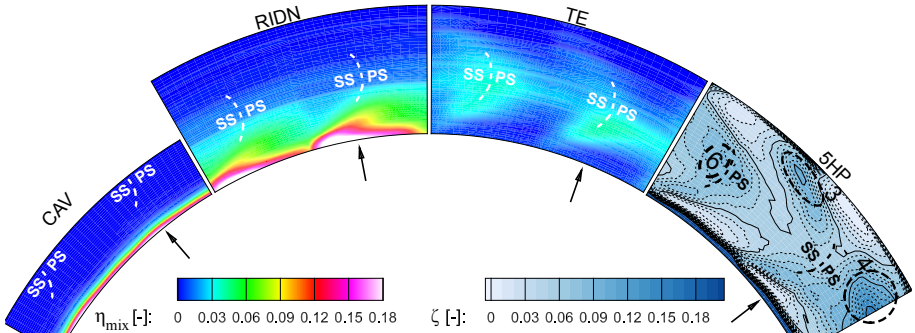
This is explained with a greater relative velocity difference between the two flows: Assuming a constant exit velocity and flow angle for the purge flow⁴⁹, the axial Mach number for the purge flow is determined to 0.02, compared to 0.08 for the main flow

⁴⁸The contours for axial inflow are shown in Fig. 5.9

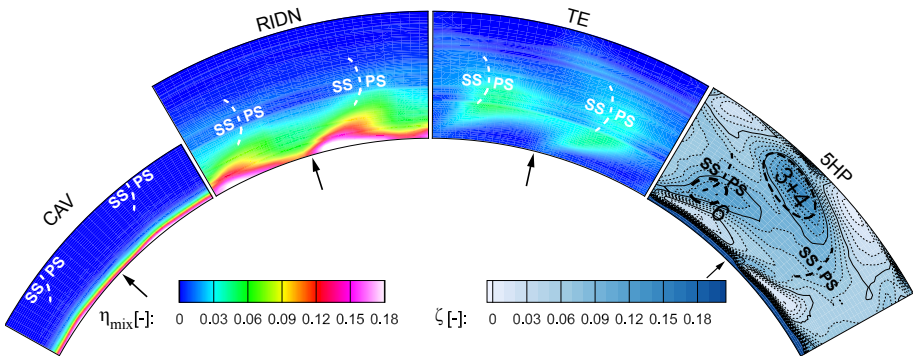
⁴⁹This is assumed because the rotor shaft speed and the ejection rate remain constant

near the hub. The purge flow enters ME02 with a lower whirl angle than the main flow according to the numerical simulation of Hilgert et al. [60]. The turning of the main flow near the hub reduces with swirl and the relative velocity difference between the two flows increases. In this way, mixing is enhanced.

RIDN coolant air reaches up to 40% span height, which agrees with the baseline result. However, the η_{mix} -level is between 0.03 and 0.04, i.e. it is higher with applied swirl for identical span positions (Fig. 6.19).



(a) SWP clocking



(b) SWL clocking

Figure 6.20: Flow tracing results for swirling inflow and CAV-/RIDN-/TE-seeding and pressure loss contours from 5HP measurements, ME02, MFR 3. Arrows indicate swirler core position, projected in flow direction

The coolant is observed with elevated concentration in the stator wake, but is spread nearly across the whole passage pitch in the lower third of the annulus. Instead of a distinct peak at 33% h_{rel} , that was observed for the reference case, the pitch averaged profile is smoother and follows an exponential characteristics instead. Comparing the

two clocking positions, η_{mix} is 0.01 greater for SWL clocking in the lower 10-25% span than for SWP clocking.

The TE-coolant spreads across half of the vane pitch, i.e. swirling inflow favors mixing of the coolant and the main flow. In this way, the wake is difficult to identify, because the measured level is very low. The pitch wise averaged profile with TE-seeding remains similar to the reference case. Thereby the influence of the trailing edge slots is minor, as discussed in the pressure loss analysis. Similar to AX inflow, the RIDN injection prevents the presence of TE-coolant directly at the hub. The pitch wise average yields a similar level for AX and SWL/SWP and the trend of increasing concentration towards the lower annulus with a peak at $0.3 h_{\text{rel}}$ is also similar. As mentioned, this results from the casing-side supply into the coolant plenum of the NGV.

6.3 Endwall film cooling

The impact of swirling inflow on the endwall cooling effectiveness is studied using infrared thermography. First, area-averaged results are presented, to compare swirling and axial inflow. The impact of the flow field is then analyzed in detail for a MFR of 3.

Subsequently, the distributions for a variation of the MFR are analyzed. In addition, a comparison to the gas concentration measurement allows differing between the cooling coverage of the RIDN holes and the air from the pressure side film-cooling.

Comparison to axial inflow

Fig.6.21 shows the area-averaged film cooling effectiveness on the NGV endwall for axial and swirling inflow. In addition, the relative change in percentage is specified with respect to axial inflow and MFR 0.8 i.e. the lowest injection rate in the study⁵⁰. Averaged results only serve as a first orientation to the designer and illustrate the global impact of the swirler on the endwall thermal load. For an evaluation of the design, the contour distributions are considered in the following.

The averaged results show that compared to axial inflow, η_{aw} is reduced by 20% on average. Thereby, for a MFR of 1.5, the values for axial and swirling inflow are close

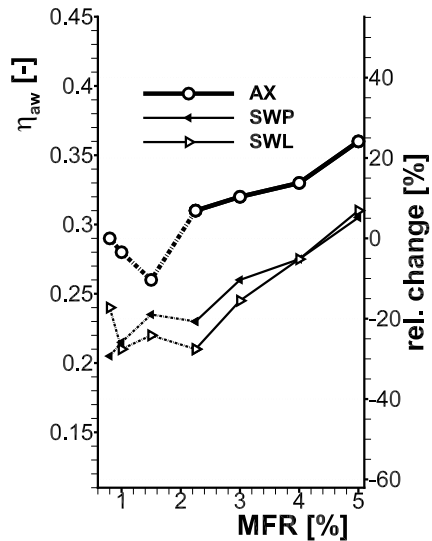


Figure 6.21: Area averaged film cooling effectiveness for the NGV endwall, per cent change referenced to AX inflow and MFR 0.8 for all data points.

⁵⁰For axial inflow, the average values up to MFR 1.5 are slightly underestimated because of the artifact identified in section 5.2. Below MFR 1 part of the cooling effect comes from the airfoil cooling. The same applies for SWL/SWP and the curves are dash-dotted for this reason.

to each other. For medium to high MFR greater than or equal to MFR 2.25, the characteristics is monotonically increasing, but with a penalty of 20 %-points between axial and swirling inflow. If the two clocking positions are compared, SWP is favored over SWL for most settings. Both at very low and very high settings, the difference due to clocking is smaller. To achieve the same averaged film cooling level with applied swirl as with axial inflow, the MFR roughly needs to be doubled⁵¹.

Responsible for the significant reduction with applied swirl is the mass flow redistribution towards the endwalls observed at turbine inlet. In this way, for an identical MFR setting with respect to axial inflow, not enough coolant air is present near the endwall. This is a global influence due to swirl. In the following, MFR 3 will be studied in detail to identify local effects due to the swirling inflow field, whereby both local effects on the coolant jet trajectory and the differences between adjacent passages due to the flow field at turbine inlet are analyzed.

Local effects due to swirl

The 5HP measurements in combination with the flow tracing measurements are sufficient to identify the overall impact of swirl and to achieve a general understanding of the aerodynamics in the vane stage. However, a decisive aspect with respect to NGV endwall heat transfer and film cooling are local changes to the flow field. They are relevant to the turbine designer, because local over-temperatures are to be avoided. To identify the local influence, the flow field in the vicinity of the two RIDN rows has been studied in detail with a 4HP for passage A at SWL clocking and MFR 3. These measurements are analyzed together with results from the infrared measurements.

To explain local differences that are observed in the contours⁵² (Fig.6.22), the local flow field is analyzed in detail: Characteristic for SWL inflow is a velocity minimum in passage A at a relative pitch position of $x/T=0.6$ to 0.9 . The Mach number in this minimum in RE1 is as low (0.025) as the near-endwall Mach number for axial inflow in the same plane. The remainder of the vane pitch faces a Mach number of 0.06 at the hub. This minimum has as well been observed in the 5HP measurements in ME01 and occurs in the interaction zone of vortices ④ and ⑥⁵³ where they impose a radial upward flow. The minimum becomes mitigated by the coolant injection but remains detectable up to plane RE3. The near-endwall Mach numbers are further increased by the contraction of the annulus and the additional momentum by the coolant injection. As it was analyzed in Fig. 6.9, the velocity minimum is responsible for high local blowing ratios. Despite of this, the downstream $\eta_{a,W}$ -contours show higher values towards vane A, whereas towards vane B, the values are lower. Less coolant air reaches the endwall and, given by the under turning near the endwall, leaves the trailing edge region poorly cooled in passage A from the SS shoulder on. The momentum increase due to the coolant in addition supports a near-endwall cross flow towards the pressure side.

However, considering the variation of the local blowing rate variation does fully explain the observed endwall effectiveness distribution. Therefore, the trajectory of the individual coolant jets is analyzed in detail: The jet contours, exemplary shown

⁵¹MFR 2.25 and MFR5 are considered for this example

⁵²Adjacent swirler passages have been recorded subsequently by clocking the swirler module by 15° i.e. half a swirler pitch.

⁵³Vortices ④ and ⑥ have been illustrated in Fig. 6.4

at $x/T=0.5$ in plane RE2 and RE3 (Fig. 6.23), are deformed⁵⁴. Instead of a circular shape, they are rather oval-shaped in RE2.

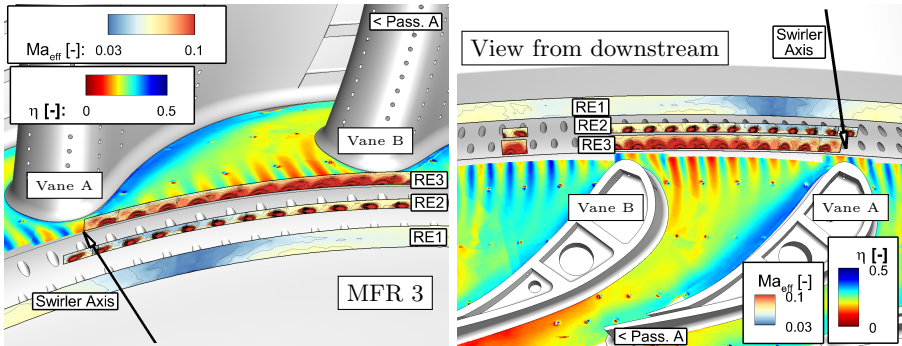


Figure 6.22: 4HP results for SWL inflow, MFR 3, Passage A

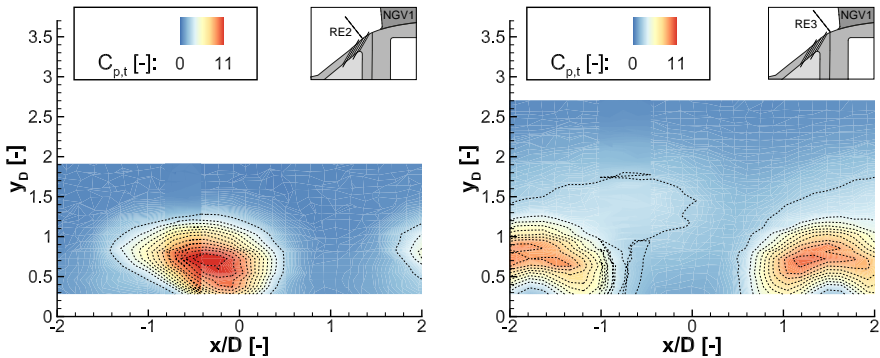


Figure 6.23: Total pressure coefficient $C_{p,t}$ at $x/T=0.5$ for MFR 3

In this way, the region of increased total pressure spreads in pitch wise direction, such that also the the adjacent jet is visible (visible at $x/D=2$ in the figure). The peak $C_{p,t}$ level is reduced as well. In consequence, the jet contour of the first RIDN row can hardly be identified in RE3. The pressure surplus of the coolant jet to the main flow is low, as mentioned before, because of the increased near-wall velocity with swirl. Finally, the contours show that the first row jet shifts towards one of the second row jets, whereas it had been detected centric between neighboring jets for AX inflow.

This is an important aspect, because the vortex interaction between neighboring jets in a staggered configuration decides on the attachment or detachment of the

⁵⁴For comparison, the circular jet shape with axial inflow is shown in Fig. 5.14

coolant film. Burdet and Abhari [26] address this aspect. Considering this aspect for the full passage (Fig. 6.24), it is assessed that the first row jets alter their trajectory depending on the whirl angle in RE1. The jet contour becomes deformed in the direction of the whirl component as well.

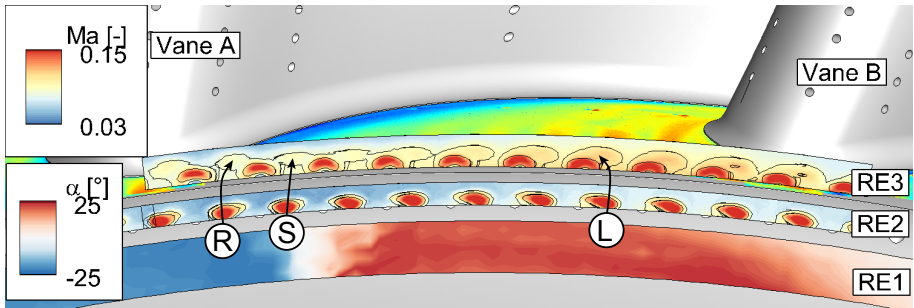


Figure 6.24: Whirl component influence on coolant trajectory, whirl angle in RE1 and effective Mach numbers in RE2/3. Contour lines according to the total pressure contours in RE2/3: (R) Jet core deflected clockwise; (S) Jet trajectory unaltered, remains in the center of second row jets; (L) jet core deflected counter clockwise, nearly on top of second row jet.

All jets of row one approach the adjacent second row jets downstream in clockwise direction for $x/T > 0.8$ (exemplary marked with (R) in Fig. 6.24) and in counterclockwise direction for $x/T < 0.6$ (L). In the velocity minimum the whirl angle remains close to zero and also the coolant jets remain centric (S) between the second row jets. All jets with (L)-trajectories approach the second row jets very closely, and some are detected nearly on top of them. Burdet and Abhari [26] show that the centric positioning is beneficial for the achieved film cooling effectiveness downstream, whereas another positioning contributes adversely and enhances jet lift-off. This is due to an interaction of the two associated CRVPs⁵⁵.

Expanding the view on both passages for SWL clocking, passage B is observed with significantly higher endwall film cooling effectiveness (Fig. 6.25). The difference to axial inflow⁵⁶ is -11% for passage B and -20% for passage A. This significant difference cannot be explained with the aforementioned alteration of the jet trajectory and vortex system. Such a conclusion is contradicted by the measured whirl and radial angles: Whereas the radial angle profile is rather similar throughout the pitch, except for a maximum in passage A, the whirl angle shows equally high values with opposing sign for both passages. In consequence, a similar impact on the trajectory of the first row jet is expected to be present in passage B. However, this endwall is considerably better cooled.

If in turn both clocking positions are compared, it can be deduced that the relevant impact comes from the swirler: For SWP clocking, the film cooling effectiveness distribution is more equal between both passages (Fig 6.26). Thereby, the flow field

⁵⁵The 4HP cannot resolve the CRVP due to their small scale with respect to the probe's size

⁵⁶The contour for axial inflow is shown in Figure 5.13

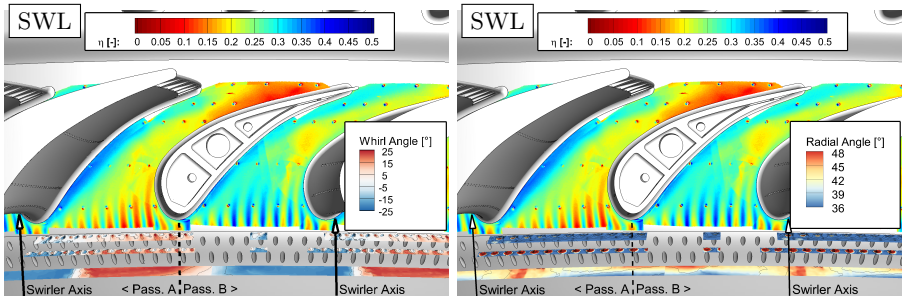


Figure 6.25: Whirl and radial angle for SWL, MFR 3

presented exemplarily with the effective Mach number contour in RE1 clocks with the swirler position and no significant upstream effect occurs. This applies for the measured radial and whirl angles as well. The influence on the trajectory of the coolant jets is therefore expected as well, but it is not decisive for the observed difference in adjacent passages.

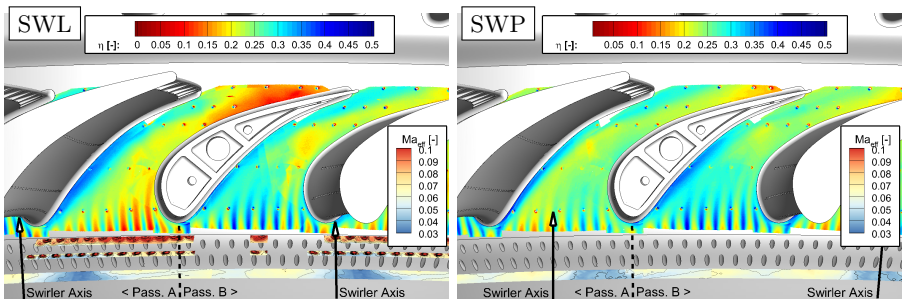


Figure 6.26: Clocking influence on the flow field and film cooling effectiveness contours for MFR 3

The key to the observed behavior is the vortex system that enters the vane row, illustrated by the flow model in Fig. 6.27⁵⁷. In between the vortices ④ and ⑥, there is an interaction zone in passage A and the vortices impose a positive radial component on the flow field. In the adjacent passage B, the imposed radial component is negative. With SWL clocking, the main swirl is directed on the leading edge of vane A and the counter-rotating vortex ⑥ enters the vane row near the leading edge of vane B. In this way, the film cooling air is washed off the surface in passage A and pushed onto the surface in passage B. In addition, vortex ⑥ causes positive incidence at vane B which results in a poor coolant coverage of the endwall near the SS of vane B.

⁵⁷It is noted, that the vortex positions shown have not been measured. Instead, the positions are concluded only based on findings from the presented measurement results on the endwall and in the turbine inflow

Passage clocking in contrast yields a more even distribution. Both vortices enter into adjacent passages and in this way, the imposed upward or downward component is ahead of the leading edge instead of the passage. In this way, adjacent endwalls receive a more similar film cooling coverage for this clocking position.

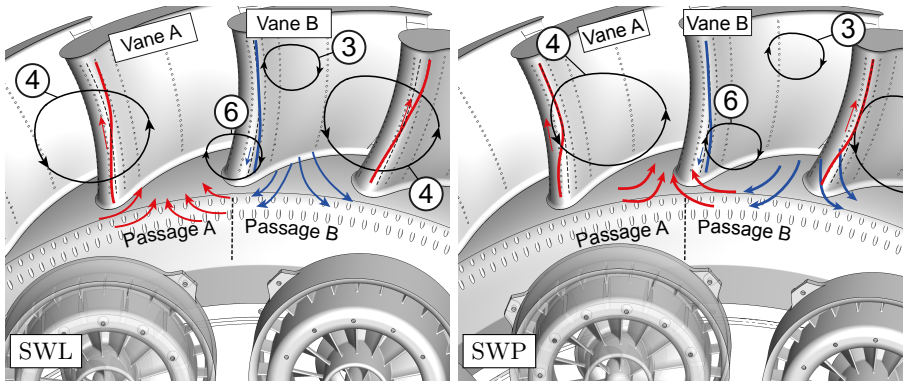


Figure 6.27: Schematic flow field with swirler. The assumed position of the vortices ③, ④ and ⑥ is illustrated for SWL and SWP clocking. The stagnation line for vanes A (red) and B (blue) shown schematically is based on the NGV aerodynamic loading measurements.

In conclusion, three main aspects are determined that reduce the endwall film cooling effectiveness with swirling inflow. Their associated spatial influence on the turbine endwall cooling varies (in descending order):

- As a **global** influence on the vane endwall, the mass flow redistribution towards the endwall on one hand reduces the local blowing ratio at identical MFR. But on the other hand it means that not enough coolant air is injected into the near-endwall flow.
- On the level of a single **vane passage**, the flow field and vortex system that enters at turbine inlet is responsible for a different cooling level between adjacent passages. An homogenous (SWL) or in homogenous cooling of the vane endwall results.
- The trajectory and CRVP of **individual coolant jets** is altered, depending on the whirl angle of the inflow to the coolant hole by smallest extent. This effect has the lowest impact on the overall cooling effectiveness in a passage, but yields the large local variation among the three discussed effects.

In the following, the contours for varied MFR are shown and discussed with special regard to these three effects.

Influence of a varied MFR

In the discussion of the local effects due to swirl, it has already been mentioned that the film cooling effectiveness values are considerably lower than in the baseline case. This is observed for the full range of MFR studied. The aerodynamic flow field with applied swirl changes significantly by a mass flow redistribution towards the endwalls, because of the blockage of the annulus by the recirculation zone. It has been measured locally, that this causes the effective blowing ratio to decrease, when the coolant mass flow is held constant⁵⁸. Consequently, despite the constant amount of coolant air injected at identical MFR, a lower level of film cooling effectiveness is achieved. The full range of MFR studied for both clocking positions is discussed in the following and a comparison to the gas concentration sampling results is given. It is determined which injection setting has to be applied to achieve a similar coolant coverage.

For a MFR of 1, the observed flow field contour in RE1 remains very similar to MFR 3 (Fig. 6.28): As a relevant difference, only the increase of the average velocity in the main flow is to be mentioned. This is a result of the increased main mass flow in plane RE1⁵⁹. Similar to the analysis of MFR 3 before, the adjacent passages show a very different η_{aw} -level due to swirling inflow. Passage B is better cooled, whereas in passage A beginning at midpassage, there is no coolant coverage anymore. This is reasoned with a regime change of the coolant injection: While for MFR 3, the jets are "penetrating jets" according to Baldauf et al. [14], they are "attached jets" for low MFR. The higher inflow velocity due to swirl near the endwall reduces the local blowing rate. This in turn is of great importance for attached jets and enhances their film cooling capability on the downstream wall. Even though the endwall cooling improves initially in this way, there is not enough coolant air to achieve a cooling effect further downstream and the midpassage and downstream area is not covered anymore. The mass flow redistribution that goes in hand with the velocity distribution means that significantly more main flow air is present.

The lowest injection rate MFR 0.8 shows a similar distribution to MFR 1 (Fig. 6.29). The entrance area is well cooled, before the values become quickly lower towards the midpassage region. The highest values at this injection setting are observed for SWP in passage B. The inflow velocity is higher in this passage, which results in a lower local blowing rate, allowing for a well cooling coverage of the endwall in the "attached jet" regime. A wedge shaped area in the entrance region forms, known from the literature. Deviating however, there is a region of high η_{aw} in the pressure side corner. This is observed for passage B and SWP clocking and for both passages with SWL clocking as well. With the findings from the axial inflow, one can already assume that this comes due to pressure side airfoil cooling. The low coolant momentum does not allow it to reach the pressure side corner and instead the downwash from the pressure side onto the endwall brings airfoil coolant with it. As stated by Baldauf et al. [14] the incoming high turbulence intensity favors lateral spread of the coolant jets. This in turn enhances the mixing between coolant and main flow as well and results in a quick deterioration of endwall cooling coverage. Passage A receives notably less

⁵⁸The absolute mass flow of cooling air is held constant for AX, SWP and SWL and identical MFR. The main mass flow is measured in the venturi pipe upstream of the swirler and held constant as well.

⁵⁹To achieve a constant mass flow at turbine inlet and also at rotor inlet, a variation of the RIDN MFR implies a variation of the main mass flow as well, as explained in section 3.3

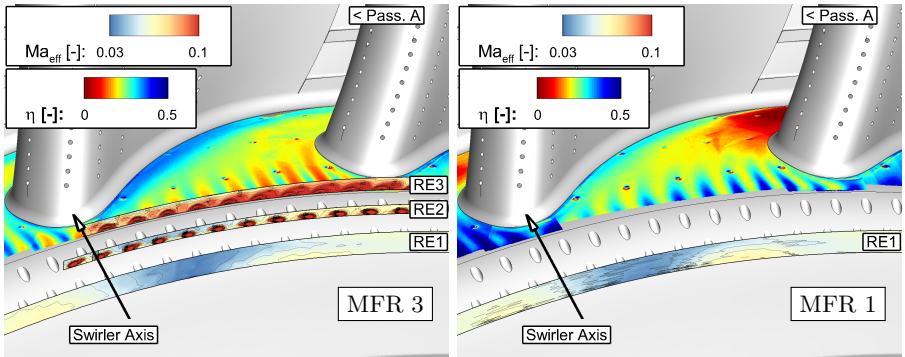


Figure 6.28: Influence of a MFR variation on the velocity contours and the film cooling effectiveness for SWL clocking

coolant and, beginning at $x/C_{ax}=0.5$, eventually none at all. The entrance region shows the stripe pattern that was observed for the reference case.

At higher MFR than 1, the cooling injection is in the regime of "penetrating jets". Instead of the local impact on the coolant jets, the contours are therefore mainly influenced by the incoming vortex system that has been analyzed for MFR 3.

With increasing coolant momentum at MFR 1.5 (not shown) and MFR 2.25, the coolant is able to reach further downstream. The reduced turning in the vane passage thereby yields a gradient with increasing values from SS to PS. The stripe pattern in the entrance area intensifies, causing increased local differences. SWP is observed with higher values compared to SWL clocking. For the latter, in passage A, especially near the leading edge of vane B, the coolant coverage worsens under the influence of the swirler-induced vortex system, as it has been discussed for MFR 3.

Increasing the MFR further improves η_{aw} throughout and for MFR 5, only few minor local differences remain, both between adjacent passages and between the two clocking positions. The MFR setting of 5 results in a similar η_{aw} -level as it has been measured for the axial baseline at the design setting MFR 3. In other words, a 67% increase was necessary.

In conclusion, the MFR variation emphasizes that, aside from the considerably lower η_{aw} -level for identical MFR settings to axial inflow, the film cooling design performs very sensitive to these MFR changes. It is susceptible to significant local differences and uncooled areas in both the entrance and the downstream region and increased coolant mass flow is required to achieve a film cooling effectiveness at the same level as for the reference case.

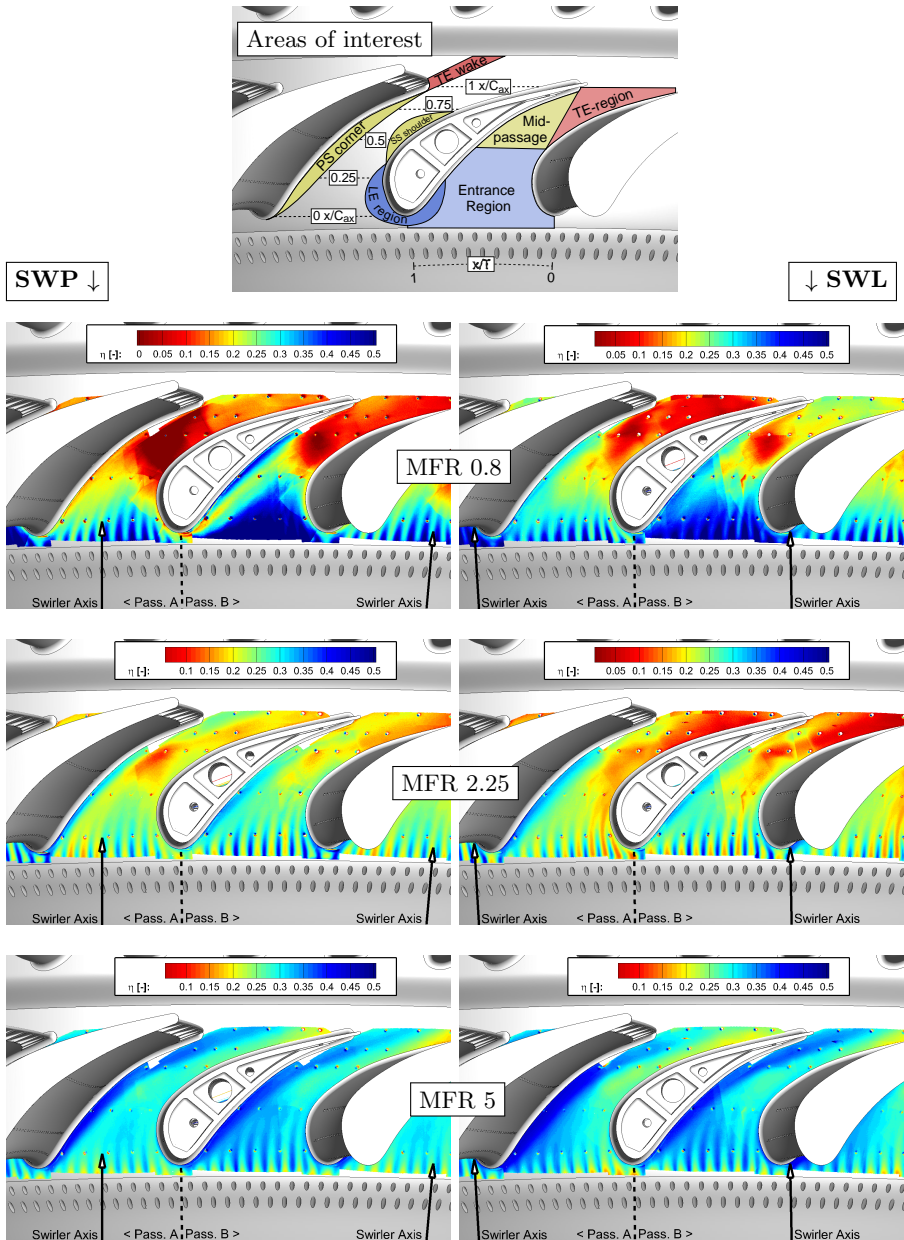


Figure 6.29: η_{aw} on NGV endwall fow SWP (left) and SWL (right) inflow and varied MFR

Comparison to endwall gas sampling measurements

In comparison with the infrared thermography (IR) contours, the gas concentration (GC) results for SWP clocking (Fig. 6.30) show a contribution of the airfoil film cooling on the endwall in the pressure side corner. In passage B, this region spreads further into the passage than for axial inflow⁶⁰ and reaches high cooling effectiveness values of up to $\eta_{aw}=0.5$. In passage A, there are as well differences between IR and GC measurements, but no significant level of film cooling is achieved by the pressure side coolant. In conclusion, this effect is strongly dependent on the inflow. The positive incidence at the hub on vane B assists the cooling contribution of the pressure side airfoil coolant. At the leading edge, it evokes a downward pressure gradient that assists the downwash of the coolant. In contrast, on vane A, the upward pressure gradient due to the negative incidence acts in the opposite way. For SWL the effect is observed similarly, but disappears already from MFR 1 on. Whereas the difference between IR and GC measurements decrease for MFR 1 in the pressure side corner, there appears a deviation in the TE-wake region on the endwall.

Similar to axial inflow, a deviation is detected between the two techniques in the midpassage area. For the observed low η_{aw} , the linear regression does not perform stable with the combined influence of the reflection in the camera image and the low slope of the regression curve.

6.4 Endwall heat transfer

The impact of swirling inflow on endwall heat transfer is discussed first using area-averaged results. They are compared to the axial inflow and the two clocking positions are analyzed. Second, the contour distributions on the endwall are investigated for a variation of the MFR.

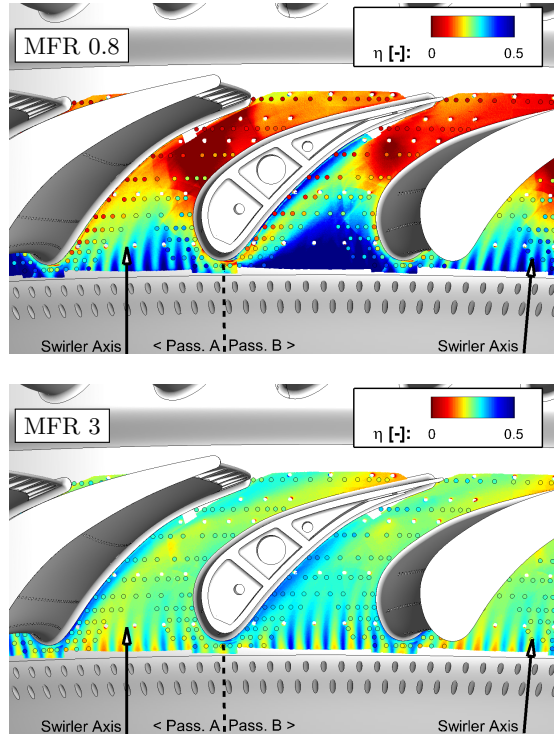


Figure 6.30: Comparison of IR (contours) and GC (data points) for SWP inflow

⁶⁰The contour for axial inflow is shown in Fig. 5.16

Comparison to axial inflow

Area-averaged values for the endwall heat transfer are presented in Fig. 6.31. In addition to the absolute value, the change in %-points is specified with respect to axial inflow and MFR 0.8. It is observed that initially, with applied swirl, the Nusselt numbers are increased by 25 % to 35 %. Lower values are determined for SWP clocking. Beginning from a MFR of 1.5 the Nusselt numbers increase significantly under the influence of the coolant injection. This influence becomes dominant and brings the Nusselt number of the axial inflow and swirling inflow to a similar level. Their characteristics follows roughly the same slope such until MFR 5. SWL is the clocking position with higher heat transfer in comparison to SWP. They remain about 5 % apart for medium and high MFR, whereby at MFR 0.8 and 1, SWL is determined up to 15 % greater. This underlines a dominant impact of the flow field on Nusselt numbers on the endwall. Finally, at MFR 5, the Nusselt numbers have increased by 80 % from the initial value for all inflow configurations.

The reason for the initial difference between axial and swirling inflow is the higher effective Mach number near the wall that in turn increases the Nusselt numbers. This is caused by the radial mass flow redistribution towards the endwalls. At low MFR, where the coolant impact is not predominant, in addition the impact of the flow field is observed by differences between the two clocking positions. This aspect is addressed in detail with the contour distributions in the following. The influence of a variation of the MFR is studied as well. From a MFR of 1.5 on, the local impact of the coolant injection dominates over the influence of swirl.

Local effects and the influence of a MFR variation

Swirling inflow increases the endwall heat transfer in comparison to the axial inflow⁶¹ for low and medium MFR up to 1.5. The increase varies and lies between 10 % and 40 % compared to the axial baseline. This is mainly influenced by the increased inflow velocity to the turbine, which in turn is responsible for increased Nusselt numbers. In addition, the higher level of turbulence at turbine inlet caters for a thinned boundary layer. This has been observed with the 4HP in RE1 as well. Consequently, heat transfer increases in the entrance area. With increasing MFR however, the coolant injection dominates the Nusselt number level. Due to the associated production of small-scale turbulence and the CRVP patterns, a steep rise in endwall Nusselt numbers

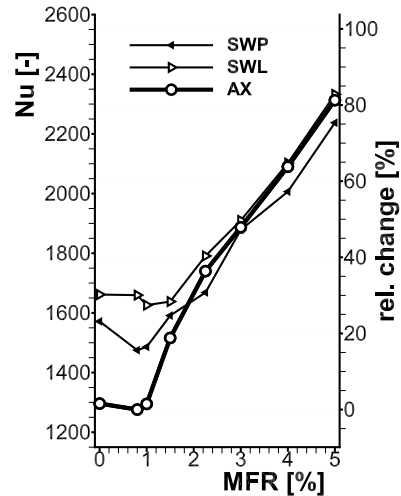


Figure 6.31: Area averaged Nusselt numbers for the NGV endwall

⁶¹The heat transfer results for axial inflow are shown in Fig. 5.20

is observed, similar to axial inflow. In this way, for MFR greater than 1.5 the level is of the same magnitude as in the axial baseline case. Local differences are observed with a Nusselt level that is either slightly greater or lower than for the reference at identical MFR. In the following, the details for both clocking positions are analyzed and discussed below.

The measurement results are shown in Fig. 6.32. Two general observations are made at low film cooling injection (MFR 0 to MFR 1.5): The heat transfer is increased in the entrance region in comparison to axial inflow. The mass flow redistribution increases the axial and effective Mach number in this region. In contrast, for the trailing edge region, similar values are detected. This is explained in turn with the similar effective Mach number at the vane exit. The mass flow redistribution is transported through the vane stage, but reduced turning results near the endwall⁶². Therefore, the effective velocity is at a comparable level to the axial inflow and the Nusselt numbers are at similar levels as well.

Furthermore, the results show more homogeneous Nusselt contours with applied swirl. A comparison of the near hole area for AX and SWL inflow for MFR 1 (Fig. 6.33) shows that instead of two local maxima per cooling hole, only one smeared peak is visible. The pitch wise spread of the maximum is increased. In this way, instead of a stripe pattern in the entrance area rather a gradient in flow direction is determined. This change is attributed to the higher turbulence intensity caused by the swirler. In this way, also the vortex pattern and the coolant injection itself fluctuates more, resulting in a smeared distribution. Increased fluctuations were observed in the infrared recordings, but the measurement method is not suitable to resolve them quantitatively.

Between passages A and B and the two clocking positions, differences are apparent especially for the uncooled case (MFR 0): For SWP clocking, passage A is measured with passage B with increased Nusselt numbers in the entrance area with respect to the average value for swirling inflow and this MFR. SWL clocking yields a more homogenous distribution between the two passages. The average for SWL thereby lies in between the values for SWP clocking. Schmid [112] observed such a heat transfer distribution among adjacent passages with a simulation of a linear cascade with counter-rotating swirl orientation. Given by the swirler to vane count of 1:1 in that study, adjacent passages were either exposed to a radial upward or downward flow at turbine inlet. The incidence of adjacent vanes in this way was similar to the present investigation. It is thereby concluded that the difference between the two passages is due to the counter-rotating vortices that have been observed in ME01. For SWP clocking i.e. if the main swirl ④ and counter-rotating vortex ⑥ pass through a vane passage each, peak and minimum heat transfer in adjacent vane passages occur. In particular vortex ⑥, which is close to the endwall, increases the heat transfer along its trajectory through passage B. Even though adjacent passages have a different level for SWP, the

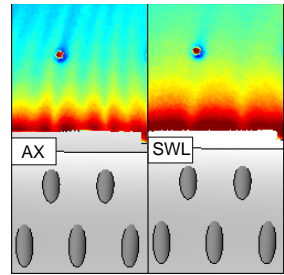


Figure 6.33: Comparison of Nusselt contours near the cooling holes, AX and SWL inflow at MFR 1

⁶²Refer to Fig. 6.15

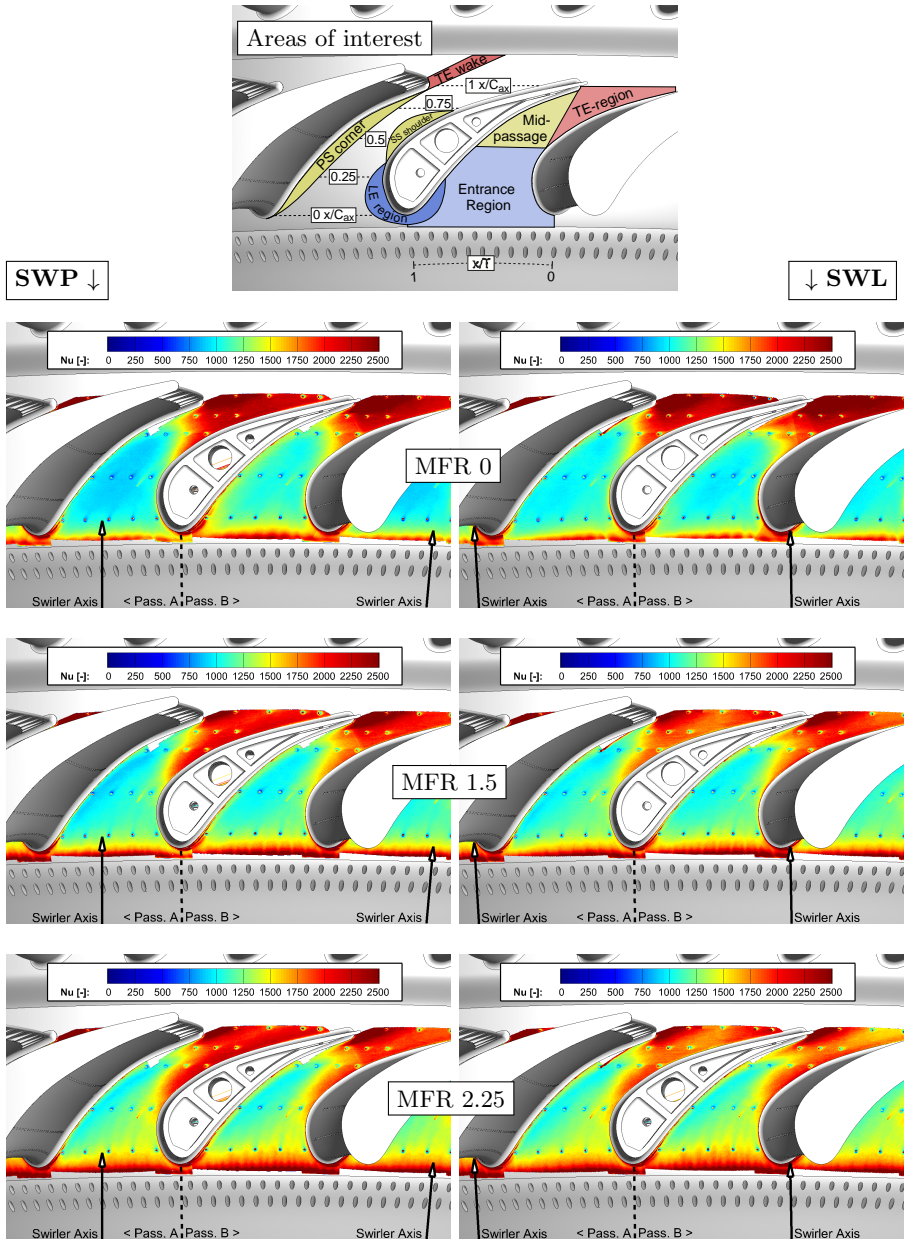


Figure 6.32: Nusselt numbers on NGV endwall fow SWP (left) and SWL (right) inflow and varied MFR

average for the two passages is lower than for SWL. Therefore this clocking position is preferential with respect to the thermal load.

The heat transfer contours are less sensitive to the change of the inflow situation than the film cooling effectiveness contours. Hence, the most important impact on endwall heat transfer remains the coolant injection. As mentioned, only up to a MFR of 1.5 increased differences between swirling and axial inflow are observed. With further increased MFR to 2.25 and more (contours not shown), the difference both between adjacent passages and the two clocking positions diminish. Instead, the heat transfer increase due to film cooling dominates the endwall contours and the level follows the one measured with axial inflow closely. Fig. 6.34 illustrates this in comparison for SWP and AX inflow at MFR 0 and MFR 3. The contours for axial inflow are repeated for this reason in the figure.

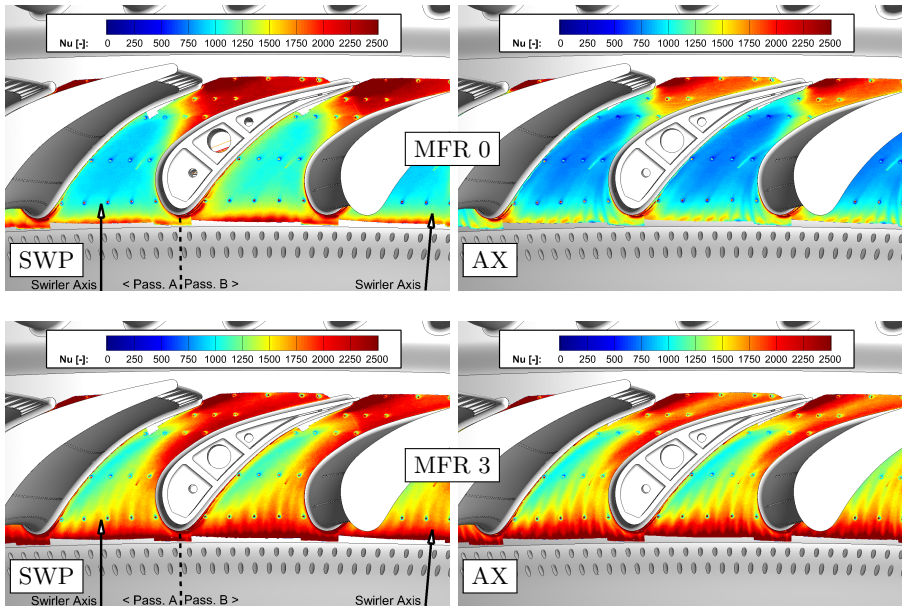


Figure 6.34: Comparison of Nusselt numbers for SWP (left) and AX (right) inflow at MFR 0 and MFR 3

6.5 Heat Flux Reduction due to film cooling

The two thermal parameters are analyzed combined in form of the heat flux reduction Θ . For swirling inflow this is intended as the measure to evaluate the film cooling design's robustness to the changed inflow. Consequently, the heat flux reduction is not calculated in comparison to the uncooled endwall for swirling inflow, but for axial

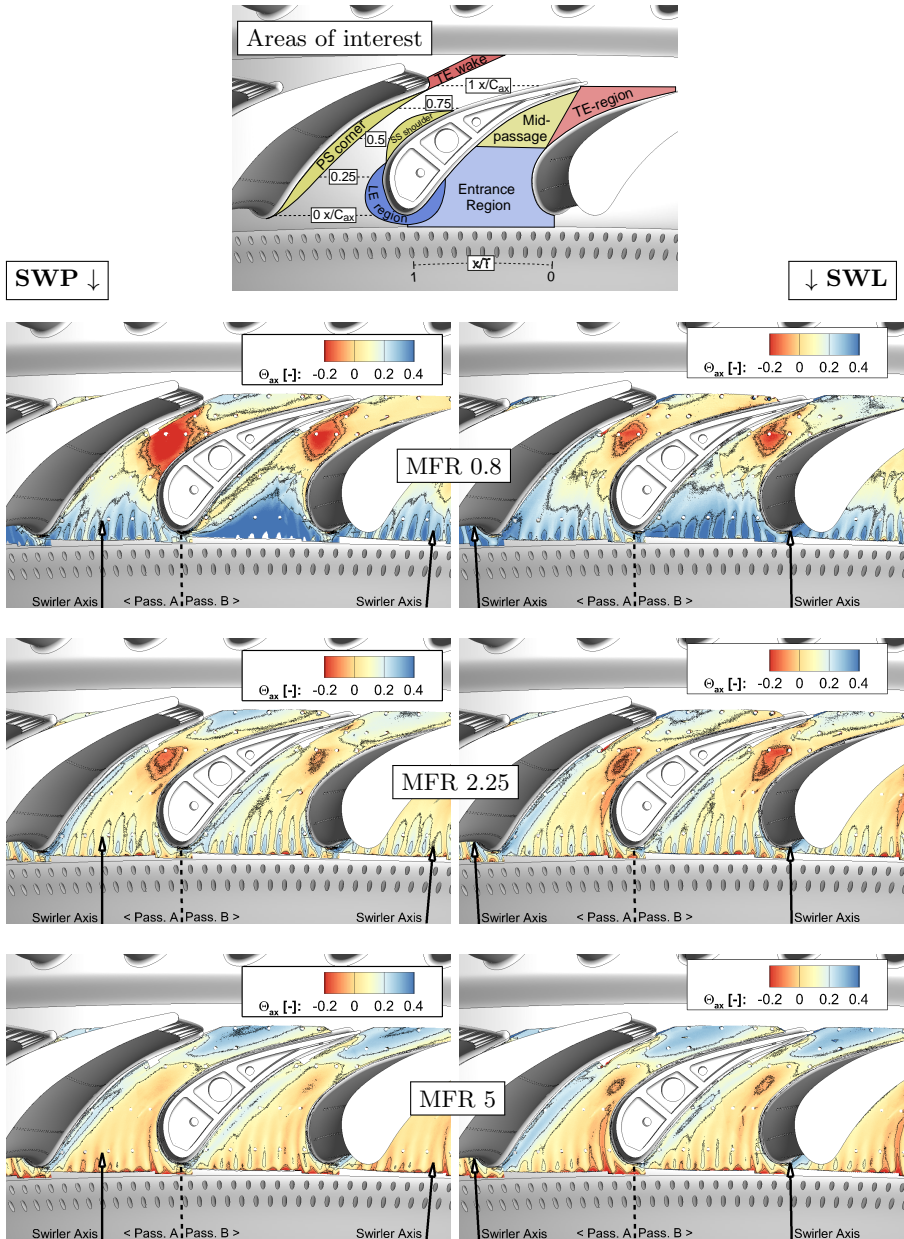


Figure 6.35: Heat flux reduction Θ_{ax} due to film cooling for swirling inflow with respect to the uncooled endwall for axial inflow

inflow. Therefore, the variable is denoted Θ_{ax} in the following. In this way, it can be visualized, which area of the endwall is subject to an increase in heat flux and for which areas the coolant design remains beneficial under the imposed thermal load with applied swirl. The color map contains a red bar that illustrates a value of $\Theta_{ax}=0$ which encircles these regions of a heat flux increase.

The contour distribution (Fig. 6.35) shows that in agreement with the findings for axial inflow⁶³, the heat flux reduction due to film cooling is significant where high film cooling effectiveness is achieved. In contrast to axial inflow both a significant reduction but also a heat flux increase is observed locally. This underlines the susceptibility of the film cooling design to swirling inflow. For low injection (MFR 0.8 shown exemplary), the entrance area is well cooled and a significant heat flux reduction occurs. Comparing passage A and B, the observed differences in the Nusselt numbers for SWP inflow cater for a variation in the heat flux reduction between the two passages.

Consequently, the reduction is greater in passage B up to MFR 1.5, where the two passages show a comparable level. Beginning at this injection setting, the simultaneous Nusselt number increase counteracts the further increase in η_{aw} . The pressure side corner, throat and trailing edge region receive an increasing benefit from the coolant injection, similar to axial inflow. On the other hand, near zero Θ_{ax} regions are observed and beginning from MFR 3, the Nusselt number increase is so great that an increase of heat flux occurs. Consequently, even though the Nusselt number is similar to axial inflow for these high injection settings, the radial mass flow redistribution due to swirl is decisive for an inferior performance of this cooling design with applied swirl.

Using Θ_{ax} to evaluate the design, low MFR show the better performance, because the attachment of the coolant to the wall in the entrance region is good and a significant reduction in heat flux is achieved. However, the downstream regions are scarcely cooled, and in consequence, there is no optimum. The pressure side corner and the trailing edge region are well covered by coolant for MFR of 2.25 and greater. This has the drawback of uncooled areas in the entrance region.

6.6 Summary of the findings for the swirling inflow case

Swirling combustor inflow has been investigated for two clocking positions. For the investigated counter-rotating swirl orientation relative to the vane turning direction, a significant influence on the flow field is observed. The **aerodynamic impact** on the turbine includes several findings:

- With global influence on the vane row, the mass flow is redistributed towards the endwalls due to the swirl-induced recirculation zone. In this way, the near-endwall velocity increases and a low-velocity zone appears in the central annulus.
- A vortex system develops at turbine inlet that follows the swirler clocking position with respect to the vane leading edge. In addition to the main vortices, in the interaction zone between adjacent swirlers, two counter-rotating vortices

⁶³The heat flux reduction due to film cooling for the axial inflow is shown in Fig. 5.21

appear. Their peak vorticity at turbine inlet is equal to two third main swirl peak vorticity.

- In consequence of this vortex system, the inflow boundary layer contains a low-velocity zone and is divided into sign-inverse whirl angle zones of $\pm 25^\circ$ for each half swirler pitch at turbine inlet.
- Negative incidence at one vane and positive incidence at the adjacent vane occurs. This is observed for both leading edge and passage clocking and alters the vane loading.
- In the exit flow field, clocking effects are observed. The contour is dominated by the inflow field and not by coolant flows.
- Mixing of coolant and main flow is enhanced and the concentration of coolant flows in the main annulus increases for identical injection settings.

The changes in the flow field influence the **endwall heat transfer and film cooling**. In particular, the following aspects are observed:

- As a result of the mass flow redistribution, η_{aw} decreases and Nu increases.
- The vortex system causes adjacent vane passages to vary. An upward flow upstream of one passage and a downward flow in the adjacent passage is determined which decreases and increases the film cooling effectiveness by turns.
- Locally, the trajectory of individual coolant jets follows the inflow whirl angle. The first row jets approach the second row jets and a detrimental interaction occurs. The impact is limited to the immediate vicinity of the jets and varies locally.
- Because of the sensitivity to the inflow situation and injection setting, the film cooling coverage of the endwall varies strongly within the range of the investigated parameters. This goes in line with a variation of the heat flux reduction due to film cooling. Increased heat flux is observed in the downstream regions at low MFR and in the entrance region between second row coolant streaks for high MFR.

Based on the results, a **design recommendation** for a swirler to vane count of 1:2 is given:

- Passage clocking (SWP) is preferential regarding the thermal load of the endwall. In this way, the heat flux reduction with film cooling is greater. Endwall heat transfer is lower than for SWL clocking and the film cooling effectiveness is improved.

In addition the following aspects are relevant to the design, but are not in the focus of this investigation:

- The main swirl core is transported further toward the casing for SWL. This happens because of the incidence at the vane which is impacted by the swirl. The resulting swirl trajectory may have an influence on the cooling of the casing side and as well be relevant for rotor tip cooling.

The investigated **design** is **robust** to swirling inflow in the sense that it achieves a significant heat flux reduction in the pressure side corner and trailing edge regions. In contrast to axial inflow, the entrance and mid-passage region show a moderate increase of the heat flux in between coolant streaks. Because of the reduction of η_{aw} by 20%, the increase in Nusselt numbers cannot be compensated under the influence of the coolant injection.

- The film cooling design behaves similar to axial inflow and therefore it is expected that an optimization for axial inflow is suitable to improve the film cooling effectiveness for swirling inflow as well (Werschnik et al. [139]). The high-momentum injection cases demonstrate that this film cooling design is a good option to cool the pressure side corner and trailing edge regions, both crucial for the design.
- Only for low MFR up to MFR 1.5, Nusselt numbers increase additionally under the influence of swirling inflow. From MFR 2.25 on, the level remains similar to axial inflow. The endwall heat transfer becomes dominated by the coolant injection and is robust to the change of the inflow.
- With the measurements it has been shown that even though for some injection settings uncooled areas appear, a coolant contribution of the pressure side airfoil compensates this in the pressure side corner. This effect is strongly dependent on the inflow and in consequence varies strongly with applied swirl. Positive incidence acts favorable on this aspect and assists the downwash of the coolant by the spanwise downward pointing pressure gradient at the hub.

7 Summary and Outlook

The development of new gas turbines and aero engines is more and more dedicated to reduce pollutant emissions in addition to the continuous strive to improve component efficiency and reduces the consumption of fossil fuels. To foster this change in paradigms, new combustion concepts have come into play such as lean combustion. Whereas the emission of carbon dioxide can also be reduced by a reduced fuel consumption, a further reduction of nitrogen oxide emissions can only be achieved by a leaner fuel-to-air mixture. The formation of nitrogen oxides is hindered by lower peak temperatures and avoiding stoichiometric concentrations in the combustion chamber. This combustion process however is stabilized by swirl. As a result a recirculation zone and a redistribution of mass flow to the endwalls occurs. Additionally, a flatter temperature profile due to the reduced injection of dilution air in the combustor approach the subsequent turbine stage. Associated, turbine design is challenged by incidence, high turbulence intensities and increased thermal load to the endwalls.

To assist in the understanding of the complex aerodynamic and aerothermal interactions, the aerodynamic impact of combustor swirl on the nozzle guide vane stage of a turbine is investigated at the Large Scale Turbine Rig (LSTR) in Darmstadt in a 1.5-stage turbine stage that is subject to an engine-representative swirl. A combustor simulator is used to vary the inflow to the turbine to evaluate the robustness of its endwall film cooling design and to investigate endwall heat transfer and film cooling effectiveness experimentally using infrared thermography and the auxiliary wall method.

Axial, low-turbulent inflow to the turbine stage is investigated as a reference. A variation of the coolant mass flow rate from 0% to 5% of the main flow is studied to understand the influence on the flow field. The flow in the vane row is influenced by the coolant injection. The high momentum caters for a reversed direction of the cross flow near the endwall. An additional vortex develops at the leading edge and is transported to higher span and into the passage. In addition, there is also a significant contribution of the trailing edge coolant on the vane row losses. An increase of Nusselt numbers by 80% is observed with a concurrent increase of the film cooling effectiveness level by 25%. In combination a significant heat flux reduction by 30% due to film cooling is achieved. A low injection MFR of one shows the greatest benefit. For higher MFR the further improvement of the film cooling effectiveness is counteracted by the even greater increase in heat transfer.

With applied swirl, the flow field changes significantly at turbine inlet: Averaged whirl angles of 15 to 20° and a mass flow redistribution to the endwalls are detected. This has a predominant influence on the vane flow field and increases the pressure loss in the row by 30% compared to axial inflow and an identical MFR of 3. The two clocking positions SWL and SWP do not show differences in the level. In the interaction zone between adjacent main swirl vortices two additional, counter-rotating vortices are formed. They have a vorticity of two thirds of the main swirl and alter the

flow field at turbine inlet. Near the hub, alternating negative and positive incidence and flow angles of $\pm 25^\circ$ occur. In the pressure loss contour, these vortices can be identified. They are transported differently through the vane passage, whereby for SWL clocking the swirl core is transported further towards the casing.

The mixing of coolant flow and main stream is enhanced and more RIDN coolant air is detected in the main annulus. An increase in Nusselt numbers by 40 % is observed, while the film cooling effectiveness is reduced by up to 30 %. For MFR greater than 1.5, the increase in Nusselt numbers compared to the baseline case is smaller and eventually the heat transfer remains at a similar level to the reference case. To achieve the same level of film cooling, the coolant MFR has to be practically doubled. On the other hand, the heat flux reduction due to film cooling shows a greater benefit for MFR of 1 and 1.5, whereas the benefit for higher MFR is counteracted by the increase in Nusselt numbers. These general trends are resolved for both clocking positions whereby local differences occur.

Three main factors of influence have been identified whereby the spatial zone of influence differs. A global impact on the thermal load of the endwall occurs due to the mass flow redistribution towards the endwall. This is responsible for the general reduction of the film cooling effectiveness because not enough coolant air is injected into the near wall flow for an identical mass flow setting. In addition, the effective velocity near the wall increases in this way and explains the increase in Nusselt numbers for low MFR. For MFR 1.5 and greater, the increase under the influence of the film cooling injection is even greater such that a diminishing difference to axial inflow is observed.

The described vortex system due to swirl influences the thermal load and caters for differences between adjacent passages. The orientation of the vortices results in an upward or downward tendency of the flow and thereby enhances or deteriorates the film cooling performance. Passage clocking is beneficial on one hand based on the averaged level of film cooling effectiveness and Nusselt numbers. However, with respect to the Nusselt numbers, differences between adjacent passages are greater in the case of SWL clocking. In addition, the incidence at turbine inlet means that for example the region near the SS in the downstream region of the endwall is poorly cooled.

On the smallest scale, the trajectory of individual coolant jets is altered by the whirl angle profile at the inlet. The first row coolant jets approach the second row's jets in agreement with the whirl angle in the inflow. Thereby, they appear nearly on top of each other and a detrimental interaction of their vortex system reduces the film cooling effectiveness locally.

A heat flux reduction due to the film cooling is observed with applied swirl as well. It is about 50 % lower on average for the same MFR. The design is very susceptible to MFR changes and especially the local level of film cooling effectiveness and thereby Θ_{ax} varies strongly.

The robustness of the design to the change of the inflow is evaluated for applied swirl. It is observed that the well-cooled areas for axial inflow are well-cooled as well for swirling inflow. Due to the significant decrease of the film cooling effectiveness however, the improvement to the uncooled wall is small. In the entrance area, the increase of the Nusselt number under the influence of the coolant injection cannot be compensated and locally increasing heat flux is observed. A contribution of the

pressure side airfoil coolant has been determined for axial inflow. This effect is observed with swirling inflow as well. However, it is strongly dependent on the inflow. Whereby it can be enhanced by positive incidence and the imposed downward pressure gradient at the leading edge, a reduction of the effect is observed for leading edge swirl. The coolant injection for MFR 2.25 enhances the Nusselt numbers to a level similar to axial inflow. In this way, the design is robust to the incoming swirl because it shields the endwall from an additional increase that is observed for the uncooled endwall and low MFR up to 1.5.

7.1 Suggestions for further research

To build on the work presented, the investigation of combustor-turbine interaction can be continued within the turbine stage. On one hand, based on the results obtained, the NGV stage can be optimized to cope with the imposed flow situation. A relevant concern is the robustness of such an optimization process, given that small uncertainties in the combustor outflow profile exist in the real engine and consequently should be investigated simultaneously. On the other hand, the investigation of the effects of applied swirl especially on the rotor row is a suitable focus for a further investigation. Together with the flow field investigation the performance of the full stage should be investigated and the associated influence on turbine efficiency can be measured. In the following, all suggestions and possible approaches will be discussed briefly.

Robustness of an optimized vane row for swirling inflow

Building on the observed flow field impact of the swirler, the vane row can be optimized to cope with the observed changes. There are two aspects that can be addressed. On one hand, the thermal point of view is a focus and an optimization of the film cooling design to increase the film cooling effectiveness while limiting the Nusselt number increase should be desired. Whereas several approaches exist in the literature (Abdelmohimen [1], Heidmann and Ekkad [57], Dittmar et al. [35]). Many approaches, such as fan-shaping aim on reducing the momentum of the coolant. The intention is to keep it close to the wall whereby a high mass flow is injected. Mixing losses are reduced as well due to the lowered injection velocity. As it was shown in this investigation, adequate coolant momentum is necessary to cool the whole endwall. Because of the low initial film cooling effectiveness associated to the first row of holes, they should be the focus of an optimization. Of any optimized design, its robustness towards inflow variations such as swirling inflow should be investigated, where on the other hand a high coolant jet momentum can be beneficial.

The other aspect that can be addressed is the aerodynamic optimization of the vane with an adapted geometry. Both the aerodynamic and the thermal benefit of such a design needs to be evaluated. Panchal et al. [102] and Kneer et al. [76] have shown approaches dedicated to reducing endwall heat transfer, also taking into account the endwall cooling. Optimized vane row geometries have been designed and investigated numerically by Shahpar and Caloni [121], with an adapted design for a adapted vane geometry. A new approach is presented by Wang et al. [132] with the vane row design oriented on the flow path rather than on optimizing an existing vane and endwall geometry.

Any optimization however has the drawback that it may only work in favor when the inflow conditions are close to the expected profile, which was used as input to the optimization process. A relevant question is therefore in any case the robustness of such a design to inflow deviations. Similar to the film cooling design in this study, an experimental investigation of an optimized endwall geometry addressing these questions can be used to evaluate a numerical approach that yields the optimized endwall contour. A superior design under optimized conditions might perform inferior, when the boundary conditions change. In the development process of an engine, the predicted and actual combustor outflow traverse differ and is subject to uncertainty and a design needs to be carefully studied. Thomas [126] and Schneider and Schiffer [115] investigate this problem numerically and highlight the importance of this approach. An experimental validation can give additional insight and can be used as a validation.

Interaction between the vane row coolant flows

An interdependency is observed between the different vane row coolant flows. In the case of an overturning of the RIDN injection flows to the suction side for low momentum injection settings, the airfoil coolant compensates this and cools the endwall in the pressure side corner. In addition, in the vane exit flow plane, it is observed that the trailing edge coolant is radially shifted outward from the hub endwall, when more RIDN air is injected. Therefore, the design of a vane row cooling scheme should take this influence of platform coolant injection on airfoil coolant injection into account. An optimized scheme can be developed when this influence is known. Swirling inflow brings in additional parameters that need to be considered.

Unsteady effects of combustor-turbine interaction

Whereas an understanding of the steady influence of combustor swirl on the vane row could be achieved with the present investigation, the unsteady effects of combustor-turbine interaction should be considered as well. Jacobi et al. [64] have shown an unsteady influence of vortex systems and resulting unsteady variations of the local heat transfer level. Furthermore, the rotor passes through an alternating flow field coming from the vane row. Pressure losses and the radial mass flow distribution depend largely on clocking and cater for deviations between alternating passages. For this reason, unsteady effects with respect to rotor cooling are expected as well.

Impact on rotor row and stage efficiency

It has been observed that the mass flow redistribution due to swirl persists through the vane row and is transported into the rotor. Additional changes such as the observed local span wise underturning or overturning should be investigated. Even though they are limited and a HPT rotor design can cope with them, the influence on aerodynamic loading and associated losses within the row are an important aspect that should be addressed. It has been shown that the swirling inflow generates additional pressure loss. Furthermore, the radial mass flow redistribution persists at the vane exit and enters the rotor row. For a combustor-vane count of 1:2, the thermal load is lower with passage clocking. The flow field impact on the stage turbine efficiency should

be studied and another clocking position might be beneficial. Schmid's [112] findings agree with the present investigation with respect to the thermal endwall load but reveal a greater efficiency for leading edge centered swirl.

Influence of the interdependence between the combustor geometry, vane turning orientation and swirler orientation on the trajectory of the swirler core

Combustor-turbine investigations by Insinna et al. [62] and Vagnoli [129] mentioned the migration of the swirler core within the combustor. Investigations with linear geometry do not show this variations in the trajectory. They state a gyroscopic effect and a momentum imbalance due to the annular geometry as reasons for their observation, but additional insight is required to explain this behavior fully. The phenomenon is design relevant because it is responsible for an uncertainty component in the trajectory of the swirler core. Thereby, it is a factor of influence on the hot-streak within the combustor and on endwall temperatures in the engine.

The explanation of the phenomenon has been expanded in this thesis for annular geometries, stating that this momentum imbalance is already introduced to the flow by the swirler. Responsible boundary conditions, such as the combustor geometry, the swirler orientation in respect to the vane turning orientation or the main flow and wall inclination can be varied to identify phenomena and to quantify the depicted interdependence. A numerical simulation is the most suitable tool for such an investigation.

Bibliography

- [1] Abdelmohimen MAH (2015) Numerical investigation of film cooling from two rows of holes with anti-vortex holes attached to the upstream row. In: International Journal of Engineering and Technology Innovation, vol 5, pp 87–98 (84), (123)
- [2] ACARE - Advisory Council for Aviation Research and Innovation in Europe (2011) Flightpath 2050 - europe's vision for aviation (3)
- [3] Airbus SAS (2016) Global market forecast 2016 (3)
- [4] Andreini A, Bacci T, Insinna M, Mazzei L, Salvadori S (2016) Hybrid rans-les modeling of the aero-thermal field in an annular hot streak generator for the study of combustor-turbine interaction: Gt2016-56583. In: ASME Turbo Expo 2016 (10)
- [5] Andreini A, Becchi R, Facchini B, Mazzei L, Picchi A, Turrini F (2016) Adiabatic effectiveness and flow field measurements in a realistic effusion cooled lean burn combustor. Journal of Engineering for Gas Turbines and Power 138(3):031,506, DOI 10.1115/1.4031309 (87)
- [6] Andreopoulos J, Rodi W (1984) Experimental investigation of jets in a crossflow. Journal of Fluid Mechanics 138(-1):93, DOI 10.1017/S0022112084000057 (18), (19)
- [7] Apell N (2016) Einfluss der verdrallten Brennkammerströmung auf die Kühlluftausblasung der Statorstufe einer Turbine: engl: Influence of swirling combustor inflow on the coolant injection in a stator stage of a turbine. Bachelor's thesis, Technische Universität Darmstadt, Darmstadt (57)
- [8] Arne V (2016) Experimental analysis of the boundary layer profile to the nozzle guide vane stage of a high pressure turbine under the influence of coolant injection: Untersuchung des Grenzschichtprofils in der Zuströmung der ersten Leitschaufelreihe einer Hochdruckturbine unter dem Einfluss von Kühlluft einblasung. Bachelor's thesis, Technische Universität Darmstadt, Darmstadt (55)
- [9] Arts T, Lambert de Rouvroit M (1992) Aero-thermal performance of a two-dimensional highly loaded transonic turbine nozzle guide vane: A test case for inviscid and viscous flow computations. Journal of Turbomachinery 114(1):147, DOI 10.1115/1.2927978 (13)
- [10] Bacci T, Caciolli G, Facchini B, Tarchi L, Koupper C, Champion JL (2015) Flowfield and temperature profiles measurements on a combustor simulator dedicated to hot streaks generation. In: ASME Turbo Expo 2015: Turbine Technical Conference and Exposition, p V05CT17A001, DOI 10.1115/GT2015-42217 (11), (13)

- [11] Bacci T, Facchini B, Picchi A, Tarchi L, Koupper C, Champion JL (2015) Turbulence field measurements at the exit of a combustor simulator dedicated to hot streaks generation. In: ASME Turbo Expo 2015: Turbine Technical Conference and Exposition, p V05CT17A002, DOI 10.1115/GT2015-42218 (11), (86)
- [12] Baldauf S (2001) Filmkühlung thermisch höchstbelasteter Oberflächen: Korrelation thermographischer Messungen: Univ., Diss–Karlsruhe, 2001, Forschungsberichte aus dem Institut für Thermische Strömungsmaschinen / Universität Karlsruhe (TH), vol 12. Logos-Verl., Berlin (14), (15), (25), (26), (27), (28), (29), (74), (78), (83)
- [13] Baldauf S, Schulz A, Wittig S (2001) High-resolution measurements of local heat transfer coefficients from discrete hole film cooling. *Journal of Turbomachinery* 123(4):749, DOI 10.1115/1.1387245 (26)
- [14] Baldauf S, Scheurlen M, Schulz A, Wittig S (2002) Correlation of film-cooling effectiveness from thermographic measurements at enginelike conditions. *Journal of Turbomachinery* 124(4):686, DOI 10.1115/1.1504443 (15), (16), (108)
- [15] Baldauf S, Scheurlen M, Schulz A, Wittig S (2002) Heat flux reduction from film cooling and correlation of heat transfer coefficients from thermographic measurements at enginelike conditions. *Journal of Turbomachinery* 124(4):699, DOI 10.1115/1.1505848 (19), (26)
- [16] Baumann S (2014) Design and implementation of a measurement technique for the analysis of unsteady aerodynamic effects at the large scale turbine rig and experimental validation of a turbulence generator module: Auslegung und Implementierung einer Messtechnik für instationäre Aerodynamikuntersuchungen am Turbinenversuchsstand LSTR und experimentelle Validierung eines Turbulenzerzeugermoduls. Master's thesis, Technische Universität Darmstadt, Darmstadt (169)
- [17] Beard PF, Smith A, Povey T (2013) Impact of severe temperature distortion on turbine efficiency. *Journal of Turbomachinery* 135(1):011,018, DOI 10.1115/1.4006389 (10)
- [18] Benton R, Rabe G, Schiffer HP, Berg P (2005) Ballistic cooling of turbine nozzle guide vane platforms: Isabe 2005-1113. In: International Society of Air Breathing Engines (Hg.) 2005 – Proceedings of the ISABE 2005 (21), (80)
- [19] Bernsdorf S, Rose MG, Abhari RS (2005) Modelling of film cooling: Part i — experimental study of flow structure. In: ASME Turbo Expo 2005: Power for Land, Sea, and Air, pp 677–687, DOI 10.1115/GT2005-68783 (19), (25)
- [20] Blair MF (1974) An experimental study of heat transfer and film cooling on large-scale turbine endwalls. *Journal of Heat Transfer* 96(4):524, DOI 10.1115/1.3450239 (23), (25)
- [21] Bogard DG, Thole KA (2006) Gas turbine film cooling. *Journal of Propulsion and Power* 22(2):249–270, DOI 10.2514/1.18034 (17)

- [22] Bräunling WJG (2015) Flugzeugtriebwerke: Grundlagen, Aero-Thermodynamik, ideale und reale Kreisprozesse, thermische Turbomaschinen, Komponenten, Emissionen und Systeme, 4th edn. VDI-Buch, Springer Vieweg, Berlin, DOI 10.1007/978-3-642-34539-5, URL <http://dx.doi.org/10.1007/978-3-642-34539-5> (2), (14)
- [23] Bunker RS (2006) Gas turbine heat transfer: 10 remaining hot gas path challenges. In: ASME Turbo Expo 2006: Power for Land, Sea, and Air, pp 1–14, DOI 10.1115/GT2006-90002 (8), (84)
- [24] Bunker RS (2009) Film cooling: breaking the limits of diffusion shaped holes. In: International Symposium on Heat Transfer in Gas Turbine Systems (15)
- [25] Burd SW, Kaszeta RW, Simon TW (1998) Measurements in film cooling flows: Hole l/d and turbulence intensity effects. *Journal of Turbomachinery* 120(4):791, DOI 10.1115/1.2841791 (16)
- [26] Burdet A, Abhari RS (2006) 3d flow prediction and improvement of holes arrangement of a film-cooled turbine blade using a feature-based jet model. In: ASME Turbo Expo 2006: Power for Land, Sea, and Air, pp 849–863, DOI 10.1115/GT2006-91073 (17), (105)
- [27] Burdet A, Abhari RS, Rose MG (2005) Modeling of film cooling: Part ii — model for use in 3d cfd. In: ASME Turbo Expo 2005: Power for Land, Sea, and Air, pp 663–676, DOI 10.1115/GT2005-68780 (18)
- [28] Butler T, SHARMA OP, JOSLYN HD, DRING RP (1989) Redistribution of an inlet temperature distortion in an axial flow turbine stage: *Journal of Propulsion and Power* 5(1):64–71, DOI 10.2514/3.23116 (11)
- [29] Cha CM, Hong S, Ireland PT, Denman P, Savarianandam V (2012) Experimental and numerical investigation of combustor-turbine interaction using an isothermal, nonreacting tracer. *Journal of Engineering for Gas Turbines and Power* 134(8):081,501, DOI 10.1115/1.4005815 (11), (13), (14)
- [30] Cha CM, Ireland PT, Denman PA, Savarianandam V (2012) Turbulence levels are high at the combustor-turbine interface. In: ASME Turbo Expo 2012: Turbine Technical Conference and Exposition, p 1371, DOI 10.1115/GT2012-69130 (13)
- [31] Chavez K, Slavens T, Bogard DG (2016) Effects of internal and film cooling on the overall effectiveness of a fully cooled turbine airfoil with shaped holes: Gt2016-57992. In: ASME Turbo Expo 2016 (27)
- [32] Colban WF, Lethander AT, Thole KA, Zess G (2003) Combustor turbine interface studies—part 2: Flow and thermal field measurements. *Journal of Turbomachinery* 125(2):203, DOI 10.1115/1.1561812 (22)
- [33] Colban WF, Thole KA, Zess G (2003) Combustor turbine interface studies—part 1: Endwall effectiveness measurements. *Journal of Turbomachinery* 125(2):193, DOI 10.1115/1.1561811 (22), (49), (163)

- [34] Cresci I, Ireland PT, Bacic M, Tibbott I, Rawlinson A (2015) Velocity and turbulence intensity profiles downstream of a long reach endwall double row of film cooling holes in a gas turbine combustor representative environment. In: ASME Turbo Expo 2015, p V02BT40A002, DOI 10.1115/GT2015-42307 (13), (17), (75)
- [35] Dittmar J, Schulz A, Wittig S (2003) Assessment of various film-cooling configurations including shaped and compound angle holes based on large-scale experiments. *Journal of Turbomachinery* 125(1):57, DOI 10.1115/1.1515337 (17), (123)
- [36] Dittmar J, Schulz A, Wittig S (2004) Adiabatic effectiveness and heat transfer coefficient of shaped film cooling holes on a scaled guide vane pressure side model. *The International Journal of Rotating Machinery* 10(5):345–354, DOI 10.1080/10236210490474458 (17)
- [37] Dückershoff R (2004) Filmkühlung in Gebieten mit verzögerter Hauptströmung und in Bereichen lokaler Strömungsablösung: (engl.: "film cooling in areas of decelerated main flow and in areas of local separation"). Dissertation, Aachen (16), (18)
- [38] Eitenmüller J (2016) Experimentelle Untersuchung der Statorzuströmung einer Axialturbine unter Anwendung der Particle Image Velocimetry: engl.: Experimental investigation of the nozzle guide vane inlet flow field of an axial turbine with particle image velocimetry. Master's thesis, Technische Universität Darmstadt, Darmstadt (63)
- [39] Feiereisen J, Paolillo R, Wagner J (2000) UTRC turbine rim seal ingestion and platform cooling experiments. In: 36th AIAA/ASME/SAE/ASEE Joint Propulsion Conference and Exhibit, DOI 10.2514/6.2000-3371 (50)
- [40] Fric TF, Roshko A (1994) Vortical structure in the wake of a transverse jet. *Journal of Fluid Mechanics* 279(-1):1, DOI 10.1017/S0022112094003800 (18)
- [41] Friedrichs S (1997) Aerodynamic aspects of endwall film-cooling. *Journal of Turbomachinery* 119(4):786, DOI 10.1115/1.2841189 (15), (20), (24), (25), (50), (54), (70)
- [42] Friedrichs S (1997) Endwall film cooling in axial flow turbines. Dissertation, Cambridge University, Cambridge (50)
- [43] Giel PW (1999) Blade heat transfer measurements and predictions in a transonic turbine cascade 1999-209296 (24), (47)
- [44] Giel PW, Thurman DR, van Fossen GJ, Hippensteele SA, Boyle RJ (1996) End-wall heat transfer measurements in a transonic turbine cascade. NASA Technical Memorandum 107387 (24), (47)
- [45] Giel PW, Boyle RJ, Bunker RS (2004) Measurements and predictions of heat transfer on rotor blades in a transonic turbine cascade. *Journal of Turbomachinery* 126(1):110, DOI 10.1115/1.1643383 (13)

- [46] Giller L (2015) Einfluss der drallbehafteten Brennkammerströmung auf die Hochdruckturbine: (engl.: "film cooling in areas of decelerated main flow and in areas of local separation"). Dissertation, Technische Universität Darmstadt, Darmstadt (4), (8), (11), (36), (86), (88), (95)
- [47] Goldstein RJ (1971) Film cooling. In: *Advances in Heat Transfer*, vol 7 (23), (47)
- [48] Goldstein RJ, Spores RA (1988) Turbulent transport on the endwall in the region between adjacent turbine blades. *Journal of Heat Transfer* 110(4a):862, DOI 10.1115/1.3250586 (19), (20), (23), (24), (25)
- [49] Graziani RA, Blair MF, Taylor JR, Mayle RE (1980) An experimental study of endwall and airfoil surface heat transfer in a large scale turbine blade cascade. *Journal of Engineering for Power* 102(2):257, DOI 10.1115/1.3230246 (24), (25)
- [50] Griffini D, Insinna M, Salvadori S, Martelli F (2015) On the effects of inlet swirl on adiabatic film cooling effectiveness and net heat flux reduction of a heavily film-cooled vane. In: *International Society of Air Breathing Engines* (ed.) *Proceedings of the ISABE 2015* (27)
- [51] Griffini D, Insinna M, Salvadori S, Martelli F (2016) Clocking effects of inlet nonuniformities in a fully cooled high-pressure vane: A conjugate heat transfer analysis. *Journal of Turbomachinery* 138(2):021,006, DOI 10.1115/1.4031864 (9), (10)
- [52] Gritsch M, Baldauf S, Martiny M, Schulz A, Wittig S (1999) The superposition approach to local heat transfer coefficients in high density ratio film cooling flows. In: *ASME 1999 International Gas Turbine and Aeroengine Congress and Exhibition*, p V003T01A048, DOI 10.1115/99-GT-168 (23), (47)
- [53] Gupta AK, Lilley DG, Syred N (1985) Swirl flows, repr edn. *Energy and engineering science series*, Abacus Pr, Tunbridge Wellsu.a. (35), (36), (37)
- [54] Hada S, Thole KA (2011) Computational study of a midpassage gap and upstream slot on vane endwall film-cooling. *Journal of Turbomachinery* 133(1):011,024, DOI 10.1115/1.4001135 (166)
- [55] Hall BF, Chana KS, Povey T (2014) Design of a nonreacting combustor simulator with swirl and temperature distortion with experimental validation. *Journal of Engineering for Gas Turbines and Power* 136(8):081,501, DOI 10.1115/1.4026809 (11)
- [56] Han S, Goldstein RJ (2007) Heat transfer study in a linear turbine cascade using a thermal boundary layer measurement technique. *Journal of Heat Transfer* 129(10):1384, DOI 10.1115/1.2754972 (23)
- [57] Heidmann JD, Ekkad S (2008) A novel antivortex turbine film-cooling hole concept. *Journal of Turbomachinery* 130(3):031,020, DOI 10.1115/1.2777194 (84), (123)

- [58] Hennecke DK, Wörrlein K (2000) *Flugantriebe und Gasturbinen*. Skriptum, Technische Universität Darmstadt, Darmstadt (7)
- [59] Herrmann J (2016) Flow tracing of the hub side coolant injection in the nozzle guide vane row of a high pressure turbine: Bestimmung der Ausbreitung der nabenseitigen Kühlluft einblasung in der ersten Leitschaufelreihe einer Hochdruckturbinen. Bachelor's thesis, Technische Universität Darmstadt, Darmstadt (51), (52)
- [60] Hilgert J, Bruscheck M, Werschnik H, Schiffer HP (2017) Numerical studies on combustor-turbine interaction at the large scale turbine rig (lstr): Gt2017-64504. In: ASME Turbo Expo 2017, vol 2017 (66), (74), (85), (93), (97), (101)
- [61] Huang Y, Yang V (2009) Dynamics and stability of lean-premixed swirl-stabilized combustion. *Progress in Energy and Combustion Science* 35(4):293–364, DOI 10.1016/j.pecs.2009.01.002 (8)
- [62] Insinna M, Salvadori S, Martelli F (2014) Simulation of combustor/ngv interaction using coupled rans solvers: Validation and application to a realistic test case. In: ASME Turbo Expo 2014: Turbine Technical Conference and Exposition, p V02CT38A010, DOI 10.1115/GT2014-25433 (11), (13), (86), (125)
- [63] Ivanov D (2017) Numerische Untersuchung der Sensitivität von Filmkühlung in Hochdruckturbinen gegenüber Variation der Zuströmbedingung: engl.: Numerical Investigation of the Sensitivity of Film Cooling Designs in High Pressure Turbines against Variation of Inlet Conditions. Master's thesis, Technische Universität Darmstadt, Darmstadt (52)
- [64] Jacobi S, Mazzoni C, Chana K, Rosic B (2016) Investigation of unsteady flow phenomena in first vane caused by combustor flow with swirl: Gt2016-57358 (8), (9), (11), (124)
- [65] Joint Committee for Guides in Metrology (2008) *Evaluation of measurement data - guide to the expression of uncertainty in measurement* (48)
- [66] Kaiser E (1981) *Zur Wärmestrommessung an Oberflächen unter besonderer Berücksichtigung von Hilswand-Wärmestromaufnehmern: engl.: On surface heat flux measurement with special regard to auxiliary wall heat flux sensors*. Dissertation, Dresden (24)
- [67] Kegalj M (2013) *Hochaufgelöste strömungsfeldvermessungen in der rotorpassage einer niedermachzahl-turbine für verschiedene schaufelspitzengeometrien*. Dissertation, Technische Universität Darmstadt, Darmstadt (86)
- [68] Kegalj M, Winter N, Schiffer HP, Pyliouras S, Täge J (2007) Through flow modelling of a modern turbine stator cooling system. In: *Proceedings of the 8th International Symposium on Experimental and Computational Aerothermodynamics of Internal Flows*, vol ISAI8-0052 (69)

- [69] Kirollos B, Povey T (2014) Reverse-pass cooling systems for improved performance. *Journal of Turbomachinery* 136(11):111,004, DOI 10.1115/1.4028161 (28)
- [70] Kirollos B, Povey T (2015) An energy-based method for predicting the additive effect of multiple film cooling rows. *Journal of Engineering for Gas Turbines and Power* 137(12):122,608, DOI 10.1115/1.4030907 (17)
- [71] Kirollos B, Povey T (2016) Cooling optimization theory—part i: Optimum wall temperature, coolant exit temperature, and the effect of wall/film properties on performance. *Journal of Turbomachinery* 138(8):081,002, DOI 10.1115/1.4032612 (28)
- [72] Kirollos B, Povey T (2016) Cooling optimization theory—part ii: Optimum internal heat transfer coefficient distribution. *Journal of Turbomachinery* 138(8):081,003, DOI 10.1115/1.4032613 (28)
- [73] Klapdor EV (2011) Simulation of combustor-turbine interaction in a jet engine. Dissertation, Technische Universität Darmstadt (14), (86), (88)
- [74] Klinger H, Lazik W, Wunderlich T (2008) The engine 3e core engine. In: *ASME Turbo Expo 2008: Power for Land, Sea, and Air*, pp 93–102, DOI 10.1115/GT2008-50679 (4), (34)
- [75] Kloss M (2015) Stoffübergang in durchströmten, rotierten relativsystemen: Aussagefähigkeit der naphthalin-sublimations-methode. Dissertation, Technische Universität Darmstadt, Darmstadt (45)
- [76] Kneer J, Puetz F, Schulz A, Bauer HJ (2016) A new test facility to investigate film cooling on a nonaxisymmetric contoured turbine endwall—part ii: Heat transfer and film cooling measurements. *Journal of Turbomachinery* 138(7):071,004, DOI 10.1115/1.4032364 (17), (123)
- [77] Knost DG, Thole KA (2005) Adiabatic effectiveness measurements of endwall film-cooling for a first-stage vane. *Journal of Turbomachinery* 127(2):297, DOI 10.1115/1.1811099 (22), (70), (166)
- [78] Kodzwa PM JR, Eaton JK (2005) Measurements of Film Cooling Performance in a Transonic Single Passage Model. Report, Stanford (17), (19)
- [79] Koupper C, Cacioli G, Gicquel L, Duchaine F, Bonneau G, Tarchi L, Facchini B (2014) Development of an engine representative combustor simulator dedicated to hot streak generation. *Journal of Turbomachinery* 136(11):111,007, DOI 10.1115/1.4028175 (13), (87)
- [80] Koupper C, Gicquel L, Duchaine F, Bacci T, Facchini B, Picchi A, Tarchi L, Bonneau G (2016) Experimental and numerical calculation of turbulent timescales at the exit of an engine representative combustor simulator. *Journal of Engineering for Gas Turbines and Power* 138(2):021,503, DOI 10.1115/1.4031262 (10), (11), (14)

- [81] Krichbaum A, Werschnik H, Wilhelm M, Schiffer HP, Lehmann K (2015) A large scale turbine test rig for the investigation of high pressure turbine aerodynamics and heat transfer with variable inflow conditions: GT2015-43261. In: ASME Turbo Expo 2015 (32)
- [82] Laveau B (2014) Investigation of the heat transfer patterns on the vane endwall of an axial turbine. Dissertation, Eidgenössische Technische Hochschule Zürich, Zürich, DOI 10.3929/ethz-a-010273677 (24), (25), (47)
- [83] Laveau B, Abhari RS, Crawford ME, Lutum E (2013) High resolution heat transfer measurement on flat and contoured endwalls in a linear cascade. *Journal of Turbomachinery* 135(4):041,020, DOI 10.1115/1.4007725 (47)
- [84] Laveau B, Abhari RS, Crawford ME, Lutum E (2015) High resolution heat transfer measurement technique on contoured endwall with non-uniform thermal resistance. In: ASME Turbo Expo 2015: Turbine Technical Conference and Exposition, p V05BT13A023, DOI 10.1115/GT2015-43639 (47)
- [85] Laveau B, Abhari RS, Crawford ME, Lutum E (2015) High resolution heat transfer measurements on the stator endwall of an axial turbine. *Journal of Turbomachinery* 137(4):041,005, DOI 10.1115/1.4028431 (47), (49), (163)
- [86] Lechner C, Seume J (eds.) (2010) Stationäre Gasturbinen, 2nd edn. VDI-Buch, Springer, Berlin (1)
- [87] Lefrancois J, Boutet-Blais G, Dumas G, Krishnamoorthy V, Mohammed R, Yepuri GB, Felix J, Caron JF, Marini R (2011) Prediction of rim seal ingestion. In: International Society of Air Breathing Engines (ed.) Proceedings of the ISABE 2011 (50)
- [88] Lemmon CA, Kohli A, Thole KA (1999) Formation of counter-rotating vortices in film-cooling flows. In: ASME 1999 International Gas Turbine and Aeroengine Congress and Exhibition (18)
- [89] Leylek JH, Zerkle RD (1993) Discrete-jet film cooling: A comparison of computational results with experiments. In: ASME 1993 International Gas Turbine and Aeroengine Congress and Exposition, p V03AT15A058, DOI 10.1115/93-GT-207 (18)
- [90] Linker MC (2013) Quantifizierung von Sperrluft-Hauptstrom-Interaktionen in einer Turbine: engl.: Quantification of Seal air-Main flow Interactions in a Turbine. Dissertation, Technische Universität Darmstadt (31), (57)
- [91] Lohmann F (2011) Design of a combustor injector module for the large scale turbine rig: Entwicklung eines Brennkammer-Drallerzeugermoduls für den Turbinenprüfstand LSTR. Master's thesis, Technische Universität Darmstadt, Darmstadt (34), (36), (37)
- [92] Lohrengel J, Todtenhaupt R (1996) Wärmeleitfähigkeit, Gesamtemissionsgrad und spektrale Emissionsgrade der Beschichtung Nextel-Velvet-Coating 811

- (RAL 900 15 tiefschwarz matt): (engl.: "thermal conductivity, total emissivity and spectral emissivity of the coating nextel-velvet-coating 811"). In: PTB-Mitteilungen 106 (1996) (44), (46), (49)
- [93] Lorenz M (2013) Einfluss der Oberflächenrauigkeit auf den Wärmeübergang und die aerodynamischen Verluste einer Gasturbinenbeschaufelung: engl: "Influence of surface roughness on heat transfer and the aerodynamic losses of a gas turbine blading", Forschungsberichte aus dem Institut für Thermische Strömungsmaschinen, vol 54/2013. Logos Berlin, Berlin (17)
- [94] Lyko C, Rolls-Royce Deutschland Ltd & Co KG, Oberursel, Dahlewitz, Lehmann K (2016) Abschlussbericht zu Vorhaben AG Turbo 2020, 3.2.1C: Aerodynamic interaction between combustion chamber and turbine. Rolls-Royce Deutschland Ltd & Co KG, DOI 10.2314/GBV:879473754 (33)
- [95] Mellor AM (ed.) (1990) Design of modern turbine combustors. Combustion treatise, Acad. Press, London u.a. (37)
- [96] Merkle K, Haessler H, Büchner H, Zarzalis N (2003) Effect of co- and counter-swirl on the isothermal flow- and mixture-field of an airblast atomizer nozzle. International Journal of Heat and Fluid Flow 24(4):529–537, DOI 10.1016/S0142-727X(03)00047-X (13)
- [97] Moffat RJ (2004) $h_{\text{sub adiabatic}}$ and $u_{\text{sub max}}^{\text{sup}}$. Journal of Electronic Packaging 126(4):501, DOI 10.1115/1.1827265 (23), (47)
- [98] Moussa ZM, Trischka JW, Eskinazi S (1977) The near field in the mixing of a round jet with a cross-stream. Journal of Fluid Mechanics 80(01):49, DOI 10.1017/S0022112077001530 (18)
- [99] Netzsch Gerätebau GmbH (2013) Thermophysikalische Eigenschaften einer ETFE Materialprobe (46), (49)
- [100] Nicklas M (2001) Film-cooled turbine endwall in a transonic flow field: Part ii—heat transfer and film-cooling effectiveness. Journal of Turbomachinery 123(4):720, DOI 10.1115/1.1397308 (24), (49), (163)
- [101] Ochs M, Horbach T, Schulz A, Koch R, Bauer HJ (2009) A novel calibration method for an infrared thermography system applied to heat transfer experiments. Measurement Science and Technology 20(7):075,103, DOI 10.1088/0957-0233/20/7/075103 (44)
- [102] Panchal KV, Abraham S, Roy A, Ekkad SV, Ng WF, Lohaus AS, Crawford ME (2017) Effect of endwall contouring on a transonic turbine blade passage: Heat transfer performance. Journal of Turbomachinery 140(1) (24), (25), (123)
- [103] Popović I, Hodson HP, Janke E, Wolf T (2011) The effects of unsteadiness and compressibility on the interaction between hub leakage and mainstream flows in hp turbines. In: ASME 2011 Turbo Expo: Turbine Technical Conference and Exposition, pp 1011–1021, DOI 10.1115/GT2011-46608 (27)

- [104] Qureshi I, Smith AD, Povey T (2013) Hp vane aerodynamics and heat transfer in the presence of aggressive inlet swirl. *Journal of Turbomachinery* 135(2):021,040, DOI 10.1115/1.4006610 (13)
- [105] Roach PE (1987) The generation of nearly isotropic turbulence by means of grids. *International Journal of Heat and Fluid Flow* 8(2):82–92, DOI 10.1016/0142-727X(87)90001-4 (169)
- [106] Rolls-Royce plc (1986) *The Jet engine*, [5. ed.] edn. London (2)
- [107] Rolls-Royce plc (2017) ,obtained on March 14th, 2017. URL <https://www.flickr.com/photos/rolls-royceplc/14150915649/in/album-72157644584629408/> (2)
- [108] Rosic B, Denton JD, Horlock JH, Uchida S (2012) Integrated combustor and vane concept in gas turbines. *Journal of Turbomachinery* 134(3):031,005, DOI 10.1115/1.4003023 (13)
- [109] Schiffer HP (1991) Untersuchung des Stoffwerteeinflusses auf die Filmkühleffektivität: (engl.: Investigation of the influence of the fluid properties on the film cooling effectiveness). dissertation, Technische Universität Darmstadt, Darmstadt (15)
- [110] Schiffer HP (2017) Lecture "basics of flight propulsion". Lecture notes, Technische Universität Darmstadt, Darmstadt (8)
- [111] Schlichting H, Gersten K (2006) *Grenzschicht-Theorie*, 10th edn. Springer Berlin Heidelberg, Berlin, Heidelberg (61)
- [112] Schmid G (2015) Effects of combustor exit flow on turbine performance and endwall heat transfer: Techn. Univ., Diss.–Darmstadt, 2014, Forschungsberichte aus dem Institut für Gasturbinen, Luft- und Raumfahrtantriebe, vol 2. Shaker, Aachen (4), (13), (33), (39), (85), (86), (88), (95), (113), (125)
- [113] Schmid G, Krichbaum A, Werschnik H, Schiffer HP (2014) The impact of realistic inlet swirl in a $1\frac{1}{2}$ stage axial turbine. In: *ASME Turbo Expo 2014*, p V02CT38A045, DOI 10.1115/GT2014-26716 (13)
- [114] Schmidt M (2016) Experimental investigation of inflow turbulence at the large scale turbine rig: Experimentelle Untersuchung der Turbulenz in der Zuströmung des Large Scale Turbine Rig. Master's thesis, Technische Universität Darmstadt, Darmstadt (60), (86), (170)
- [115] Schneider M, Schiffer HP (2017) Parameterised model of 2d combustor exit flow conditions for hpt simulations. In: *12th European Conference on Turbomachinery Fluid dynamics & Thermodynamics* (4), (12), (124)
- [116] Schrewe S (2014) Experimental investigation of the interaction between purge and main annulus flow upstream of a guide vane in a low pressure turbine. Dissertation, Technische Universität Darmstadt (31), (50), (54), (57)

- [117] Schroeder RP, Thole KA (2016) Effect of in-hole roughness on film cooling from a shaped hole. In: Proceedings of the ASME Turbo Expo: Turbine Technical Conference and Exposition - 2016, The American Society of Mechanical Engineers, New York, N.Y., p V05CT19A021, DOI 10.1115/GT2016-56978 (17)
- [118] Schuler P (2016) Einfluss der Rotor-Stator-Dichtung auf die Turbinenaerodynamik und Seitenwandkühlung: engl.: Influence of the rotor-stator-seal on turbine aerodynamics and endwall cooling. Dissertation, Karlsruhe, Karlsruher Institut für Technologie (2)
- [119] Schwarz SG, Goldstein RJ, Eckert, E R G (1991) The influence of curvature on film cooling performance. *Journal of Turbomachinery* 113(3):472, DOI 10.1115/1.2927898 (17)
- [120] Sen B, Schmidt DL, Bogard DG (1996) Film cooling with compound angle holes: Heat transfer. *Journal of Turbomachinery* 118(4):800, DOI 10.1115/1.2840937 (27)
- [121] Shahpar S, Caloni S (2012) Aerodynamic optimisation of high pressure turbines for lean-burn combustion system. In: ASME Turbo Expo 2012: Turbine Technical Conference and Exposition, 2012, p 2173, DOI 10.1115/GT2012-69228 (123)
- [122] Shih TIP, Lin YL (2003) Controlling secondary-flow structure by leading-edge airfoil fillet and inlet swirl to reduce aerodynamic loss and surface heat transfer. *Journal of Turbomachinery* 125(1):48, DOI 10.1115/1.1518503 (24), (77)
- [123] Shih TIP, Na S (2007) Momentum-preserving shaped holes for film cooling. In: Proceedings of the ASME Turbo Expo 2007, ASME, New York, NY, pp 1377–1382, DOI 10.1115/GT2007-27600 (84)
- [124] Steinhausen C (2015) Definition and application of the data analysis procedure for heat transfer and film cooling effectiveness measurements at the large scale turbine rig (lstr): Definition und Anwendung des Datenanalyseprozesses für Wärmeübergangs- und Filmkühleffektivitätsmessungen am Large Scale Turbine Rig (LSTR). Master thesis, TU Darmstadt, Darmstadt (36), (48)
- [125] Thole KA, Sinha AK, Bogard DG, Crawford ME (1990) Mean temperature measurements of jets with a crossflow for gas turbine film cooling application: Isromac-3 (15), (16)
- [126] Thomas M (2014) Optimization of endwall film-cooling in axial turbines. Dissertation, University of Oxford, Oxford, URL <http://ora.ox.ac.uk/objects/uuid:e369eb63-0c99-4ded-ab05-6b050004ce4c> (16), (21), (22), (62), (124)
- [127] Thomas M, Povey T (2016) A novel scalar tracking method for optimising film cooling systems. Proceedings of the Institution of Mechanical Engineers, Part A: Journal of Power and Energy 230(1):3–15, DOI 10.1177/0957650915605944 (21)

- [128] Turrell MD, Stopford PJ, Syed KJ, Buchanan E (2004) Cfd simulation of the flow within and downstream of a high-swirl lean premixed gas turbine combustor. In: ASME Turbo Expo 2004: Power for Land, Sea, and Air, pp 31–38, DOI 10.1115/GT2004-53112 (2), (10)
- [129] Vagnoli S (2016) Assessment of advanced numerical methods for the aero-thermal investigation of combustor-turbine interactions. Dissertation, Florence, Italy, University of Florence (13), (125)
- [130] Vagnoli S, Verstraete T (2015) Numerical study of the combustor - turbine interaction using coupled unsteady solvers: isabe2015-20179. In: International Society of Air Breathing Engines (ed.) Proceedings of the ISABE 2015, URL <http://hdl.handle.net/2374.UC/745758> (11), (13), (86)
- [131] van Fossen GJ, Bunker RS (2001) Augmentation of stagnation region heat transfer due to turbulence from a dln can combustor. *Journal of Turbomachinery* 123(1):140, DOI 10.1115/1.1330270 (13)
- [132] Wang D, Ornano F, Sheng Li Y, Wells R, Hjalmarsson C, Hedlund L, Povey T (2017) Flovane: A new approach for high-pressure vane design. *Journal of Turbomachinery* 139(6):061,002, DOI 10.1115/1.4035232 (123)
- [133] Werschnik H, Krichbaum A, Schiffer HP, Lehmann K (2015) The influence of combustor swirl on turbine stator endwall heat transfer and film cooling effectiveness in a 1.5-stage axial turbine: ISABE2015-20184. In: International Society of Air Breathing Engines (ed.) Proceedings of the ISABE 2015 (165), (174)
- [134] Werschnik H, Ostrowski T, Hilgert, J, Schneider, M, Schiffer HP (2015) Infrared thermography to study endwall cooling and heat transfer in turbine stator vane passages using the auxiliary wall method and comparison to numerical simulations. *Journal of Quantitative InfraRed Thermography* 12(2), DOI 10.1080/17686733.2015.1066135 (44)
- [135] Werschnik H, Hilgert J, Bruscheckski M, Schiffer HP (2016) Combustor-turbine aerothermal interaction in an axial turbine - influence of varied inflow conditions on endwall heat transfer and film cooling effectiveness: Gt2016-57171. In: ASME Turbo Expo 2016 (67), (173)
- [136] Werschnik H, Wilhelm M, Ostrowski T, Bruscheckski M, Schiffer HP, Lyko C, Lehmann K, Wilhelm R, Krückels J, Henze M, Ohlendorf N (2016) Untersuchung der Interaktion von Brennkammer und Turbine am Large Scale Turbine Rig (LSTR). In: TURBO A (ed.) 15. Statusseminar der AG Turbo (4)
- [137] Werschnik H, Herrmann J, Schiffer HP, Lyko C (2017) The influence of combustor swirl on pressure losses and the propagation of coolant flows at the large scale turbine rig (lstr): Etc2017-139. In: 12th European Conference on Turbomachinery Fluid dynamics & Thermodynamics (165)

- [138] Werschnik H, Hilgert J, Wilhelm M, Bruscheckski M, Schiffer HP (2017) Influence of combustor swirl on endwall heat transfer and film cooling effectiveness at the large scale turbine rig. *Journal of Turbomachinery* 139(8):081,007–081,007–12, DOI 10.1115/1.4035832 (66)
- [139] Werschnik H, Steinhausen C, Schiffer HP (2017) Robustness of a turbine endwall film cooling design to swirling combustor inflow. *AIAA Journal of Propulsion and Power* 33(4), DOI 10.2514/1.B36138 (86), (119), (153)
- [140] Wilhelm M, Schmidt M, Schiffer HP, Lyko C (2017) Influence of combustor swirl on turbulence at the large scale turbine rig (Istr). In: *International Society of Air Breathing Engines (ed.) Proceedings of the ISABE 2017* (60), (86)
- [141] Wolff S (2003) *Aerodynamische Effekte bei Vorderkanten-Filmkühlausblasung an hochbelasteten Turbinengittern unter dem Einfluss periodisch instationärer Zuströmung: engl.: Aerodynamic effects with leading edge film cooling on highly loaded turbine stages under the influence of periodically unsteady inflow. Dissertation, Universität der Bundeswehr München, München* (16)
- [142] Xue S, Roy A, Ng WF, Ekkad SV (2015) A novel transient technique to determine recovery temperature, heat transfer coefficient, and film cooling effectiveness simultaneously in a transonic turbine cascade. *Journal of Thermal Science and Engineering Applications* 7(1):011,016, DOI 10.1115/1.4029098 (24), (49), (163)
- [143] Yin H, Liu S, Feng Y, Li M, Ren J, Jiang H (2015) Experimental test rig for combustor-turbine interaction research and test results analysis. In: *ASME Turbo Expo 2015: Turbine Technical Conference and Exposition*, p V02AT38A001, DOI 10.1115/GT2015-42209 (9), (13)

Nomenclature

Latin symbols

Symbol	Unit	Description	Definition
c	ppm	Concentration	-
C_{ax}	mm	Axial chord length	-
D	mm	Cooling hole diameter	-
DR	-	Density ratio	$DR = \frac{\rho_c}{\rho_\infty}$
CFR	%	Coolant flow ratio	$CFR = \frac{\dot{m}_c}{\dot{m}_\infty}$
G	-	Ratio of maximum velocities	$G = \frac{u_{tan,max}}{u_{ax,max}}$
h	$\frac{W}{m^2K}$	Heat transfer coefficient	$h = \frac{q}{T_w - T_{ref}}$
h_{rel}	-	Relative channel height	$h_{rel} = \frac{y}{R_{cas} - R_{hub}}$
H	-	Shape factor	$H = \frac{\delta_1}{\delta_2}$
I	-	Momentum ratio	$I = \frac{\rho_c u_c^2}{\rho_\infty u_\infty^2}$
MFR	%	Mass flow ratio	$MFR = \frac{\dot{m}_c}{\dot{m}_{inlet}} = \frac{\dot{m}_c}{\dot{m}_c + \dot{m}_\infty}$
Nu	-	Nusselt number	$Nu = \frac{h C_{real,NGV}}{\lambda_{air,T_\infty}}$
L	mm	Cooling hole length	-
\dot{m}	$\frac{kg}{s}$	Mass flow	-
M	-	Blowing ratio;	$M = \frac{\rho_c u_c}{\rho_\infty u_\infty}$
Ma	-	Mach number	-
P	Pa	Pressure	-
\dot{q}	$\frac{W}{m^2}$	Local heat flux	$\dot{q} = R_{th} (T_W - T_B)$
R_{th}	$\frac{K}{W}$	Thermal resistance	$\frac{1}{R_{th}} = \frac{s_{ETFE}}{\lambda_{ETFE}} + \frac{s_{coat}}{\lambda_{coat}}$
R	mm	Radius	-
Re	-	Reynolds number	$Re = \frac{u C_{real,NGV}}{v}$
s	mm	coating thickness	-
S	-	Swirl number	$S = \frac{\dot{D}}{l_{char} I}$
T	K	Temperature	-
T	mm	Vane pitch	-
Tu	-	Turbulence intensity	$Tu = \sqrt{\langle u'_{eff}{}^2 \rangle} / \langle u_{eff} \rangle$
u	$\frac{m}{s}$	Velocity	-
y_D	-	relative wall distance	$\frac{y}{D}$
x/T	-	relative pitch pos.	$\frac{x}{T}$

Greek symbols

Symbol	Unit	Description	Definition
α	$^{\circ}$	Whirl angle	-
γ	$^{\circ}$	Radial angle	-
δ	mm	Boundary layer thickness	-
η	-	Cooling/mixing effectiveness	$\eta = \frac{T_{\infty} - T_{ad}}{T_{\infty} - T_c}$
λ	$\frac{W}{mK}$	Thermal conductivity	-
ν	$\frac{m^2}{s}$	Kinematic viscosity	-
ϕ	-	Plane inclination to turbine axis	-
Φ	-	Equivalence ratio	$\Phi = \frac{\dot{m}_{fuel}/\dot{m}_{air}}{(\dot{m}_{fuel}/\dot{m}_{fuelstoich})}$
Π	-	Pressure ratio	-
ψ	-	Wall inclination angle	-
ρ	$\frac{kg}{m^3}$	Density	-
τ	-	Transmissivity	-
θ	-	Non-dimensional temperature ratio	$\theta = \frac{T_{\infty} - T_c}{T_{\infty} - T_W}$
Θ	-	Heat flux reduction	$\Theta = 1 - \frac{2h_f/h_0}{1+h_f/h_0} (1 - \eta)$
ζ	-	Pressure loss coefficient	$\zeta = \frac{p_{t,1} - p_{t,2}}{p_{dyn,2}}$
ω	$\frac{1}{s}$	Vorticity	$\omega = \frac{\delta v_y}{\delta z} - \frac{\delta v_z}{\delta y}$

Subscripts

Symbol	Description
ad	Adiabatic
air	Air property
aW	Adiabatic wall
ax	Axial chord
amb	Ambient pressure
B	Base material
c	RIDN coolant flow property
cas	Casing
f	film temperature
cal	Calibrated
coat	Paint coating
dyn	Dynamic
eff	Effective
geom	Geometrical
hub	Hub
is	Isentropic
local	Local value
meas	Measured
mix	Mixing property
norm	Normalized
Ref	Reference value
Real	Real chord
s	Static quantity
T	NGV pitch
t	Stagnation quantity
tc	Test cell
th	Thermal
w	Wall
0	Uncooled
∞	Main flow property

Abbreviations

Index	Description
AX	Axial baseline configuration
AG	Arbeitsgemeinschaft (engl.: Research network)
CAEP	ICAO Committee on Aviation Environmental Protection
CAV	Wheel space purge flow
CFD	Computational fluid dynamics
CNC	Computer numeric control machining
CO, CO ₂	Carbon monoxide, Carbon dioxide
CRVP	Counter-rotating vortex pair
CTI	Combustor-turbine interaction
CTA	Constant temperature anemometry
CRVP	Counter-rotating vortex pair
dim.	Dimension
ETFE	Ethylene tetrafluorethylene
FKZ	Förderkennzeichen (engl.: Grant number)
4HP	Four hole probe
5HP	Five hole probe
GC	Gas concentration measurement technique
GLR	Institute of Gas Turbines and Aerospace Propulsion
GUM	Guide to the expression of uncertainty in measurement
HWA	Hot wire anemometry
HPT	High pressure turbine
IATA	International Air Transport Association
ICAO	International Civil Aviation Organization
IR	Infrared thermography measurement
LE	Leading Edge
LSTR	Large Scale Turbine Rig
LPP	Lean, premixed, prevaporized
ME	Measurement plane
NO _x	Nitrogen oxides
PS	Pressure side
PVC	Polyvinyl chloride
RE	RIDN boundary layer measurement plane
NHFR	Net heat flux reduction
NGV	Nozzle guide vane
NUC	Non uniformity correction
RIDN	Rear Inner Discharge Nozzle
RQL	Rich burn - quick quench - lean burn combustor
SWL	Leading-edge clocking swirl configuration
SWP	Passage clocking swirl configuration
SS	Suction side

Index	Description
TBC	Thermal barrier coating
TE	Trailing Edge
UHC	Unburned Hydrocarbons
UTC	Rolls-Royce University Technology Centre
VDC	Volts of direct current

Measurement plane nomenclature

Description	Position
ME00	Upstream swirler
ME01	Combustor exit / turbine inlet
ME02	NGV exit
ME03	Rotor exit
ME05	Turbine exit
RE1	RIDN coolant inlet plane
RE2	Downstream coolant row 1
RE3	Downstream coolant row 2

List of Figures

1.1	Modern gas turbine engine	2
2.1	Formation of the swirl-/leading edge interaction vortex.	9
2.2	Lateral deflection of the swirl core	11
2.3	Momentum imbalance imposed by the swirler	12
2.4	Vortex system due to a coolant jet injection	18
2.5	Jet-in-crossflow model	19
2.6	Secondary flows in a vane passage	20
2.7	Mechanism responsible for the passage cross flow	21
2.8	Endwall film cooling contours for varied coolant injection rates	22
2.9	Endwall Nusselt numbers in an axial turbine without coolant injection	25
2.10	Characteristic heat transfer pattern downstream of a coolant injection in different flow regimes	26
2.11	Heat flux analysis through the film cooled endwall	28
3.1	General setup of the Large Scale Turbine Rig	31
3.2	Cross section of the test rig	32
3.3	Main annulus geometry and measurement planes in the vicinity of the RIDN injection, dimensions specified in table 3.1	34
3.4	Triple flow LSTR Swirler design with three concentric blade rings, streamwise view. Characteristic flow parameters are listed in table 3.2	36
3.5	Illustration of clocking positions and vane passages A & B	36
3.6	Test section views. NGV row and RIDN coolant injection rows (left), combustor module with installed swirlers from upstream (right)	39
3.7	Pressure ratio across RIDN cooling holes with varied MFR	40
3.8	NGV coolant plenum and instrumentation chambers and pressure tap positions at 20 % span height. Arrows indicate position and direction of PS & SS film cooling rows (left), NGV photograph, showing the pressure side and the seven TE-Coolant Ejection Slots (right)	41
3.9	Vane passage nomenclature and pitch position of the swirler geometri- cal center for clocking positions SWL and SWP	42
4.1	Schematic of the auxiliary wall method, applied to the NGV endwall	44
4.2	Manufacturing steps of the auxiliary wall and instrumentation carrier	45
4.3	Layer thickness of ETFE- and paint-coating	46
4.4	Linear regression procedure for data evaluation at to arbitrary points A and B in the measurement area	48
4.5	Comparison of IR and gas concentration data, AX MFR 3	49
4.6	Surface tap sampling - measurement points on NGV hub endwall (A), guidance of measurement lines on the bottom side (B) and sampling taps on the NGV leading edge (C)	51

4.7	Flow tracing measurements, measurement locations and instrumentation	51
4.8	Measurement uncertainty - gas concentration measurements	53
4.9	Pneumatic measurements	55
4.10	Boundary layer measurement planes RE1/2/3 and probes used for AX measurements	55
5.1	Turbine inflow in ME01, MFR 3, AX inflow	60
5.2	Boundary layer measurement in RE1, AX, MFR 3	61
5.3	Mach number and whirl angle in RE1, 4HP data, MFR 3	62
5.4	$P_{t,ref}$ in RE3 for both rows downstream of their hole centerline in the passage center for varied MFR	63
5.5	Local blowing rate variation for AX inflow, first RIDN row	64
5.6	NGV exit Mach number, ME02, influence of the MFR (5HP data)	65
5.7	Comparison of effective and axial Mach number to the pressure loss coefficient ζ in ME02 for AX inflow, MFR 3 (5HP data)	66
5.8	Flow field influence of the RIDN coolant injection	67
5.9	Flow tracing results for varied seeding, trailing edge ejection (TE), RIDN-coolant (RIDN) and purge flow (CAV); all for AX inflow, MFR 3 in ME02	68
5.10	TE seeding with varied MFR; shows influence of the RIDN flow rate in ME02, AX inflow	68
5.11	η_{mix} in ME02 with varied MFR for RIDN-seeding	69
5.12	Flow model with endwall film cooling results	70
5.13	η_{aw} on NGV endwall, baseline case for varied MFR	71
5.14	Total pressure coefficient $C_{p,t}$ of RIDN injection, $x/T=0.5$, MFR 3	73
5.15	Boundary layer influence of RIDN injection for AX, MFR 3, view from downstream. Black framed boxes mark identical relative pitch positions.	73
5.16	Comparison of GC (Data points) and IR (contours) measurements for MFR 0.8 and 1	75
5.17	Comparison of GC (data points) and IR (contours) measurements for high momentum MFR 1.5 and 3	76
5.18	Nusselt contours for the uncooled endwall, showing the peak regions of heat transfer discussed in section 2.4	77
5.19	Local maxima (dashed lines) to the sides of each 2 nd row hole	78
5.20	Endwall Nu-contours, baseline case for varied MFR	79
5.21	Heat flux reduction Θ due to film cooling, compared to the uncooled endwall	81
5.22	Schematic model of NGV flow features for the reference case. The coloring resembles whether the observed effect is detrimental or favorable with respect to the aerodynamic or thermal design	82
6.1	Pitchwise averaged data for swirling inflow in ME01	86
6.2	Inflow in ME01 for SWP clocking	87
6.3	Flow angles for SWP clocking in ME01	87
6.4	Effective Mach number for SWP and SWL clocking. Vanes A and B are labeled for the subsequent analysis of the vane loading.	88
6.5	Position of the boundary layer evaluation in Fig. 6.6	89

6.6	Mach numbers in the boundary layer, 4HP results	90
6.7	Whirl angle comparison for AX, SWP and SWL inflow, MFR 3 in RE1, 4HP measurement. The scale has been modified for AX inflow. The pitch position of the swirler is indicated in the SWL/SWP figures, projected in the illustration along its symmetry line.	91
6.8	$P_{t,ref}$ in RE3 for both rows downstream of their hole centerline for SWL inflow and varied MFR	92
6.9	Variation of the local blowing ratio (M_{local} due to swirling inflow according to eq. 5.5. AX baseline compared to SWL, passage A, 4HP data	93
6.10	Isentropic Mach number at 20% span height, MFR 0	93
6.11	Influence of RIDN injection on NGV loading at 20% span height, uncooled (bold) and cooled (light colors)	94
6.12	Isentropic Mach number at 50% span height, MFR 0	95
6.13	Isentropic Mach number at 80% span height, MFR 0	96
6.14	Incidence situation at 20% span height (schematic)	97
6.15	5HP data in ME02, pitch wise averaged, MFR 3	98
6.16	Mach number contours for SWL and SWP clocking, trailing edge of vane A and B indicated. 5HP results, MFR 3. The arrows indicate the streamwise projected swirler center	98
6.17	Pressure loss coefficient ζ contours for SWL and SWP clocking, 5HP results, MFR 3, ME02, arrows indicate streamwise projected swirler center	99
6.18	Pitch wise averaged pressure loss coefficients in ME02	99
6.19	Pitchwise averaged η_{mix} for SWL/SWP and AX, ME02, MFR 3 and varied coolant flow seeding	100
6.20	Flow tracing results for swirling inflow, ME02, MFR 3	101
6.21	Area averaged film cooling effectiveness for the NGV endwall, per cent change referenced to AX inflow and MFR 0.8 for all data points.	102
6.22	4HP results for SWL inflow, MFR 3, Passage A	104
6.23	Total pressure coefficient at $x/T=0.5$ for MFR 3	104
6.24	Whirl component influence on coolant trajectory	105
6.25	Whirl and radial angle for SWL, MFR 3	106
6.26	Clocking influence on the flow field and film cooling	106
6.27	Schematic flow field with swirler	107
6.28	Influence of a MFR variation on the velocity contours and the film cooling effectiveness for SWL clocking	109
6.29	η_{aw} on NGV endwall for SWP (left) and SWL (right) inflow and varied MFR	110
6.30	Comparison of IR (contours) and GC (data points) for SWP inflow	111
6.31	Area averaged Nusselt numbers for the NGV endwall	112
6.33	Comparison of Nusselt contours near the cooling holes, AX and SWL inflow at MFR 1	113
6.32	Nusselt numbers on NGV endwall for SWP (left) and SWL (right) inflow and varied MFR	114
6.34	Comparison of Nusselt numbers for SWP (left) and AX (right) inflow at MFR 0 and MFR 3	115

6.35	Heat flux reduction Θ_{ax} due to film cooling for swirling inflow with respect to the uncooled endwall for axial inflow	116
B.1	η_{aW} on NGV endwall, SWL inflow for varied MFR	156
B.2	η_{aW} on NGV endwall, SWP inflow for varied MFR	157
B.3	Nusselt numbers on NGV endwall, SWL inflow for varied MFR	158
B.4	Nusselt numbers on NGV endwall, SWP inflow for varied MFR	159
B.5	Heat flux reduction Θ_{ax} due to film cooling for SWL inflow, compared to the uncooled endwall for axial inflow	160
B.6	Heat flux reduction Θ_{ax} due to film cooling for SWP inflow, compared to the uncooled endwall for axial inflow	161
D.1	Results for the commissioning measurements	167
E.1	TU inflow, ME01, MFR 3. AX inflow shown grayed for comparison	170
E.2	Nu and η_{aW} on NGV endwall, TU inflow, varied MFR	171
F.1	Endwall streamline tracing: Temperature map showing vortex from surface defect (A) and temperature increase downstream of reference position (B)	174
F.2	Endwall streamlines for varied MFR, AX inflow	174

List of Tables

3.1	Measurement planes and geometry near the RIDN injection	35
3.2	Characteristic flow parameters of the LSTR swirler	37
3.3	Coolant injection parameters for the main measurement campaign, determined with stage mass flow values	38
5.1	Corrected local blowing ratios for axial inflow based on the measurement at MFR 3	64
C.1	Uncertainty in comparable experiments	163
D.1	Coolant injection parameters for the commissioning measurements . .	165

A Appendix: Overview

The appendix contains supplementary material to the results presented in the main part of this thesis. An overview is given at this point:

Section B: Full results for swirling inflow

For swirling inflow, the results are only discussed in detail for some of the settings investigated. The full set of data is presented in this chapter without further discussion.

Section C: Comparison to the measurement uncertainty in comparable studies

An overview on the measurement uncertainty of comparable studies is given in comparison to this study.

Section D: Commissioning measurement results

A different operating point was examined during the commissioning of the test rig. Additional results are presented and illustrated in this section. The detailed analysis is presented in Werschnik et al. [139]

Section E: Increased turbulence intensity inflow

An inflow with increased turbulence intensity has been studied. For this, a turbulence grid has been implemented in the combustor module. Results are presented for a reduced measurement matrix, that has been studied to accompany the measurement campaign of the parallel project "AG Turbo 3.2.1A".

Section F: Endwall streamline detection

The endwall streamlines are analyzed using the raw infrared images. The procedure and results for axial inflow are presented.

Section G: Curriculum Vitae

The author's curriculum vitae is presented.

B Full measurement results for swirling inflow

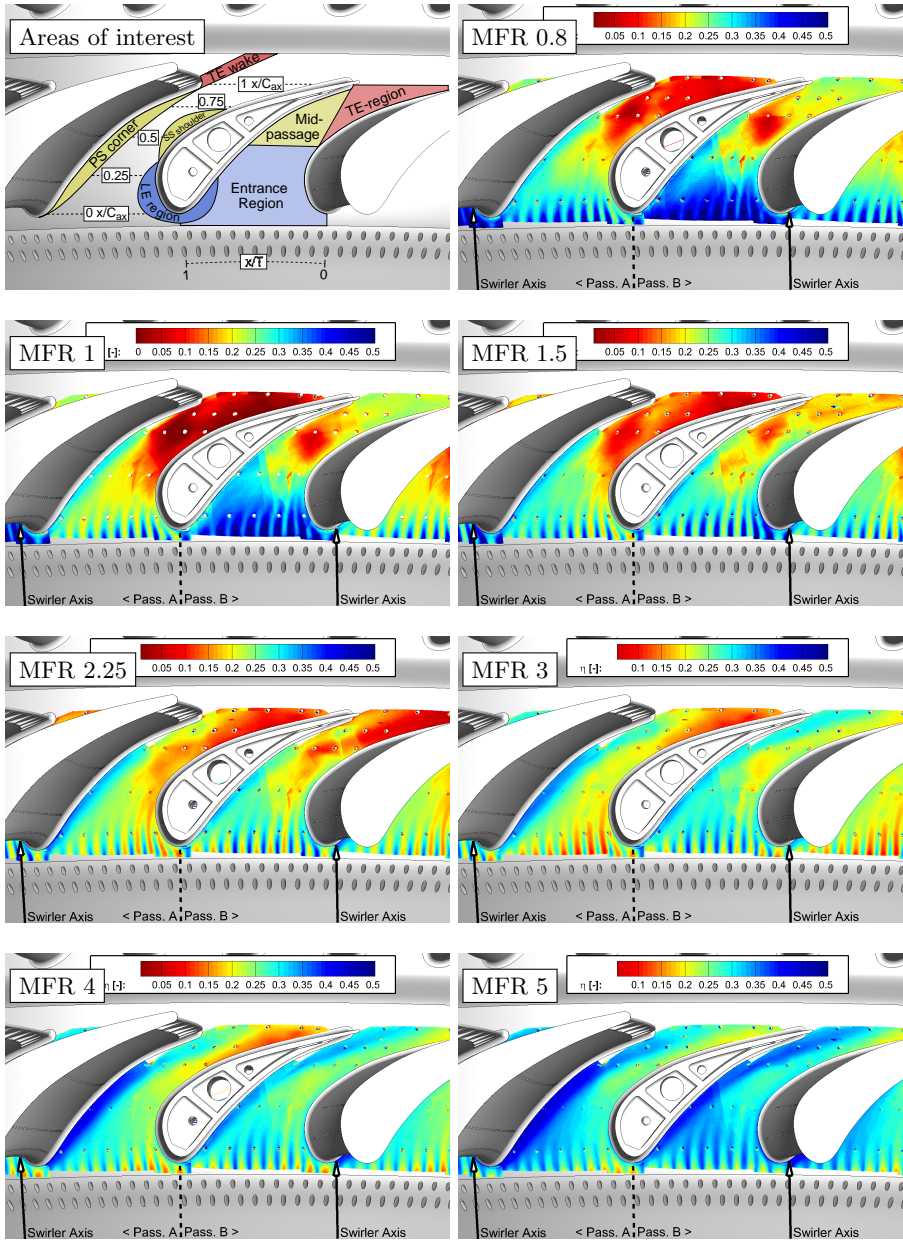


Figure B.1: η_{aW} on NGV endwall, SWL inflow for varied MFR

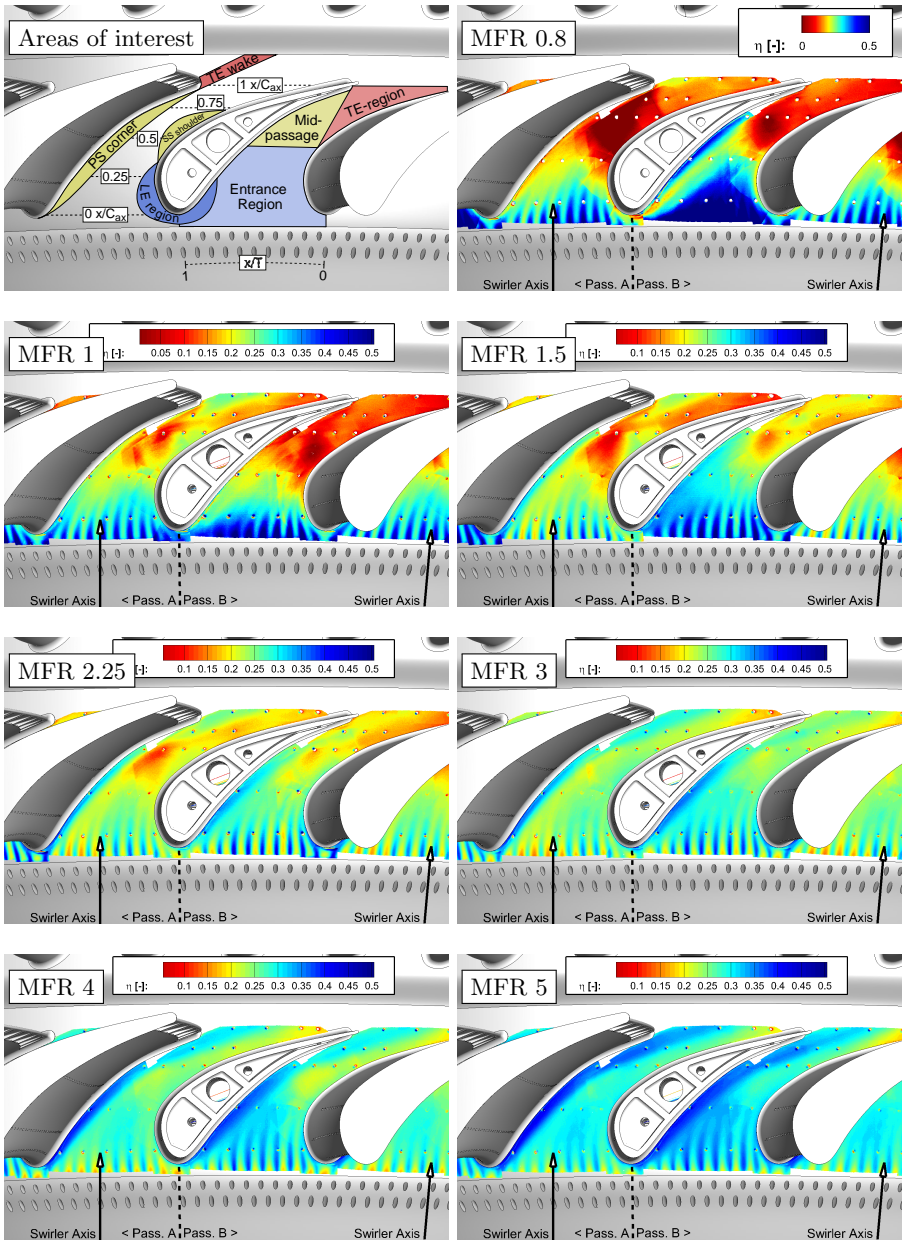


Figure B.2: η_{ax} on NGV endwall, SWP inflow for varied MFR

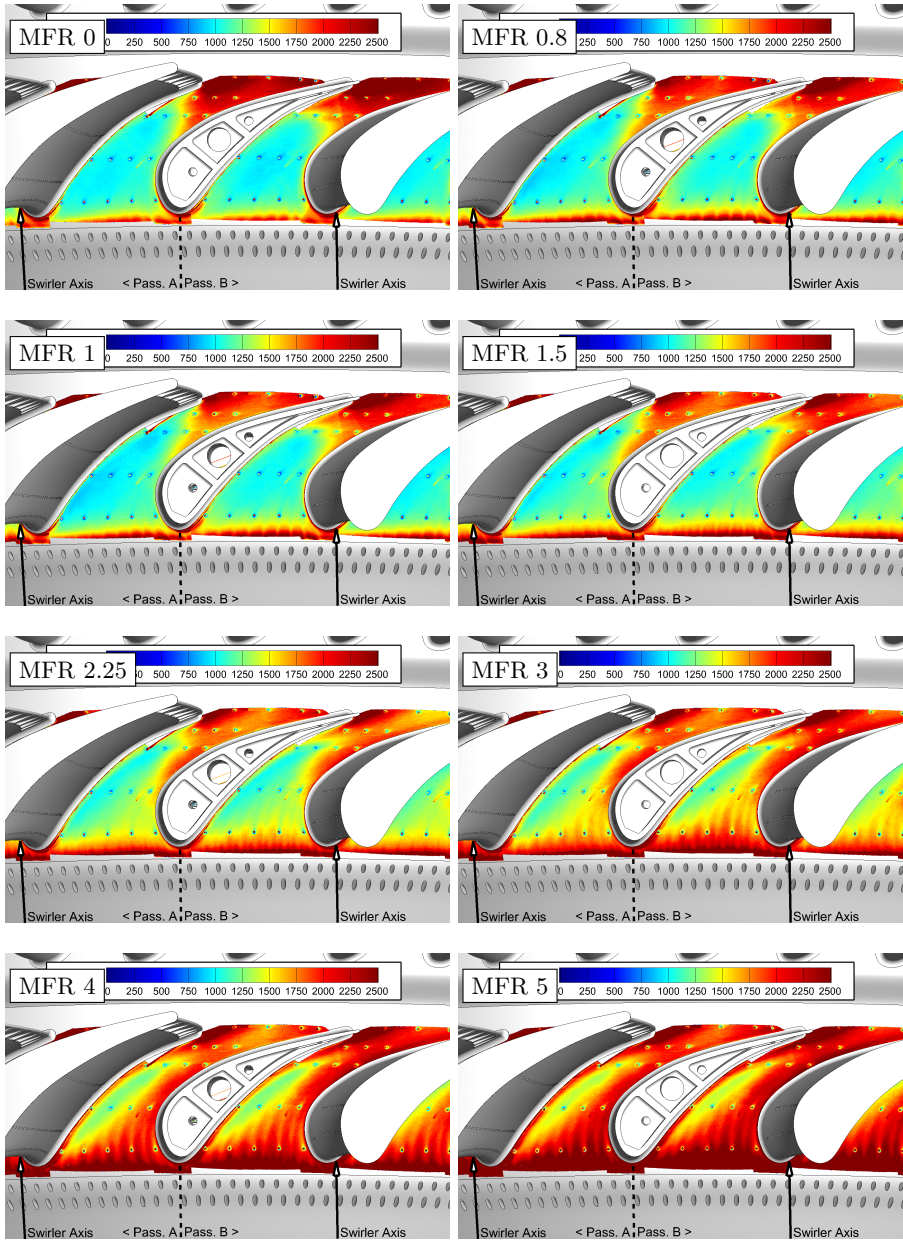


Figure B.3: Nusselt numbers on NGV endwall, SWL inflow for varied MFR

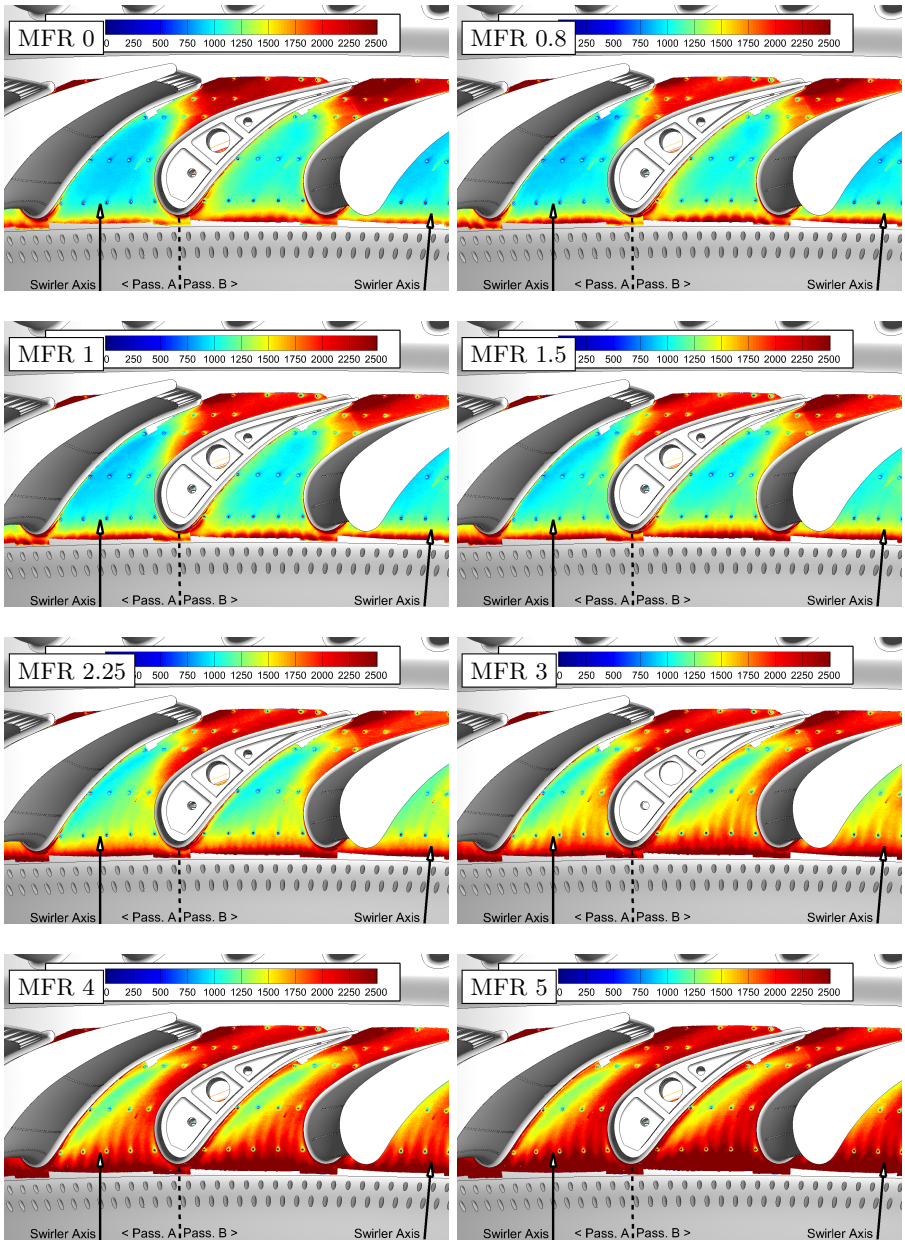


Figure B.4: Nusselt numbers on NGV endwall, SWP inflow for varied MFR

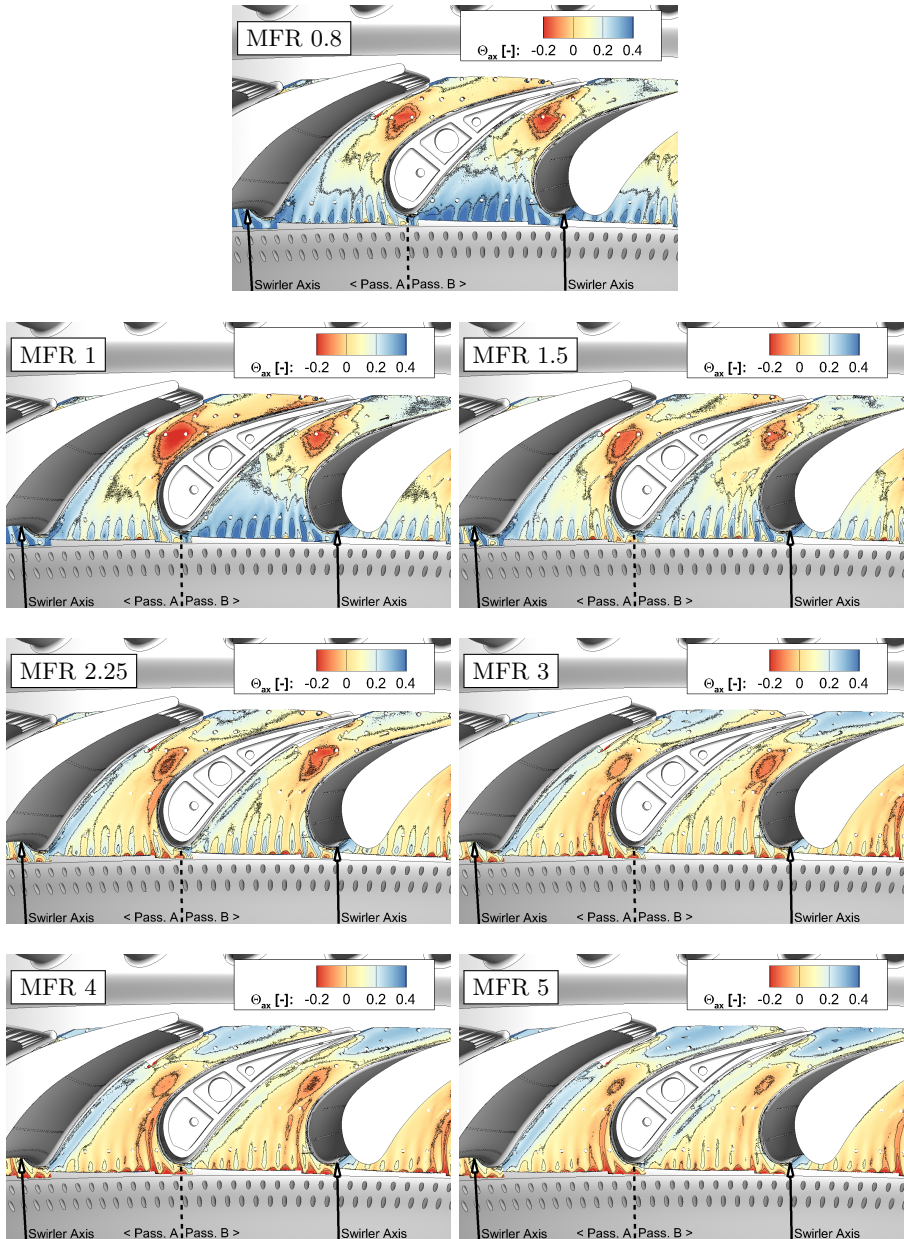


Figure B.5: Heat flux reduction Θ_{ax} due to film cooling for SWL inflow, compared to the uncooled endwall for axial inflow

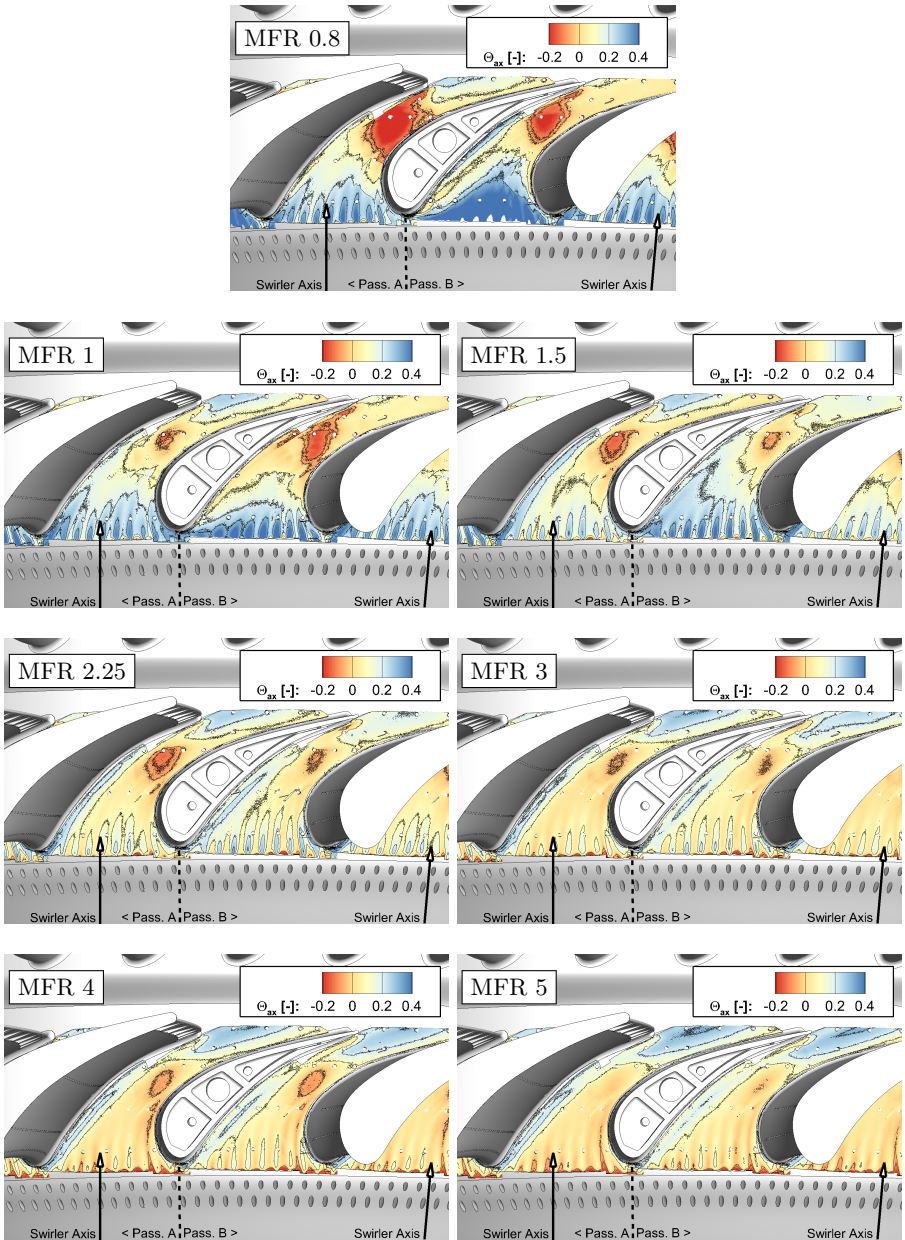


Figure B.6: Heat flux reduction Θ_{ax} due to film cooling for SWP inflow, compared to the uncooled endwall for axial inflow

C Comparison to the measurement uncertainty in comparable studies

A comparison to experiments in the referenced literature shows that uncertainty values of the present investigation are in the same order of magnitude (Table C.1).

Table C.1: Uncertainty in comparable experiments

Study	ΔNu	$\Delta T_{w,iso}$ [K]	$\Delta \eta_{aw}$
Present Investigation	$\pm 9.5\%$	± 1.2	± 0.08
Laveau et al. [85]	$\pm 9.8\%$	± 1.1	-
Xue et al. [142]	$\pm 8\%$	-	± 0.08
Nicklas [100]	$\pm 11\%$	-	± 0.04
Colban et al. [33]	-	-	± 0.04

D Commissioning measurement results

This chapter presents additional findings from the commissioning measurements. A different operating point was studied. It allowed for an injection with an attached coolant film for axial inflow.

D.1 Operating point

The rig was operated with a higher main mass flow of 14 kg/s. For clarity the mass flow ratio for the commissioning measurements is denoted coolant flow ratio, CFR. Table D.1 lists the parameters M and I calculated according to equations 3.7. In contrast to the main measurement campaign, the test rig was run with a constant inlet mass flow \dot{m}_∞ . RIDN coolant air was supplied in addition to that, resulting in an increase mass flow at the rotor inlet depending on the CFR.

Table D.1: Coolant injection parameters for the commissioning measurements

CFR [%]	0	0.4	0.9	2.0	2.9
M [-]	-	0.4	0.9	2.0	2.9
I [-]	-	0.2	0.9	5.0	10.2

Since the heat load into the water coolers was significantly greater, it was not possible to achieve a lower temperature than in the secondary flow. Instead, the secondary air flow was cooled down and a sufficient temperature difference for combined heat transfer and film cooling effectiveness measurements was achieved. The dimensioning of the secondary air system in this way allows for a coolant-to-mainstream mass flow ratio as low as 0.4. This results in an attached coolant flow on the endwall and allows for additional aspects on the heat transfer and film cooling effectiveness distribution. Results have been discussed in Werschnik et al. [133] and Werschnik et al. [137]. They are presented briefly in the appendix to this thesis because they emphasize on additional aspects regarding the robustness of this injection geometry.

D.2 Results

For the commissioning of the rig and the measurement method, a different operating point was studied (Werschnik et al. [137]). In this way, a setting with a blowing ratio and momentum ratio significantly below 1 could be studied. The results will briefly be discussed here to emphasize on the associated additional insights. Furthermore, only RIDN cooling was supplied to the NGV row and hence no effect of the airfoil film cooling on the endwall occurs.

Fig. D.1 shows Nusselt numbers and corresponding film cooling effectiveness contours for the axial inflow case. The results are qualitatively similar those of the main operating point. CFR 0.4 shows an overturning of the coolant air towards the suction side. Only a triangle-shaped area upstream of the horseshoe vortex trajectory receives cooling. Downstream, the endwall remains uncooled. The coolant momentum is not sufficient to reach this area as it is observed in the literature for low-momentum slot ejection (Knost et al. [77], Hada et al. [54]). Furthermore, the suction side corner area remains uncooled.

Despite this large uncooled region downstream of the horseshoe vortex trajectory, the heat flux reduction Θ in this region remains unchanged and does not increase, since also the Nusselt numbers remain similar to the uncooled endwall. The Θ contours emphasize that the most important parameter to control the endwall heat flux is the local film cooling effectiveness. The triangle shaped area of attached coolant films show very high film cooling effectiveness values and also superior heat flux reduction to all other settings studied in this campaign. Values up to 0.65 have been obtained. The scale has not been adapted to ensure comparability to the other cases. This low-momentum injection case however shows in addition the impossibility to cool the downstream section and the pressure side corner with such an approach.

With increased CFR to 0.9, the coolant air reaches almost all of the endwall, leaving only the pressure side corner and an area downstream of the trailing edge uncooled. In contrast to the similar MFR 0.8 and MFR 1 in the main measurement campaign, the blowing rate is still lower than one. This is an important difference and leaves the pressure side corner uncooled. In the main measurement campaign, this area receives cooling for MFR 1 which is due to the RIDN injection, as the comparison with the gas concentration measurements emphasizes. Similar to the main measurement campaign, the area around the leading edge is better cooled than the passage center due to the influence of the horseshoe vortex. The coolant momentum is low and as a consequence more air is transported towards the endwall with the horseshoe vortex. The higher CFR settings are similar to results from the main measurement campaign and show a stripe pattern in the entrance area and it is observed that the whole endwall receives coolant. The efficiently cooled pressure side corner area confirm it is due to the RIDN cooling scheme and its high momentum, i.e. verify the assumptions made in the comparison of gas concentration measurements and the infrared thermography measurements.

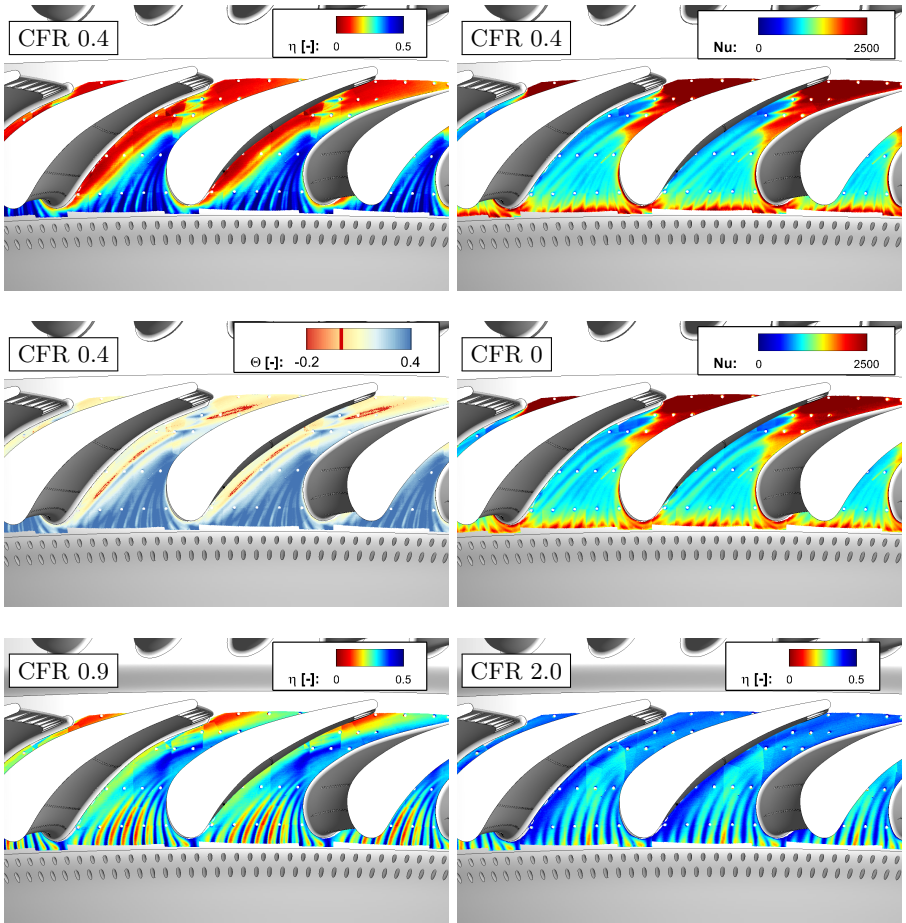


Figure D.1: Results for the commissioning measurements

E Increased turbulence intensity inflow

The effect of increased turbulence without the presence of high inflow angles is analyzed separately by means of a turbulence grid. The chapter is concluded with a comparison of the results for all configurations. The increased turbulence intensity inflow, denoted TU inflow, was examined to isolate the effect of the increased turbulence intensity from the whirl angle and pressure distortion, that is imposed by the swirler.

A reduced measurement matrix was investigated. Only the MFR 3 case was studied for aerodynamic and turbulence intensity measurements. Endwall heat transfer was evaluated at MFR 0, 1.5, 3 and 5.

Design and desired turbulence intensity for the turbulence grid

The elevated turbulence level inflow is generated by a turbulence grid, designed by Baumann [16]. The grid consists of six 60°-degree sector elements with a rectangular grid shape. The grid has been analytically designed with correlations according to Roach [105] for a rectangular duct. The design intent was to achieve a turbulence level of 15 %. The grid has a blockage of 45 % and is positioned one axial chord length C_{ax} upstream of the NGV leading edge. It has an opening area of $\beta = 57\%$, excluding the supporting frame.

E.1 Aerodynamic flow field

With applied turbulence grid (TU inflow), the flow field in the interface plane ME01 becomes altered significantly. Comparing for MFR 3, the Mach number (Fig. E.1a) is observed to increase in the annulus center between h_{rel} 0.2 and 0.8. The influence of the grid struts is visible with local minima. Near both endwalls, the obstruction due to the grid's struts reduces the pitch averaged velocity below the baseline's values. The radial angle distribution follows the baseline with less deviation, except for the lower annulus, where a significant decrease is observed, before the value converges to the endwall's inclination of 13,2°. The values immediately at the wall are locally compromised since the flow is out of the calibration range.

E.2 Endwall heat transfer and film cooling

The contours for endwall heat transfer and film cooling effectiveness are shown in figure E.2. Results have been obtained for one measurement passage and duplicated to adjacent passages, similar to the baseline case.

The Nusselt numbers are observed to increase with the MFR, similar to the baseline case. While for swirling inflow, the stripe pattern due to the coolant injection at the passage entrance, was smeared in comparison to the baseline, this is not observed for TU inflow. Contrarily, the contours are well pronounced and defined in their spatial

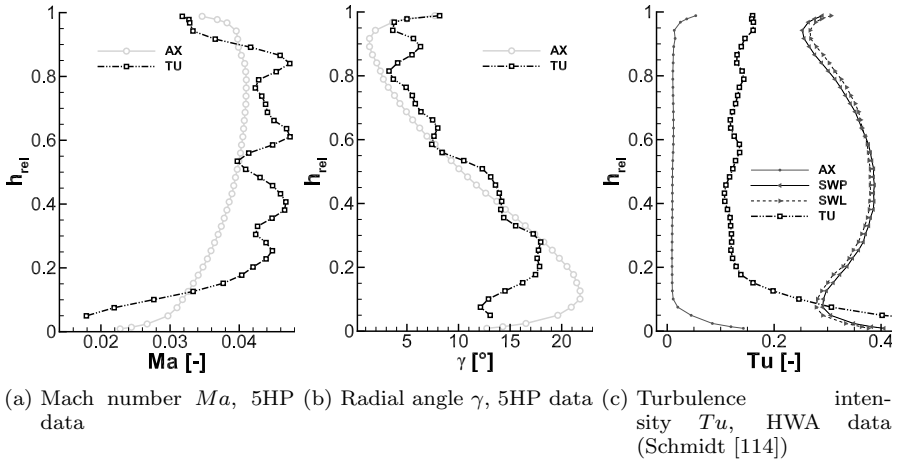
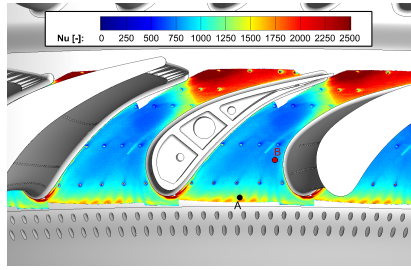


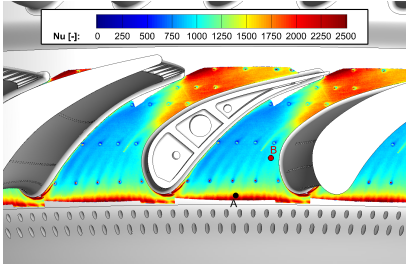
Figure E.1: TU inflow, ME01, MFR 3. AX inflow shown grayed for comparison

extent. The Nusselt number level and distribution is similar to the baseline case. The local maxima in Nusselt numbers are located in between adjacent second row holes in the entrance area for MFR 1.5 (Fig. E.2b), 3 (Fig. E.2d) and 5 (Fig. E.2f). The global peak is observed in the trailing edge wake and the Nusselt numbers increase in the passage throat in concordance with the velocity increase. Low Nusselt numbers are observed on the endwall towards the pressure side for MFR 3 (Fig. E.2d) and 5 (Fig. E.2f), while the area related area shrinks. For these MFR, high Nusselt numbers are also observed in the pressure side corner.

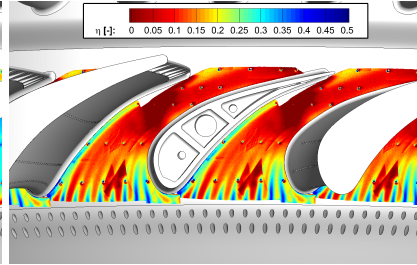
The film cooling effectiveness contours show a drastic decrease in comparison to the baseline case. For MFR 1.5 (Fig. E.2c), hardly any cooling is observed on the whole endwall and the cooling effectiveness of this setting shows the lowest within the whole measurement campaign. The coolant jets protrude far into the main stream, indicating a very large blowing rate M , which results of the low main flow velocity near the endwall. Only small traces of coolant are observed in the entrance area and in a confined area very close to the pressure side corner. With increasing injection at MFR 3 (Fig. E.2e), this area enlarges and shows peak η_{aW} . The accumulation of film coolant is due to its high momentum and velocity, that allows the coolant to travel along a trajectory with a greater radius due to the radial equilibrium. This also explains the aforementioned Nusselt number peak, since the velocity increased due to coolant also increases the heat transfer level. The coverage of the remainder of the endwall increases as well, with a very good coverage near suction side of the vane in the passage entrance. Mixing and interaction of the jets enhances the cooling and a homogenous film is achieved at a position of x/C_{ax} of 0.25 with $\eta_{aW}=0.3$. Further downstream, a gradient with high values from the pressure side to $\eta_{aW}=0.2$ at the suction side at the trailing edge. At MFR 5 (Fig. E.2g), the film cooling effectiveness level is comparable to SWL/SWP at the same MFR. However, at passage entrance,



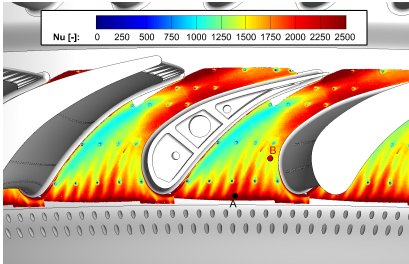
(a) Nu , MFR 0



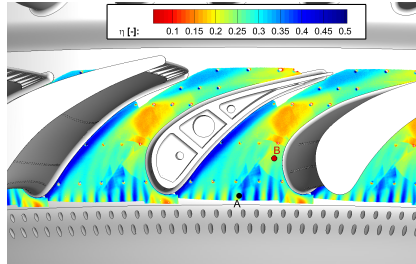
(b) Nu , MFR 1.5



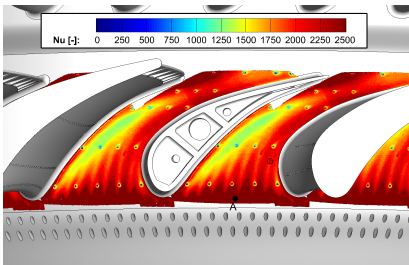
(c) η_{aw} , MFR 1.5



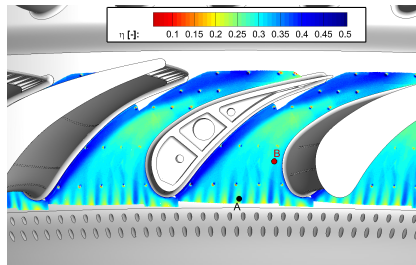
(d) Nu , MFR 3



(e) η_{aw} , MFR 3



(f) Nu , MFR 5



(g) η_{aw} , MFR 5

Figure E.2: Nu and η_{aw} on NGV endwall, TU inflow, varied MFR

the local maxima are lower and the coverage towards the trailing edge is enhanced. The first aspect indicates, that the blowing rate is too high, since the boundary layer

E.3 Summary of the findings for the increased turbulence intensity case

The increased turbulence level case highlights the importance of the local blowing rate on the endwall heat transfer and film cooling effectiveness contours. While a definition with respect to machine parameters such as main flow \dot{m}_∞ and coolant mass flow \dot{m}_c omits

Strong distortions of the boundary layer inflow, such as a separation as it appears with the turbulence grid, makes the film cooling design very susceptible to the mass flow ratio. While at higher MFR, the difference to swirling inflow are rather local, at MFR 1.5, hardly any coolant reaches the endwall. Towards the robustness of the cooling design, this highlights the limitations of a coolant mass flow setting with respect to global machine parameters and underlines the importance of the boundary layer for endwall cooling.

F Endwall streamline detection

The reference positions for the calibration of the infrared camera were further used as a point wise indicator for endwall streamlines: Since the surface temperature above the reference cylinders in the wind-on experiment was significantly higher compared to the immediate surrounding, the thermal boundary condition is changed, resulting in higher near-wall air temperatures. This on one hand compromises the measurement accuracy downstream of these cylinders: The air temperature receives a step change to a higher value and consequently, the local heat flux rate is decreased due to the lower temperature gradient and the calculated heat transfer coefficient is underestimated. On the other hand, this allowed to trace the flow path on the endwall: The downstream area of the reference positions appears as a trace of locally increased temperatures in the infrared image (Figure F.1).

This was used to estimate the flow direction at each reference position. Moreover, a small defect in the surface coating, consisting of a protruding particle, causes a small downstream vortex which locally increases heat transfer and therefore was visible as temperature value significantly lower than in the surrounding. At this position, the flow direction could be estimated likewise. The results for the axial inflow case and a variation of the MFR are shown in Fig. F.2.

The streamlines agree with the previous findings, showing a reduced turning for higher MFR on the endwall. This enables the coolant to reach to the pressure side corner. The results are in good agreement with the CFD, as it has been illustrated by Werschnik et al. [135].

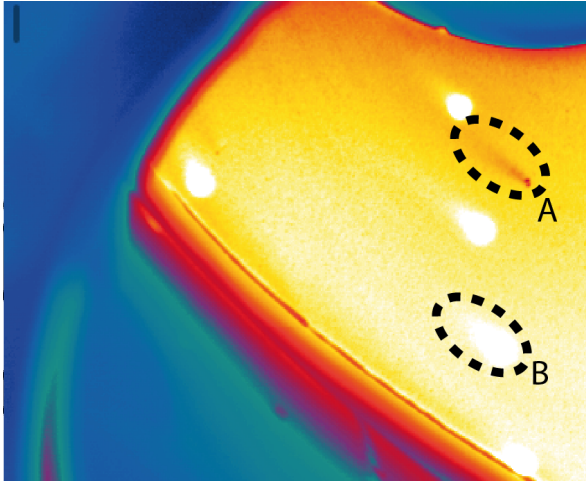


Figure F.1: Endwall streamline tracing: Temperature map showing vortex from surface defect (A) and temperature increase downstream of reference position (B), Werschnik et al.[133]

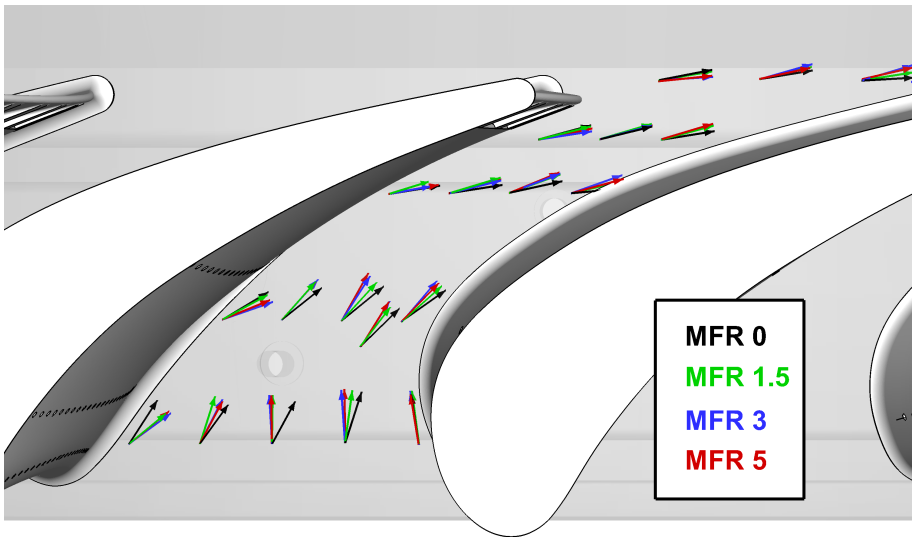


Figure F.2: Endwall streamlines for varied MFR, AX inflow

G Curriculum Vitae

Personal Information

Name: Holger Werschnik
Date of Birth: December 14th, 1985
Place of Birth: Mainz
Family Status: Married, one daughter (*2013)

Work Experience

2011 - 2017 Research Assistant, Institute of Gas Turbines and Aerospace Propulsion, Technische Universität Darmstadt

2005 - 2011 Student Intern & Dual Studies Program, Lufthansa Technik AG, Frankfurt am Main and Hamburg

Education

2008 - 2011 Master of Science, Mechanical and Process Engineering, Technische Universität Darmstadt

2009 Bachelor of Science, Mechanical Engineering, Virginia Polytechnic Institute and State University, Blacksburg, VA/USA

2007 - 2008 Dual Degree Program "Atlantis", Student exchange to Virginia Polytechnic Institute and State University, Blacksburg, VA/USA and Kungliga Tekniska Högskolan (KTH), Stockholm, Sweden

2005 - 2008 Bachelor of Science, Mechanical and Process Engineering, Technische Universität Darmstadt

1996 - 2005 Abitur at Max-Planck-Gymnasium, Rüsselsheim

1992 - 1996 Primary School in Kelsterbach

List of Publications

Werschnik H, Hilgert J, Wilhelm M, Bruscheckowski M, Schiffer HP (2017) Influence of combustor swirl on endwall heat transfer and film cooling effectiveness at the large scale turbine rig. *Journal of Turbomachinery* 139(8)

Hilgert J, Bruscheckowski M, Werschnik H, Schiffer HP (2017) Numerical studies on combustor-turbine interaction at the large scale turbine rig (LSTR): GT2017-64504

Werschnik H, Steinhausen C, Schiffer HP (2017) Robustness of a turbine end-wall film cooling design to swirling combustor inflow. *AIAA Journal of Propulsion and Power* 33

Werschnik H, Herrmann J, Schiffer HP, Lyko C (2017) The influence of combustor swirl on pressure losses and the propagation of coolant flows at the Large scale turbine rig (LSTR): ETC2017-139

Werschnik H, Hilgert J, Bruscheckowski M, Schiffer HP (2016) Combustor-turbine aerothermal interaction in an axial turbine - influence of varied inflow conditions on endwall heat transfer and film cooling effectiveness: GT2016-57171

Krichbaum A, Werschnik H, Wilhelm M, Schiffer HP, Lehmann K (2015) A large scale turbine test rig for the investigation of high pressure turbine aerodynamics and heat transfer with variable inflow conditions: GT2015-43261

Werschnik H, Ostrowski T, Hilgert, J, Schneider, M, Schiffer HP (2015) Infrared thermography to study endwall cooling and heat transfer in turbine stator vane passages using the auxiliary wall method and comparison to numerical simulations. *Journal of Quantitative InfraRed Thermography* 12(2)

Werschnik H, Krichbaum A, Schiffer HP, Lehmann K (2015) The influence of combustor swirl on turbine stator endwall heat transfer and film cooling effectiveness in a 1.5-stage axial turbine: ISABE2015-20184

Schmid G, Krichbaum A, Werschnik H, Schiffer HP (2014) The impact of realistic inlet swirl in a $1\frac{1}{2}$ stage axial turbine. GT2014-26716

Werschnik H, Ostrowski T, Schmid G, Schiffer HP (2014) Infrared thermography to study endwall cooling and heat transfer in turbine stator vane passages using the auxiliary wall method. *Conference on Quantitative Infrared Thermography, QIRT2014-007*

Schrewe S, Werschnik H, Schiffer HP (2013) Experimental Analysis of the Interaction between rim seal and main annulus flow in a low pressure two stage axial turbine. *Journal of Turbomachinery* 135 (5)